Ultraviolet and EUV studies of selected structures in the solar corona

Susanna Parenti

A thesis submitted in partial fulfilment
of the requirements for the degree of
Doctor of Philosophy.

Centre for Astrophysics
Department of Physics, Astronomy and Mathematics
University of Central Lancashire

June 2001

"It is so small a thing
To have enjoyed the sun,
To have lived light in the spring,
To have loved, to have thought, to have done."

Matthew Arnold, *Empedocles on Etna* (1852)

Abstract

New UV and EUV observations of off-limb and upper solar corona made by the UltraViolet Coronagraph Spectrometer (UVCS) and the Coronal Diagnostic Spectrometer (CDS) on SOHO (Solar and Heliospheric Observatory) are presented in this thesis. These data were used to establish the physical properties, such as temperature, density and element abundances, of different structures of the off-limb and upper corona.

For this project, the UVCS team provided UV spectra of the extended solar corona, which included lines of primary interest for the characterization of this region and the solar wind. CDS data consisted of NIS (Normal Incidence Spectrometer) EUV spectra of the low corona. The data included several density-sensitive and temperature-sensitive lines which enabled diagnostic studies to be made.

Absolute element abundances were derived from UVCS data; *relative* element abundances were derived from CDS data. The Differential Emission Measure (DEM) technique was used (for the first time on UVCS data) as the primary method for abundance study. Electron temperatures along the line of sight were derived applying the line ratio and the DEM techniques to both CDS and UVCS data. From the CDS data, electron densities along the line of sight were derived using the line ratio technique. For the UVCS data, the density was inferred using the O VI radiative and collisional components of the line.

One equatorial and two mid-latitude streamers were observed with the two instruments, in the low corona and at about 1.6 $R_\odot$. Electron density and temperature profiles with the solar distance were derived. They appeared to satisfy the hydrostatic equilibrium condition. The equatorial streamer appeared to be cooler than the mid-latitude one. Moreover, while the former tended to isothermal values already in the low corona, the latter was multithermal at the base and isothermal at 1.6 $R_\odot$. The derived composition at 1.6 $R_\odot$ showed a depletion with respect to the photospheric values for almost all the elements. The Fe/O ratio found here was consistent with values found in the solar wind. Moreover, a depletion in element composition with increasing solar distance was also found.

While observing off-limb in the south polar coronal hole, CDS observations of a macrospicule were obtained. For the first time the background emission was isolated from that of the macrospicule itself, and a diagnostic study of both regions was made. The ambient coronal hole appeared to have a density of $\approx 2 \times 10^8$ cm^{-3} that was about half the density found in the streamer base studied in this thesis. Multithermal components were found at the coronal hole base. The macrospicule spectrum indicated chromospheric

and transition region temperatures, and fluctuations in density along the feature were registered. In particular, the data showed the presence of an outward-moving cloud of cool material. Its time evolution and velocity were studied. The maximum (initial) outflow velocity was about 80 km s^{-1}, consistent with the outflow velocity measured in interplume regions.

An off-limb hot loop system was observed with CDS at mid-latitude. Its top and base were selected for diagnostic studies. Some newly observed hot lines were identified. The loop system appeared to be composed of multi-thermal plasma. The highest temperature registered was log T=6.4 at the top of the loop. A depletion of element abundances which mainly involves the plasma at the top of the loop was found.

A coronal hole bounded by a loop system was observed with CDS. Electron density appeared up to a factor two higher in the boundary than in the coronal hole, and the loop system appeared multi-thermal. The ambient coronal hole temperature appeared to be enhanced by the proximity of this loop arcade. Abundances were derived in both regions, and the coronal hole boundary showed slight depletions relative to photospheric values.

New coordinated observations with CDS and UVCS were made during one of the SOHO-Ulysses quadratures. Preliminary results regarding temperatures and densities of the core and boundary regions of streamers were obtained from UVCS data.

Contents

Acknowledgement

I wish first to thank my supervisors, Gordon and Barbara Bromage for their support, guidance and useful advice throughout these three years. I have appreciated their great patience with the difficulties I have encountered during this period, which they know have been many, and their willingness to help me.

My acknowledgement go to the University of Central Lancashire, for the financial support of a university studentship it granted me.

My thanks to Giannina Poletto. She is not only an excellent collaborator and advisor, but is also a friend, wonderful in the way she always encourages me.

Thanks to Prof. Giancarlo Noci, with whom I have had precious discussions. Also for his faith in my work, that enabled it to be presented at several meetings and conferences. I acknowledge the Dipartimento di Astronomia e Scienza dello Spazio of the University of Florence for the financial support.

I wish to thank John Raymond, for giving me the opportunity to work with him, and for the time he generously gave to answer all my (sometime silly) questions. His knowledge and experience have been very fruitful to my work. These thanks also extend to the Harvard-Smithsonian Centre for Astrophysics, Cambridge (USA) for hosting me. Thank to Peter Smith, that kindly made his office available to me.

I am grateful to the whole CDS team, for its support during the observations, and for providing the software to analyse the data. My acknowledgement to MEDOC and its staff, for hosting me and giving their technical support during the observations.

I am also grateful to the whole UVCS team, for their guidance and advice during the data reduction and the software it made available.

Thanks to the CHIANTI consortium for providing the atomic database used in this thesis.

I thank Pete Newman and Andy Adamson for their computing support as STARLINK Managers. I acknowledge the use of facilities provided by the PPARC STARLINK project.

Thanks to the EIT, LASCO and Ulysses consortium, for providing some of the images and figures used in this thesis. Yuan-Kuen Ko, the curator of the JOP 112 WEB page, and all the JOP participants for the useful material they made available on the JOP WEB page.

My friend Giulio, who has given me moral and practical support since the day I first arrived in Preston. Thanks to him for having shared good and bad times with me.

Thanks to Vinicio Barocas, for his help during the preparation of this thesis, for the good company and for sharing with me some of his life-story.

I thank all the friends and colleagues I met in England. It has been a pleasant surprise and great experience to share the differences in culture and personality. We had good time and I learned a lot from them. I would like to thank (a lot) all my friends in Italy, for keeping in touch with me during this long period. They gave me great support.

Finally, a special thanks to my parents and my family, for all they have done for me. At the beginning of my university career neither I, nor them, probably knew I would have reached this point. But they believed in me, giving continuous support and encouragement, keeping silent that they were missing my presence back home. This thesis is dedicated to them.

Chapter 1

Introduction

1.1 The Solar Corona: General Characteristics

The object of study of this research program was the solar corona, the external part of the solar atmosphere.

Decades of studies of the Sun revealed that it is a complex and dynamic system. Due to the different characteristics encountered, the solar atmosphere is classically divided into three regions: the *photosphere*, that is 'the naked eye Sun'; the *chromosphere* (just above the photosphere, coloured pink when seen during solar eclipse); and, the outer part, the *corona*, just visible during the eclipse. As we travel from the Sun's surface, the average density decreases and the average temperature increases gradually apart from a narrow region (the *transition region*) between the chromosphere and the corona, where the temperature rises dramatically from about 10,000 K to about 2×10^6 K. It is not easy to define the boundaries of this region in terms of altitude, because of the inhomogeneity in density and temperature in the external part of the solar atmosphere. The limit of the transition region is generally given in terms of temperature.

The variation of the physical parameters is evident when we look at the solar spectrum. When the Sun is observed in the visual waveband, we see mainly the yellow light emitted by the photosphere. In contrast, the emission from the corona is so faint (10^{-6} times that of the photosphere) that it is only visible during a total solar eclipse (or when an artificial occultation is provided, as in the case of the coronograph, see later in the section), when the solar disc is hidden and the photospheric light is blocked. Spectra of the chromosphere and corona are instead rich in UV and EUV emission lines, most of which are formed in the corona by atoms at a high level of ionization, indicating a temperature reaching a million degrees or more. Furthermore, the coronal emission extends also to the X-ray waveband. This emission is localized in some areas of the Sun (called *active regions* and *X-ray bright*

points) where the solar activity is high and produces an increase of the local temperature and hence the formation of highly-ionized elements. A drastic increase from EUV to hard X-ray emissions (just for a few minutes) is seen from time to time in active regions and it is caused by short time scale events (of the order of tens of minutes) called *flares*.

More generally, the coronal spectrum is due to three major components (Foukal, 1990):

- the K (*Kontinuierlich*) corona. This is visible at optical wavelength and is formed by scattering of photospheric light by fast moving coronal electrons. This process creates a polarized continuous emission spectrum that dominates the optical spectrum up to 2 $R_\odot$, where $R_\odot$indicates the solar radius, that is, the distance from the Sun centre to the photosphere.

- the F (*Fraunhofer*) corona. This visual unpolarized continuum radiation becomes important beyond 2 $R_\odot$ and is due to the scattering of photospheric light by the interplanetary dust.

- the E (Emission) corona, is the spectrum from UV to X-ray, comprising emission lines formed by the highly ionized ions in the actual corona.

Here we must mention the most intense line in the far ultraviolet solar spectrum: namely the H-Lyα at 1216 Å. This line is produced in the chromosphere, so when it was observed in the corona during the total eclipse of 1970 questions arose about its origin (Gabriel, 1971). It was surprising to find such a strong line (visible as far as 1.7 $R_\odot$) coming from neutral hydrogen in an environment of a million degrees where a very low fraction of neutral particles is expected. The solution to this dilemma is found in the realization that enough neutral hydrogen is left in the corona to explain the emission as excitation from Lyα photons emitted from the underlying chromosphere. To explain this the most efficient process was found to be resonant scattering, but it was also recognised that a much smaller (about the order of three magnitude smaller) contribution arises from electron scattering. This line is today one of the most powerful diagnostic tools for studying the corona plasma. This topic will be further developed later in this thesis.

In recent years much progress has been made in coronal studies, following the launch of new satellites such as the Solar and Heliospheric Observatory (SOHO) in 1995 (Domingo et al., 1995) and the Transition Region and Corona Explorer (TRACE) (Handy et al., 1999) in 1998. In particular, SOHO has the unique property of continuously observing the Sun (details in Section 2.1). Such progress was made because the high temperature emission from the solar corona can only be observed outside the terrestrial atmosphere. The corona in white light, UV and EUV can be observed with SOHO, using a coronograph,

which is an instrument that produces an artificial eclipse using an occulter in front of the solar disk.

Looking at the corona, it is evident that it is not composed of homogeneous plasma but that it consists of various *structures*, with different properties, that may change in number and/or size during the different periods of the solar activity. It is this inhomogeneity that makes difficult the understanding of the Sun's properties and the mechanisms that govern it.

It has been recognized that the Sun's activity is strictly related to the photospheric magnetic field, monitored by looking at dark spots of intense magnetic fields, called *sunspots*. Their variation in number, position on the disk (always between 0° and 30° in latitude), and polarity of their fields, is cyclic over approximately 11 years. The period of minimum of sunspots number is generally associated with a minimum in the solar activity. Moreover, to this oscillation is also associated a longer periodicity of 22 years of polarity reversal of the photospheric polar magnetic field. This field reversal occurs near the maximum of sunspot number and is about half-cycle out of phase with the polarity reversal of the spots. The evolution of the Sun's structures is related to the magnetic field. This can be strong enough to constrain the plasma in the corona. *Coronal streamers* are

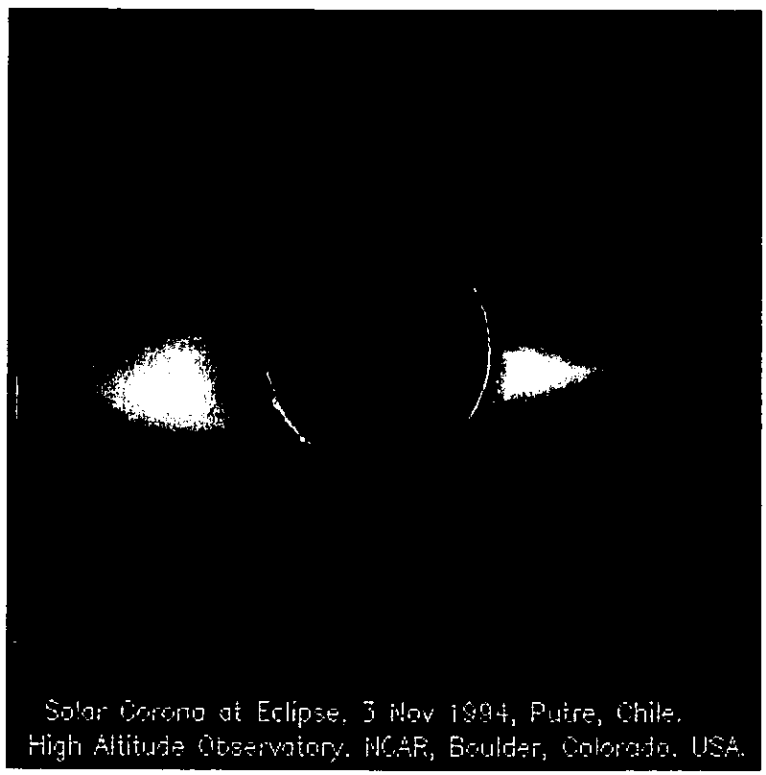

Figure 1.1: White light image of the solar corona during the 1994 eclipse. The bright streamers extend into the corona for several solar radii. The polar regions are filled by the darker coronal holes

one of the most evident manifestations of solar activity. Visible in white and UV light, they appear as bright, large and long-lived structures that extend into the solar corona for several solar radii. White light images (Fig. 1.1) show streamers shaped like pointed helmets, sometimes arch-like at the base, that taper off and elongate into the interplanetary medium. During solar maximum activity they can be found at almost any latitude, while during minimum they are located around the solar equator, where most of the activity is concentrated (see also Figure 1.2). They are believed to be the source of the *slow wind*, a flow of particles emitted from the Sun that reaches the Earth at a velocity of about 300 km s^{-1}.

Figure 1.2 is a composite image of the solar corona with superimposed the solar wind velocity measured at different solar latitudes by Ulysses satellite during its first solar orbit (McComas et al., 1998) (more details on this mission will be given later in the section and in Chapter 2). These measurements refer to a period of low solar activity. As already mentioned, the coronal streamers, bright in the Figure 1.2, are limited to the equatorial regions, where the plasma velocity is of the order of 300 km s^{-1}. One of the unresolved questions in studying the corona is the location of the source of slow wind. Part of this research project involves study of streamers (Chapter 5). The results here obtained give an indication of the contribution of streamers to the solar wind. More details on streamer studies are given in Section 1.2.

The large dark areas at the poles of the Sun shown in Figure 1.2 are called *coronal holes*, and delineate the less dense and active regions of the corona. They are characterized by occupying a large region where one polarity of the magnetic field dominates (blue and red color in Figure 1.2), and whose open field lines extend into the interplanetary medium allowing the plasma from these regions to flow out of the Sun more easily. This plasma is the source of the *fast solar wind*, that is, the wind with a velocity higher than 500 km s^{-1} (see Figure 1.2). During the minimum of the solar activity, like the case of the figure, the oppositely directed magnetic field and the fast wind divide the heliosphere, on average, into two regions with opposite polarity. These are separated by a neutral surface called *the heliospheric current sheet.* Figure 1.3 shows a EUV image of the corona with superimposed a modelled magnetic field topology by Guhathakurta et al. (1999). In the low latitude regions, where the activity of the Sun is predominant, the magnetic field has a closed topology, and the field lines connect regions of different polarities. The polar regions are occupied by darker coronal holes and the magnetic field filling them has an open topology.

The corona in an EUV image appears more structured and complex than in a white

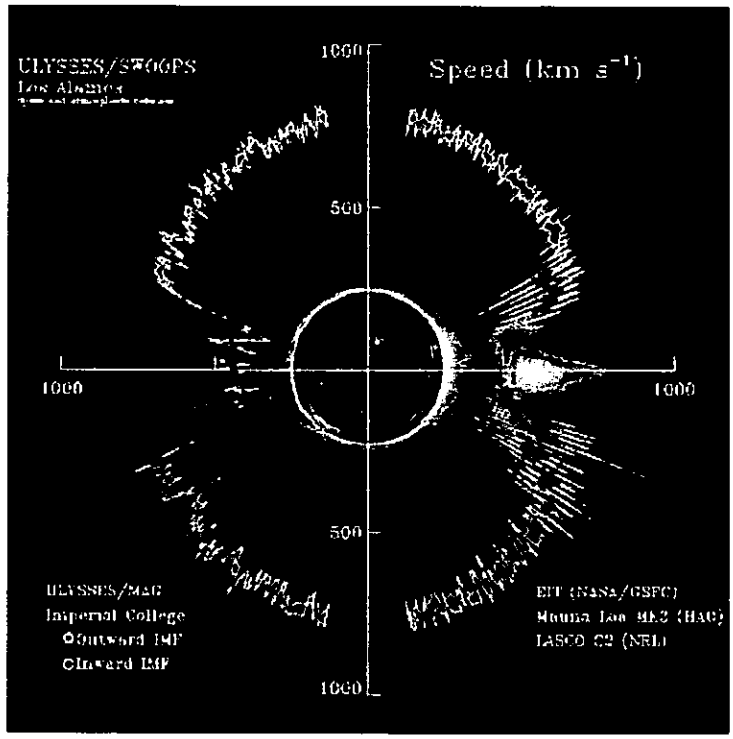

Figure 1.2: Polar overlay plot of solar wind speed data from Ulysses/SWOOP, and SOHO/EIT-LASCO Manua Loa images of the solar corona (McComas et al., 1998).

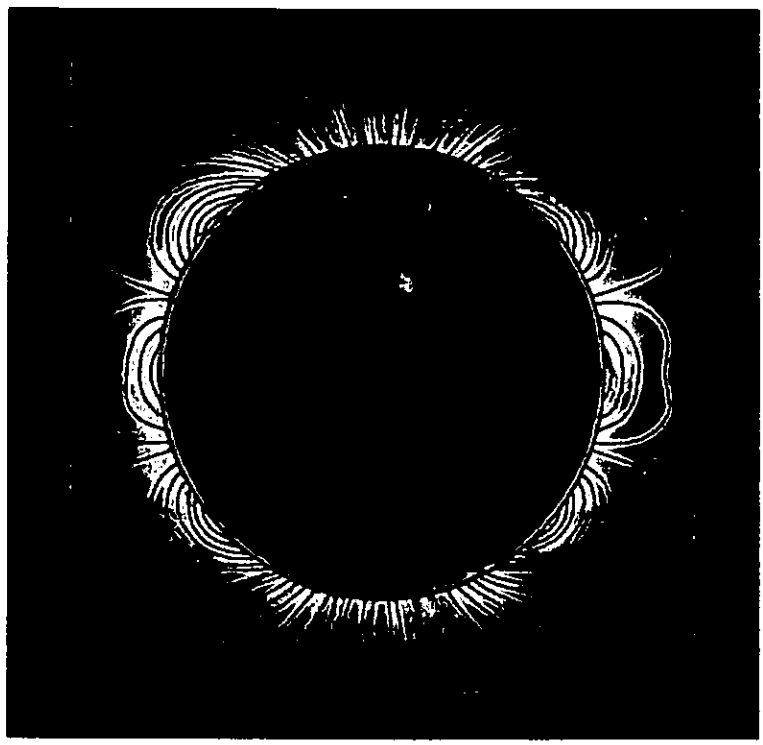

Figure 1.3: Solar magnetic field modeled by Guhathakurta et al. (1999). The model is fitted to the boundary of the polar coronal hole from WL and EUV observations indicated by the symbols *. Superposition of field lines on EIT image at wavelength 171 for August 18, 1996.

light image. The base of the streamers may be occupied by closed magnetic field regions, forming systems of *loops* at different temperatures, which may or may not be part of *active regions*, the brightest features visible in these images. Figure 1.4 *top* shows an example of an EUV image of the solar corona at 1.4 $\times 10^6$ K. Active regions are clearly recognizable as the brightest regions. These are areas where the solar activity is higher. Moreover, they are characterised by a strong magnetic flux. Figure 1.4 *bottom* shows a SOHO/MDI magnetogram of the photospheric magnetic field taken a few hours before the EIT image. The areas occupied by active regions in the EUV image are marked, on the magnetogram, by a strong bi-polar magnetic flux (white and dark spots).

In addition to active regions, several types of small scale structures have been recognized in the quiet Sun. No more details are given here since they are not of primary interest to this thesis.

Coronal holes, even if less active, contain features such as *plumes* (see Fig.1.4) and *macrospicules*. These will be introduced and described later in the next Sections.

Figures 1.1, 1.5, 1.4 show respectively how the solar corona may appear: in the white light image from ground based observation; from SOHO/LASCO (2-6 $R_\odot$, 4-30 $R_\odot$); and from SOHO in EUV wavelengths. In Figures 1.1 and 1.5 *top*, the bright streamers are easily recognizable. The first Figure was taken during the minimum of solar activity, when the streamers were confined to the equatorial regions, while the dark poles were occupied by coronal holes. During the following ascending phase of the solar cycle, the streamers expand towards higher latitudes, as shown in Figure 1.5. At EUV wavelengths coronal holes are well defined as dark patches at the poles (Figure 1.4). The brighter rays inside it are plumes. The bright narrow polar crown that marks the boundary of the hole is also visible at the north polar hole. The solar corona expands into the interplanetary region as the solar wind. Information about physical parameters of the solar wind derives from *in situ* measurements by rockets and satellites. The first measurements of this type were performed in the nineteen sixties by Soviet Union rockets that measured a flux of positively charged particles of about 10^8 cm^{-2} s^{-1}. In 1961 the first measurement of flow speed was performed by Explorer 10, which found a value of 280 km s^{-1} (Hundhausen, 1972). These results were later confirmed by the spacecraft Mariner 2, launched in 1962 to explore Venus. In addition, it is worth mentioning the *Helios* satellites (Rosembauer, 1977), which were launched in 1974 (Helios 1) and 1976 (Helios2) to explore the interplanetary medium between 0.3 and 1 AU. Their measurements confirmed that the interplanetary magnetic field polarity of the Sun reverses in the equatorial regions and that each polarity, mapped back to the solar surface, originated in a single hemisphere (Figure 1.2).

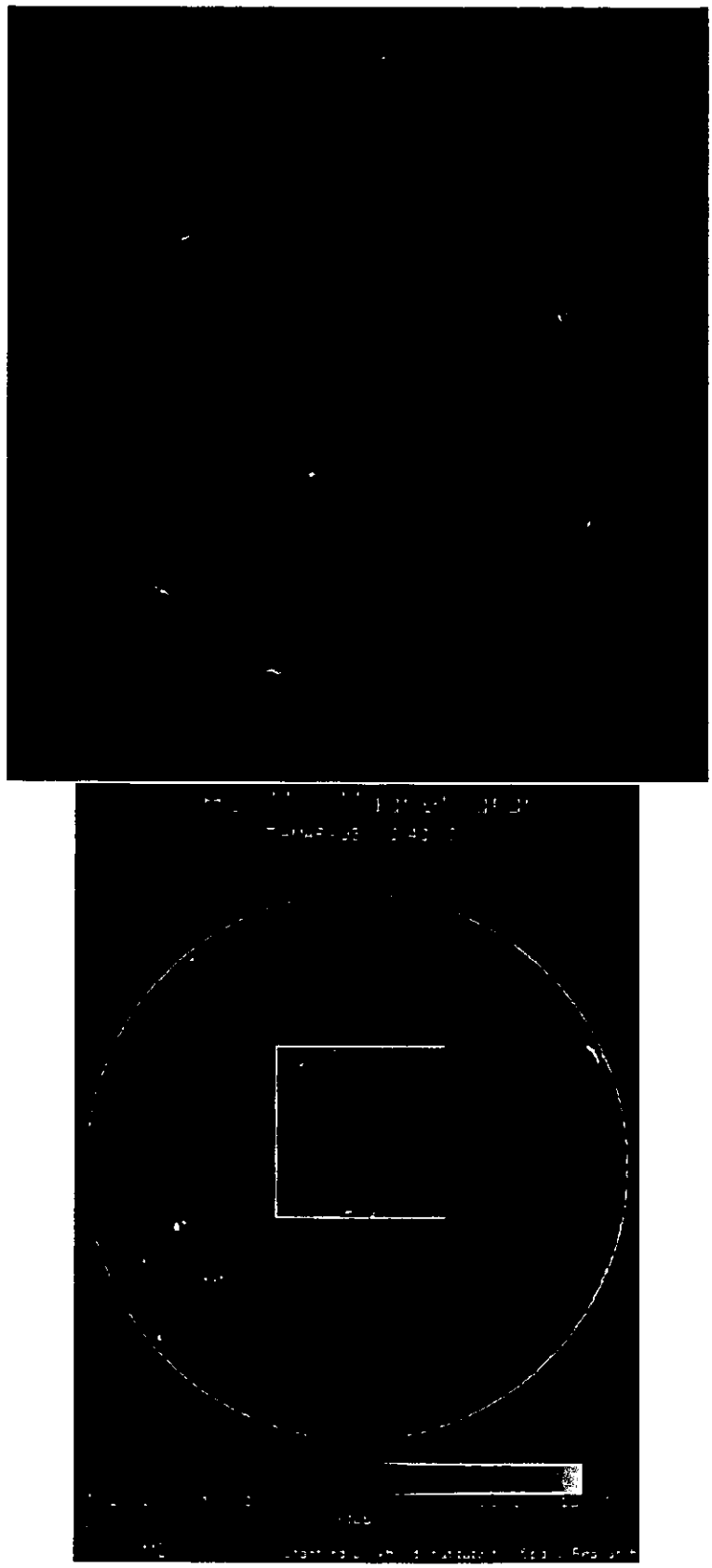

Figure 1.4: Top: SOHO/EIT image of the solar corona in the EUV at 195 Å on 1998 March 6 at the 23:32 UT. The coronal hole are recognizable as dark regions at the poles. Active regions are seen as bright spots. Bottom: SOHO/MDI magnetogram on March 7 at 12:48 UT

Figure 1.5: SOHO/Lasco C2 (top) and C3 (bottom) white light images of the solar corona on 2001 January 1. The C2 coronograph extends from 2 to 6 $R_\odot$; C3 from 4 to 30 $R_\odot$

Since placing a satellite in polar orbit is more complicated and expensive, *in situ* measurements of all these satellites were located in the ecliptic plane. However, in 1990 with the advent of the *Ulysses* mission (Wenzel et al., 1992) (Section 2.4), measurements in the solar polar regions were first performed. Ulysses moves in a polar orbit reaching up to $\sim 80°$ of solar latitude. Naturally this mission gave a new impetus to the knowledge of solar wind and the interplanetary magnetic field.

One of the main results from this mission was the measurement of the solar wind from the equator up to 80° of heliospheric latitude. This is what Figure 1.2 shows. The measurements confirmed that the solar wind has two main components, and that the transit between the two happens within a short range of latitudes (McComas et al., 1998). Moreover, one of the recent Ulysses results shows the slow wind fluctuates in velocity much more than the fast wind.

One of the most important opportunities provided by Ulysses is the sampling of plasma at several AU from the Sun, one or two weeks after the same plasma was observed by the SOHO satellite near Earth. This opportunity occurs when the SOHO-Sun-Ulysses angle is 90°. Such "quadrature" configurations have become a suitable time for coordinated observations that involve several instruments on board the two satellites. Part of this PhD project involved the analysis of data from the June 2000 quadrature (see Chapter 7). More about the Ulysses mission itself is presented in Chapter 2.

The best approximation in order to model the complex solar corona is found in the physics that describes the motion of a continuous single fluid plasma in a magnetic field: the *MagnetoHydroDynamics*, or MHD. Electromagnetic equations together with plasma equations and energy equations are solved under some main conditions (Priest, 1982): the electromagnetic variations are non-relativistic; the electric field is secondary to the magnetic field; the local accumulation in time of charge is negligible and the gas is considered a *plasma*, that is an ionized gas for which λ_D, the Debye length ($\lambda_D = (kT/(4\pi ne^2))^{1/2}$), is much smaller than other scales of interest.

Pneuman & Kopp (1971) presented the first MHD model of the global corona in which streamers were represented by open and closed field regions separated by thin current sheets. This model, however, did not reproduce the depletion of the electron density in coronal holes, but it did reproduce many quiescent streamers in white light. Various improvements have been made in recent years, e.g. adding a heat source function for the corona to reproduce both fast and slow winds. In addition, a variation of density with latitude was in addition introduced by Suess et al. (e.g. 1996) so that the streamers were then predicted to be the source of the slow wind. Predictions of coronal holes still

did not completely reproduce the observed parameters. Wang et al. (1998) developed a global 2-D MHD model of the solar corona for one fluid, fully ionized plasma, whose properties are governed by thermal conduction, volumetric heating and by a momentum source addition. This last term, non time-dependent, together with the volumetric heating, can reproduce the empirical wind speeds, density and temperature conditions in coronal holes and streamers. However, as the authors remark, these terms are arbitrarily specified, and more constraint to their properties need to be added with the help of observations. The modeled physical parameters derived here for the streamer will be used in Chapter 3, to test the ionization equilibrium conditions in those regions.

The last model mentioned here is the empirical Cranmer et al. (1999) model for coronal holes. The observational values used to build the model come from the UVCS instrument on SOHO and were taken during a period of minimum activity. The electron density as function of latitude and radius, the hydrogen velocity distribution, the oxygen velocity distributions and abundance, for coronal hole and polar plume were derived in the model. Some more details are given in Chapter 3 where part of this model will be used, together with Wang et al. (1998), to test the ionization equilibrium conditions in the solar corona.

1.2 Coronal Streamers

Until a few years ago, most information on streamers came from visible observations of the continuum during a solar eclipse. These yield profiles of density v. height in streamers, imaged at different times during the solar activity cycle. Following the launch of SOHO in 1995, considerable new information on streamer properties has become available. For example, a "Whole Sun Month" campaign in 1996 was specifically designed to study the structure of the solar atmosphere at solar minimum, and, as a consequence, descriptions of the 3-D structure of streamers, of their magnetic field, and further density and temperature profiles in streamers have been obtained (Gibson et al. 1999a; 1999b).

However, an unexpected result (Noci & al., 1997) revealed by UVCS, showed that the hydrogen Lyα (1215 Å) streamer morphology can be quite different from that seen in O VI lines (at 1032 and 1037 Å): the *maximum* Lyα intensity in the streamer's core may correspond to a *minimum* in O VI line intensities. Raymond et al. (1997) found that the oxygen abundance in the streamer core is typically depleted by a factor ≈ 3, with respect to its coronal value. Further work showed that element abundance can vary from streamer to streamer (Raymond et al., 1998; Li & Hu, 1998) and even within a streamer (Raymond et al., 1997): along the streamers' edges they resemble the slow wind abundances.

This result if confirmed has an important consequence. In fact, there is even observational evidence that the slow wind originates from streamers, although the source of this wind inside the streamer is not yet localised. If Raymond's results are confirmed, then the scenario where the slow wind originates in or around streamers will be more clear. Moreover, Wimmer Schweingruber (1994) has shown that the interface between what was originally slow plasma from the streamer belt and what was fast plasma from coronal holes, is fairly well identified by variations in composition, even at the great heliocentric distances sampled by the Ulysses satellite.

One of the early theories of the slow wind source was that it flows from the edges of the streamer (Hundhausen, 1972; Gosling et al., 1981). This was mainly deduced by its association with the heliospheric current sheet, which lies within the streamer belt. Further observational evidence in the upper corona is in agreement with this picture (Woo & Habbal, 1997; Habbal et al., 1997). However, the problem which is still unresolved relates to the mechanism that generates it. Uchida et al. (1992) proposed that the slow wind originates from loop destabilization at the streamer base.

On the other hand, Noci & al. (1997) proposed a model in which the slow wind originates from an open field region inside the streamers. The model they proposed is based on observational evidence that streamers may be filled, at their base, by loop systems, bounded by open magnetic regions. The open field lines converge at about 4 $R_{\odot}$. In this picture, the slow wind flows between the loops along the open field lines.

This problem of the origin of the slow wind from the streamer is not yet completely solved. In this thesis, streamer studies are performed with the aim of defining their physical parameters, including element composition. As will be explained in Section 1.4, element composition is a "proxy" that distinguishes fast wind from slow wind. Following Raymond et al. (1997), in this work the candidate tries to extract information about physical parameters in different parts of the streamers, that may contribute to the solution of the problems mentioned above (Chapters 5 and 7).

1.3 Coronal Holes

Coronal Holes are clearly visible as dark regions on the solar disk when observing in UV and EUV lines (Figure 1.4), which are emitted mainly by the transition region and coronal plasma. They may be persistent for several solar rotations and may be located at different latitudes. Preferentially, during the phase of solar low-activity they occupy the polar caps, while during an intermediate period between maximum and minimum of solar activity

they may appear at low latitudes, in the equatorial region. During the maximum of solar activity the polar holes disappear to reappear later with inverted magnetic polarity.

As already mentioned, coronal holes are believed to be the source of the fast wind. But, like the slow wind, the location of this source is not yet well established. Originally, polar plumes were considered as possible sources for the wind (Walker et al., 1993), but later the new possibility of a fast wind originating in interplume regions has become more popular (e.g. Fisher & Guhathakurta, 1995; Hassler et al., 1997). So far, the problem is not solved. More details on this topic are given in Section 1.3.3.

1.3.1 Electron Temperature Measurements

Determining the temperature in coronal holes, especially at their base, is a fundamental part of understanding the acceleration process in the solar wind which may promote the mass flux observed at 1 AU (e.g. Withbroe, 1988). Temperatures in coronal holes have been obtained using different techniques, from optical light to X-ray data. Habbal et al. (1993) reviewed these temperatures and concluded that within 1.2 $R_\odot$ the average temperature is below one million degrees, reaching approximately one million degrees between 1.2 and 1.6 $R_\odot$, even though the polar base can have different values. More recent results (Del Zanna & Bromage, 1999b) of on- disk emission measure (EM) measurements (that is a measure of the amount of plasma along the line of sight that emits the observed intensities) of CDS data (see Chapter 3), gave a peak of EM at about 8×10^5 K with very low emission measure at a million degrees. The temperature derived for the coronal hole boundary was $1.1\times\ 10^6$ K, while the same study made with Yohkoh SXT observations, the soft X-ray telescope of a Japanese mission that observes the Sun in X-rays and gamma-rays, gave slightly higher values of $1.37\times\ 10^6$ K (Bromage et al., 2000).

1.3.2 Electron Density Measurements

Early density measurements for coronal holes were carried out using data from Skylab (Bhattacharya, 1973), the first US space station (1973) that included eight solar instruments. For example, Mariska (1978) gave a density of 1.7×10^8 cm^3 at 1.3 $R_\odot$, a value very close to more recent data.

Several studies have been carried out using different instruments on board SOHO. From the line ratio technique (Chapter 3) using UV and EUV spectra, chromospheric, transition region and coronal densities have been derived (see reference below), even if in the latter case, the faintness of the line intensities gives more uncertainty to the results.

Results from SOHO/SUMER (Solar Ultraviolet Measurements of Emitted Radiation,

Wilhelm et al. (1995)) a UV spectrometer, and SOHO/Coronal Diagnostic Spectrometer (Harrison et al., 1995), an EUV spectrometer (see Chapter 2), showed that at the solar base the density ($\approx 2 \times 10^8$ cm^{-3}) is about half that in the quiet Sun region and that it declines exponentially with increasing heliospheric distance (Doschek et al., 1997, 1998a; Del Zanna & Bromage, 1999b; Fludra et al., 1999a).

1.3.3 Coronal Hole Substructure

Polar plumes have been observed within coronal holes in visible light for many years (e.g. Saito, 1965; Koutchmy, 1977) and also in EUV lines Walker et al. (e.g. 1988, 1993). Their main characteristics are recognizable as being denser than the surrounding (ambient) hole, and of expanding 'superradially' (Fisher & Guhathakurta, 1995; Ahmad & Withbroe, 1977). Their appearance suggests that they are composed of unipolar magnetic flux tubes that may be underlaid by dipoles at the base (Habbal, 1992; Fisher & Guhathakurta, 1995).

A more recent investigation (Deforest et al., 1997) in which several instruments on board SOHO were involved, together with daily average images from the White-Light Coronograph Mk 3 at the Mauna Loa Observatory (Hawaii, USA), confirmed previous results and gave a more complete view of their morphology and properties. Moreover, those authors found that plumes lie on the cell boundary in the chromospheric network, are quite stable for several days, expand superradially and are visible out to 10-15 $R_\odot$. They are denser and cooler than the interplume regions.

Further research has increased the available information about these features. An anti-correlation between intensity and line width in the plume/interplume regions below 1.4 $R_\odot$ was discovered by Hassler et al. (1997) and Wilhelm et al. (1998b). Up to then plumes were thought to be the origin of the fast wind. This new result questioned the origin of the fast wind in the plume.

In addition, recent results from Habbal & Woo (2001) give even more insight into the origin of the solar wind. The authors combined the latitudinal distribution of pB from High Altitude Observatory Mk III Mauna Loa K-coronameter and solar wind data from SWOOPS on Ulysses, during a period of low solar activity. New results show that the fast wind not only originates from coronal holes, but also from the adjacent quiet Sun. Electron density seems to be the principal factor that determines the solar wind speed. Moreover, they emphasize that the coronal hole boundary cannot be identified at the same physical location as that of the streamer boundary.

Another interesting aspect of the corona is, in fact, the interface between the coronal

hole and the surrounding regions. Close to the solar surface, this boundary is sometimes recognizable because it is formed by an arcade system that follows the shape of the adjacent coronal hole. This arcade connects the unipolar magnetic field of the hole to the neighbouring bipolar field of the surrounding regions. Sometimes a dark prominence channel is also visible running along the arcade system (Bromage et al., 2000).

Woo et al. (1999) studied such a boundary by combining images from the Mk III Mauna Loa optical K-coronameter, Yohkoh soft X-ray telescope, SOHO/LASCO C2 and C3 coronagraphs and the Kitt Peak daily H I 1083 nm coronal-hole maps. From the observations they identified the boundary from an enhancement of the azimuthal density profile, as derived from radio occultation measurements. This enhancement may not coincide with the border visible in white light, which is often marked by a strong contrast between bright streamer and dark hole. This increase in density depends on whether there is a streamer, an active region or the quiet sun immediately adjacent to the hole. Woo et al. (1999) also derived information about the radial extension of this boundary into the interplanetary medium. This was a controversial result because other authors found that the boundary diverged in following the adjacent streamer edge (e.g. Gosling et al., 1995). Such a 'radial' expansion of the boundary, together with the solar wind measurements in which a fast wind was found to emerge even at low solar latitudes (Geiss et al., 1995; McComas et al., 1998), support the contention that the quiet Sun is also contains open magnetic field (Habbal & Woo, 2001).

If the coronal hole boundary is instead defined by means of measured line intensities, different results are obtained. Bromage et al. (2000) studied the "Elephant's trunk" coronal hole that extended from the pole to the equatorial regions, observed during the "Whole Sun Month" campaign of 1996. Using SOHO/EIT-CDS and Yohkoh SXT data, they studied the expansion of the coronal hole boundary up to 1.01 $R_{\odot}$with the result that an inclination of 37 deg $\pm$ 3 from the radial direction was found at this distance from the Sun.

Dobrzycka et al. (1999) mapped the boundary from 1.75 to 2.25 $R_{\odot}$ using Lyα and O VI lines and the Lyα intensity distribution with latitude. They found that the two lines behave similarly, by mapping a superadial expansion of the boundary that reached 60 deg from the radial direction at 2.25 $R_{\odot}$.

From these studies it is clear that there is some confusion on the definition of coronal hole boundary. However, it appears that more work needs to be done to establish the physical conditions at the boundary. Part of Chapter 6 of this thesis is deals with a spectroscopic study of the coronal hole boundary. The main aim is to establish how much

the coronal hole properties are different from those of its boundary.

1.3.4 Macrospicules

This section deals with the *macrospicules*, short-lived features of the coronal holes. These features are unique in their properties and part of this research project is to study one of them (Chapter 5). As will be shown below, knowledge about them is scarce. The aim of this research is to establish their physical properties, which have not yet been completely defined in previous studies. This was helped by the fact that the available data allowed the separation of the macrospicule plasma emission from the background emission. This has lead to unique results.

The first observation of EUV macrospicules was made by Bohlin et al. (1975) who attributed this name to jet-like features of the coronal hole that looked similar, although larger than, Hα spicules. Since then more EUV observations have been made with the result that some of the main characteristics could be defined, even if a complete knowledge of this phenomenon is still not available.

An EUV macrospicule appears to be a column of chromospheric material extending from the limb into the corona. Their widths range between 5″ and 15″ and they are between 5″ to 60″ in length, with a lifetime from a few minutes to about 40 min (Dere et al. 1989, Bohlin et al. 1975). The determination of the characteristic temperature and density range of the macrospicule plasma is more difficult. The brightest images of these features in the corona are given by the He I (log T = 4.5), He II (log T = 4.9) and O V (log T = 5.4) lines. Bohlin et al. (1975) did not find evidence of emission above 3×10^5 K. However, more recently Pike & Harrison (1997) have observed macrospicule emission in a Mg IX line, emitted at around 1 MK.

Karovska & Habbal (1994) studied the evolution of C III (T=7.4×10^4 K) macrospicules using the Harvard/S-O55 spectroheliometer on Skylab. With its 5″ telescope resolution, they were able to resolve the fine scale morphology of these structures and their evolution. The macrospicules often consisted of an arch-like base, that extended into the corona as a column-like structure. These structures were also characterized by ejection of material followed by the disappearance of the macrospicule, on a time-scale of a few minutes. This study seems to suggests that macrospicules are dynamic events that evolve rapidly. Habbal & Gonzalez (1991) observed some macrospicules at radio frequencies of 4.8 GHz which had the same dimensions as the EUV macrospicule. Moreover, they found that these structures were composed of a cool core (4-8$\times10^4$ K) surrounded by a hotter sheath (1-2$\times10^5$ K) that released plasma from the upper part of the structures. This multithermal structure

of the macrospicule was also observed in the EUV waveband by Pike & Harrison (1997).

Velocity studies of macrospicules have revealed red and blue Doppler shifts on opposite sides of the feature's central axis (Pike & Mason, 1998; Pike & Harrison, 1997; Banerjee et al., 2000). The apparent velocities deduced increase with solar distance and reach a maximum value between 20 and 30 arcsec above the macrospicule footpoints. Pike & Harrison (1997) referred to this apparently rotating plasma as a *solar tornado.*

Macrospicules have also been identified as Hα features (e.g Cook et al., 1984). Studies addressing the relationship between Hα and EUV macrospicules have produced conflicting results. Wang (1998) found that each of the He II (304 Å) macrospicules they observed had a Hα counterpart, while Moore et al. (1977) found that this was not always the case. In the light of all these unresolved properties of macrospicules, Georgakilas et al. (1999) suggested that there might be two subclasses of He II macrospicules: polar surges and giant spicules. The former appear as complex structures, with strong velocity gradients. The latter are jet-like features, more similar to spicules, but larger.

1.4 Element Abundances in the Corona and Solar Wind

The knowledge of the element abundances in the Sun gives a fundamental contribution to the understanding and explanation of the solar observations. Variations in the composition of the solar atmosphere and solar wind appear to exist, so that a proper understanding of these variations are important for the following main reasons:

- Most of the UV, EUV and X-ray radiation comes from optically thin plasma in the corona. In this case, the element abundance is a parameter that is proportional to the line intensity of the emitting plasma. This implies that the understanding of the coronal composition plays an important role in the use of the plasma diagnostics, such as temperature and density estimates (see Sections 3.5, 3.4) at those wavebands, and a wrong value could seriously affect the results.

- Element abundance variations provide a means to connect coronal features with solar wind structures. This may help to understand the origin of the solar wind, because it can connect its characteristics with those of coronal structures in the low corona.

- Element abundance is a factor in the radiative cooling rate that is used in modeling the coronal heating.

The source for the study of the solar composition is the photosphere, where most of the heavy and a few of the light elements are believed to reflect the composition of the

solar nebula from which the solar system emerged. However, not all element abundances can be measured from photospheric spectra. The noble gases He, Ne, Ar, are not visible because the lower excited levels of the neutral atoms are not populated at photospheric temperatures. Therefore, the abundance of those elements is derived from other astrophysical sources or indirectly from an interpretation of the abundance in the upper layers of the solar atmosphere.

Another source for the study of photospheric composition is the C1 Carbonaceous chondrite meteorites, which were formed from the same nebula and are thought to preserve the original nebular composition. It is known that the solar nebula contained $\approx$ 90% hydrogen, $\approx$ 10% helium and $\approx$ 0.1% heavier elements (by number of atom/ions). Table 1.1 (Feldman, 1992) shows the first ionization potential and logarithmic solar abundance (relative to hydrogen) that will be taken as reference for the photospheric composition in the abundance studies throughout this thesis.

Table 1.1: First Ionization Potential (FIP) and photospheric abundances (used as reference set for the photosphere used in this thesis), relative to hydrogen (log (Abundance) =12.00) (Feldman, 1992).

Element	F.I.P. (eV)	log (Abundances)
1 H	13.6	12.00
2 He	24.6	10.99
6 C	11.3	8.60
7 N	14.5	8.00
8 O	13.6	8.93
10 Ne	21.6	8.11
11 Na	5.1	6.33
12 Mg	7.6	7.58
13 Al	6.0	6.47
14 Si	8.2	7.55
16 S	10.4	7.21
18 Ar	15.8	6.65
20 Ca	6.1	6.36
26 Fe	7.9	7.51
28 Ni	7.6	6.25

As early as the 1960s the UV-EUV spectra obtained from rocket flights showed anomalies in the measured composition of the upper-solar-atmosphere. Pottasch (1964) for example, reported abundances of Mg, Al, Si and Fe higher than photospheric values by a factor of three (Goldberg et al., 1960).

Further studies in the following decades confirmed and extended this result. Until then, it was assumed that the composition did not vary spatially in the upper layer of the Sun. Having realised that this assumption was not valid, the astronomers renewed their interest in the topic.

The main studies involved confirming the composition anomaly of the outer atmosphere used measurements of the slow wind (SW) at the Earth's distance and also measurements of the Solar Energetic Particles (SEP), which are believed to originate in the solar corona. The SEP are shock-accelerated ions which propagate towards the Earth along the interplanetary magnetic field. They may originate in the ≤ 2 MK coronal plasma above active regions or in hot (>10 MK) plasma during flares.

Several reviews (Meyer, 1985b, 1996; Haisch et al., 1996; Feldman, 1992; Fludra et al., 1999b) collect together the main results from these studies and from UV and EUV spectrosopy, and they agree on the following main points:

- The composition of the outer solar atmosphere suggests that the elements can be divided into two groups according to their *First Ionization Potential* (FIP). For the elements with first ionization potential below 10 eV (low FIP elements) their abundance, compared with photospheric, is 3-4 times higher than for those with first ionization potential $\geq$ 10 eV (high FIP elements).

- It is unclear whether the low FIP elements are enhanced relatively to hydrogen, or conversely if the high FIP elements are depleted relatively to hydrogen.

- Different regions of the solar corona show a different FIP pattern. This result seems to be related to the magnetic field topology.

- Composition of the solar wind has the same kind of pattern as the corona. In particular, the slow wind shows an enrichment of the low FIP elements by a factor 3-5 with respect to the photosphere. This overabundance of the low FIP elements is only about a factor 1.5-2 in the fast wind.

A schematic view of the FIP effect is shown in Figure 1.6. Studies of coronal structures have revealed that on the largest scales, the closed field regions manifest a higher FIP bias compared to that of the open field regions like coronal holes (Meyer, 1985a; Widing & Feldman, 1992b). Many contributions to this topic derived from the analysis of data from the spectoheliograph on *Skylab*. Widing & Feldman (1989) analyzed several open and closed field structures, giving a large scatter in values for the Mg/Ne ratio (low/high FIP). In particular they found values of 5-10 times the photospheric value for the diffuse,

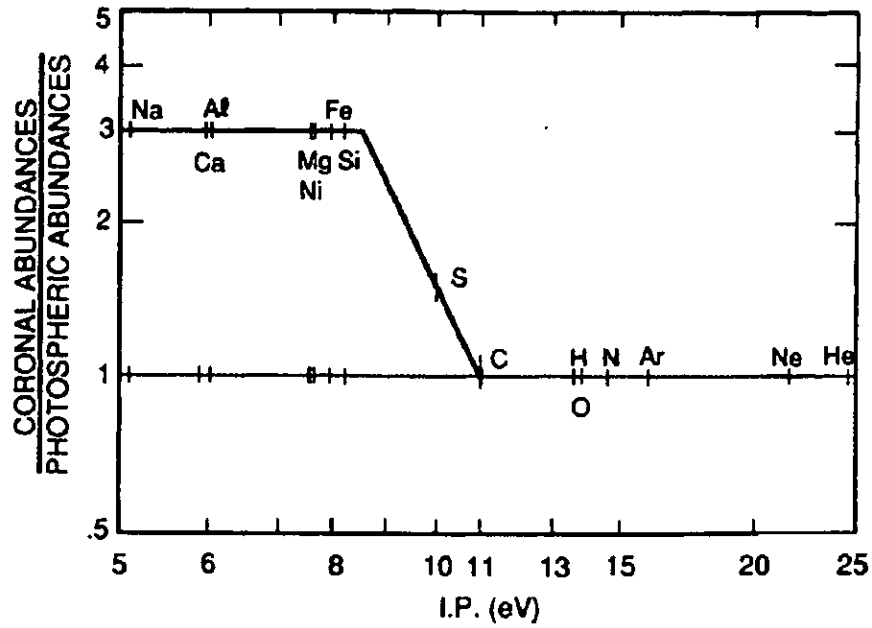

Figure 1.6: A schematic representation of the solar wind and SEP relative to those in the photosphere. Values are plotted against the First Ionization Potential. Figure taken from Feldman (1993)

open-field structures, but only 0.3-0.5 for the closed-field, active regions and in impulsive flares. They attributed the variation of the ratio to changes in Ne, while Mg maintained its photospheric values. Feldman & Widing (1993) derived the Mg/Ne values for the quiet sun and coronal holes. Their results showed that the FIP bias was about 2.5 in the quiet regions and about 2 in coronal holes. On the other hand, these results do not apply to the smaller coronal structures. The denser, unipolar polar plumes observed in the coronal holes yielded one of the highest FIP biases ever recorded (Widing & Feldman, 1992a; Del Zanna & Bromage, 1999a). This is an important issue when the elements abundance are compared with the solar wind composition in order to understand the wind origin.

More recently, with the SOHO mission, renewed importance has been given to the determinations of the coronal composition. Feldman et al. (1998), using SUMER spectra taken in 1996 at less then 1.03 $R_{\odot}$, did not find any signature of FIP bias above the polar coronal hole, while a value of about 4 was found for the low/high FIP ratio. For this study the high FIP oxygen was taken as reference element.

Another interesting aspect of the FIP effect at places where the effect is more evident, is a further enhancement ($\approx$ 2.5) that can be seen in the very low FIP elements (Al, Ca) (Falconer et al., 1997; Doschek et al., 1985; Monsignori Fossi et al., 1994; Fludra & Schmelz, 1995).

As mentioned before, the SW and SEP have been the main sources for the coronal composition. Until the launch of Ulysses in 1990, which has a solar polar orbit, the solar wind observations came from satellites orbiting in the ecliptic plane. In that case the results obtained reflected the composition from the low corona that extended from the solar equatorial regions. No direct information about the polar regions were available prior to Ulysses.

With the Ulysses measurements, unknown properties of the solar wind were observed. A strong positive correlation was found between *(a)* low/high FIP element abundance ratios and *(b)* coronal temperature, and in addition an anticorrelation with the solar wind velocity (von Steiger et al., 1995).

The more up to date results on solar wind measurements can be found in von Steiger et al. (2000). The authors derived the average wind charge state and the average element composition of about 40 ion species, using long period data from Ulysses/SWICS. They found that the FIP bias of low FIP element relative to photospheric abundance is present in both fast and slow wind. The FIP bias of the low FIP elements is only a factor of 2 in the slow wind with respect to the fast wind. This turned out to be a new result, because previous studies indicate higher FIP bias of the order of 3-5 (Geiss, 1998; von Steiger, 1998). Moreover, a higher variability of elements abundance was found in the slow wind in relation to the fast wind.

The FIP bias between photosphere and corona is believed to be caused by an ion-neutral fractionation process, in a medium where neutral and first ions coexist. As a consequence, excluding the thermal diffusion process in the transition region where the temperature gradient is high and all the elements will be ionized, the chromospheric plateau at T $\sim$ 7000 K is considered to be the possible site where the ion-neutral fractionaction process occurs, because at that temperature the low FIP elements are ionized, while the high FIP elements are still neutral (Meyer, 1991; Feldman, 1992). Moreover, considering that the chromospheric material moves up into the corona and then, ionized, falls back, the ion-neutral fractionation must take place only on the way up. Following Meyer, 9$\sim$10 eV is the border between low and high FIP elements, and can be related to the 10.2 eV energy for the Balmer level of H, that is considered to be responsible for stabilising the temperature of the chromospheric plateau (Athay, 1981) and hence for controlling the element ionization.

A recent model (Schwadron et al., 1999) for elemental fractionation seems to be able to justify the high variability in the composition of the slow wind found by von Steiger et al. (2000). In the model, the slow wind is formed by reconnections of large coronal loop,

wave heated, with open magnetic field. The low FIP elements are almost ionized close to the transition region, and the wave heating causes them to have a larger scale height than the high FIP ions, that are almost neutral there. In addition, this depends on the loop size. Because the slow wind can be formed by an array of loops different for temperature and height, these can justify the variability of the measured composition of the slow wind. On the other hand, the low presence of loops in coronal holes together with the small variation in composition observed, suggests that the fractionation happen somewhere else. The idea of the chromospheric fractionation is then again taken into consideration.

Gravitational settling is a mechanism that is also considered to be responsible for the discrepancy in the FIP bias between the corona and the solar wind. Support for this cames, for example, from the results obtained at 1.3 $R_{\odot}$(Feldman et al., 1998) and at 1.5 $R_{\odot}$(Raymond et al., 1997) for the ratio O/H. Feldman et al. found an approximately photospheric value, while Raymond et al. found a greater depletion of oxygen.

Despite all these observational results, many questions remain unanswered. It is still not clear if the FIP bias is caused by an enhancement of absolute abundances of low FIP elements or by a depletion of the high FIP elements with respect to photospheric values (see for example Fludra & Schmelz (1999); Schmelz (1999)). The difficulty comes mainly from the hydrogen measurements which at coronal temperature do not have any corresponding spectral lines, and so the continuum is used. However, what is generally given in list of coronal abundances is the relative abundance of the elements. In addition, only recently with the SOHO mission, the H-Lyman lines were measured in the corona and used as reference for the absolute element abundance studies (Raymond et al., 1997, 1998). The work developed in Chapters 4 and 6 will deal with this problem.

Chapter 2

Instrumentation and Data Analysis

The studies carried out for this thesis make use of data collected by two of the instruments on board SOHO: the Coronal Diagnostic Spectrometer (CDS), and the UltraViolet Coronal Spectrometer (UVCS). These instruments allow studies of electron density, temperature and element abundances to be made in the solar atmosphere from the chromosphere to the corona.

This chapter is organized as follows: the first Section will give a brief description of the SOHO mission; the Second Section describes the ultraviolet experiment UVCS; the third Section describes the extreme-ultraviolet instrument CDS; and the last Section is dedicated to the Ulysses mission. Coordinated SOHO-Ulysses observations were done as part of this PhD project, whose details will be given in Chapter 7.

2.1 The SOHO Mission

The Solar and Heliospheric Observatory (SOHO) is a mission aimed at studying the Sun from its interior to the outer corona and solar wind, in order to understand the coronal heating processes and the wind's acceleration mechanisms (Domingo et al., 1995). The mission is a cooperation between the European Space Agency (ESA) and the National Aeronautics and Space Administration (NASA).

The satellite carries twelve instruments which can be divided into three categories depending on their area of research: helioseismology, the solar corona, and solar wind *in situ* measurements.

SOHO was launched in 1995 and after a transfer orbit, it was put into its final halo orbit around the Earth-Sun Lagrangian L1 point (Figure 2.1), at about 1.5×10^6 km

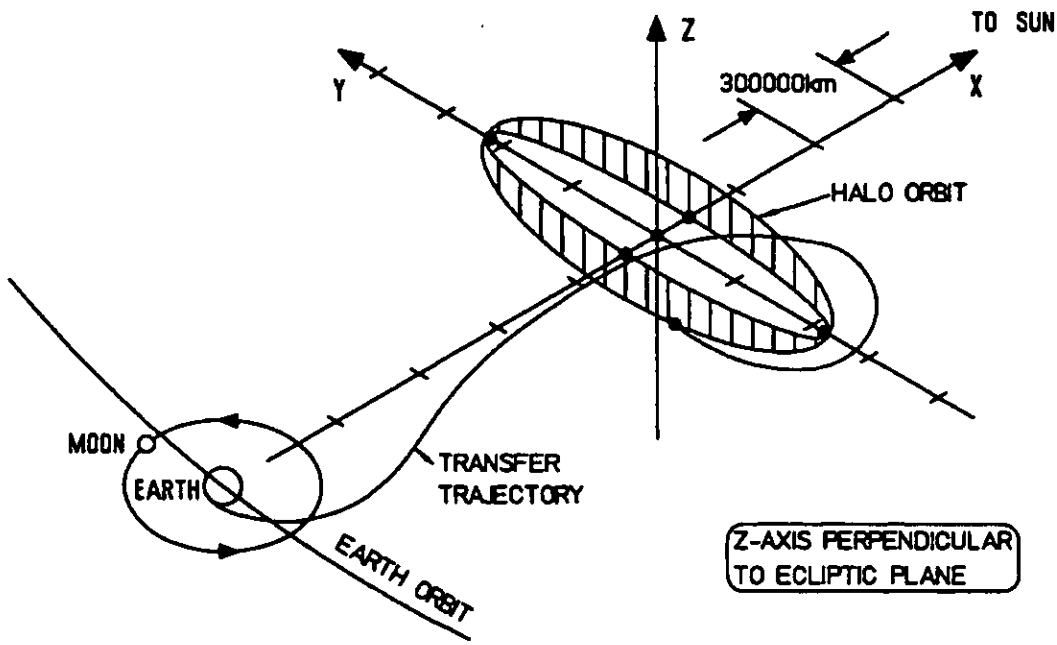

Figure 2.1: SOHO orbit. The continuous view of the Sun is achieved by operating SOHO from a permanent vantage point 1.5 million kilometers sunward of the Earth in a halo orbit around the L1 Lagrangian point. Figure from Kohl et al. (1995).

from the Sun. This orbit is perpendicular to the Sun-Earth direction and has a period of 180 days during which the satellite is constantly pointing to the Sun's centre with an accuracy of 10″. SOHO's position has many advantages over an orbit around the Earth. For example, it provides a small change in velocity along the orbit, which is essential for accurate helioseismology measurements; it is permanently outside the magnetosphere, appropriate for *in situ* measurements of the solar wind; it allows uninterrupted observation of the Sun.

The mission was initially designed for two years life, covering the period of minimum of the solar cycle. Results from that period of observations have been collected in Fleck (1997). An extension of the mission was then accepted, so that the satellite could continue to work during to the rising phase of the solar cycle.

2.2 The SOHO/UltraViolet Coronagraph Spectrometer

The UVCS is a coronagraph spectrometer (Section 1.1) designed for ultraviolet spectroscopy and white light polarimetry of the extended solar corona to investigate the physical processes that control it and generate the solar wind. Determining mechanisms for wind acceleration and coronal heating, identifying the source of the solar wind, and study-

ing plasma properties are among the primary UVCS scientific objectives. These are investigated by observing large and small scale structures of the corona such as streamers, coronal mass ejections, coronal holes and polar plumes. All these structures can be observed by UVCS in the range 1.5-12 $R_\odot$ and their evolution can be followed because it is continuously pointed toward the Sun.

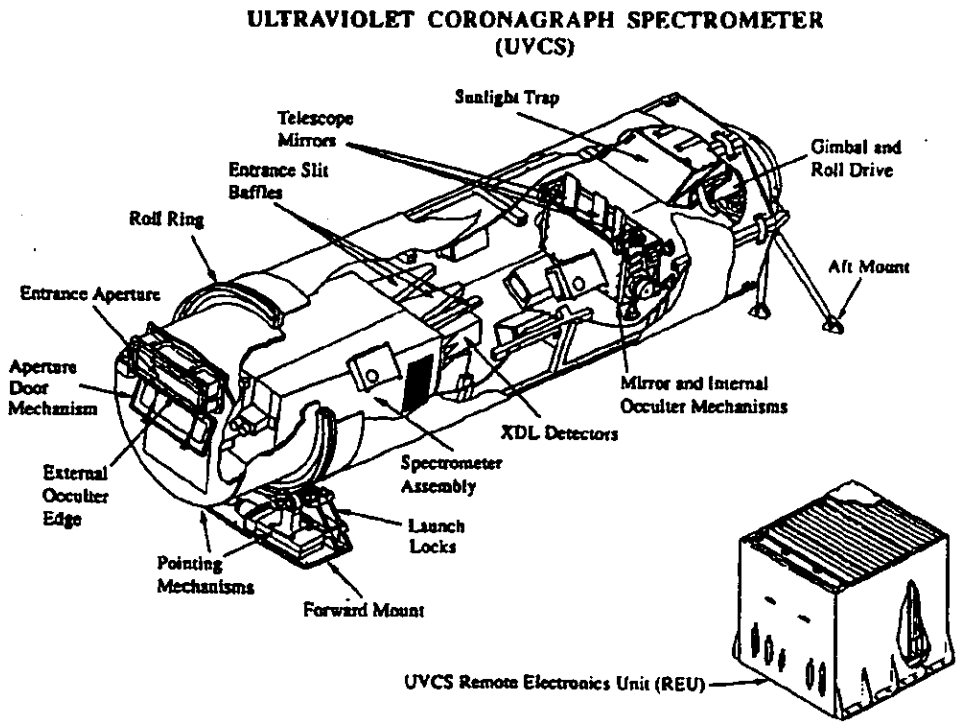

Figure 2.2: The SOHO/UVCS instrument. Figure from Kohl et al. (1995).

The instrument consists of a Telescope Spectrometer Unit (TSU) and a Remote Electronic Unit (REU) (Figure 2.2). The TSU is formed by a high resolution occulted spectrometer which has three coaligned channels, and internal and external occulters. Three simultaneous images of the extended corona are formed by focusing the light with three spherical mirrors onto three entrance slits of the spectrometer assembly. The three channels produced by the spectrometer assembly are:

- The *Lyα channel*, optimized for Lyα 1216 Å line profile measurements. This covers a wavelength range from 1145 Å to 1287 Å which can be extended by rotating the grating (Section 2.2.2);

- The *O VI channel*, optimized for measurements of the O VI 1032, 1037 Å lines. It covers the range 984 - 1080 Å (first order) and 492 - 540 Å (second order). Also in this case, an extension from 937 to 1126 Å of the first order and 469 Å to 563

Å for the second order can be obtained by rotating the grating. Moreover, a convex mirror between the grating and the detector allows the focusing of Lyα , Mg X 625 Å and other lines onto the O VI detector (Figure 2.3 and Section 2.2.2 for details);

- The *white light channel* (WLC), is a visible light polarimeter which covers the wavelength band from 4500 Å to 6000 Å.

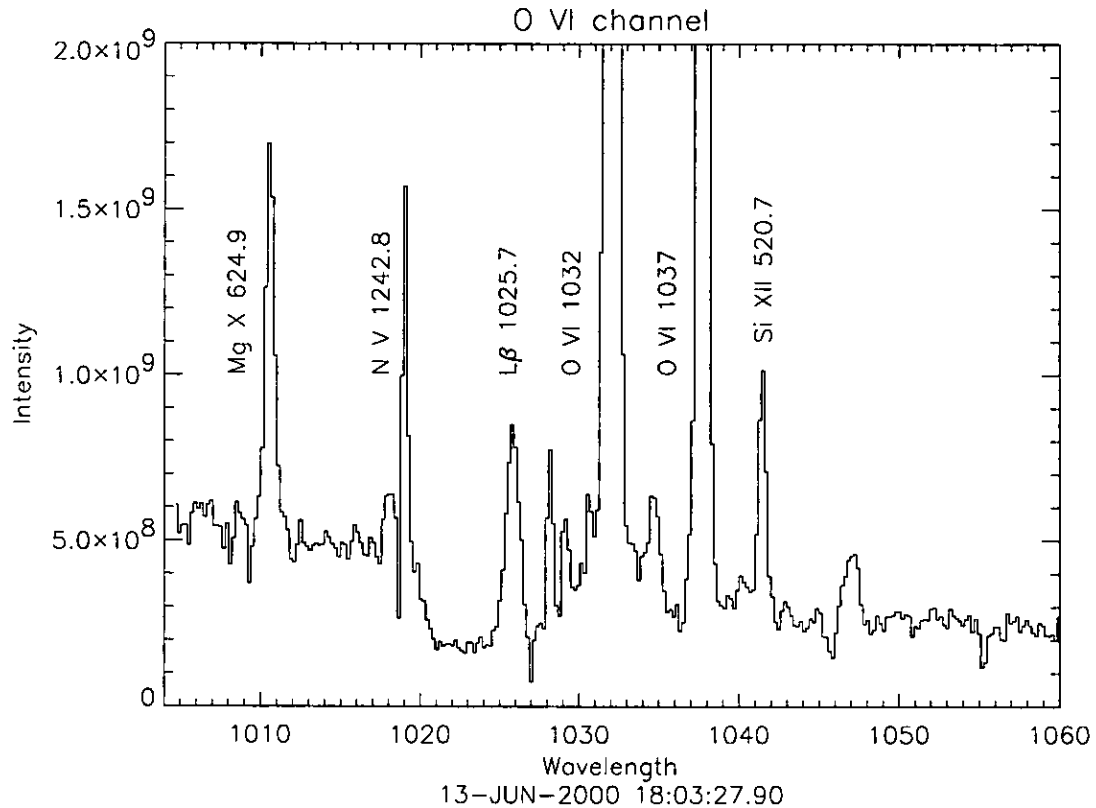

Figure 2.3: An O VI channel spectrum of a streamer at 1.6 $R_\odot$, taken 13 June 2000. The "redundant channel" can be recognized by the step in intensity at about 1020 Å. The Mg an Nv lines are focused on the O VI detector by the convex mirror (see Section 2.2.2).

The upper part of Figure 2.4 shows the total UVCS field of view (FOV) that the instrument can cover. During each exposure, the portion of the image of the solar corona that falls on the entrance slits of the UV channels determines the so-called instantaneous field of view. The FOV of each slit is 40 arcmin long, as shown in Figure 2.4. They are aligned perpendicular to the radial direction from the Sun that passes through their centre. The WLC field of view is given by a $14'' \times 14''$ slit located in a position that corresponds to the centre of the instantaneous FOV of the UV channels (see Figure 2.4). The extended corona can be observed by moving the instantaneous FOV along the radial direction. This is achieved by rotating internal mirrors. In this way the image of the corona can be scanned across 141 arcmin to cover an heliospheric distance from 1.2 to 10 $R_\odot$ (the

primary FOV shown in the Figure). The full corona can be observed by rotating the FOV around the Sun centre. Figure 2.4 bottom shows an example of the Lyα solar corona obtained by scanning the instantaneous FOV from 1.6 $R_\odot$ to 3 $R_\odot$, and rotating the entire FOV around the Sun centre.

2.2.1 Occulted Telescope

All three occulted telescopes are similar, with the main differences relating to the telescope mirrors and the design of the entrance slit baffles. Figure 2.5 shows the optical layout of the Lyα channel. This is the same for the O VI channel.

A first selection of the light entering the telescope is made by the rectangular entrance aperture, composed of three knife edges that limit the FOV and the amount of solar disc light, together with a serrated edge. This shape of the aperture has the function of an external occulter that protects the telescope mirror from the direct sunlight. The light that comes from the solar disc, is attenuated by passing through a series of three baffles (to protect from stray light) and then enters a sunlight trap where it will be further attenuated.

The telescope mirror is placed so that the light entering the telescope and coming from 1.2 $R_\odot$ reaches its edge, while the light coming from 10 $R_\odot$ completely fills it. However, together with this coronal light, some light diffracted by the external occulter can reach the telescope mirror. To minimize this effect, an internal occulter, parallel to the external occulter, intercepts this light that is specularly reflected by the mirror. As the mirror is tilted to observe at different heliospheric distances, the internal occulted is moved to maintain a position that blocks this reflected light.

Once reflected by the mirror, the coronal light enters the spectrometer through the entrance slit, where only that part corresponding to the instantaneous FOV is selected. By rotating the mirror, different portions of the solar corona image are selected to enter the spectrometer.

The sunlight trap (Figure 2.6) consists of three regions, two of which are directly illuminated by the solar disc, and a dark one in the middle of the two. The lines of sight of these two illuminated regions are blocked by the telescope mirror and by the entrance slit baffle. The light entering these cavities is attenuated (about 2×10^{-5} times) by multiple reflections from low reflectivity (3% in the UV) plates. The resulting heat is dissipated by an external thermal radiator.

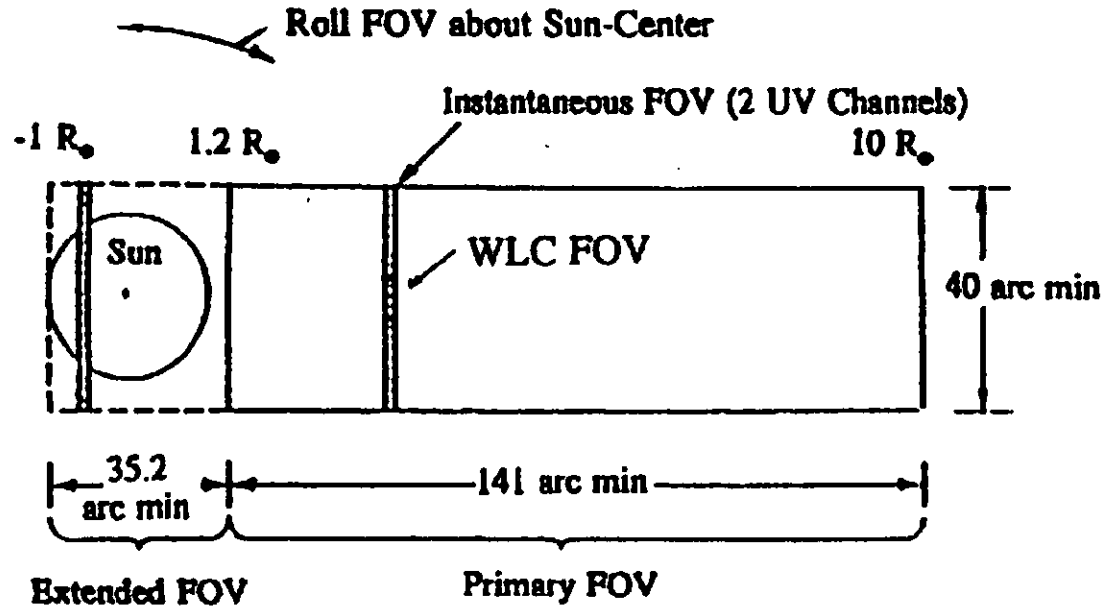

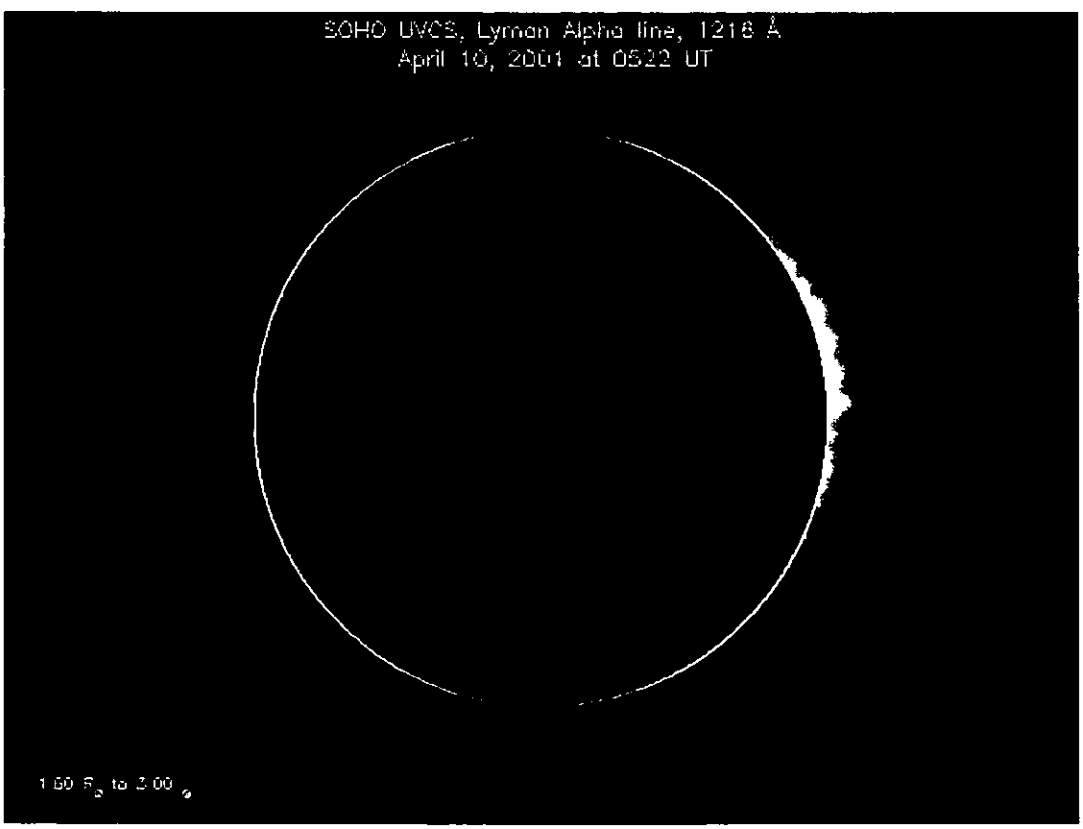

Figure 2.4: Top: the field of view (FOV) of UVCS. Bottom: Lyα image of the solar corona from 1.6 $R_\odot$ to 3 $R_\odot$. Figure from Kohl et al. (1995).

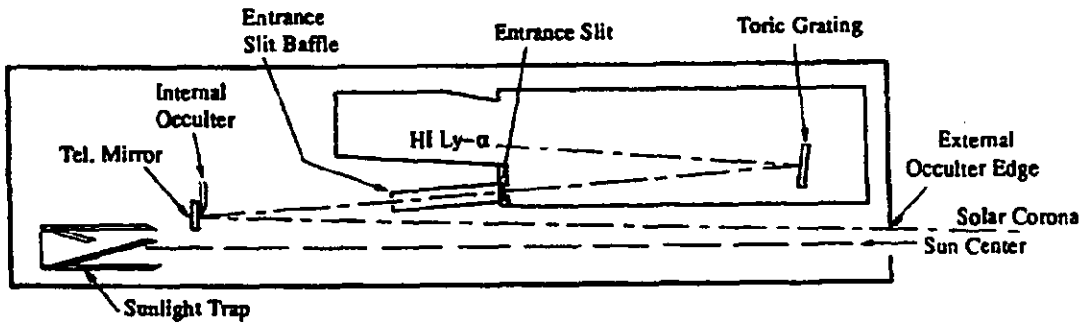

Figure 2.5: Optical layout of the Lyα channel. Figure from Kohl et al. (1995).

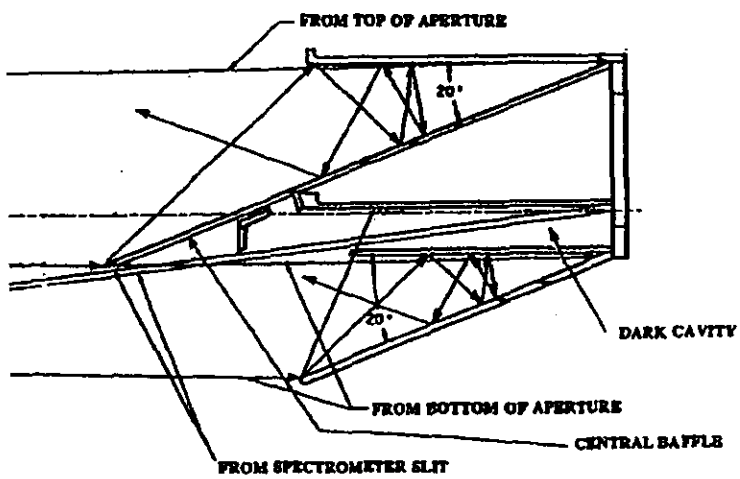

Figure 2.6: Illustration of the UVCS Sunlight Trap. Figure from Kohl et al. (1995).

2.2.2 The Lyα and O VI Channels

The two UV spectrometers use toric gratings mounted in the Rowland-circle configuration, with a diffraction angle β near the grating normal (Figure 2.7). The toric surface of the grating has the horizontal radius (R_h) equal to the diameter of the Rowland circle. The focus in the horizontal direction (the direction of dispersion) lies on this circle. The vertical radius of curvature (R_v) of the grating is smaller then the horizontal, and the vertical focusing surface (stigmatic surface), that is the spatial direction, intersects the Rowland circle at an angle $\beta = \pm\beta_0$. These two points of intersection are called stigmatic points. These are the points where the astigmatic correction and the spectral focus occur.

The incidence angle α is kept small to reduce aberration effects. Table 2.1 lists the parameters of the optical design. Measurements during laboratory tests indicated an overall efficiency of 23% and 10% for the Lyα and O VI gratings respectively (Fineschi et al., 1994).

In order to cover a wide spectral range throughout the FOV of the detector, the gratings can rotate around a point that is located at 127 mm from its vertex, along a direction nearly perpendicular to the bisector of the angle between the incident and diffracted rays. This point was the best choice which also allowed the grating to translate to maintain the best spectral focus on the detector. Unlike from the Lyα channel, the O VI channel has a grazing incidence mirror mounted between the grating and the detector, which for a certain grating angle, will deflect the Lyα line onto the detector. The deflected spectral range is called the *redundant channel.*

The spectrometer is provided with several slits of different widths. The primary widths are 355 μm (92″), 213 μm (58.6″), 53 μm (14.6″), 25 μm (6.9″) and 10 μm (2.8″).

The detectors used for both of the UV channels are two dimensional photon counting microchannel plate sensors with electronic readout (Siegmund et al., 1994). The detector has a dimension of 1024×360 pixels. In front of the O VI detector and close to the microchannel plates is placed a grid, biased at +15 V, to attenuate the low energy ions which enter the detector. This grid produces a *shadow* on the detector that results in an almost regular pattern on the spectra. A clear example is shown in Figure 2.3 where the N V line is almost cut in half. The regular pattern of the shadows can also be seen. More details will be given later (Section 2.2.3).

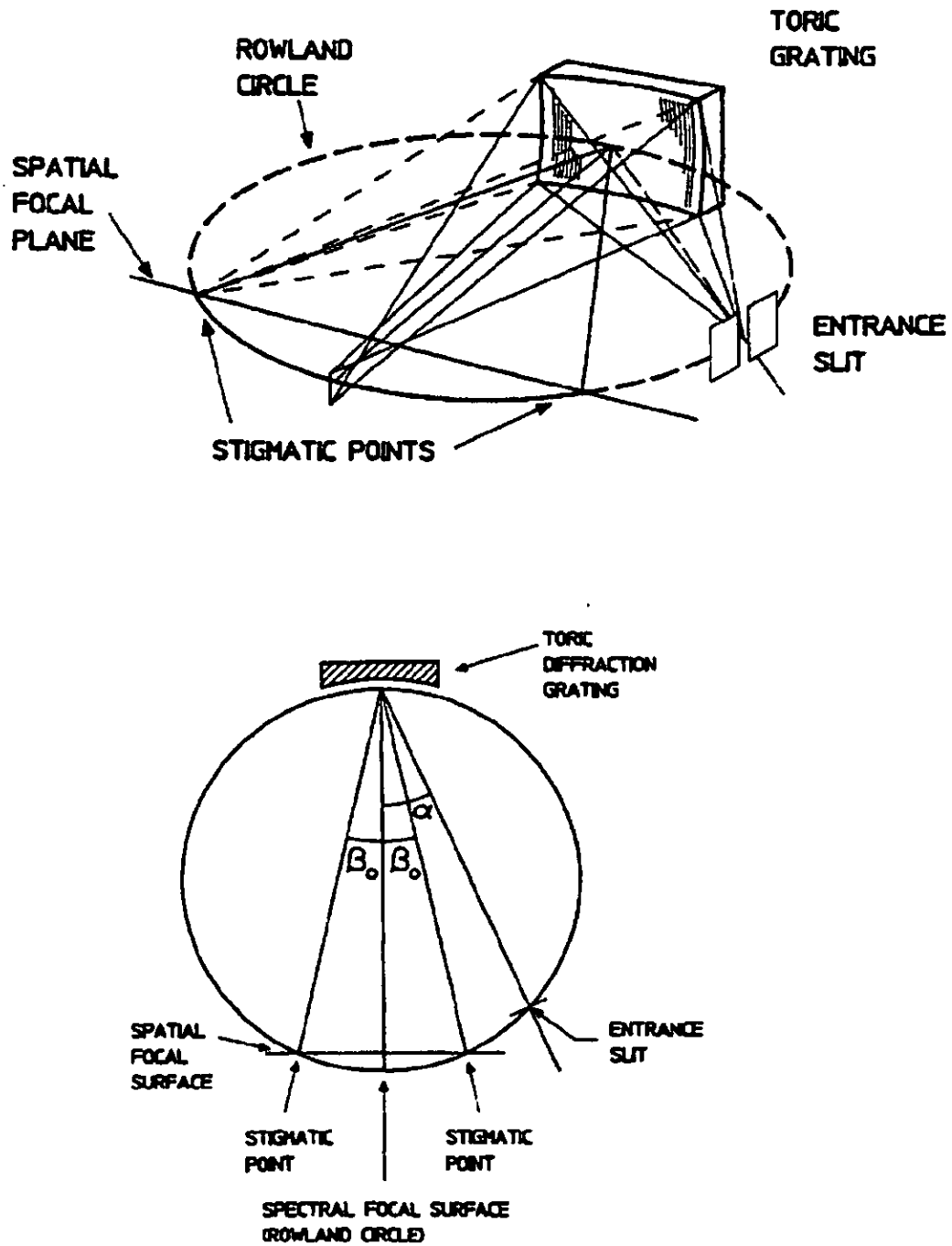

Figure 2.7: Top: Isometric display of the imaging properties between the two stigmatic points $\pm\beta_0$. Bottom: Schematic of the spectral and spatial imaging of a single toric grating. Exact stigmatic focusing is obtained at angle of diffraction $\pm\beta_0$, effective stigmatic focusing (with respect to the pixel size) can be achieved between and somewhat beyond the two stigmatic points. Figure from Kohl et al. (1995).

Table 2.1: Optical parameters of the UVCS channels

	Lyα channel	O VI channel
Ruling frequency	2400 1/mm	2600 1/mm
Angle of incidence α	12.85°	18.85°
Angle of diffraction β	3.98°	2.78°
Main horizontal radius of curvature R_h	750 mm	750 mm
Main vertical radius of curvature R_v	729.5	708.9 mm
Dispersion	5.54 Å/mm (1st order)	3.70Å/mm (1st order)
Spectral bandwidth of pixel	0.14 Å(1st order)	0.0925 (1st order)
Spatial width of pixel	7″(0.025 mm)	7″(0.025 mm)

2.2.3 Stray Light in the UVCS

One of the main problems encountered by any off-limb spectrometer measurements is the stray light. Stray light is part of the disc light that enters the instrument because it is not blocked by the external occulter or is diffracted by the edges of the entrance aperture. This light, if not properly determined, can produce an over-estimate of the coronal line intensities that are emitted by the observed off-limb region of the solar atmosphere. For the UVCS, the correct determination of the stray light is especially important for the Lyα channel, because it affects the determination of the profile of the faint electron scattered component of the Lyα . The Lyα line is composed of a faint, broad component due to electron-scattering (from which electron temperature is determined), and a more intense, narrower resonant component (see Chapter 1).

The disc intensity that enters the instrument directly is totally removed by a light trap that absorbs or reflects away this radiation. The other components of the stray light, instead are only attenuated, given the optical geometry that reduces the amount of stray light that reaches the detectors. The level of contamination in the instrument due to stray light is shown in Figure 2.8. The Figure shows the ratio of the expected stray light irradiance level on the slit in units of solar disc irradiance (phots cm^{-2}) versus heliocentric distance for the Lyα wavelength. Each single contribution to stray light and their total are plotted as dotted curves. The solid curves are the estimated signal irradiance at the entrance slit. The irradiance on the ordinate is normalized to the expected irradiance at 1AU. It is clear from the figure that the major contribution comes from the light diffracted by the external occulter into the telescope mirror and scattered into the spectrometer. Laboratory tests revealed that this contribution changes with the angle of incidence on the mirror, so that the dominant contribution comes from just inside the solar limb (Romoli

et al., 1993). More accurate stray light determination requires the use of intensity observed at the limb. In this thesis (see Chapter 4) the full disc intensities (Vernazza & Reeves, 1978) have been used for stray light determination.

In the UVCS coronal spectra, chromospheric lines due to stray light are visible. For example Si III (1206.5 Å) in the Lyα channel and CIII (977 Å) in the O VI channel (Chapter 4 and Figure A.1). These lines are called "stray light monitor lines" and have been used to infer the stray light contribution. For each observed line the stray light (I^{stray}) contribution to the total intensity has been calculated by

$$I^{stray} = I^{disc} \times \frac{I^{osb}_{CIII}}{I^{disc}_{CIII}} \tag{2.1}$$

Where I^{disc} is the disc intensity of the observed line, I^{osb}_{CIII} is the observed intensity of C III and I^{disc}_{CIII} is the disc intensity at the C III wavelength. In this thesis, the averaged disc intensities of Vernazza & Reeves (1978) have been used. These intensities were obtained using Skylab data.

As shown in the previous equation, the stray light depends on the disc intensity. If the observations involve lines emitted at coronal temperatures, then the disc intensity of those lines is generally small and the stray light is negligible. For the bright O VI lines, for example, it can be a few % at 1.2 $R_\odot$ in streamers. The Lyα instead has a much larger contribution due to its bright disc intensity. While in a coronal streamer it is usually 5-10% for heights below 1.5 $R_\odot$, it can reach 25% in coronal holes, where the coronal emission decreases (Giordano, 1998). Chapter 4 will give values derived for greater distances in streamer.

Data Processing

The UVCS data used for this thesis have been collected using the 100 μm (Chapter 7) and 150 μm (Chapter 4) slits. The instrument was always pointed at the outer corona where a faint signal was obtained. For this reason the data have been binned over 10 pixels along the slit direction for the O VI channel and 9 pixels for the Lyα channel, giving 70″ and 63″ for the spatial resolution, respectively. Along the dispersion direction, 2-pixel binning was used for the O VI channel (0.1986 Å resulting in spectral resolution). Because the Lyα intensity is high enough, no binning for the Lyα channel was needed.

The duration of the observations varied depending on the channel used and, for the O VI channel, whether the Lyα line was projected or not in the redundant channel. The large difference in intensity between this line and all the others (between 2 and 4 orders of magnitude, see e.g. Table 4.1) requires, in fact, different exposure times.

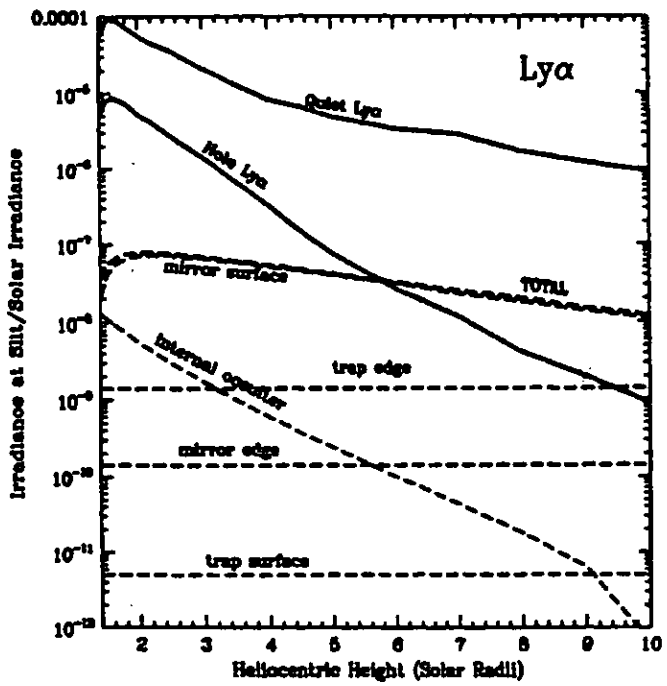

Figure 2.8: Estimated signal and expected stray-light contributions to irradiance at the slit, relative to the solar disc irradiance, versus the heliocentric height at Lyα wavelength. Figure from Kohl et al. (1995).

The observations taken in March and May 1998 (Chapter 4) involved the use of both channels. The data from the Lyα channel were composed of 161 exposures of 200 s each over one grating position (wavelength mask) while the O VI channel data were composed by 160 exposures of 200 s each distributed over three grating positions. The observation for the Joint Observing Program, JOP 112 (Chapter 7), did not make use of the Lyα channel, and the Lyα line was observed on the redundant part of the O VI channel. For this reason, the data that made use of masks (grating positions) whose selected wavelength bands did not include this line, were taken as 36 exposures of 200 s. The data which included the Lyα line were instead taken using 21 exposures of 200 s.

Before starting the scientific analysis on the data, a series of standard procedures need to be applied to the data. The UVCS science team provides the user with a software package (written in IDL language), called Data Analysis System (DAS), which includes these standard procedures. The calibration process is automatic, and can be run directly by the DAS interface.

Once the observations are made, the data are generally received in two type of FITS format: the uncalibrated (*.dat, in count/pixel) file and the calibrated (*.rad, in phot cm^{-2} s^{-1} str^{-1} Å). The calibrated file is processed using the standard procedures contained in the DAS. The raw data are also given in case the user wants to apply a different calibration.

The first step in processing the data is the removal of cosmic rays. This is a DAS facility. As mentioned before, the data generally consist of a set of exposures over the same target. The cosmic ray impact on UVCS is quite a rare event, with only one or two cases over the whole data set. So a straightforward way of dealing with it is to discard the exposure where the event happened. Otherwise, a filter in intensity can be applied over all the spectra. It generally cuts the data above an imposed intensity level. The second step is the correction for the flat field. In the third step the wavelength calibration is applied. This includes both the primary and redundant channels in the case of O VI channel.

The radiometric calibration is the last step, where the resulted data are converted to phot cm^{-2} s^{-1} str^{-1} Å.

Once the data are calibrated, unless the scientific target is a fast evolving feature, the exposures are integrated to increase the signal/noise ratio.

After all this has been done, the data still contain instrumental effects that are not corrected for in the calibration version used here. One of these effects is the shadow of the grid wires along the dispersion direction. As mentioned before, in front of the O VI channel detector a grid is placed to stop low energy ions entering. This produces a shadow that appears as a sharp drop (involving 2-3 pixels in the dispersion direction) of the intensity at almost equi-spaced points along the spectrum (Figure 2.3). The distances between two successive grid shadows can vary from 94-96 pixels to 100, that means about 9 Å(Naletto, 1996). The non-regularity of the spacing is due to the effect of the light coming from the mirror that generates the redundant part of the spectrum and that has a different incoming direction from that of the primary spectrum. In many cases the shadow falls on one of the spectral lines so that it appears partially cut. When this happens, in most cases the line is not usable. Examples are also given in the Appendix sections.

What the DAS does not include is the procedure for line fitting. Unlike the CDS spectrum (see Section 2.3.1), the UV channels of UVCS contain far fewer lines (see for example Table 4.1) with scarcely any blended lines. For this reason procedures were written for this work to perform line intensity determination by summing the counts over the line instead of line- fitting. This was found to be the quickest way to proceed with the data. The procedures were written using the IDL package.

2.3 The SOHO/Coronal Diagnostic Spectrometer

Following the common goals of all the SOHO instruments, the Coronal Diagnostic Spectrometer (CDS) on SOHO was designed to collect data that would help researchers to

answer questions regarding the characteristics of the solar corona, such as how is it heated and how is the solar wind accelerated. To answer these questions it is fundamental to determine the physical parameters of the corona.

CDS was designed to cover a wide EUV wavelength range (150– 800 Å), to include lines emitted over a large range of temperatures 4 $<\log T <$ 7, which are useful for density and temperature diagnostics (see Sections 3.4 and 3.5). In the EUV waveband light is easily absorbed by any material (Jenkins & White, 1957). For this reason, for wavelengths short-ward of 300 Å a grazing incidence spectrometer has to be used. To cover the above wavelength range, two different gratings (and spectrometers) are used: the Normal Incidence Spectrometer (NIS) and the Grazing Incidence Spectrometer (GIS).

The NIS is composed of the NIS 1, that covers the wavelengths from 308–381 Å, and of the NIS 2, that covers the range 513–633 Å. The spectra are produced by the dispersion of the incoming normal-incident beam by two toroidal gratings and focused onto a CCD detector. The main advantage of this spectrometer is that the instrument is stigmatic. This allows us to produce extended images of the solar corona (details are given in the next Section).

In the GIS, instead, the incoming beam is dispersed by the grazing incidence on a spherical grating, and focused on four microchannel plate detectors around the Rowland circle. This system is astigmatic, so only a single spectrum is produced from each exposure. In this case, an image can be produced by moving the slit by arcsec steps in the direction perpendicular to the dispersion and the scan mirror in the plane of dispersion. The wavelength ranges covered by GIS are: 151 - 221 Å, 256 - 338 Å, 393 - 493 and 656 - 785 Å.

The details of the CDS instrument, together with its pre-flight capabilities, can be found in Harrison et al. (1995). Information on the in-flight performance has been continuously provided by the CDS team and can be found on the CDS WWW pages and links therein. In particular, the CDS Software Notes contain details of the instruments, together with guides to the data analysis. Further information on the CDS in-flight performance can be found in Del Zanna (1999).
Here, only some of the main CDS characteristics are described.

2.3.1 Instrument Overview

During this PhD project, the data were collected using both CDS spectrometers, but the GIS data have not yet been used, and therefore the following description will focus on the Normal Incidence Spectrometer. Table 2.2 shows some of its main characteristics. Figure

2.9 shows the optical layout of the CDS. The light enters into the grazing incidence Wolter-Schwartzchild type 2 telescope and, after being reflected by the two internal surfaces, is also grazing reflected (about 5°) by a flat scan mirror. It then passes through the spectrometer slit (a choice of six sizes, common to both NIS and GIS). This scan mirror can rotate with steps of ±3°, corresponding to a 2.032″ movement of field of the view. This movement allows different regions of Sun to be imaged by the slit, with a maximum scan of 4 arcmin. The nominal SOHO roll angle is such that the scan mirror movements are along the East-West direction. This so-called *rastering* is performed from West to East.

By using the 2″× 240″ or the 4″× 240″ slits and simply moving the mirror, it is possible to scan a large area of the Sun, with an effective field of view of 4′ × 4′.

The Normal Incidence Spectrometer has a Rowland mounting such that the incoming beam falls at near normal incidence (about 7.9°) onto two adjacent toroidal gratings. This configuration leads to an image along the slit of the field of view in each wavelength. Moreover, the dispersed spectra are free from astigmatism. Each of the toroidal gratings has a different ruling density so that the resulting wavelength range is different for the two gratings: the NIS 1 grating has 4000 lines/mm and gives a wavelength range 308−381 Å; the NIS 2 grating has 2400 lines/mm which gives a waveband of 513−633 Å. The two spectra are simultaneously displayed above one other on the same imaging detector by applying a small out-of-plane tilt to the gratings.

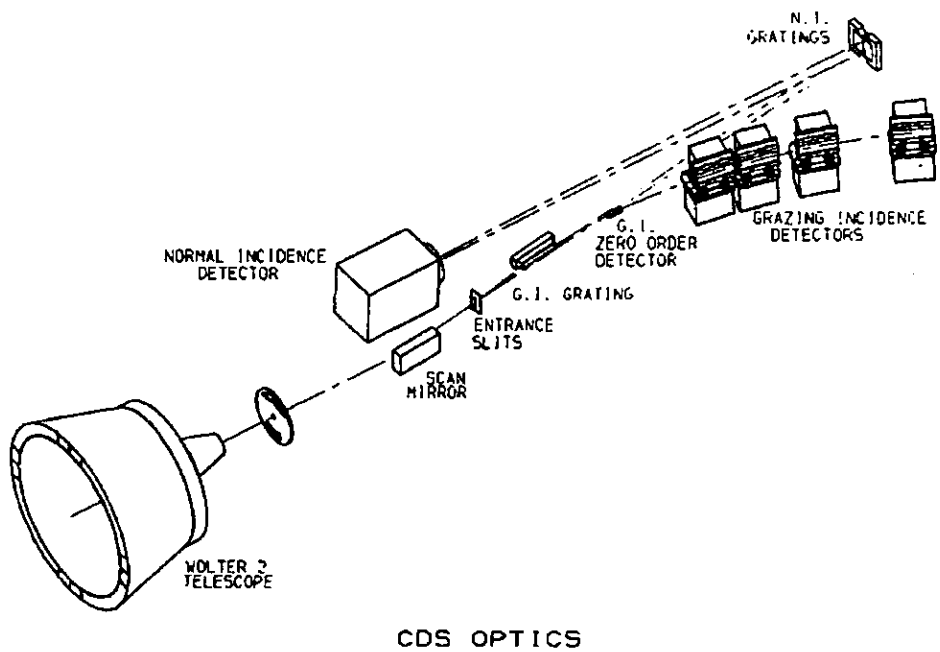

Figure 2.9: The optical elements in CDS. Figure from Harrison et al. (1995)

The NIS detector, known as the VDS (Viewfinder Detector Subsystem), is composed of: a microchannel plate, to intensify the signal; a phosphor converter to visible light; a lens system, to focus the visible light; and a 1024×1024 charge coupled device (CCD) with 21 μm square pixels. The CCD is composed of four panels to reduce the readout time.

The dynamic range estimated in flight tests gives value of about 2000:1 for each exposure.

The image scale is such that a pixel in the detector Y direction corresponds to 1.68″. The spatial resolution of the telescope is however a few seconds of arc (see e.g. Haugan (1999)).

(The spatial resolution is normally defined by the full width at half maximum intensity (FWHM) of the point spread function, that is the FWHM of the intensity distribution resulting from the observation of an infinitely distant point source.)

A pixel in the detector X direction corresponds to about 0.07 Å for NIS 1 and 0.11 Å for NIS 2. The spectral resolution is such that the FWHM of the lines in the NIS 1 and NIS 2 channels is about 0.3 Å and 0.5 Å respectively.

CDS has been carefully designed to control the stray light in the instrument. Even if the instrument is sensitive only to EUV wavelengths, the major source of unwanted light that may reach the detector is due to the strong H-Lyα 1216 Å. To minimise this effect, the surfaces directly viewed by the detector have a very low reflecting efficiency around 1216 Å.

The detector's quantum efficiency was measured to be $\sim$ 20% in the range 300-650 Å, reducing to a few % at 1216 Å (H- Lyα). This further limits the effects on the detector of this line scattered inside the spectrometer.

The total absence of chromospheric lines in the NIS spectra of the off-limb low corona confirms that stray light is negligible for such observations. More details on the corrections needed for CDS observations of the off-limb corona can be found in David et al. (1998) and references therein.

Due to telemetry limitations, the spectra recorded may be limited to a selected number of wavelength windows. The availability of different slits, mirror rastering and wavelength selection makes CDS an extremely versatile instrument that can be used for a large variety of different scientific studies. Several types of CDS *studies* can be defined, in order to optimise the observations of different scientific targets. Each of these CDS *studies* is characterised by different values for the input parameters.

Table 2.2: Some general characteristics of NIS spectrometer

	NIS 1	NIS 2
Ruling frequency	4000 1/mm	2400 1/mm
Average angle of incidence α	7.9°	7.9°
Angle of diffraction	$7° < \beta < 9°$	$7° < \beta < 9°$
Radius of curvature R_h	743.6 mm	743.6 mm
Radious of curvature R_v	736.4 mm	same
Prime slits	2 × 240, 4× 240, 90× 240 arcsec	same
Wavelength Ranges	308 - 381 Å	513 - 633 Å
Dispersion	3.17 Å/mm	5.56 Å/mm
Spectral bandwidth of pixel	0.07 Å(1st order)	0.12 Å(1st order)
Spatial width of the pixel	1.68″(0.021 mm)	same

Data Analysis

The project for this thesis required observations of large off-limb areas, in coronal hole and quiet Sun regions. The signal even in coronal lines fades away above the solar limb quite rapidly, and it was therefore necessary to have long exposure times. Moreover, it was necessary to obtain the full NIS spectrum in order to use the maximum number of lines for a full application of the plasma diagnostic techniques (Chapter 3). The CDS *study* selected for this purpose was the UCLAN_N2. This records the full NIS spectrum and scans the 4×240 arcsec slit, recording an area limited to 120×150 arcsec. Two versions of the study were used. In the old version the exposure time was 160 s, for the new version it is 120s.

A series of standard procedures was applied to correct the data for instrumental effects, remove cosmic rays and to calibrate it. These procedures are provided in the CDS software package that has been developed and upgraded since the launch of SOHO. The first step was the CCD bias subtraction, accomplished by the CDS routine VDS_DEBIAS that removes an average readout bias from each of the four CCD sectors.

The second step was the cosmic ray removal. This process takes a long time because each exposure has to be visually inspected for the presence of cosmic rays. The CDS routines CDS_CLEAN_IMAGE and XCDS_COSMIC were used, with the cosmic ray hits flagged as missing pixels. In 120-160 s a large number of cosmic ray hits is usually present, and their negative effect can be compensated for by spatial averaging or by averaging repeated exposures of the same target.

The third step was the application of the CDS routine VDS_CALIB. This routine

applies corrections for the flat field, and for nonlinear effects (only present when the detector reaches saturation). These corrections are minor. VDS_CALIB also corrects for the "burn-in" of the lines, which is considerable for the brightest ones. This is caused by local gain depression. The burn-in of all the brightest lines has been accurately monitored since launch, and estimated from the images obtained when the instrument is operated in "spectroheliogram mode" with the 90x240 arcsec slit. Such images reveal a marked depression of the line intensity at the core of the line.

The fourth step consisted in the correction for the tilt of the NIS spectra. Probably during launch, the CDS instrument suffered some distortion, resulting mainly in a small tilt of the dispersion direction relative to the CCD alignment. This tilt is different for the NIS 1 and NIS 2 channels and was corrected using the CDS routine VDS_ROTATE.

For all the observations analysed here, a binning over 2 pixels along the Y direction of the slit has been applied. In this way the total amount of data to be further analysed was reduced, and the signal/noise increased. By doing this no information has been lost because the spatial resolution given by the NIS Point Spread Function is approximately equivalent to 2 pixels.

Once all the above corrections had been applied to the data, line intensities were initially calculated at each spatial location by removing a polynomial background and summing the counts in all the pixels where each line emission was expected. This was achieved by pre-defining a set of line positions and widths for the NIS channels. Monochromatic images in all the unblended lines could therefore be quickly produced in this way.

For spectroscopic analysis, line intensities were calculated using the CFIT software package (Haugan, 1997). This package provides procedures (CFIT_BLOCK) that fit the lines using multiple-Gaussian profiles with linear or quadratic backgrounds. This allows blended lines to be resolved. The fitting is done after a series of initial parameters that define each line to be fitted is passed to the procedures. The programs fit peak intensity, peak wavelength, FWHM, and provides errors for each fitted line profile.

The fitting procedure was used in a semi-automatic way, with only a few visual spot-check inspections. In fact, data from a full NIS spectrum can result in more that 150 lines fitted for each spatial location. The fitting procedure was therefore quite lengthy, because of the large number of lines involved and because of the characteristics of off-limb spectra, where most of the lines are quite faint.

However, in most of the cases the line intensities used for subsequent study were calculated after spatial averaging, thus reducing the fitting to a single spectrum. In this case, the XCFIT program was used, and a careful visual inspection of the results of the

fits performed.

Examples of results from the fitting procedure are given in the Appendix, Section A.2 and A.4.

Indicating with I_0 the peak amplitude and with FWHM the Full Width at Half Maximum derived from the fit, the total intensity for each line was calculated by

$$I_{tot} = \frac{1}{2}\sqrt{\frac{\pi}{ln2}}\, I_0\, FWHM \tag{2.2}$$

In this thesis the error on the total line intensity was estimated by using the Gaussian parameters derived from the fit (Thompson, 1998). Because the Gaussian width is not statistically independent from the peak, then the error on total intensity (σ_I) is given by

$$\left(\frac{\sigma_I}{I}\right)^2 = \frac{1}{2}\left[\left(\frac{\sigma_{I_0}}{I_0}\right)^2 + \left(\frac{\sigma_{FWHM}}{FWHM}\right)^2\right] \tag{2.3}$$

where σ indicates the error on the respective parameter.

There is another way to derive the error on the signal, by estimating the photon noise, the background noise, and the various detector noises (Thompson, 1998). In most cases, the two error estimates are similar Del Zanna (1999).

The intensity calibration was always performed as a final step, after line fitting. A good NIS calibration is a key issue, because many CDS diagnostic capabilities depend on it. A NIS laboratory calibration was performed 18 months before launch (Bromage et al., 1996; Lang et al., 1999). Post-launch, large differences, in particular in the relative NIS 1/NIS 2 calibration, were evident (Landi et al., 1997). The detailed NIS calibration presented by Del Zanna (1999) was adopted in this work. This calibration is in good agreement with the other in-flight cross-calibrations with rocket flights (Brekke et al., 2000; Thomas et al., 1999) which were incorporated into the NIS calibration that is currently in the standard CDS software.

2.4 The Ulysses Mission

The Ulysses mission has as its primary objective the investigation of the three dimensional inner heliosphere with *in situ* measurements which cover heliospheric latitude from the equator to close to the poles. Its importance is unique because it is the first mission having an orbit around the Sun but out of the ecliptic. As already mentioned (Section 1.1), until Ulysses the highest heliospheric latitude reached by a satellite was about 30° (Voyager 1), so that our knowledge of the three dimensional heliosphere was limited to low solar latitudes.

Understanding the mechanisms that heat the solar corona and the generation of the solar wind are common scientific objectives for SOHO and Ulysses. With Ulysses, scientists are trying to:

- understand the three-dimensional properties of the interplanetary magnetic field and the solar wind
- study the origin of the solar wind by measuring its composition at different solar latitudes
- to study plasma waves and shocks under different plasma conditions from those found in the ecliptic
- improve the understanding of galactic cosmic rays by sampling these particles in the polar regions where the low energy cosmic rays have easier access to the inner solar system than near the ecliptic plane
- improve our knowledge of the neutral components of the interstellar gas that enters the heliosphere, by measuring their properties at different solar latitudes
- improve our understanding of interplanetary dust by measuring its properties as a function of heliospheric latitude.

The data suitable to address the study to the above objectives are collected by nine payloads on board the satellite. These include: two magnetometers, two solar wind plasma instruments, a unified radio/plasma wave instrument, three energetic charged particle instruments, an interstellar neutral gas sensor, a solar X-ray/cosmic ray burst instrument and a cosmic dust sensor. Moreover, Ulysses also includes two radio-science investigations which also make use of ground communication systems at specific periods of the mission to study the solar corona and search for gravitational waves.

These instruments are able to collect data at different latitudes because of the unusual orbit that the satellite is in.

Ulysses was launched in 1990 towards Jupiter, in the standard ecliptic orbit, reaching the planet in 1992. Then, with the help of Jupiter's gravity (fly-by) the satellite was placed in a new polar orbit with a period of 6.2 years (Figure 2.10). This elliptical orbit has its aphelion at 5.4 AU and the perihelion at 1.3 AU. The maximum heliospheric latitude reached by Ulysses is 80°, with a total of 234 days per orbit spent at a latitude between 70° and 80°.

Among the numerous publications from Ulysses data, Forsyth et al. (1996) and McComas et al. (2000) review results from the first orbit completed in 1998. It is worth

mentioning the study from McComas et al. (1998) whose results confirm, for the first time, that the fast wind sampled by Ulysses, mapped back to the Sun, had its origin in the polar region occupied at that time by coronal hole (see also Figure 1.2).

The results obtained by all the scientific payloads on board Ulysses, and their excellent condition after the first orbit, allowed the mission to continue into the second orbit. This started when the satellite reached aphelion at the orbit of Jupiter. Because Jupiter's orbit is 11.9 years against the 6.2 years of Ulysses, this time there was no interaction between the two, Jupiter being far away in another position on its orbit. This second orbit also gave the opportunity to investigate and compare the heliosphere during low (during the first orbit) and high (during the second orbit) solar activity.

The quadrature configurations that periodically SOHO, the Sun and Ulysses form, mentioned in Section 1.1, provide an opportunity for scientists to learn more from the data. Chapter 7 will be dedicated to explaining such a configuration and describing the observations made by the author during the December 1999 and June 2000 quadratures. The geometry of the quadrature will be explained here in Section 2.5.

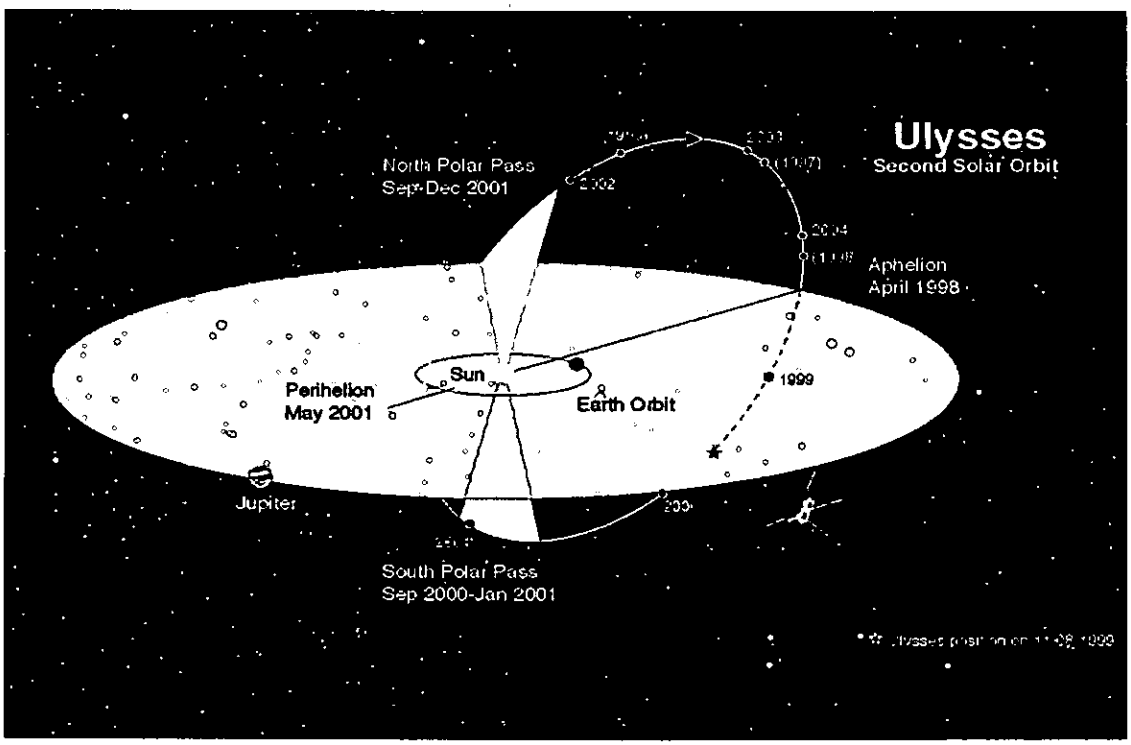

Figure 2.10: The second orbit of Ulysses from a perspective which shows the 80 degree inclination of the Ulysses orbit to the ecliptic. The yellow sectors represent the polar passes (Figure from Ulysses WWW page).

2.5 The SOHO-Sun-Ulysses Quadrature

SOHO is orbiting around a location at approximately 1% of the Sun-Earth distance from the Earth. In relation to Ulysses, it may be considered placed at the Earth distance. The change of the SOHO-Sun-Ulysses angle is about 1 degree per day.

When the angle formed between SOHO, the Sun and Ulysses is 90° then the plasma observed above the solar limb by SOHO in the direction of Ulysses will eventually be sampled later by the *in situ* measurements of Ulysses. Figure 2.11 shows the relative positions of the two satellites compared to the Sun during a quadrature.

The uncertainty in mapping back to the Sun's surface the origin of the plasma sampled by Ulysses is ±5%. This number has two origins: the inaccuracies in the assumptions made in mapping back the wind to the Sun and the non radial flow of the wind in the corona (Suess et al., 2000). To reduce this uncertainty, the coordinated observations are planned for a couple of weeks before and after the quadrature to cover a variation in the SOHO-Sun-Ulysses angle corresponding to this uncertainty. Figure 2.12 shows the Ulysses orbit projected back on the Sun surface as seen from Earth. This map helps to identify the location of the source of the wind sampled by Ulysses along its orbit.

Further details of the quadrature will be given in Chapter 7.

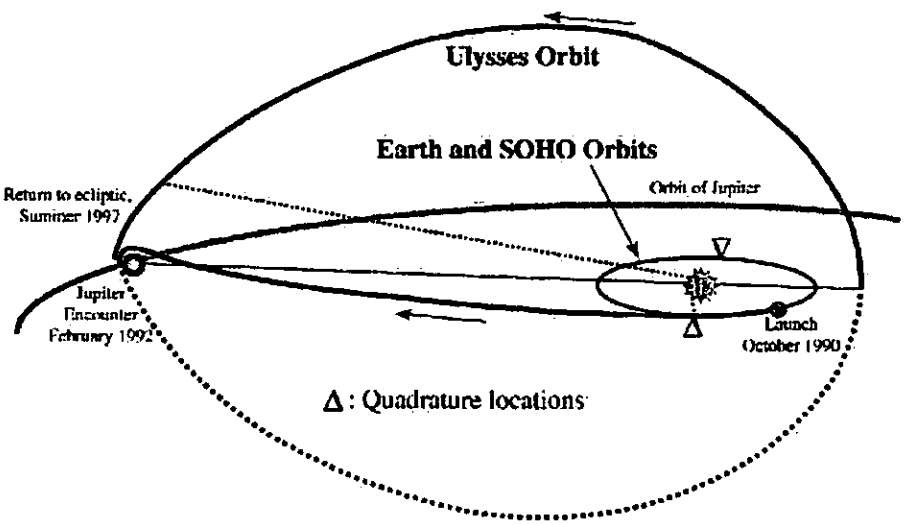

Figure 2.11: SOHO orbit (almost coincident with Earth's orbit around the Sun) and Ulysses' first orbit, after the Jupiter fly-by. The angle Ulysses-Sun-SOHO is 90 degrees twice a year. The triangles shown on the SOHO orbit indicate the location where the quadratures occur. Dotted lines indicate the May 1997 quadrature as example. Figure from Suess et al. (2000)

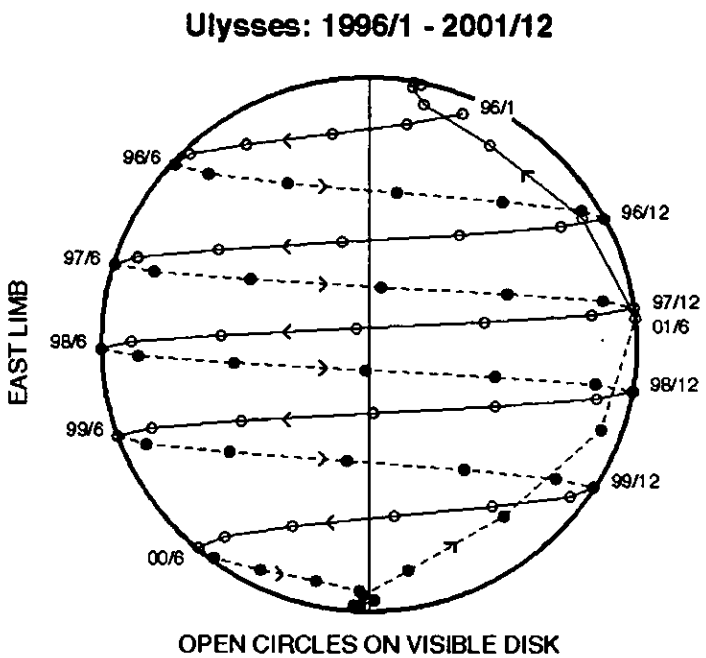

Figure 2.12: Orbit of Ulysses projected on the solar disc as seen from Earth. The vertical line joins the north and south ecliptic pole. Symbols are plotted for the first day of each calendar month, and open circles mark positions on the visible disc. At latitudes below 50 degrees, the ecliptic longitude of the spacecraft is within 90 degrees of the Sun-Earth line for 6 months of each year, typically between January and June. (Figure from Ulysses WEB page).

Chapter 3

Diagnostic Techniques

This chapter describes the diagnostic techniques used in this thesis to derive density, temperature and element abundances. These techniques take advantage of the plasma conditions under which the UV and EUV lines form in the chromosphere and corona, where several line formation processes can be neglected.

3.1 Line Emission from a Hot Thin Plasma

The UV and EUV lines of the solar spectra are emitted in the chromosphere and corona. Most of these are optically thin at such wavelengths: the radiation that forms here escapes from the source without being absorbed in the source itself. The environment in which lines form is composed of hot (T> 2 10^4 K) low density ($N_e < 10^{13}$ cm^{-3}) plasma. Many processes can in principle excite, de-excite, ionize or de-ionize the gas, but these extreme conditions impose a selection on possible processes.

An optically thin emission line forms, mainly, through the *spontaneous emission* process, in which the transition of the electron from the upper level j to lower level i occurs with the emission of a photon of energy $h\nu_{ji}$ (Mariska, 1992). If N_j is the number density of atoms that populate the j level and A_{ji} is the transition probability (s^{-1}) for the spontaneous emission of a photon with energy $h\nu_{ji}$, then the total emissivity of the transition is given by

$$\epsilon_{ji} = A_{ji} N_j \qquad phot\ cm^{-3} s^{-1} \tag{3.1}$$

The line intensity is obtained by integrating the emissivity (per unit solid angle) along the line of sight

$$I_{ji} = \frac{1}{4\pi} \int \epsilon_{ji} dh \qquad phot\ cm^{-2} s^{-1} sr^{-1} \tag{3.2}$$

The unknown quantity N_j of Equation 3.1 can be expressed in terms of other parameters of the plasma that are more easy to calculate:

$$N_j = \frac{N_j}{N_{ion}} \frac{N_{ion}}{N_{el}} \frac{N_{el}}{N_H} \frac{N_H}{N_e} N_e \tag{3.3}$$

where N_j/N_{ion} is the population of the level j relative to the total number density of the ion N_{ion} and is a function of density and temperature; N_{ion}/N_{el} is the relative abundance of the ionic species, and is predominantly a function of temperature; N_{el}/N_H is the element abundance relative to hydrogen; N_H/N_e is the hydrogen abundance compared to electron density. This last quantity is estimated to be ≈ 0.8, due to the almost complete ionization of hydrogen and helium in the hot plasma, and by a small contribution from the much less abundant heavier elements. From the expressions 3.2 and 3.3 it can be seen that the intensity of the line observed strongly depends on the physical conditions of the emitting plasma. The line intensity is then an important element from which physical information of the plasma can be derived, even if this often requires simplified assumptions for some of the factors of Equation 3.3.

3.1.1 Ionization State

The state of ionization of an atom (N_{ion}/N_{el}) is calculated considering all the contributions that can arrive from upper and lower stages of ionization for each particular ion state. So, for example, if the atom has atomic number X, there will be X+1 ionization stages to consider. The calculation is simplified by the low density and low photon flux of the corona, which allows the ions to be considered as in their ground states (the coronal approximation) and the ionization equilibrium is valid for each state:

$$\frac{1}{N_e}\left(\frac{dN_m}{dt}\right) = 0 = q_{m-1}N_{m-1} - (q_m + \alpha_m)N_m + \alpha_{m+1}N_{m+1} \tag{3.4}$$

where q_m and α_m are the ionization and recombination rates of the ion m. To obtain the density N_m, the X+1 Equations 3.4 must be solved.

The dominant processes for ionization and recombination in the optically thin plasma are:

- *collisional ionization* from the ground configuration by electron impact

$$X_n^m + e \Rightarrow X_{n'}^{m+1} + e + e' \tag{3.5}$$

  where X indicates the atom species, m the ionization stage, n and n' the quantum states of the ions.

- *radiative recombination*

$$X_n^{m+1} + e \Rightarrow X_{n'}^m + h\nu \tag{3.6}$$

- *dielectronic recombination*

$$X_n^{m+1} + e \Rightarrow (X_{n'}^m)^{**} \Rightarrow X_{n''}^m + h\nu \tag{3.7}$$

where ** indicates the doubly excited level. This can be followed by either its reverse process *autoionization*, or by a spontaneous radiative transition. Dielectronic recombination in the corona is often more important than radiative recombination.

- *autoionization* is the inverse of dielectonic recombination.

The calculations, which involve free electron collisions, assume electrons are in thermal equilibrium at a certain temperature T_{max} and density N_e. Moreover it is assumed that no external radiation field is present.

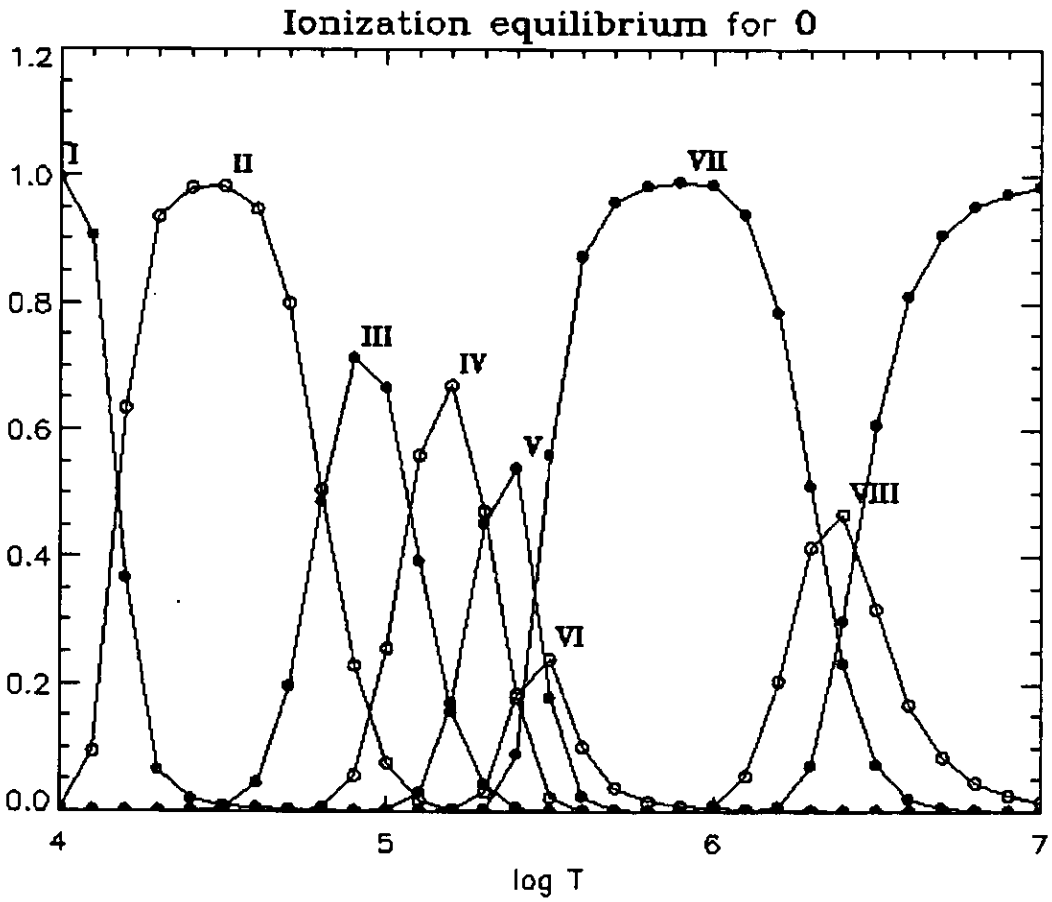

Figure 3.1: Ion fractions for oxygen as a function of temperature for the Mazzotta et al. (1998) ionization equilibrium

An example of ionization equilibrium calculations from Mazzotta et al. (1998) is given in Figure 3.1 where the ion densities are plotted as a function of temperature for oxygen.

3.1.2 Excitation

The N_j/N_{ion} term on the right hand side of Equation 3.3 represents the relative population density for the level j. This term is calculated by summing over the contributions of the collisional and radiative processes for excitation and de-excitation from the adjacent levels. In the chromosphere and the lower corona, ionization and recombination processes are much slower (tens to thousands of seconds) than excitation and de-excitation processes (fractions of a second), so the level populations can be calculated independently from the ionization/recombination processes. Moreover, because the characteristic time scale for excitation/de-excitation is short (e.g. $10^{12}/N_e$ (Harrison & Thompson, 1992)), the plasma can be considered to be in steady state and the population of a level j of the ion X^m can be calculated by solving the statistical equilibrium equation

$$N_j(N_e \sum_i C^e_{ji} + N_p \sum_i C^p_{ji} + \sum_{i<j} A_{ji} + \sum_{i>j} R_{ji}) \quad =$$

$$\sum_i N_i(N_e C^e_{ij} + N_p C^p_{ij}) + \sum_{i>j} N_i A_{ij} + \sum_{i<j} N_i R_{ij} \tag{3.8}$$

where C^e_{ji} and C^p_{ji} are the electron and proton collisional excitation coefficients, R_{ji} the stimulated absorption rate coefficient and A_{jk} is the spontaneous emission coefficient.

The Coronal Model Approximation

In the low corona, this calculation is made simpler by applying the *coronal approximation* (Mason & Monsignori Fossi, 1994), which assumes the main processes are electron collisional excitation from the ground level (g) and radiative decay for de-excitation. (Following this approximation the population of the level j is negligible compared to the population of the ground level). As will be shown below, under this approximation it is easier to express the different dependencies on electron density of the different energy levels. However, the atomic database used for this thesis does not make use of the coronal model approximation.

The statistical equilibrium 3.8 can be rewritten

$$N_g(X^m)N_e C^e_{gj} = N_j(X^m) \sum_{k<j} A_{jk} \tag{3.9}$$

where C^e_{gj} is the electron collisional excitation coefficient for the transition from the ground level, and A_{jk} are the spontaneous emission coefficients to the lower levels. This equation states that the density population of the excited level j does not change with time because the rate at which it is populated by collisions ($N_g(X^m)N_e C^e_{gj}$) is balanced by the rate at which it is depopulated by spontaneous emission ($N_j(X^m) \sum_{k<j} A_{jk}$).

If a Maxwellian distribution of velocity for the incident electrons is assumed, the collisional coefficient can be expressed as a function of the kinetic temperature T:

$$C^e_{gj} = \frac{8.63 \times 10^{-6}\ \Omega_{gj}}{\omega_g T^{1/2}}\ exp(\frac{-\Delta E_{gj}}{kT}) \qquad cm^{-3}\ s^{-1} \tag{3.10}$$

where Ω_{gj} is the collision strength for the excitation, k is Boltzmann's constant, ΔE_{gj} is the threshold energy for the transition, and ω_g is the statistical weight of the ground state. This last quantity is the number of electrons that can occupy the level (the degeneracy of the level).

Equation 3.9 can be solved for $N_j(X^m)$ and, together with Equation 3.3 can be used to rewrite Equation 3.1, as follows:

$$I_{jg} = \frac{1}{4\pi} 0.8 \int A_X \frac{N_{ion}}{N_{el}} B_{jg} C^e_{gj} N_e^2 dh \tag{3.11}$$

where A_X is the element abundance relative to hydrogen, the figure of 0.8 is the hydrogen abundance relative to electron density and B_{jg} is the radiative cascade coefficient (or branching ratio)

$$B_{jg} \equiv \frac{A_{jg}}{\sum_{k<j} A_{jk}} \qquad k < j \tag{3.12}$$

(the branching ratio of the transition from j to g compared to all the radiative transitions out of level j).

The equation for intensity is generally rewritten collecting together the temperature-dependent terms in a function called the *contribution function*:

$$C(T)_{N_e} = 0.8 \frac{N_{ion}}{N_{el}} B_{jg} C^e_{gj} \tag{3.13}$$

so that the line intensity can be expressed as:

$$I_{jg} = \frac{1}{4\pi} \int A_X\ C(T)_{N_e}\ N_e^2\ dh \tag{3.14}$$

The contribution function may or may not be density-sensitive depending which transitions are involved in the line formation. For most cases the above approximation can be used. These electric dipole transitions to and from the ground level, and for which there is no change in the spin are called *allowed* transitions and their probability is high. There are also less probable transitions for which a change of spin occurs (*intercombination*) or which are not electric dipole transitions but instead are magnetic dipole or electric quadrupole transitions (*forbidden*). These less probable transitions (typically $A_{mg} \approx 10^0 - 10^2$ s (Mason & Monsignori Fossi, 1994)) involve a *metastable* level (m), for which the de-excitation

process is often collisional de-excitation. So, the population of an intercombination level is given by

$$N_m = \frac{N_g N_e C^e_{gm}}{N_e C_{mg} + A_{mg}} \tag{3.15}$$

For low density, radiative depopulation dominates and $I_{jg} \approx N_e^2$. For high densities collisional de-excitation dominates and the metastable level is in Boltznam equilibrium with the ground level

$$\frac{N_m}{N_g} = \frac{C^e_{gm}}{C^e_{mg}} = \frac{\omega_m}{\omega_g} exp(\frac{-\Delta E_{gm}}{kT}) \tag{3.16}$$

and so $I_{jg} \approx N_e$. So, depending on which levels are involved in the line formation, the contribution function can be a function of density.

Figure 3.2 shows examples of the contribution functions of Fe lines from various Fe ions, as a function of temperature.

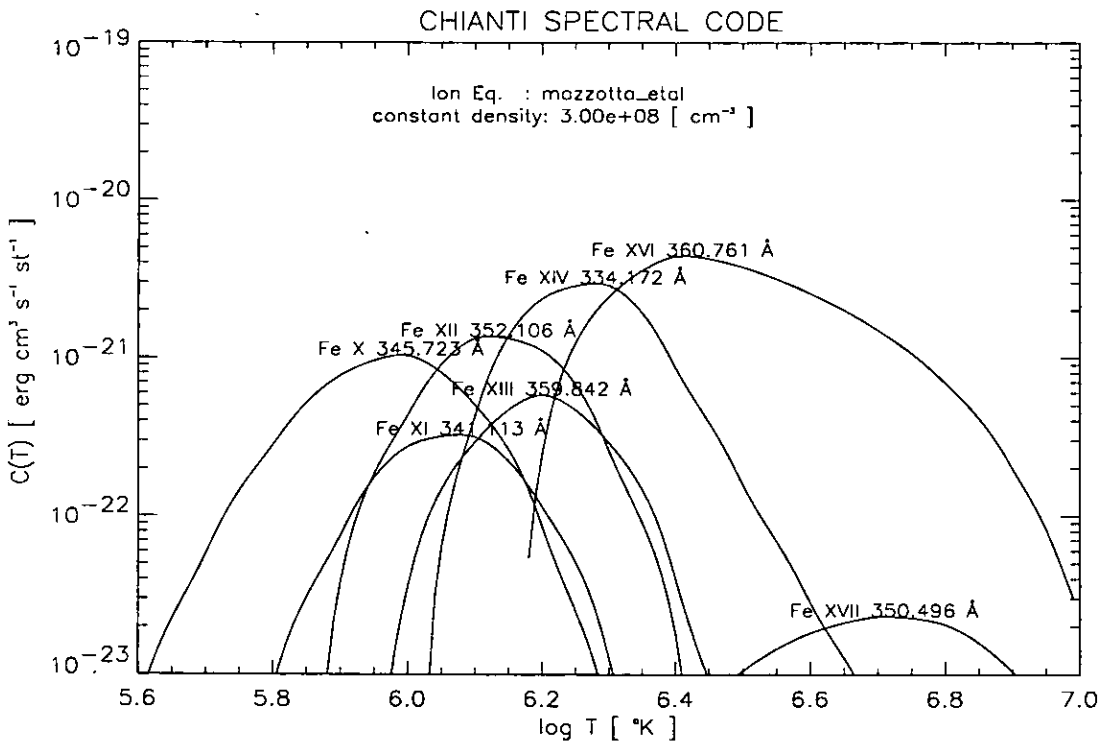

Figure 3.2: Contribution functions for some Fe ions as function of temperature. Each curve is labeled at its peak position.

Throughout this thesis the CHIANTI version 2 (Landi et al., 1999) database has been used. As mentioned above, it does not use the coronal approximation, but includes electron excitation and de-excitation, and spontaneous radiative decay (Del Zanna, 1999). (Note that the radiative excitation described in the next section is not included in CHIANTI version 2).

Several ionization equilibrium calculations are available in the CHIANTI package. The more reliable of which, because more up-to-date and tested (e.g. Del Zanna, 1999; Allen et al., 2000), are Arnaud & Rothenflug (1985); Arnaud & Raymond (1992) and Mazzotta et al. (1998). Several tests have been made using the Arnaud & Raymond (1992) calculations (Chapter 4) but most calculations performed for this thesis have adopted the Mazzotta et al. calculations.

The Radiation Scattering Process and Doppler Dimming

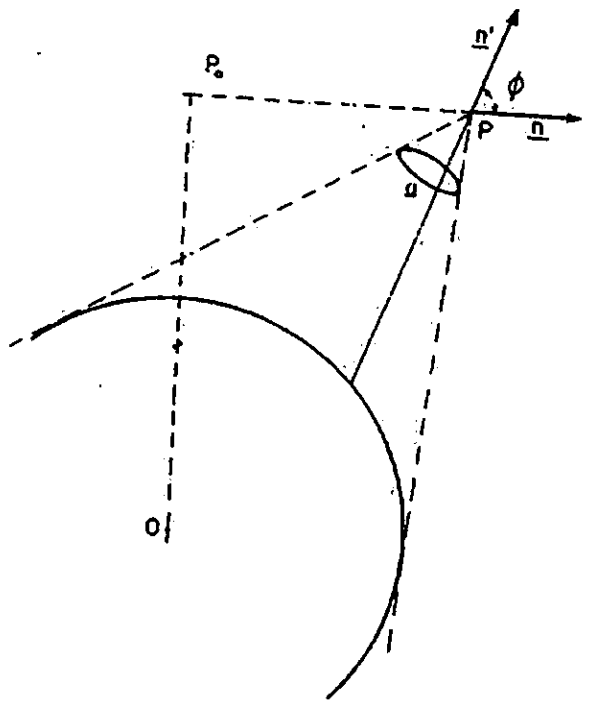

Figure 3.3: Geometry of the radiative scattering process. (Figure from Noci et al. (1987)).

In the very low density upper corona, it can happen that exciting via radiative absorption can compete with electron collisional excitation. In such a case the coronal model approximation cannot strictly be applied. This is the case, for example, for the H-Lyman and O VI lines. For these lines the emissivity is given by

$$\epsilon_{jg} = N_g(N_e C_{gj} + 4\pi h\nu B_{gj} J_{gj}) \qquad phot\ cm^{-3}s^{-1} \tag{3.17}$$

where B_{gj} is the Einstein absorption coefficient and J_{gj} is the mean intensity of the exciting radiation coming from the disk. The process of radiative excitation involves absorption by coronal ions of photons coming from the underlying atmosphere, with sufficient energy to

excite an electron from the ground level to an upper one. In determining the expression for the intensity emitted due to this process, it must take into account the case where the excited ions are in motion (as in the upper corona). When this happens, the emitted spectrum will appear red shifted in the frame of reference of the outflowing ions. For high enough outflow velocity the intensity of the resonantly scattered radiation will appear to be decreased. This effect, called *Doppler Dimming*, will be discussed further at the end of this section.

For the following description the formalism of Noci et al. (1987) will be used. In a frame of reference at rest with the ions, the intensity at a point P (see Figure 3.3) is given by

$$I_{rad} = \frac{1}{4\pi} 0.8\ h\nu_0 \int_0^H A_X \frac{N_{ion}}{N_{el}} N_e dh \int_\Omega p(\phi) d\omega' \int_0^\infty I(\lambda - \delta\lambda, \mathbf{n}') \Phi(\lambda - \lambda_0) d\lambda \quad (3.18)$$

Here ϕ is the angle between $\mathbf{n}'$, the direction of the incident photon, and $\mathbf{n}$, the lin-of-sight direction; Ω is the solid angle subtended by the source of the exciting radiation; and $p(\phi)d\omega'$ is the probability that a photon moving along the direction $\mathbf{n}$ would have been in $d\omega'$ before scattering (i.e. that the scattering process has changed its direction by an angle ϕ). This function was estimated for the main lines used here by Beckers & Chipman (1974):

$Ly\alpha$	$4\pi p(\phi) = (11 + 3\cos^2\phi)/12$
$O\ VI$ 1032 $\AA$	$4\pi p(\phi) = (7 + 3\cos^2\phi)/8$
$O\ VI$ 1037 $\AA$	$4\pi p(\phi) = 1$

In Equation 3.18, $I(\lambda, \mathbf{n}')$ is the exciting intensity per unit wavelength as measured in this reference frame; λ_0 is the transition wavelength of the exciting radiation in the laboratory reference frame and $\delta\lambda$ is the Doppler shift of λ_0 in the ion reference frame. For the upper coronal ions with an outflow velocity $\mathbf{w}$ the shift in wavelength is given by

$$\delta\lambda = \lambda_0 \frac{\mathbf{w} \cdot \mathbf{n}'}{c} \quad (3.19)$$

where c the velocity of light. The $\delta\lambda$ is thus a function of the direction of the incident radiation. The function Φ is the normalized absorption profile along the direction of the incident radiation. If the ions have a Maxellian velocity distribution then

$$\Phi(\lambda - \lambda_0) = \frac{c}{\lambda} \sqrt{\frac{m_i}{2\pi k_B T_{\mathbf{n}'}}}\ exp(-\frac{m_i c^2}{2k_B T_{\mathbf{n}'} \lambda^2} (\lambda - \lambda_0)^2) \quad (3.20)$$

It is important to note that all coronal lines have a radiative contribution (I_{rad}), and its importance compared to the collisional component (I_{col}) depends on the physical condition

of the plasma. In particular, it is important to point out the different density dependence of these two components. Comparing Equation 3.14 and Equation 3.18 it is easy to see that $I_{col} \sim N_e^2$ and $I_{rad} \sim N_e$, so that the radiative component becomes more and more important with increasing solar distance.

Figure 3.4 shows intensities from the radiative and collisional components for different ions, plotted as a function of solar distance. This calculation was performed by Kohl & Withbroe (1982), assuming an isothermal plasma at T= 1.5 $\times 10^6$ K. The equatorial model for a static corona (V_W=0) by Allen (1963) has been used together with the corresponding intensities of the white light continuum (K component). From the Figure it is evident that, apart from H Lyα , the radiative component is already important by about 2 $R_\odot$.

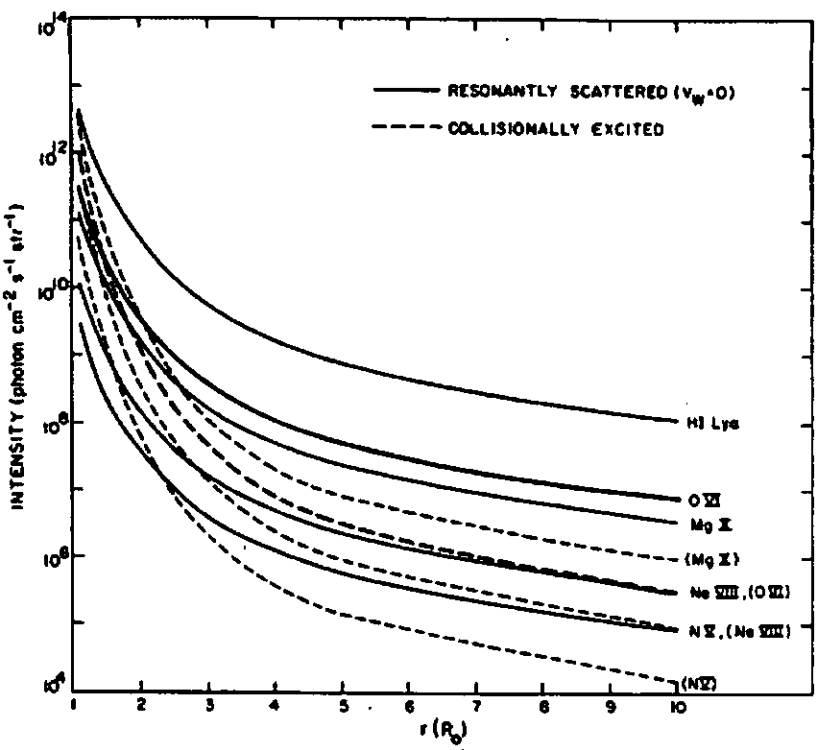

Figure 3.4: Intensity of the collisionally excited (dashed lines, ion name in parentheses) and resonantly scattered (solid lines, ion name without parentheses) components of H I Lyα , N V (1238 Å), O VI (1032 Å), Ne VIII (770 Å) and Mg X (610 Å). These intensities have been calculated for a static corona by Kohl & Withbroe (1982). Figure from Kohl & Withbroe (1982).

For the lithium and sodium isoelectronic sequence lines it is possible to separate empirically the collisional and radiative contributions from the total intensity (Kohl & Withbroe, 1982). These lines are produced as doublets whose ratio of intensities is 2:1 for the collisional part (because it is proportional to the ratio of the collisional strengths), and 4:1 for the radiative part. This last factor 4 is due to a factor of 2 from the disc intensities (because they form collisionally), times a factor of two from the oscillator strengths). If the

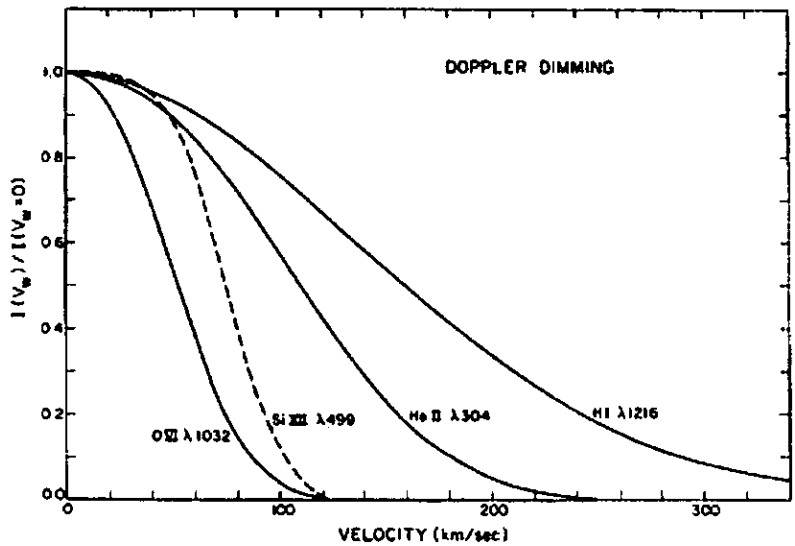

Figure 3.5: Doppler Dimming calculated as a function of flow velocity assuming an isothermal corona at T= 1.5 $\times 10^6$ K. (Figure from Kohl & Withbroe (1982)).

ratio from the observed lines equals 2, then the lines are produced only from the collisional excitation, and if the ratio is 4, they are produced only from the radiative scattering. In the more general case, the ratio will be between two and four. More details of this radiation scattering process in the solar corona can be found in Noci et al. (1987) and Noci & Maccari (1999).

As already mentioned, the presence of the solar wind flow results in a reduction of the scattered radiation. Figure 3.5 shows an example taken from Kohl & Withbroe (1982), of Doppler dimming effect calculated for different lines as a function of flow velocity. The quantity plotted is the ratio of the dimmed line intensity to the intensity at rest (V_W=0). The O VI 1032 Å is the most affected by the plasma velocity, being significantly reduced even for velocity $\sim$ 30 km s^{-1}. In contrast, Lyα is unaffected until about 100 km s^{-1}.

The amount of Doppler dimming of the line intensity can be used as a diagnostic tool for plasma velocity. For a reliable determination, an accurate measure of the width of the disc intensity is needed, because the magnitude of the dimming effect depends on this (see Equation 3.18). However the presence of a dimming effect in the data can be a warning that the plasma velocity is affecting the ionization equilibrium.

3.1.3 Departure from Ionization Equilibrium

In Section 3.1.2 the line intensity expression has been derived for a plasma for which the coronal approximation applies. Several factors can contribute to the departure from

equilibrium, and in this section the main one will be discussed.

The solar corona is a dynamic and structured body so that local change in physical conditions can alter the ionization balance. To establish the conditions for equilibrium to hold, the time scale for ionization (τ_{ions}) and recombinations (τ_{rec}) must be compared to the characteristic time scale of other competing events. For an ion of charge m, the collisional ionization time to reach the state $m+1$ is

$$\tau_{ion}(m) = \frac{1}{N_e q_m} \tag{3.21}$$

and the time scale for recombination from the state $m+1$ to m is

$$\tau_{rec}(m+1) = \frac{1}{N_e \alpha_{m+1}} \tag{3.22}$$

When τ_{ions} and τ_{rec} become too long compared to the time the plasma takes to change, then time-dependent ionization and recombination equations (Equation 3.4) must be considered.

For the upper solar corona, the low density and the velocity fields can breake the equilibrium conditions. A plasma with a significant velocity (v) can breake its equilibrium if the time scale for expansion (τ_{exp}) is much shorter then τ_{ion} and τ_{rec}, where τ_{exp} is defined by

$$\tau_{exp} = (\frac{v}{n}\frac{dn}{dr})^{-1} \tag{3.23}$$

where v indicates the plasma velocity and n is the plasma density.

In order to estimate all these time scales, a coronal model that gives density, temperature and velocity at different solar distances is needed. Figure 3.6 shows a comparison between several time scales as a function of solar distance as derived by Withbroe et al. (1982). For these calculations the density models were from Saito (1970), Munro & Mariska (1977) and Allen (1963). As the density drops with distance, the lifetime of the ion increases until the ionization balance become 'frozen-in' and no further change in the ion state occurs. This condition is reached when the expansion time is comparable with the time scales of the atomic processes. For heavier elements (e.g. O, Si, Fe) this is expected to happen within few solar radii (Hundhausen, 1972). In the hydrogen case, the time scales involved in the ionization equilibrium are τ_ν and τ_c (Figure 3.6). In the high density equatorial regions, within 5 $R_\odot$ the ionization equilibrium condition is driven by the collisional ionization time and its dependence on the electron temperature. In coronal holes, where the density is low, the ionization balance freezes-in at a distance of about 3-4 $R_\odot$.

Another effect of the low density in the upper corona is the lack of thermalization between electrons, protons and other ions, with the result that each can have a velocity distribution function chatacterized by different temperatures: Figure 3.6 (τ_{ep} against τ_{exp}) shows that this condition can be reached within 2 $R_\odot$. Due to the lower density of coronal holes compared to equatorial regions, and the higher velocities, ionization equilibrium is expected to brake down at lower distances in the coronal holes.

In the low corona, departure from equilibrium can occur where there are high velocity fields, e.g. in transients or coronal holes (Joselyn et al., 1979). Moreover, non-Maxwellian velocity distributions can affect the ionization balance calculations.

Rapid changes in temperature can also cause departure from equilibrium. In a rapidly cooling gas (e.g. in post flare loops) the departure from equilibrium occurs when the τ_{rec} is greater than the cooling time. In the opposite situation, in a rapidly heating environment, it is the slow ionization time that can cause a departure from equilibrium. As for the case described above, the time dependent Equation 3.4 must be solved. In this case a proper description of the ionization state depends upon the model used to describe the time-dependence of the plasma conditions and its reliability to fit the observations (Raymond, 1988).

3.1.4 Departure from Ionization Equilibrium Condition: a Test

Tests have been performed in order to validate whether ionization equilibrium applied at 1.5–1.6 $R_\odot$ to UVCS data (as assumed in Chapter 4). As mentioned in the previous section, this needs to be checked when the plasma studied is moving, and in this case at 1.5-1.6 $R_\odot$, the plasma can already have reached several tens of kilometers per second.

The test consisted of comparing the expansion time scales of the plasma with the ionization and recombination times for H-like and He-like ions. The first class of ions has a shell configuration almost close, so it is expected to react easily. The latter is in a stable shell configuration, so it is expected not to react easily.

The O VI and O VII cases were chosen as representative of these sequences, because oxygen is abundant in the solar corona and solar wind. The test was performed for both streamer and coronal hole plasma conditions, and Cranmer et al. (1999) and Wang et al. (1998) models (respectively) for those regions were used.

Temperature and velocity values were taken from the models already mentioned, whilst ionization and recombination values were taken from Summers (1979). In the Summers calculations, the free electrons involved in the processes are considered thermalized with a Maxwellian temperature distribution; the contribution from proton collisions is neglected;

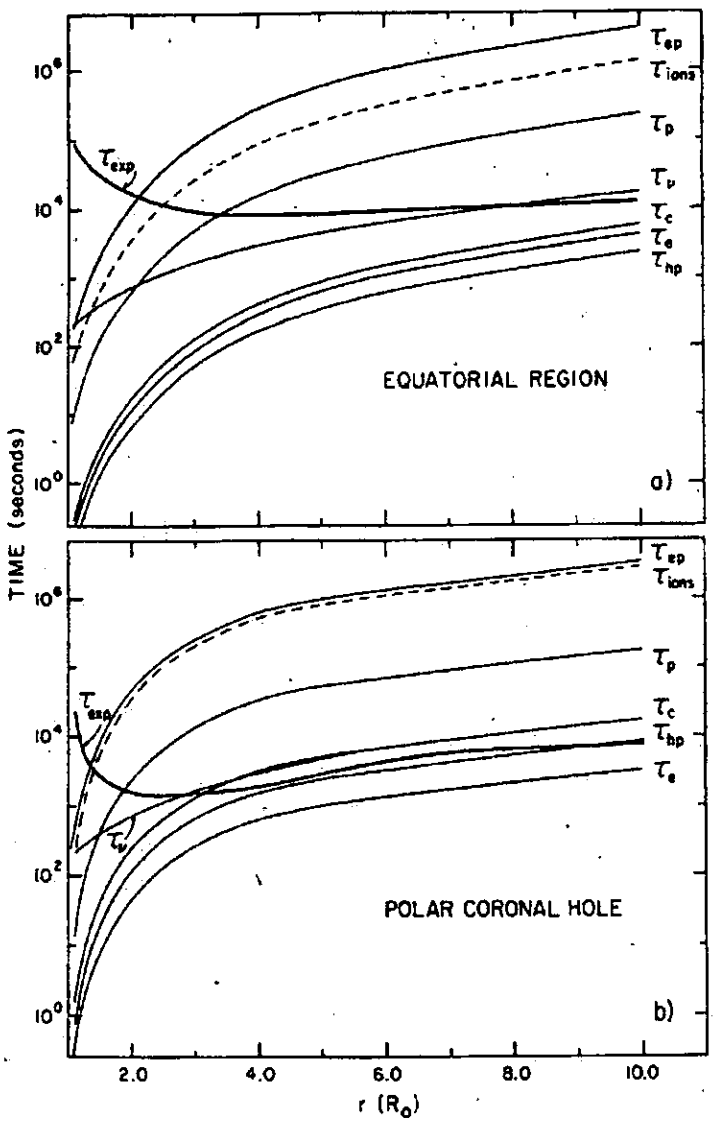

Figure 3.6: Characteristic time scales plotted as function of solar distance for equatorial region (top) and coronal hole (bottom). τ_{exp} is the expansion time; τ_{ions} is ionization equilibrium time for ions; τ_ν is the time for H I photoionization; τ_c the H I collisional ionization; τ_e is the electron thermalization; τ_p is the proton thermalization time; τ_{hp} is the time for hydrogen-proton charge exchange and τ_{ep} is the time for electron and proton temperature to equalize. (Figure from Withbroe et al. (1982)).

the statistical equilibrium equation for the population levels for each stage of ionization includes collisional excitation, de-excitation and ionization together with spontaneous emission, and radiative, dielectronic and three-body recombination; and inner shell ionizations are also included. Finally, to calculate the expansion time, instead of using Equation 3.23, the expression

$$\tau_{exp} = \frac{1}{v}\left(\frac{dlogT}{dr}\right)^{-1} \tag{3.24}$$

was used. The two are essentially equivalent, and the choice to use this latter was guided by the desire to use the temperature as variable, instead of the density (J. Raymond, private communication).

Coronal Hole Results

The first model to be considered here is the coronal hole model by Cranmer et al. (1999). Figure 3.7 shows, from top to bottom, the electron density, temperature and mass flux outflow velocity taken from the model.

Under the assumption of a spherically symmetric distribution for density, Cranmer et al. derived N_e using polarized brightness measurements. The values as a function of distance are given by:

$$N_e(r) = 1 \times 10^5 \ cm^{-3}\left[3890\left(\frac{R_\odot}{r}\right)^{10.5} + 8.69\left(\frac{R_\odot}{r}\right)^{2.57}\right] \tag{3.25}$$

This model for density was used in this thesis to derive τ_{ion} and τ_{rec} of Equations 3.21 and 3.22.

The temperature profile shown in Figure 3.7 was obtained by Cranmer et al. (1999), by parameterizing in radius (r) the Ko et al. (1997) results from *in situ* charge state measurements in the fast solar wind, to obtain

$$T_e(r) = 10^6 \ K \ \left[0.35\left(\frac{r}{R_\odot}\right)^{1.1} + 1.9\left(\frac{r}{R_\odot}\right)^{-6.6}\right]^{-1} \tag{3.26}$$

This profile is a good fit ($< 5\%$) to the Ko et al. values in the interval $1\ R_\odot < r < 10\ R_\odot$.

Figure 3.7 (bottom) shows the empirical neutral H outflow velocity over the pole, derived from H-Lyα Doppler dimming. For the present calculation the A1 model was taken, which assumes that the parallel hydrogen motion ($u_{||}^2 = 2kT_{k||}/m_H$) is in thermal equilibrium with the electrons ($u_{||} = u_e$). The expression for the magnitude of the outflow velocity is then given by

$$v(r) = 110 + 445\left(1 - \frac{R_\odot}{r}\right)^{3.47} \tag{3.27}$$

As explained by Cranmer et al., the condition imposed on $u_{||}$ results in a lower limit for the velocity v, since $T_{ion} > T_p > T_e$.

The results for the time scales derived at different distances are plotted in Figure 3.9: the top left for O VI and top right for O VII. As expected, in the coronal hole the ionization equilibrium is broken at radial distances as low as 1.5 $R_\odot$. These plots show that, while the recombination time is similar for the two ions, this is not true for the collisional ionization time. The recombination is, in both cases, the cause of the lack of equilibrium. This is understandable because above 1.5 $R_\odot$the plasma is cooling down (Figure 3.7) and so the time for recombination becomes the important process.

Coronal Streamer Results

The model used here to test ionization equilibrium in a streamer, was built under the assumption that the corona is composed of one fluid plasma, heated by a volumetric heat source. Moreover, a time-independent momentum function was added to the momentum equation to reproduce the observed wind speed. The results for the coronal streamer parameters are plotted in Figure 3.8. As expected, the streamer is characterized by a higher density and temperature plasma and by a lower wind velocity than the to coronal hole.

The ionization, recombination and expansion times have been derived in the same way as for the coronal hole. The results are plotted in the lower part of Figure 3.9. Note the slower expansion of the plasma in the streamer compared with in the coronal hole. This is mostly due to the different expansion velocities. The recombination and ionization times are much shorter than for the coronal hole, mainly because of the higher density. As in the case of coronal hole, the ionization time is more dependent from the state of ionization than the recombination time but, again for O VI, is this latter that first reaches the condition that breakes the equilibrium. The figure shows that the ionization equilibrium fails at about 2 $R_\odot$ for the O VI and slightly before for the O VII, corresponding to a velocity of about 40 Km/s. As the solar distance increases beyond the maximum of temperature, the O VII ionization probability becomes so low that the ionization time increases steeply and ends up competing with the recombination time to breake the equilibrium. This can also be seen from Figure 3.7 and 3.1. Beyond 1.8 $R_\odot$the temperature in streamer decreases from log$T$=6.3. Under these temperature the O VIII ion-fraction is becoming very low (Figure 3.1).

To conclude this section, it can be said that the streamer is a good environment for diagnostic study, because the high density and slow plasma flux help to maintain the

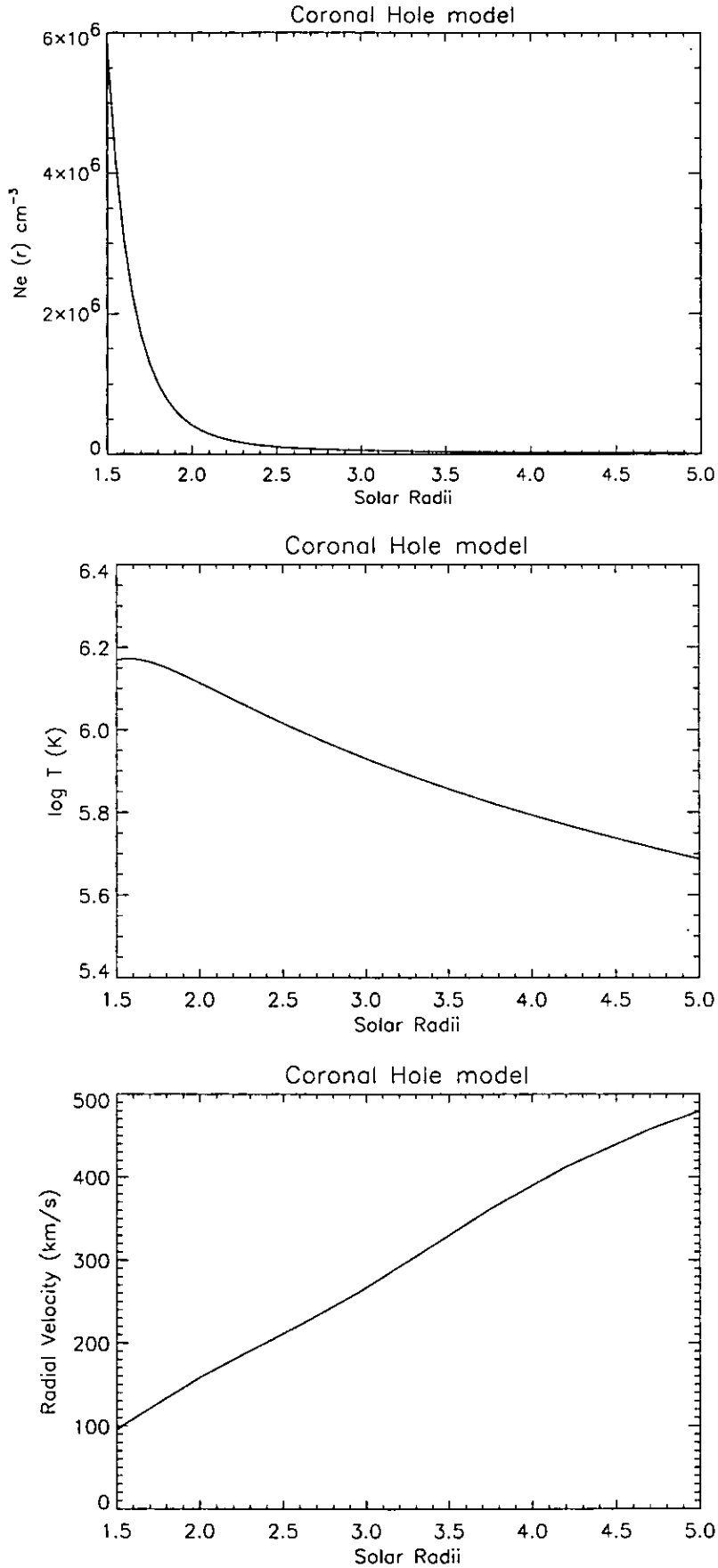

Figure 3.7: Modeled profiles of electron density (top), temperature (middle) and bulk outflow velocity (bottom, model A1). These profiles were obtained by using Equations 3.25, 3.26 and 3.27 of Cranmer et al. (1999) model.

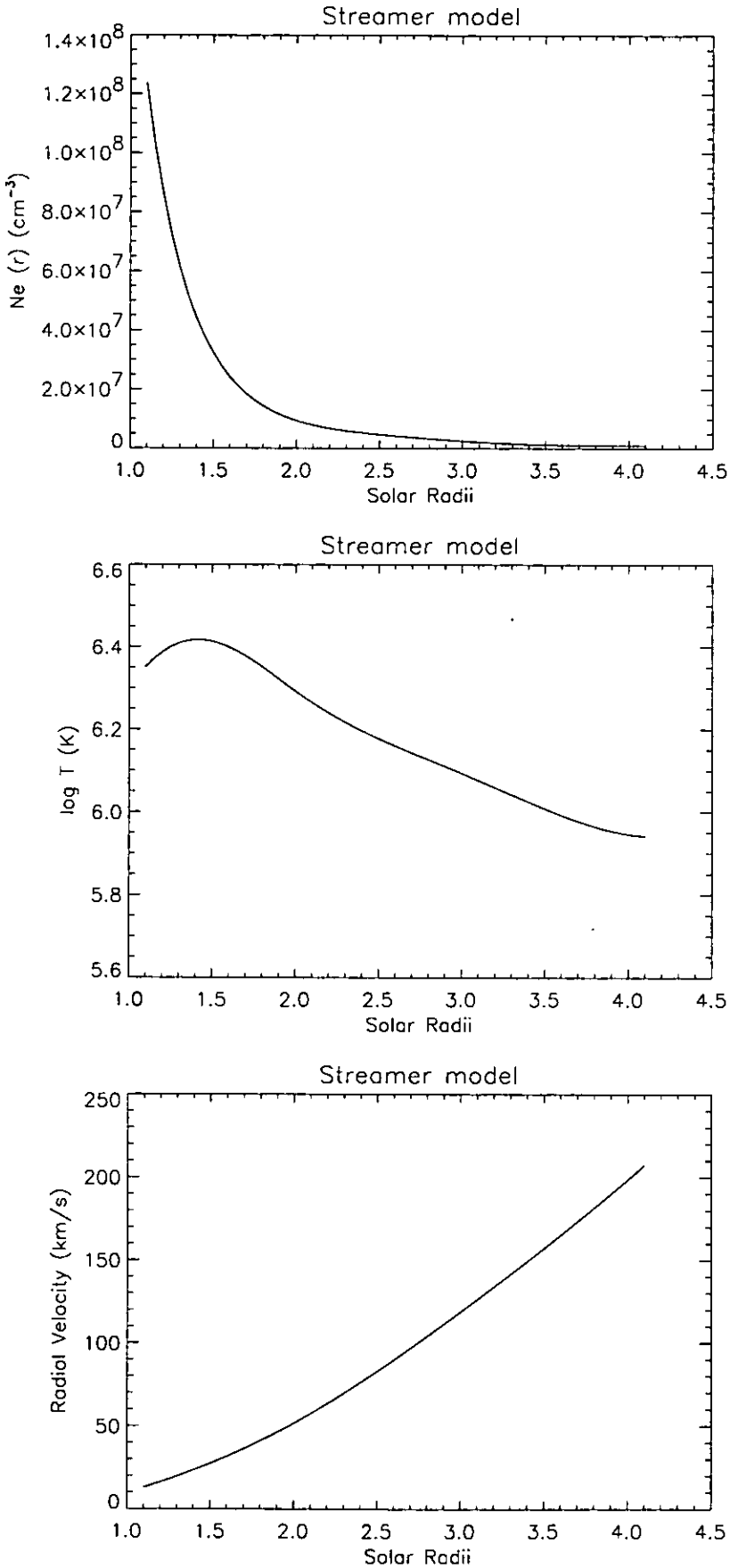

Figure 3.8: Modeled profiles of electron density (top), bulk outflow velocity (middle) and temperature for the streamer. These plots reproduce the models of Wang et al. (1998)

condition of equilibrium in the ionization state. For radial distances up to those considered in this thesis ($\approx$ 1.5 $R_\odot$) this condition holds and the standard diagnostic techniques can be applied.

We proceed now to discuss the primary diagnostic techniques that can be applied under this condition, and which have been used in this thesis.

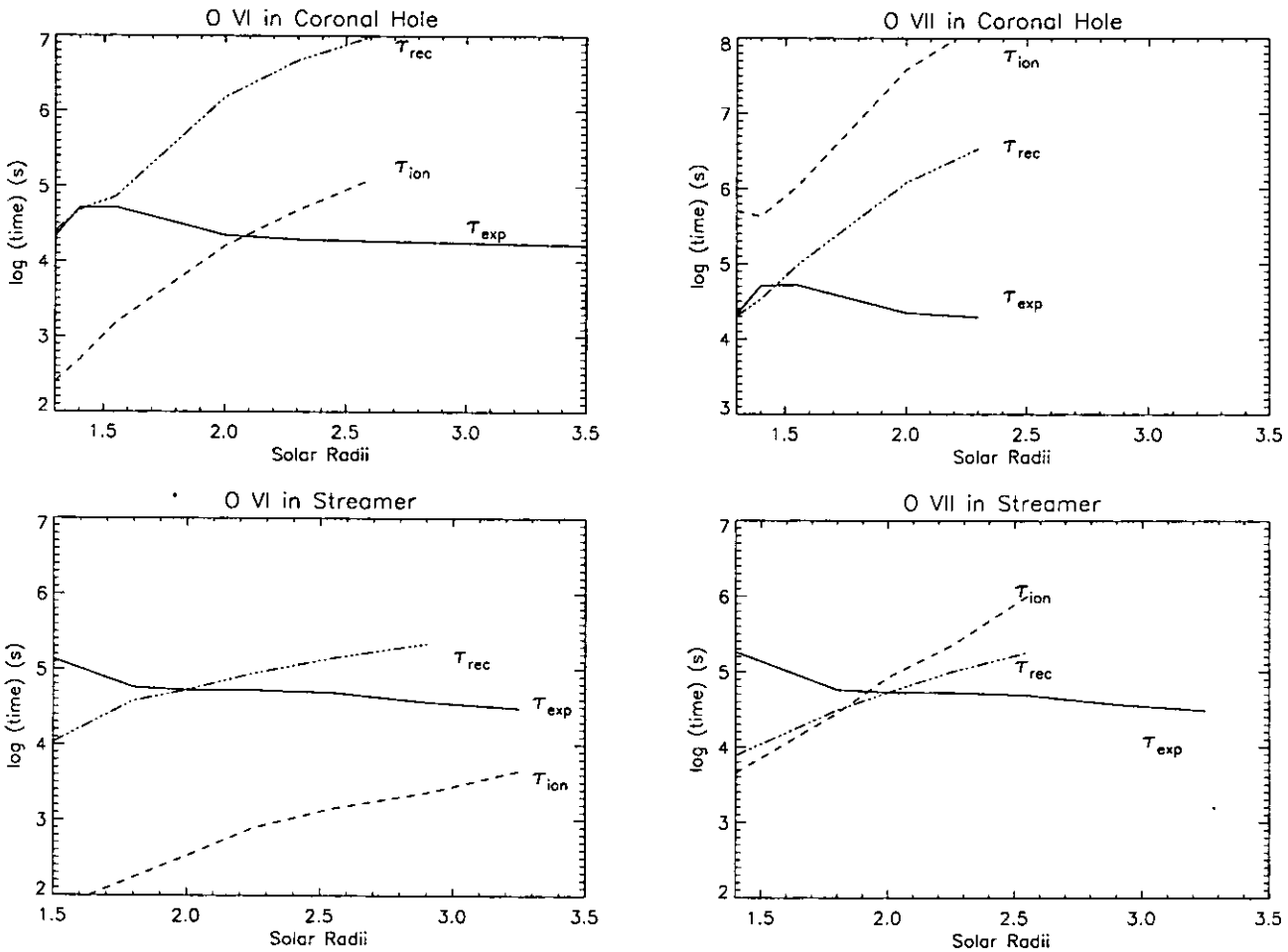

Figure 3.9: Top: coronal hole time scales for flux expansion (τ_{exp}), ionization (τ_{ion}) and recombination (τ_{rec}) as a function of solar distance for O VI (left) and O VII (right). Bottom: the same for coronal streamer.

3.2 Emission Measure and Differential Emission Measure

For an isothermal plasma at temperature T, the *Emission Measure* (EM) is the measure of the amount of plasma at that temperature that emits the observed intensity, and it is defined by (Pottasch, 1963)

$$EM = \int_0^H N_e^2 dh \tag{3.28}$$

where H is the observed total line of sight. For a multi-thermal plasma, the simplest way to estimate the above quantity is by assuming its average value along the line of sight, so that it can be derived directly from the observed intensity of the line. Pottasch (1964), taking advantage of the fact that most of the emission of a line arises from an interval ΔT around the peak of the function $C(T)$, defined the average EM value as

$$< EM >= \frac{I_{obs}}{A_X < C(T) >} \tag{3.29}$$

where the element abundance is assumed to be known, ΔT is the temperature interval where the $C(T)$ is greater than one-third of its peak value and $C(T)$ inside this interval assumes a constant value equal to 0.7 $C(T_{max})$. The value $< C(T) >$ is defined by

$$< C(T) >= \frac{\int_{\Delta T} C(T)dT}{\Delta T} \tag{3.30}$$

If lines from different ions of the same element are observed, then for each of them an averaged EM can be derived and a profile of $< EM >$ in temperature is so obtained. In this way, eliminating the uncertainty on the element abundance (and assuming it does not change with temperature), Pottasch et al. found that this profile formed a smooth curve. Even if this was a crude approximation for the EM, it was enough to be used for element abundance determinations relative to a fixed element. Several $< EM > *A_X$ curves were plotted using different elements, and considering that the emission measure is unique for each temperature, then the systematic difference encountered in magnitude between each curve and the reference one was adjusted by modifying the abundance value.

This method has been followed by improvements, mainly on the basis that the plasma along the line of sight is more realistically not isothermal, and the quantity in the integral of Equation 3.28 is a function of T. In the present thesis, this last consideration has been taken into account, and the definition of the EM through the *Differential Emission Measure* (DEM) was used.

The *Differential Emission Measure* (DEM) is defined as

$$DEM(T) = N_e N_H \frac{\mathrm{d}h}{\mathrm{d}T} \tag{3.31}$$

This quantity takes account of the change of temperature along the line of sight h, and gives the contribution only of the plasma in the interval of temperature T to $T + dT$. In a similar way of Equation 3.29, the emission measure is then given by:

$$EM = \int_T N_e N_H \frac{\mathrm{d}h}{\mathrm{d}T} dT = \int_T DEM(T)dT \tag{3.32}$$

where the DEM(T) is defined for finite values of $\mathrm{d}h/\mathrm{d}T$.

If the observed spectral line forms by collisional excitation populating the upper level ($I \sim N_e N_H \sim N_e^2$), the total intensity of the line is related to the emission measure of the plasma by summing all the contributions of DEM(T) for the different temperatures encountered along the line of sight. If the assumption of $N_H/N_e = 0.8$ is omitted from the function C(T) (this is the assumption in the CHIANTI database), then the Equation 3.14 for intensity assumes the expression:

$$I_{jg} = \frac{1}{4\pi} \int A_X \; C(T)_{N_e} \; DEM(T) \; dT \tag{3.33}$$

To have a complete description of the EM along the line of sight, the DEM must be determined using all the observed lines. The best estimate of this curve is obtained from using as many observed lines as possible, with emitting temperature covering as wide a range of T as possible. A set of inverse integral equations, one for each line, must be solved for the DEM in order to obtain a unique DEM function. It should be borne in mind that the DEM(T) is a unique function of T but not of h, and so information about its variation along the line of sight cannot be obtained.

Several techniques have been developed to determine the DEM functions, and here we refer in particular to the inversion technique reviewed by Harrison & Thompson (1992).

The DEM(T) of Equation 3.32 is not defined for those temperatures where dh/dT is not finite. On the other hand, the DEM technique has been applied in this thesis to the off-limb observations where, more so than on the disc, the variation of temperature along the line of sight is not monotonic and the condition just mentioned can be encountered. But, since the DEM(T) is determined in practice by finding the best fit of a discretised spline function to the data, the indeterminate points of the function are avoided. What is obtained in the end, for each interval dT, is a value that best fits the average DEM over the whole line of sight. To determine this curve a procedure named CHIANTI_DEM in the CHIANTI package (Landi et al., 1999) has been used. This routine receives as input a set of parameters of the fitted lines and an initial DEM function. Then the contribution function for each line is calculated by choosing the ionization equilibrium calculations, the pressure/density conditions and the element abundances. Then, starting from the initial DEM function, a best fit procedure using a cubic spline function is performed. The result of this process clearly depends on the choice of 'mesh points' for spline curve. They are generally placed at those temperatures where there are constraints from the observations. This is one of the critical points of the whole method for DEM determination: in fact, as Harrison & Thompson (1992) pointed out, the derived DEM can depend quite significantly on the way the constraints are chosen.

The DEM curve can be calculated using different ions from the same element. If another element whose lines overlap in temperature the first curve, is also used, then the DEM curve for this element should align with that one. Any shift between the two can be attributed to an error in the adopted abundance of one or the other element. In this way, the abundance of one element relative to the other can be determined and all lines fitted to the one curve. So the determination of the DEM using lines from a number of different elements necessarily results in a determination of the relative abundances of those elements, the only exception being if the lines from a particular element are the only ones in a particular range of temperature. In this case, the best that can be achieved is to ensure that the curve at this point is smoothly connected to the rest of the DEM. Example of derived DEM curves are given in Figures 4.10.

Further uncertainties in the DEM curve determination arise from the errors on the line intensities, the choice of ionization equilibrium calculation and the lack of sufficient data points to constrain the curve. The choice of spectral lines to include in the calculation is also an important factor. Ideally any included line should not be blended, otherwise a likely overestimate of intensity will underestimate the DEM at the temperature of that primary line. However, the procedure used here, in calculating the contribution function at each T sums over the contribution functions of all the theoretical lines included in an interval $\lambda_{obs} + \delta\lambda$ that contribute to the observed intensity.

The DEM technique decribed here has been used to determine element abundances from UVCS and CDS data. Moreover it also allowed a comparison to be made of oxygen abundance values derived from UVCS data using two different techniques (see for example Withbroe (1978) and Chapter 4).

3.3 Collisional and Radiative Components of the Line Intensity

In Section 3.1.2 it has been shown that radiative excitation is a non-negligible process in the upper coronal plasma. The UVCS data used for this thesis contain spectra taken at 1.6 $R_\odot$ and for some lines this contribution to the total observed intensity had to be taken into account. These lines are some from the H-Lyman series and O VI lines (1032 Å and 1037 Å), and for the purpose of a diagnostic study the two contributions (radiative and collisional) have been separated.

The radiative (*Rad*) and collisional (*Col*) components of the Lyβ line together with those of Lyα, were derived by using the observed intensities of Lyα and Lyβ lines and the predicted ratios between their radiative ($Rad_{\mathrm{Ly}\alpha}/Rad_{\mathrm{Ly}\beta}$) and collisional components

($Col_{\mathrm{Ly}\alpha}/Col_{\mathrm{Ly}\beta}$). Mazzotta et al. data do not give the ionization balance for H. The hydrogen neutral fraction was computed using the ionization rate of Scholz & Walters (1991) and recombination rates from Hubeny et al. (1994). The contribution of recombination to excited levels (from Hummer & Storey (1987)) was added to the Lyman line excitation rates of Callaway (1994). The ratio between Lyα and Lyβ radiative components is independent of electron temperature, while the ratio of their collisional components is nearly independent of temperature at coronal temperatures.

The two components of the O VI 1032 and 1037 Å lines have been derived from the simple relationships between the intensities of the collisionally excited and radiatively excited components of the doublet as mentioned in Section 3.1.2:

$$\frac{I_{\mathrm{col}}(1032)}{I_{\mathrm{col}}(1037)} = 2 \tag{3.34}$$

$$\frac{I_{\mathrm{rad}}(1032)}{I_{\mathrm{rad}}(1037)} = 4 \tag{3.35}$$

and the total intensity of the doublet lines I is given by $I = I_{\mathrm{tot}} = I_{\mathrm{rad}} + I_{\mathrm{col}}$.

3.4 Temperature Diagnostics

A fairly simple method to determine electron temperature is the use of the line ratio technique. This technique, applicable for lines excited only through electron collision, consists of expressing the ratio of two line intensities as a function only of T and assumes isothermal plasma over the temperature range of the two lines. If two allowed lines of close ionization state from the same element are taken, so that there is no dependence on density or element abundance (Section 3.1.2), and ionization equilibrium holds, from Equation (3.14) their ratio is equal to

$$\frac{I_{gj}}{I_{gk}} = \frac{C(T)_{gj}}{C(T)_{gk}} = f(T) \tag{3.36}$$

This method consists of comparing the observed ratio with the theoretical curve $f(T)$.

Figure 3.10 shows an example of the variation in theoretical contribution function and theoretical line ratio with temperature for Fe XII 364.467 Å and Fe X 345.723 Å. The interval where the ratio is sensitive to temperature is given by the range where the $C(T)$ overlap. For comments on the use of these lines for temperature diagnostics applied to the data, see Section 4.5.1.

The theoretical calculations were performed using IDL routines and the CHIANTI database. The author modified some routines written by Del Zanna (1999) in order to allow the user to choose the ionization equilibrium calculation for the theoretical ratio

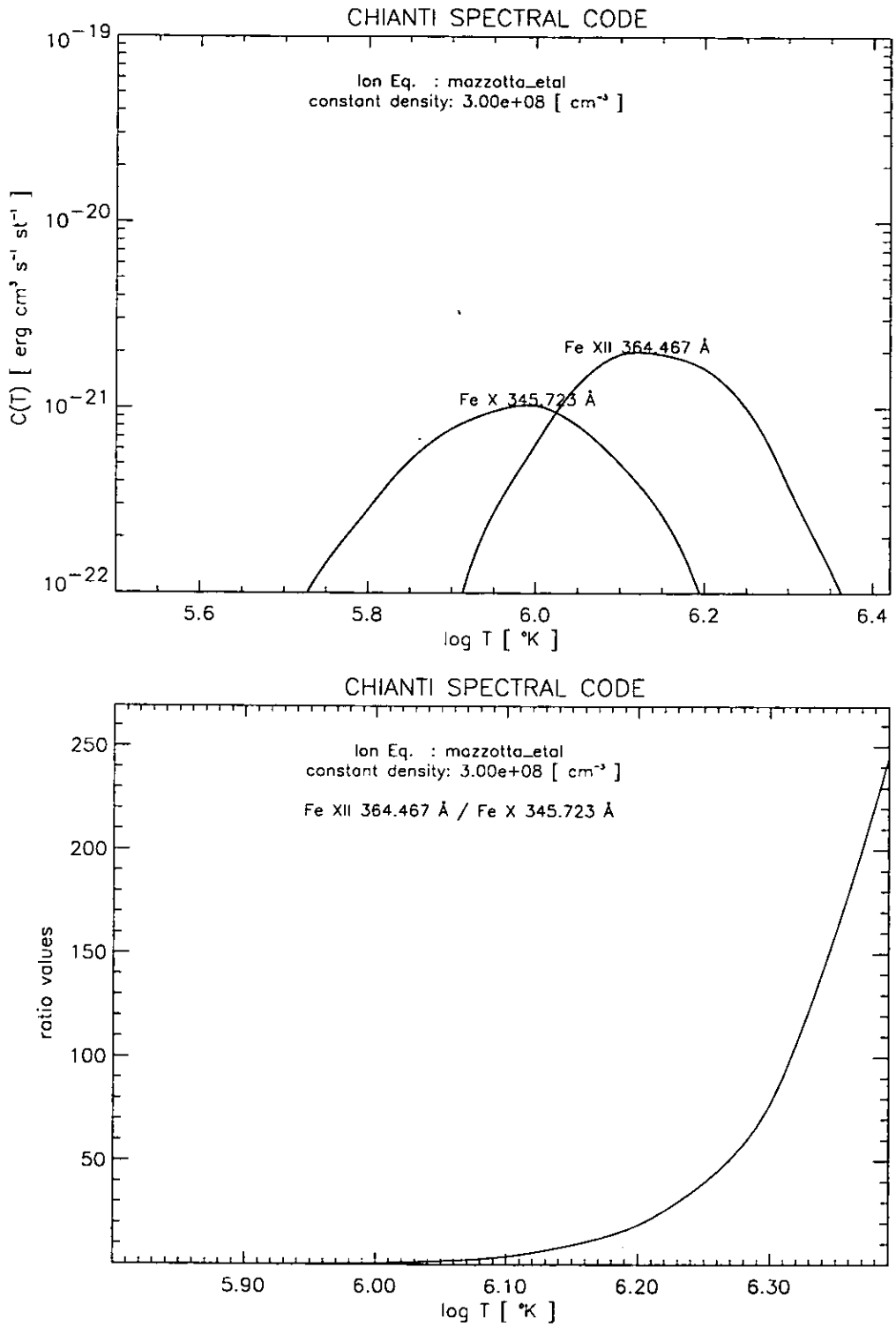

Figure 3.10: Top: contribution functions for Fe XII 364.467 Å and Fe X 345.723 AA using Mazzotta et al. (1998) ionizzation equilibrium. Bottom: their ratio value as funtion of temperature

values. A further routine that plots the results was also written by the author. In most cases the Mazzotta et al. (1998) ionization equilibrium was used.

The temperature derived from Equation 3.36 is an averaged value along the line of sight, i.e. the plasma is assumed isothermal. If the plasma along the line of sight is not isothermal, as is likely to be in the lower corona, the temperatures derived from different ratios should be different. On the other hand, this method is a good tool for identifying isothermal plasma (see Chapter 5) because ratios of lines whose emission spans a wide range of temperatures will result in of a unique temperature in this case.

This technique is most sensitive and precise for pairs of lines of ions in close stages of ionization, because the temperature obtained is within their overlapping contribution function curves. For pairs of lines using very different stage of ionization, ionization balance calculation is more sensitive to errors because the emission will be from the "tail" of the curve.

In a real case, lines from ions in close stages of ionization are not always available, or they are seen on the spectra blended with other lines. This is sometimes the case for CDS, for example. Even if the lines are de-blended through a fit procedure, a margin of uncertainty is present in the intensity calculation due to the blend separation, and this uncertainty will propagate through to the temperature determination. Hence, it is sometimes preferable to use unblended lines, even if they are not in successive stages of ionization.

Another aspect to consider in the choice of the lines is their wavelength separation: the further apart they are, the more erroneous the temperature derived because of the uncertainty in the intensity calibration. This is a reason way, for example, lines from CDS/NIS 1 and NIS 2 are not used together for this purpose.

Errors on the temperature estimate arise from errors on the intensity measurements and errors on the atomic physics calculations. What is generally assumed by other authors is only the observational error propagated from the line intensity errors, but the errors from atomic physics theoretical calculations can be as much or more 20% (Raymond et al., 1997). The use of different ionization equilibrium calculations can also result in different derived temperature values.

In CDS spectra there are several good pairs of lines for this diagnostic method and these have been reviewed by Del Zanna (1999). For this thesis, coronal ion lines were mainly used because all the observations referred to the off-limb corona, where the temperature is expected to be at least a million degrees. Only in the case of the macrospicule study (Chapter 6) did some cooler (transition region) lines need to be used.

In the case of the UVCS data, contributions from the radiative excitation to the line intensity make the temperature determination more uncertain, because the collisional part of the total intensity must be extracted. For this reason only iron ions in high stages of ionization were used, where the radiative part can be neglected (see Section 4.3).

A slightly different way to estimate the electron temperature from UVCS data, deriving at the same time the element abundance, has been developed by Raymond et al. (1998). In this technique, a ratio (R) of the predicted emissivity to the observed intensity of an ion (calculated with photospheric abundance (Feldman, 1992)), relative to the same ratio for hydrogen Lyβ collisional component is plotted as a function of temperature (see equation below). By using ions of the same element and determining the temperature at which the log R v. log T curves of the individual ions intersect, the plasma electron temperature can be identified. A common intersection is found whenever the plasma is strictly isothermal (within the uncertainties in atomic rates and instrumental radiometric calibration).

$$R_{\rm th} = \frac{[A_{\rm X} \cdot C(T)]_{\rm ion}}{[A_{\rm X} \cdot C(T)]_{{\rm Ly}\beta,{\rm c}}}; \qquad R_{\rm obs} = \frac{I_{\rm ion}}{I_{{\rm Ly}\beta,{\rm c}}};$$

$$R = R_{\rm th}/R_{\rm obs} \tag{3.37}$$

where $I_{\rm ion}$ is the observed ion intensity and $I_{{\rm Ly}\beta,{\rm c}}$ is the collisional component of the H-Lyman beta line. As a reference ion, iron has been generally adopted (see Section 4.3), because it is present in a number of ionization stages in the spectra and the results from this technique can be compared with those derived from the line ratio technique using CDS data, (in the case of coordinated observations, see Chapter 4).

An analogous set of curves can be produced for the CDS data. However, because of the absence of the H lines in the CDS spectra, the ratio $C(T)_{\rm Fe}/I_{\rm Fe}$ of the contribution function of the iron ion to the observed intensity must be used to look at the plasma temperature distribution.

Applications of this method for temperature determination can be found in Section 4.5.1.

The third method of determining electron temperature is from the DEM technique (Section 3.2). The DEM curve v. temperature can show the temperature at which the peak(s) in emission of the observed plasma occur(s) (see e.g. Figure 4.10).

3.5 Density Diagnostics

Lines that are excited only collisionally are discussed first here, followed by the case that also involves radiative excitation.

In Section 3.1.2 the dependence of the line intensity on density was discussed, together with how it changes with the type of level that is excited (Mason & Monsignori Fossi, 1994). If the line forms through an allowed transition then $I \sim N_e^2$, while if it comes from a transition that involves a metastable level then $I \sim N$. Moreover, when the metastable level population is comparable to that of the ground level, then other excited levels can be populated both from the ground and from the metastable, and the dependence of I on density changes again. The ratio of lines having different density dependence is thus a density dependent function.

The line ratio technique uses this property of line intensity: a theoretical curve of the ratio values as a function of density is calculated, and a comparison of the ratio obtained from the observed intensities with the theoretical curve gives the density estimate.

From the observational point of view, the density so derived is an averaged value along the line of sight. On the other hand, the theoretical ratios are derived assuming the plasma to be isothermal at a value corresponding to the maximun for the ionization fraction of the ion used. This assumption is not always true and introduces approximations that must be considered when this technique is used.

The choice of the pair of lines to be used is also a key point. The lines must be from the same ion in order to eliminate dependence on element abundance, ion population and hence temperature, and to ensure that the line of sight is the same for both lines. Moreover if the plasma is not isothermal, the choice of the ionization state will select the observation of plasma having a temperature in the range ΔT, that is the interval of temperatures where the ion exists. Precautions already mentioned for the temperature diagnostic, regarding wavelength separation of the two lines and blending, will also apply here.

Good diagnostic lines in CDS/NIS spectra are provided by the Si X 356, 347.4 Å lines and by Si IX 349.9, 341.9, 345.1 Å lines for coronal temperature. CDS has several transition region lines that are density-sensitive (Del Zanna, 1999), but their use for off-limb observation is not always practicable due to their weakness. Some attempts to use them have been made in Chapter 5. Figure 3.11 shows two examples of theoretical density-sensitive line ratios, for the coronal case and for the transition region case. These curves and all the others used for the line ratio techniques have been calculated using the Mazzotta et al. (1998) ionization equilibrium contained in the CHIANTI database. The data have been processed using CHIANTI IDL routines to calculate the theoretical curves, and a modified version by the author of a routine written by G. Del Zanna, to extract the observed density from the theoretical curves.

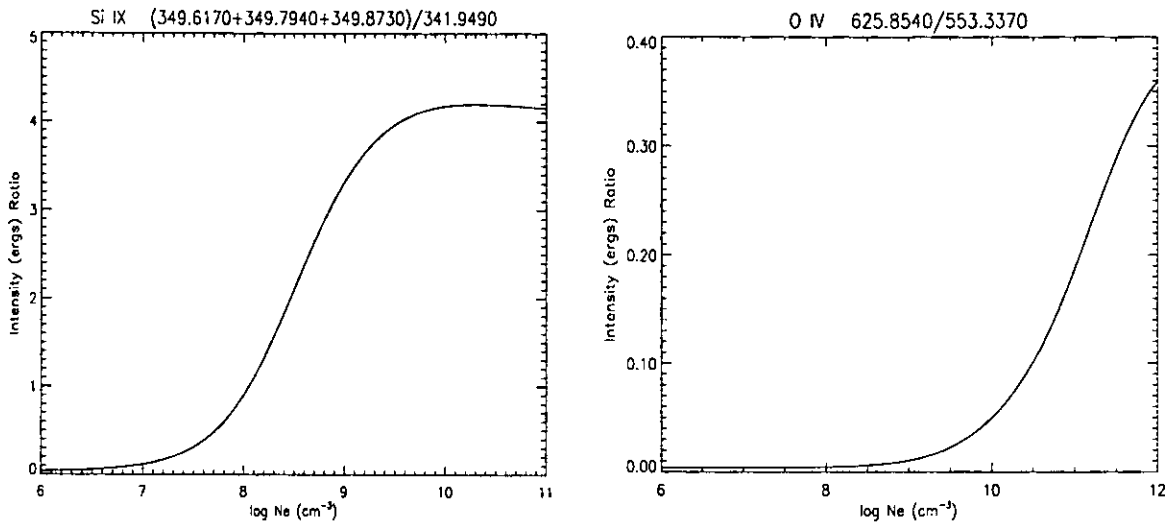

Figure 3.11: Ratio values as function of density for two pairs of lines. The oxygen ratios have been calculated at T= 1.58 10^4 K, the silicon at T=1.26 10^6 K.

No density-sensitive lines are present in UVCS spectra; hence an estimate of densities from the ratio of the radiative and collisional components of the O VI 1032 Å line is made. This line is the most intense of a doublet belonging to the Li isoelectronic sequence that forms in the transition region. A combination of bright disk intensities that contribute to the radiative excitation and a wide contribution function make these two lines bright even in the upper corona where the temperature reaches a million degrees. Due to these properties, this doublet is one of the most commonly used diagnostics for the upper corona.

The UVCS data used in this thesis always refers to streamer data at 1.6 $R_\odot$, where a nearly static plasma is expected. In this condition Doppler Dimming is negligible and the technique for density determination suggested by Noci et al. (1987) can be applied. These authors showed that the ratio of radiative to collisional intensities of O VI is given by:

$$\frac{I_{\rm rad}}{I_{\rm col}} = 5.75 \times 10^2 \frac{\lambda^2 \exp[\Delta E/kT]\sqrt{T}\int I_{\rm disk}(\lambda)d\lambda}{\overline{g} N_{\rm e}(\Delta\lambda_{\rm cor}^2 + \Delta\lambda_{\rm ex}^2)^{1/2}} \times \left(\frac{R_\odot}{r}\right)^2 Q(r) \qquad (3.38)$$

where λ = 1031.912 Å; ΔE is the energy difference between the levels involved in the transition (1.9251×10^{-11} erg); T is the electron temperature; $I_{\rm disk}$ is the line intensity integrated over the disk (305 ergs cm^{-2} s^{-1} sr^{-1}, Vernazza & Reeves (1978)); $\overline{g}$ is the effective Gaunt factor (1.13); $\Delta\lambda_{\rm ex}$ is the e^{-1} half-width of the exciting line from the lower atmosphere (0.10 Å) assuming Gaussian shape; $\Delta\lambda_{\rm cor}$ is the e^{-1} half-width of the Gaussian shaped coronal absorption profile (0.11 Å); $Q(r) = 2[1-(1-R_\odot^2/r^2)^{0.5}]r^2/R_\odot^2$ is the solid angle subtended by the solar disk at a distance r and $N_{\rm e}$ is the electron density. Values of

I_{rad}/I_{col} have been derived from the data; for T, values from the line ratio technique (see Section 4.5.1) were adopted.

3.6 Determining Element Abundances

One of the methods used to determine absolute (i.e. relative to hydrogen) abundances from the UVCS data is from the log R v. log T curve described above in Section 3.4 (Equation 3.37). The variation of the observed plasma abundance from the reference value chosen to plot the curves is given by the vertical offset from zero of log R, where the curves from different ions of the same element cross. The application of this technique is discussed in Section 4.5.1 with results shown in Figure 4.6. Unfortunately for the UVCS data there are few ions of the same element available so, as discussed for the temperature determination, this technique has been applied only to iron.

UVCS data can also be used to derive the *absolute* abundance of oxygen using O VI 1032 Å. The description of the method and the values used for the parameters in the following equations are taken from Raymond et al. (1997). As representative of a hydrogen line the Lyβ 1025 Å was chosen, because it is close in wavelength to oxygen, thus minimising the uncertainty from the instrument calibration. Once the collisional and radiative contributions of the O VI 1032 and Lyβ lines are known (see Section 3.3), then the following ratios can be determined:

$$\left(\frac{N_O}{N_H}\right)_{rad} = \frac{I_{rad}(1032)}{I_{rad}(L\beta)} \frac{C_{HI}}{C_{OVI}} \frac{B_{L\beta}}{B_{OVI}} \frac{f_{L\beta}}{f_{1032}} \frac{I_{disk}(L\beta)}{I_{disk}(1032)} \frac{\delta\nu_{OVI}}{\delta\nu_{HI}} \tag{3.39}$$

and:

$$\left(\frac{N_O}{N_H}\right)_{col} = \frac{I_{col}(1032)}{I_{col}(L\beta)} \frac{C_{HI}}{C_{OVI}} \frac{B_{L\beta}}{B_{OVI}} \frac{q_{L\beta}}{q_{1032}} \tag{3.40}$$

where $(N_O/N_H)_{col}$ and $(N_O/N_H)_{rad}$ indicates the oxygen abundance value derived from the collisional and radiative components of the line intensity; I_{col} and I_{rad} are the collisional and radiative components of the intensity in phot/cm^2/s/str; C_{OVI}/C_{HI} is the ratio of ion concentration (given by 15200 which, in the log T interval 6.1-6.3 changes by $\leq$ 16%); f is the oscillator strength which is 0.0791 for Lyβ and 0.131 for O VI (Wiese et al., 1966); B is the branching ratio and it is 0.88 for Lyβ and 1.0 for O VI; I_{disk} is the disk intensity in O VI/Lyβ lines equal to 2.13; $\delta\nu$ is the line width of the exciting intensity and the ratio of the O VI to Lyβ width is 1/4, with the assumption that the O and H are in thermal equilibrium (Section 3.1.3); and q is the excitation rate. The results from this analysis are presented in Section 4.5.3.

Chapter 4

Observations of Coronal Streamers

4.1 Introduction

This chapter presents analysis and results on coronal streamer characteristics by evaluating their physical parameters - density, temperature and abundance - from observations taken by two SOHO instruments, CDS (Harrison et al., 1995) and UVCS (Kohl et al., 1995). These instruments observe at different altitudes within the streamer, with CDS data obtained closer to the limb. This kind of analysis has only been attempted twice before. Li & Hu (1998) derived the physical parameters of a helmet streamer observed in 1996 from Yohkoh/SXT and SOHO/UVCS data, while Gibson et al. (1999b) compared parameters derived from white light data taken by SOHO/LASCO and HAO/Mark 3 coronographs with densities derived from SOHO/CDS spectra, using the line ratio technique. The present analysis is similar to that of Li & Hu, but refers to a slightly different altitude range: Li & Hu give values at 1.15 and 1.5 $R_{\odot}$, while here results from $\approx$ 1.02 to $\approx$ 1.19 $R_{\odot}$ from CDS, and at $\approx 1.6R_{\odot}$ from UVCS data, are presented. The present derivation of physical parameters over a more extended altitude span out to 1.2 $R_{\odot}$, gives improved altitude profiles. Gibson et al. (1999b), give more extended density and temperature versus altitude profiles (1.1 - 4 $R_{\odot}$), but do not determine composition.

Element abundances are derived here from UVCS data using the DEM method for the first time. Whilst the DEM technique has been used in the analysis of spectra acquired by a number of spacecraft (see, e.g., Brosius et al. (1996); Del Zanna & Bromage (1999a,b)), UVCS data have never been analyzed before using this method, although results from this kind of analysis need to be treated with some caution (see below). A comparison of the DEM results with estimates obtained by other techniques, supports the present evaluation (see Section 4.5.3). Crucially, the use of UVCS data has provided the collisional components of the hydrogen Lyα and Lyβ lines in the DEM curve, and hence, the *absolute*

values of element abundances have been determined here, rather than those calculated relative to oxygen or iron as is usually the case.

It should be mentioned, that the streamers analyzed in this work do not show the same morphology as those reported by Raymond et al. (1997), where a weak O VI streamer core corresponds to intense Lyα emission. It is possible that the stable solar minimum streamers observed by Raymond et al. behave differently from active region streamers. Alternatively, the observed differences may simply be due to a projection effect.

The diagnostic techniques used here have been described in Chapter 3.
Section 4.2 and 4.3 summarise the observations and the analysis techniques, respectively. Section 4.4 describes some preliminary tests performed using various different atomic parameters. The main body of results and their discussion are in Section 4.5, whilst Section 4.6 gives some wide discussion and list the main conclusions. Most of the work discussed in this chapter has been published in Parenti et al. (2000a).

4.2 The Observations

The work presented here is from two data sets obtained on 8 March 1998 and 7 May 1998. The goal of the March observations was to study the physical characteristics of the streamers at different heliocentric altitudes. To this end, the UVCS and CDS instruments were used to make coordinated observations of two streamers, at different positions along the same radial direction (see Figure 4.1). The first streamer was located close to the equator (the "equatorial" streamer) and the second was at a more southerly latitude (the "mid-latitude" streamer).

A similarly located mid-latitude streamer was observed with UVCS in May, for comparison with the March data.

The University of Central Lancashire, in the person of Dr. Barbara Bromage, was the leader for the CDS observations. The observations plan was done in situ in Preston and sent to the SOHO Experiment Operation Facility (EOF) at Goddard Space Flight Center (US). There, a CDS EOF staff sent the command to the satellite and collected back the science data. These data were then converted in FITS format and stored in an accessible database, were they were taken for the scientific analysis.

The Florence Astrophysical Observatory, in the person of Dr. Poletto, was the planner for UVCS observations. The planning was done at the EOF at Goddard Space Flight Center. The data were collected and converted to FITS data (see description in Section 2.2.3). The data were then given to the candidate for the analysis developed here. After

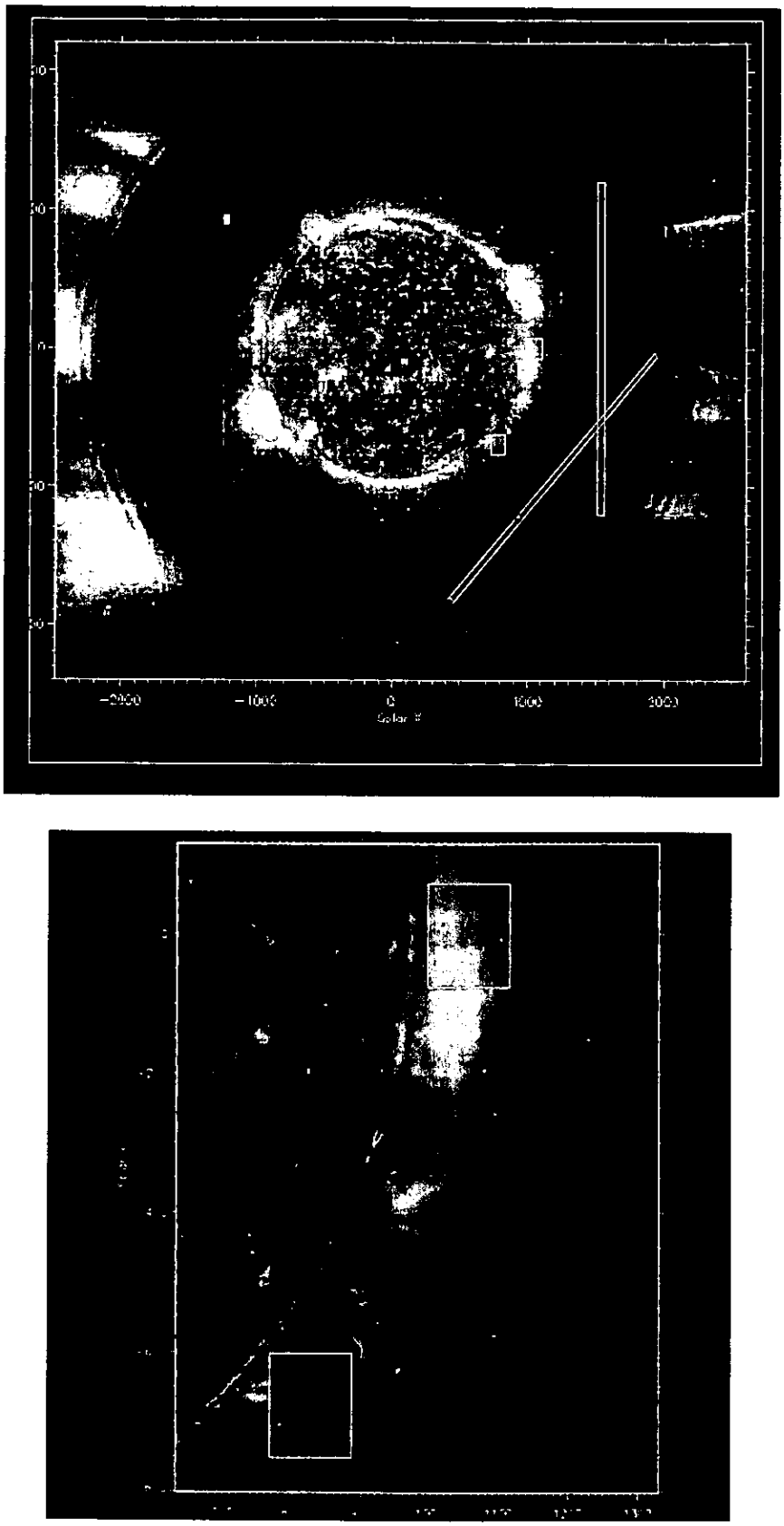

Figure 4.1: Composite image of the solar corona from SOHO/EIT and LASCO (top) on 1998 March 8. The CDS rasters and the UVCS slit positions are superimposed on the image. The lower image shows a closer view of the CDS observations, superimposed on the EIT (171 Å) image. A small loop-system can be clearly seen in the top left corner of the mid-latitude raster.

one year they became public.

4.2.1 UVCS Observations

UVCS observed the streamers both in the Lyman-alpha and O VI channels with, respectively, 50 μm and 150 μm wide slits, centred in the South-West quadrant at a heliocentric latitude of: $-0.1°$, for the March equatorial observation; $-40°$ for the March mid-latitude data; and $-45°$ for the May observation. In each case, the slit was tangential to the solar limb, at a central distance of $\approx 1.6 R_{\odot}$, its central portion crossing through the brightest Lyα and O VI part of the streamer (see Figure 4.2). In the O VI channel, a wide wavelength range was obtained by using three different grating positions, each covering ≈ 100 Å. Individual exposures of 200 s have been integrated over the whole observing time, at each grating position, to increase the statistical significance of the data (see Section 2.2.3). The overall integration time was ≈ 5 hours. Data have been taken with the O VI channel with a spatial binning of 10 pixels, giving a spatial resolution of 70″ (7″ for each pixel). The Lyα channel covers a wavelength range of about 50 Å with a spatial resolution of 63″, given by a spatial binning of 9 pixels (7″ for each pixel). The binning was to be necessary because of the faint signal of the upper corona, as already discussed in Section 2.2.3.

The UVCS data have been calibrated using standard calibration procedures and corrections for flat field effects have been applied (Gardner et al., 1996). Stray light corrections have also been applied, by using UVCS stray light measurements (Gardner, private communication) and disc line intensities from Vernazza & Reeves (1978). The corrections have been made using the C III 977 Å line visible in the oxygen channel, which can be considered completely due to stray light. This ion, in fact, forms at about $\log T = 4.9$ and it is completely absent in 10^6 K coronal gas. The streamer spectra analysed were obtained by further averaging over the brightest 7 Lyα pixels of the streamer centre, because this was the present scientific target. For the oxygen channel, the pixels covering the same area were identified and then averaged. Note that the peak of the streamer intensity in O VI corresponded to the peak in the Lyα image.

It is important to remark here, that the March streamer observations were not compensated for cross-talk effects between the telescope mirror mechanism, which determines the pointing, and the grating mechanisms. As a consequence, spectra acquired at different grating positions refer to slightly different heliocentric distances (the difference amounting to no more than 2%). Table 4.1 lists the spectral lines observed by UVCS which were used in this work and gives the integrated line intensities. Note that the intensities are given for two different distances for the March data. This is the result of the cross-talk error

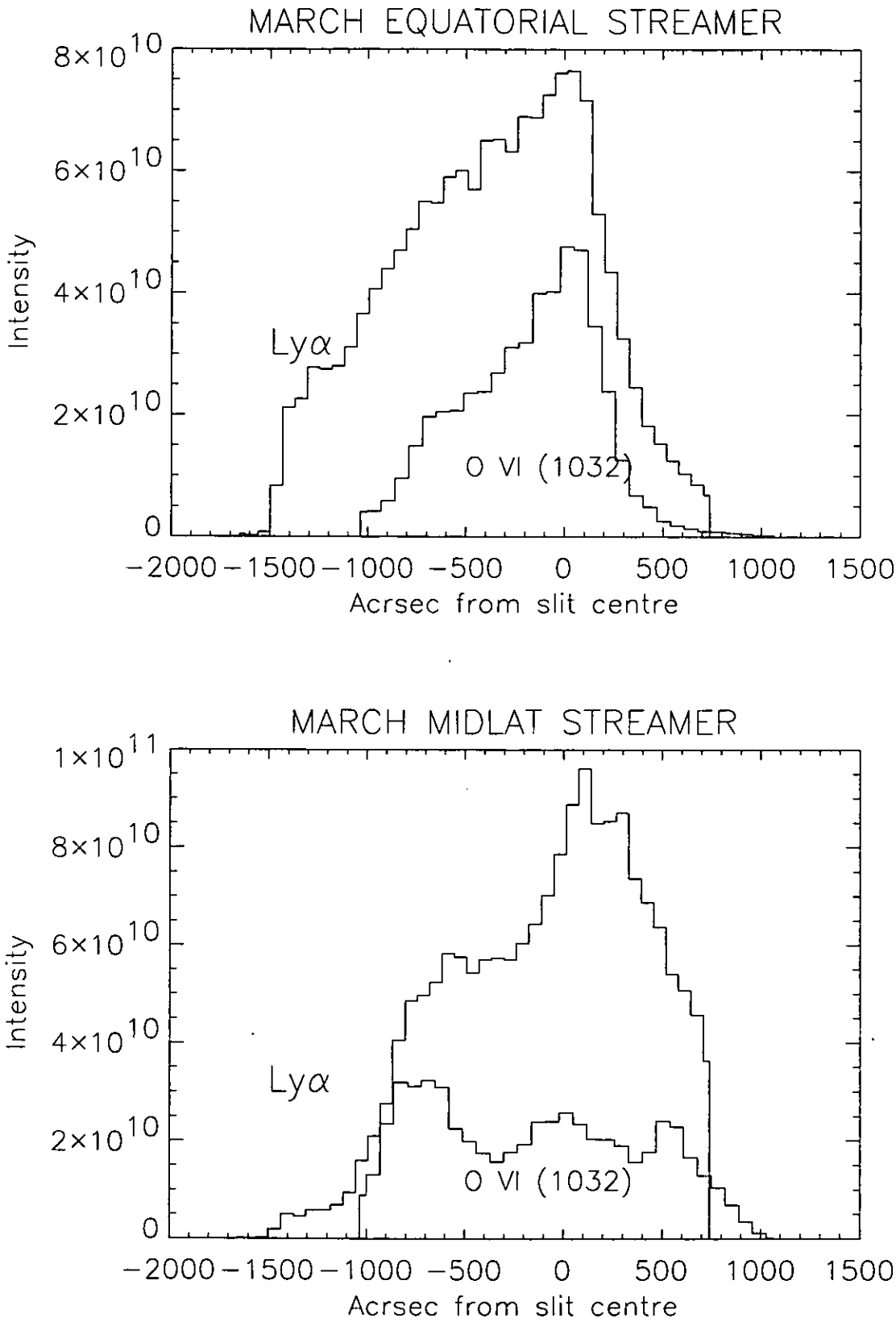

Figure 4.2: Profiles of the peak intensities along the UVCS slit for Lyα and O VI (1032) lines, for the March 8th observations of the equatorial streamer (top) and mid-latitude streamer (bottom). The intensity scale ($phot\ cm^{-2}\ s^{-1}\ str^{-1}\ \AA^{-1}$) refers to Ly$\alpha$ line.

described above and in Section 4.2.1. A 20% error on total line intensity was estimated. The software to calculate line intensities was developed by the candidate, as described in Section 2.2.3. Examples of the UVCS spectra used for the analysis are given in the Appendix (from Figure A.1 to A.7).

Table 4.1: Line intensities from UVCS observation in the March and May 1998 (10^{-4} erg/cm^2/s/str). λ_{ID} indicates the theoretical wavelength (in Å) taken from the CHIANTI database. The error on the intensity was estimated to be ±20%.

Spectrum and λ_{ID} (Å)	Transition	Equator Mar		Midlat Mar		Midlat May
		$1.58R_\odot$	$1.6R_\odot$	$1.58R_\odot$	$1.6R_\odot$	$1.6R_\odot$
Fe XV 481.450	$3s3p\ ^1P_1$ - $3p^2\ ^1D_2$	-	-	21.5	-	24.7
Fe XIII] 487.048	$3s^23p^2\ ^3P_1$ - $3s3p^3\ ^5S_2$	5.40	-	16.4	-	-
S XIII] 491.463	$2s^2\ ^1S_0$ - $2s.2p^3P_1$	-	-	8.9	-	46.3
Si XII 499.406	$2s\ ^2S_{1/2}$ - $2p\ ^2P_{3/2}$	194.6	-	753.3	-	1962.5
Fe XIII] 510.055	$3s^2\ 3p^2\ ^3P_2$ - $3s3p^3\ ^5S_2$	18.3	14.2	-	22.0	10.7
Si XII 520.665	$2s\ ^2S_{1/2}$ - $2p\ ^2P_{1/2}$	131.9	122.8	505.8	418.3	1148.5
S XII] 538.680	$2s^2\ 2p\ ^2P_{3/2}$ - $2s2p^2\ ^4P_{3/2}$	-	-	-	-	17.9
Al XI 550.031	$2s\ ^2S_{1/2}$ - $2p\ ^2P_{3/2}$	-	61.5	-	82.1	180.0
Mg X 624.941	$2s\ ^2S_{1/2}$ - $2p\ ^2P_{1/2}$	-	392.9	-	592.5	1156.4
[Ca XIV] 943.701	$2s^22p^3\ ^4S_{3/2}$ - $2s^22p^3\ ^2D_{3/2}$	-	-	-	-	9.8
[Fe XVIII] 974.858	$2s^22p^5\ ^2P_{3/2}$ - $2s^22p^5\ ^2P_{1/2}$	-	-	-	-	14.2
[Ar XII] 1021.219	$2s^22p^3\ ^4S_{3/2}$ - $2s^22p^3\ ^2D_{5/2}$	4.1	5.7	16.1	10.9	15.0
H I 1025.720	$L\beta$	77.2	74.7	71.8	85.9	166.4
[Fe X] 1028.394	$3d\ ^4D_{7/2}$ - $3d\ ^4F_{7/2}$	7.8	6.4	6.5	5.7	6.8
O VI 1031.912	$2s\ ^2S_{1/2}$ - $2p\ ^2P_{3/2}$	827.0	577.6	1441.0	1061.1	2014.7
O VI 1037.614	$2s\ ^2S_{1/2}$ - $2p\ ^2P_{1/2}$	293.8	194.6	570.6	410.3	748.0
[S X] 1196.244	$2p^3\ ^4S_{3/2}$ - $2p^3\ ^2D_{5/2}$	-	-	-	-	34.7
H I 1215.740	$L\alpha$	26058.2	23452.4	23126.7	20683.7	27198.2
[Fe XII] 1242.005	$3p^3\ ^4S_{3/2}$ - $3p^3\ ^2P_{3/2}$	54.3	31.2	21.7	15.9	16.1

4.2.2 CDS Observations

CDS data were acquired over a 120 × 150 arcsec raster in the South-West quadrant, at a heliocentric latitude of −0.1° for the equatorial streamer, and −35.35° for the mid-latitude streamer, both centred at a heliocentric distance of $1.1R_\odot$. The raster was built up by scanning the slit from west to east over 30 steps. The exposure time at each position was 160 s, and the full wavelength range of the Normal Incidence Spectrometer (NIS) of CDS was used (from 308 to 381 Å and from 513 to 633 Å). The spatial resolution was about 4″in both the N-S and the W-E directions. Standard procedures to remove the effects

of cosmic rays, together with flat-field, debiasing and geometric corrections were applied using the official CDS software (Section 2.3.1); the spectral lines were fitted using multiple gaussian line-fitting (Haugan, 1997) and the intensity calibration from Del Zanna (1999) was applied.

Table 4.2 shows the lines from the CDS spectra which were used in this study, while the observed spectra and their gaussian fits are shown in Appendix A.2.

4.2.3 Correspondence Between CDS and UVCS March Data

Figure 4.1 shows an EIT and LASCO composite image of the solar corona on the 8th of March, 1998, with the CDS rasters and the UVCS slits superimposed, indicating the location of the observations with respect to the streamers. On the west limb of the Sun three streamers can be seen, one in the northen hemisphere and two close together in the southern hemisphere.

Consideration of the images in Figure 4.1 along with the profiles in Figure 4.2 suggests that the CDS equatorial observation corresponds to the upper edge of the streamers seen by LASCO immediately to the south of the equator, while the plasma in the mid-latitude CDS observation corresponds to the central portion of the lower streamer at that side of the Sun. Obviously the range of latitude sampled by CDS is contained within that used for the UVCS analysis and it is much smaller. During the time of the observation, the LASCO images showed that the extended corona sampled by UVCS was largely filled by quiet streamers. Close to the Sun, the EIT images showed the CDS raster to be filled by quiet corona at the equator, while a small loop system is seen near the limb in the mid-latitude observation. For the purpose of the abundance determination, a small area ($50'' \times 20''$) external to the loop system was selected and the spectra from each pixel of this area were co-added to obtain an averaged spectrum, representative of the background emission of the streamer. A more detailed study of the hot loop itself will be discussed in Chapter 6.

4.3 The Diagnostic Techniques

The diagnostic techniques described in Chapter 3 have been applied here to derive temperature, density and element abundances in the streamers' centre.

The line ratio technique for temperature determination (Section 3.4) was applied to data from both CDS and UVCS, on the grounds that the streamer plasma should be static (Raymond et al., 1997) (at least at the low altitudes considered in this work) and that

Table 4.2: Line intensities from CDS (erg/cm^2/s/str) for March 8th 1998. λ_{ID} indicates the theoretical wavelength taken from the CHIANTI database. If a blend is present, the intensity is attributed to the brightest line of the blend, but it is calculated as the total contribution from all the lines that form the blend.

Spectrum and λ_{ID} (Å)	Transition	Equator 1.1 $R_\odot$	Midlat 1.1 $R_\odot$
Mg VIII 313.754	$2s^22p^2P_{1/2}$ - $2s\ 2p^2\ ^2P_{1/2}$	4.4 ± 0.06	3.5 ± 0.7
Mg VIII 315.039	$2s^22p^2P_{3/2}$ - $2s.2p^2\ ^2P_{3/2}$	9.4 ± 0.1	10.5 ±0.76
Si VIII 316.205	$2s^22p^34S_{3/2}$ - $2s2p^4\ ^4P_{3/2}$	11.6 ± 0.1	19.3 ± 0.79
Mg VIII 317.039	$2s^22p^2P_{3/2}$ - $2s.2p^2\ ^2P_{1/2}$	3.6 ± 0.1	-
Si VIII 319.826	$2s^22p^3\ ^4S_{3/2}$ - $2s2p^4\ ^4P_{5/2}$	19.5 ± 0.06	-
Fe XIII 321.400	$3s^2\ 3p^2\ ^3P_2$ - $3s\ 3p^3\ ^3P_1$	3.1 ± 0.1	32.2 ± 0.84
Fe XV] 327.011	$3s3p^3P_2$ - $3p^2\ ^1D_2$	-	24.3 ± 1.13
Al X 332.789	$2s^2\ ^1S_0$ - $2s2p\ ^1P_1$	15.6 ± 0.22	59.9 ± 2.45
Fe XIV 334.172	$3s^2\ 3p\ ^2P_{1/2}$ - $3s\ 3p^2\ ^2D_{3/2}$	13.6 ± 0.18	358.7 ± 2.6
Mg VIII 339.006	$2s^22p\ ^2P_{3/2}$ - $2s2p^2\ ^2S_{1/2}$	2.6 ± 0.1	2.9 ± 0.8
Fe XI 341.113	$3s^23p^4\ ^3P_2$ - $3s3p^5\ ^3P_1$	7.9±0.2	16.9 ± 0.5
Fe X 345.723	$3s^23p^5\ ^2P_{3/2}$ - $3s3p^6\ ^2S_{1/2}$	9.8 ± 0.2	9.7 ± 0.4
Fe XII 346.852	$3s^23p^3\ ^4S_{3/2}$ - $3s3p^4\ ^4P_{1/2}$	11.6 ± 0.34	41.5 ± 0.6
Si X 347.403	$2s^22p\ ^2P_{1/2}$ - $2s2p^2\ ^2D_{3/2}$	44.6 ± 0.6	-
Fe XIII 348.183	$3s^2\ 3p^2\ ^3P_0$ - $3s\ 3p^3\ ^3D_1$	16.6 ± 0.56	110.8± 0.8
Fe XII 352.106	$3s^23p^3\ ^4S_{3/2}$ - $3s3p^4\ ^4P_{3/2}$	-	68.2 ± 0.6
Fe XI 352.662	$3s^23p^4\ ^3P_2$ - $3s3p^5\ ^3P_2$	23.5 ± 0.75	44.5 ± 0.6
Fe XVI 360.8	$3s\ ^2S_{1/2}$ - $3p\ ^2P_{1/2}$	2.0 ±0.1	434.3 ± 1.2
Fe XII 364.467	$3s^23p^3\ ^4S_{3/2}$ - $3s.3p^4\ ^4P_{5/2}$	31.5 ± 0.18	113.2 ±9.1
Mg IX 368.070	$2s^2\ ^1S_0$ - $2s.2p\ ^1P_1$	88.7 ± 0.24	137.1 ± 1.2
Fe XI 369.153	$3s^23p^4\ ^3P_1$ - $3s3p^5\ ^3P_2$	6.0± 0.1	10.4 ± 0.4
Si XII 520.665	$2s^2S_{1/2}$ - $2p^2P_{1/2}$	4.6 ± 0.1	107.4 ± 0.4
Al XI 550.031	$2s\ ^2S_{1/2}$ - $2p\ ^2P_{3/2}$	3.1 ± 0.1	24.7
O IV 554.513	$2s^22p\ ^2P_{3/2}$ - $2s2p^2\ ^2P_{3/2}$	0.2 ± 0.01	0.4 ± 0.1
Ca X 557.765	$3s\ ^2S_{1/2}$ - $3p\ ^2P_{3/2}$	2.9± 0.02	10.4 ± 0.1
Ne VII 561.728	$2s2p\ ^3P_2$ - $2p^2\ ^3P_2$	0.1± 0.01	-
Ne VII 561.4	$2s2p\ ^3P_1$ - $2p^2\ ^3P_1$		
Ne VI 562.803	$2s^2\ 2p\ ^2P_{3/2}$ - $2s\ 2p^2\ ^2D_{5/2}$	0.1± 0.01	0.5 ± 0.1
Al XI 568.120	$2s\ ^2S_{1/2}$ - $2p\ ^2P_{1/2}$	1.5 ± 0.1	-
Ca X 574.010	$3s\ ^2S_{1/2}$ - $3p\ ^2P_{1/2}$	-	5.7 ± 0.4
O III 599.597	$2s^2p^2\ ^1D_2$ - $2s2p^3\ ^1D_2$	-	0.3 ± 0.1
Mg X 609.793	$2s\ ^2S_{1/2}$ - $2p\ ^2P_{3/2}$	43.9 ± 0.15	160.7 ± 0.5
Si X] 621.079	$2s^22p\ ^2P_{1/2}$ - $2s.2p^24P_{1/2}$	-	1.6 ± 0.1
Mg X 624.941	$2s\ ^2S_{1/2}$ - $2p\ ^2P_{1/2}$	19.5 ± 0.19	75.9 ± 0.4
O V 629.730	$2s^2\ ^1S_0$ - $2s.2p\ ^1P_1$	0.4± 0.06	0.6 ± 0.09

for UVCS most of the emission should come from the high density plasma close to the streamer's axis with negligible contribution from the surrounding low density atmosphere.

The best element to be used for this technique turned out to be Fe because it is present in both the UVCS and CDS spectra, in bright and well-defined lines from different stages of ionization. For CDS data diagnostics, the ratios Fe XII (364.467 Å)/ Fe XI (352.662 Å), Fe XI (352.662 Å)/Fe X (345.723) and Fe XIII (348.183 Å)/ Fe X (345.723 Å) have been used. The last ratio allows a direct comparison with UVCS because the Fe XIII (510 Å) and Fe X (1028 Å) lines are the brightest Fe lines in the UVCS spectra (Fe XII will be partially used, see explanation later). Moreover, the chosen lines, at a given temperature T, have a constant ratio over the range of density encountered here (within a few % in $10^6 < N_e < 10^8$ cm^{-3}). Electron temperatures have been calculated using ionization equilibrium calculations from Arnaud & Raymond (1992) for the preliminary study (Section 4.4) and from (Mazzotta et al., 1998) for the main work presented here (Section 4.5). For a comparison, the Fe lines have been used also in the application of the log R v. log T technique (Section 3.4).

Good density-sensitive ratios in CDS spectra are provided by the Si X 356/347.4 Å line ratio and by the Si IX 349.9/341.9 Å line ratio. These ratios are density-dependent for $10^6 < N_e < 10^9$ cm^{-3}. The coronal densities are expected to fall within this range. Note that these lines are not listed in Table 4.2. In fact those refer to the intensities obtained averaging over the selected area of the raster as previously explained. As shown later (Section 4.5.2) the densities derived from the Si lines refer to other areas of the raster.

UVCS densities have been derived from the O VI Å line as described in Section 3.5 (Equation 3.38).

The DEM technique (Section 3.2) has been used to derive the element abundances for both UVCS and CDS data. Moreover, it also allows a comparison of oxygen abundance values derived from UVCS data using two different techniques (Withbroe, 1978) (see Section 4.5.3). The DEM technique requires lines to be collisionally excited, hence, only the collisional components of the O VI and neutral hydrogen lines in the UVCS data are used, and all other lines listed in Table 4.1 have been assumed to have no radiative component. This is certainly the case for lines which form at such high temperatures that their disc emission may be considered negligible. For the CDS data, as already mentioned, all lines can be considered to be formed collisionally.

4.4 Results from a Preliminary Study

Several preliminary tests were performed on the data, using various different atomic parameters. In this section some details of that phase of the work are given, in order to emphasize how the results can be affected by the atomic physics used and the particular observed lines chosen.

Some of these preliminary results were descussed in Parenti et al. (1999b). At that time, only the CDS and the O VI channel data from UVCS were available. The UVCS Lyα channel, and in particular Lyα itself was not available.

As described in Section 3.3, the separation between the radiative and collisional components of the H-Lyman lines, is one of the starting points of the analysis, and it was decided to use the only available Lyβ and Lyγ lines for this purpose. Following Section 3.3, the theoretical ratios of Lyα /Lyβ/Lyγ (from the same references) together with the observed intensities of Lyβ and Lyγ were used to derive the individual radiative and collisional components of the lines. The theoretical predictions for these lines are: 13020:14.3:1.0 ($Rad_{L\alpha}$:$Rad_{L\beta}$:$Rad_{L\gamma}$) and 21.8:2.88:1.0 ($Col_{L\alpha}$:$Col_{L\beta}$:$Col_{L\gamma}$). Table 4.3 anticipates some observational results that will be given later in the chapter in order to check this method with hindsight. The Table shows the fractional collisional components of Lyβ derived using (1) the observed Lyα and Lyβ and theoretical Lyα /Lyβ ratio (discussed later in Section 4.5) and (2) the theoretical Lyβ/Lyγ ratio and observed Lyα and Lyβ. A clear discrepancy is evident. Several factors can contribute to explain this. The

Table 4.3: Percentage values of the collisional component of the H-Ly β to the total intensity, expressed as percentages, derived using two methods: the Lyα (case 1) and the Lyγ (case 2). The results are for the March equatorial streamer and March midlat streamer.

Region	$Col_{L\beta}$ (1)	$Col_{L\beta}$ (2)
Equator Mar	30.1 %	60 %
Midlat Mar	25 %	67 %

observed intensities are one of them. The Lyγ line at the distance involved (1.6 $R_\odot$) is about one order of magnitude fainter than Lyβ. Moreover, on our spectra the Lyγ falls close to the shadow of the grid wire (see Section 2.2.3) and thus the measured intensity might be underestimated. In fact, one of the problems of UVCS spectra is that they are regularly interrupted by the shadow of a wire grid positioned in front of the detector. This limits the line avaliability. This is generally visible every $\approx$ 10 Å as a deep drop in

the intensity. Examples of UVCS spectra are shown in Section A.1. However, the main uncertainty in the derivation of separate collisional and radiative components seems to be the theoretical values for the Lyγ lines (J. Raymond, private communication). An error in the relative intensities of the collisional and radiative components would propagate through the calculation of the absolute element abundances determinations.

The UVCS data included three grating positions, covering different wavelength windows. All of them included the O VI 1032 and 1037 lines. This was an important factor that allowed comparison of the intensities of the same line at three different grating positions. When first the line intensities were derived in this study, a systematic discrepancy of the order of 20-30% was registered between the O VI intensity in one of the windows, compared to the other two. Lack of experience first, led the author to attribute this to temporal variation of the intensity, and/or calibration of the different windows. Later, the UVCS Science Team was contacted, and the reason for this discrepancy was deduced to be due to their error in the application of a standard procedure for the cross-talk calibration (see Section 4.2.1) at the time the present observations were made in 1998. The error effectively meant that one of the observations was done at a different solar distance from the other two.

The preliminary study (e.g Parenti et al., 1999b) used the Arnaud & Raymond (1992) ionization equilibrium calculations for DEM analysis of the CDS March 1998 data. Later work (see Section 4.5 below) used the new Mazzotta et al. (1998) ionization equilibrium as mentioned in Chapter 3.

The reference values of element abundances were first taken from the Feldman et al. (1992) "coronal abundances". Iron was the chosen reference element as discussed later (Section 4.5.1), and the values derived for the abundances in this preliminary study are listed in Table 4.4. These values can be compared with those listed later in Table 4.11, after the final analysis was completed using different ionization equilibrium and different reference element abundances. In both calculations the error on abundance is estimated to be $\pm$ 0.05 in logarithmic scale (see discussion below, Section 4.5.3). Note that Feldman et al. (1992) is a reference generally used for data in the lower corona, whereas abundance studies in the upper corona generally refer to a separate list in Feldman (1992), where the abundances are the "photospheric" ones. For the purpose of the main study (see Section 4.5 below), which aimed to compare abundances in both the lower and upper corona, the second one (Feldman, 1992) was chosen and used for both the upper and lower corona. Although a comparison between the two Tables (4.4 and 4.11) of abundances is not straightforward, it is worth noting that qualitatively the variations in the relative

abundances (compared to the particular reference chosen) are in agreement: e.g. there is a decrease of Si from the equatorial streamer to the midlatitude one, while Mg and Ca increase. Figure 4.3 shows the DEM from the preliminary study. A comparison with that derived later (Figure 4.10) using different atomic parameters, shows that overall they are similar in shape. However, in the case of the mid-latitude streamer the peak at higher temperature (log T=6.4) is less pronounced than in the final result in Figure 4.10. The differences between the curves can be attributed to the ionization equilibrium differences and/or to the different reference for iron abundances. The coronal abundances from Feld-

Table 4.4: Element abundances obtained from the CDS data, on a log scale where [H]=12.00, relative to the abundance of Fe, assumed coronal (Feldman et al., 1992).

Region	O	Ne	Mg	Al	Si	Ca	Fe
Corona	8.89	8.08	8.15	7.04	8.10	6.93	8.10
Equator Mar	8.89	8.08	8.00	7.06	8.10	7.40	8.10
Midlat Mar	8.89	8.08	8.05	-	8.08	7.7	8.10

man et al. (1992) were also used to derive the composition for the UVCS May 1998 data, when the Lyα channel was not yet available. For a comparison with the CDS results it was decided to take iron as reference element. Figure 4.4 shows the DEM distribution in temperature. The derived abundances are listed in Table 4.5. This preliminary study made use of only a few lines, because of the limited data available, and the results in the final analysis (Section 4.5), obtained from the use of a larger number of lines are much is more reliable. The preliminary results for March 1998 data from UVCS involved the

Table 4.5: Element abundances obtained for May 1998 from the UVCS data, on log scale where [H]=12.00, relative to the abundance of Fe, assumed coronal (Feldman et al., 1992).

Region	O	Al	Si	S	Fe
Coronal	8.89	7.04	8.10	7.27	8.10
May midlat	8.89	6.85	8.70	8.27	8.10

previously mentioned error in the cross-talk correction, and are not discussed further here.

The final results from the analysis of these streamers including UVCS data from both the O VI channel and the Lyα channel, are discussed in detail in the following Section 4.5.

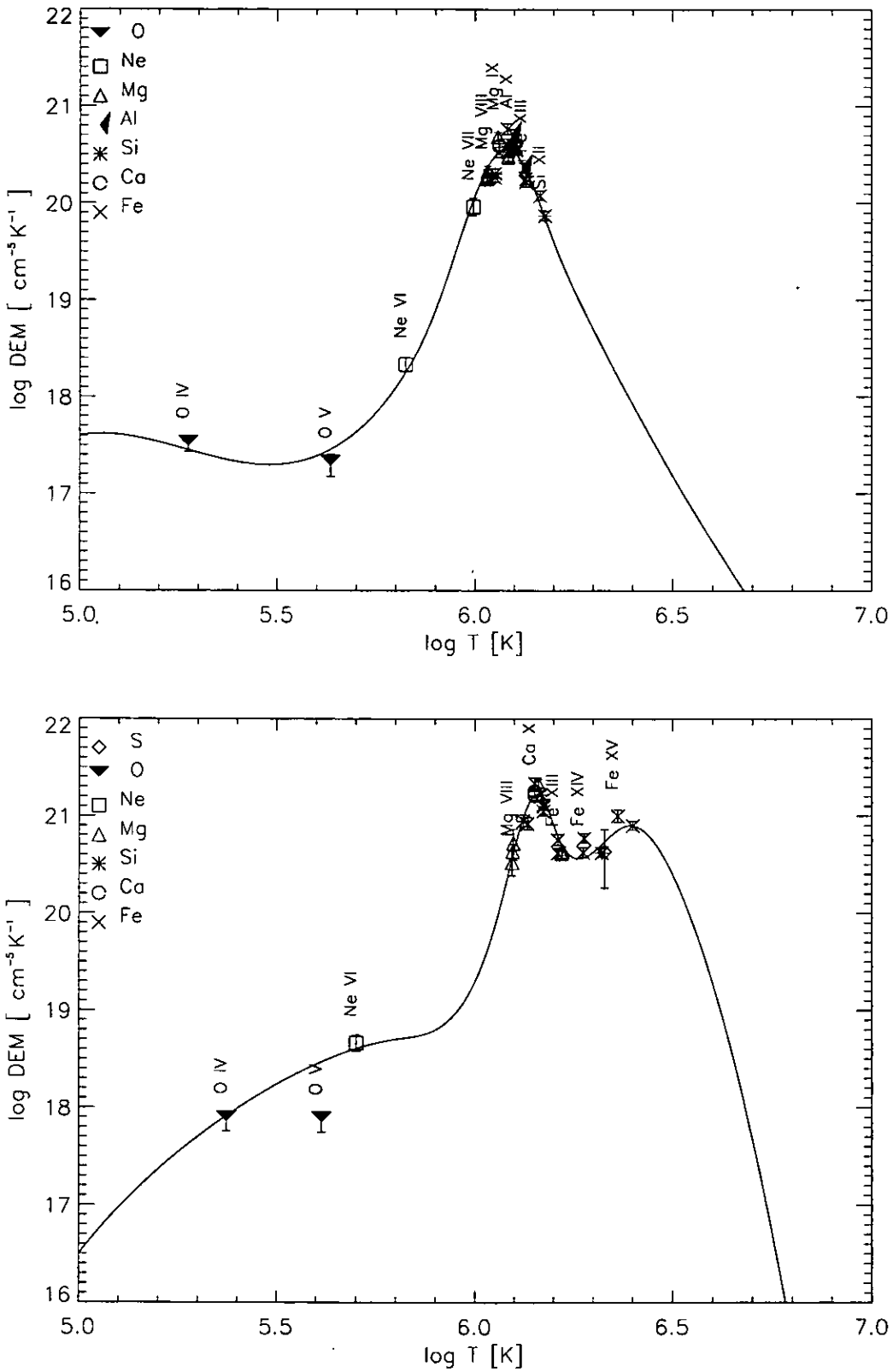

Figure 4.3: log DEM v. log T for the CDS March 1998 data (preliminary study). Top: equatorial streamer. Bottom: mid latitude streamer. The observations are the same as shown in Figure 4.10. The ionization equilibrium is from Arnaud & Raymond (1992) and the derived abundances are listed in Table 4.4

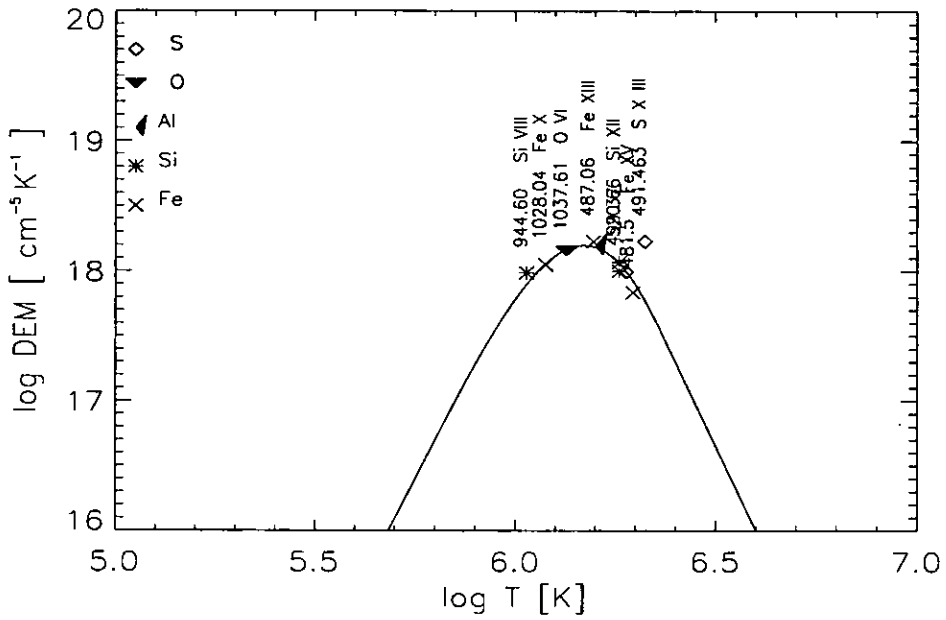

Figure 4.4: log DEM v. log T for the UVCS May 1998 data of the mid-latitude streamer (preliminary results). The ionization equilibrium of Arnaud & Raymond (1992) was used.

4.5 Final Results and Discussion

4.5.1 Temperatures

From CDS data, the profile of temperature v. heliocentric distance over the range 1.02 - 1.19 $R_{\odot}$, both for the March equatorial and the March mid-latitude streamers, has been derived from spatially-resolved spectra obtained by dividing the rasters into section of concentric slices, centred on Sun centre, and averaging the spectra over all the pixels in a slice. These slices were 10″ wide for the equatorial and 15″ wide for the mid-latitude case. The profile for the equatorial streamer data is given in Figure 4.5 (top panel) and the profile for the mid-latitude streamer appears in the bottom panel of the same Figure. The temperature increases with distance, from the limb up to the maximum distance covered by our spectra, in both profiles. Although CDS spectra have been taken low in the corona, where coronal activity may well affect the data and show up as a multithermal plasma, temperatures from different ion ratios are very similar, suggesting, at each altitude, a quasi-isothermal plasma. Moreover, the equatorial data seems to converge to isothermal at 1.1 $R_{\odot}$ from the Sun centre. However, it is possible that the temperatures of the mid-latitude streamer, which are higher than those of the equatorial streamer, are raised due to "contamination" by some of the hot loop plasma seen in the overall CDS field of view.

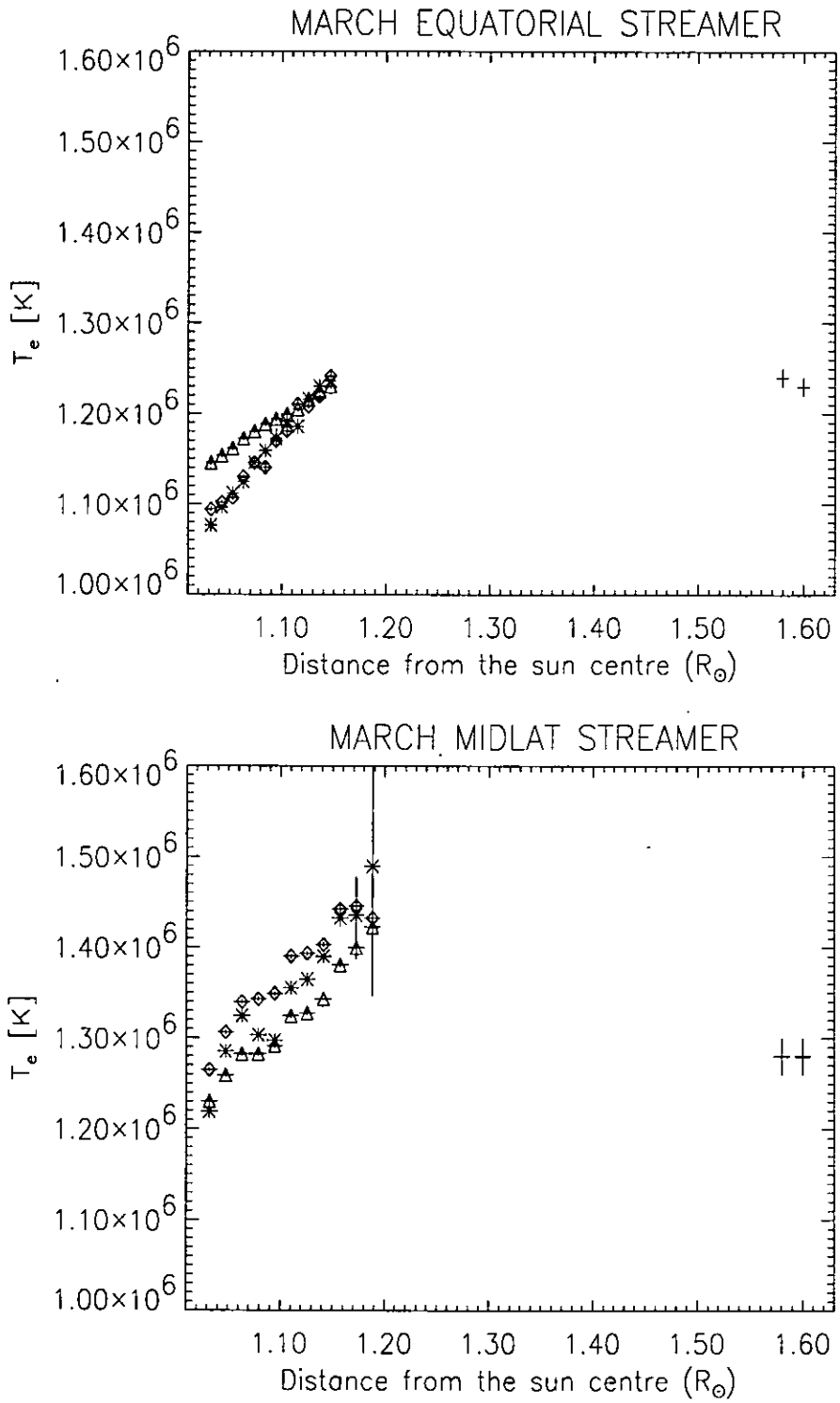

Figure 4.5: Temperature *v.* distance from the Sun centre for the March equatorial (top panel) and midlatitude (bottom panel) streamers. The triangles are the temperatures from CDS Fe XIII 348.183/ Fe X 345.723; asterisks are the temperature from CDS Fe XI352.662/ Fe X 345.723; diamonds are the temperatures from CDS Fe XII 364.467/ Fe XI 352.662; crosses are the temperatures from UVCS Fe XIII 510/ Fe X 1028.

The data points at 1.58 $R_\odot$ and 1.6 $R_\odot$ on Figure 4.5 represent the temperatures derived from UVCS spectra taken at different grating positions, which for the March observations corresponded to different solar distances. At 1.58 $R_\odot$ temperatures obtained from the Fe XIII/ Fe X line ratio are $1.28 \pm 0.02 \times 10^6$ K for the mid-latitude and $1.24 \pm 0.01 \times 10^6$ K for the equatorial streamer; at 1.6 $R_\odot$ temperatures are $1.28 \pm 0.02 \times 10^6$ K at mid-latitude and $1.23 \pm 0.01 \times 10^6$ at the equator. These values are consistent with CDS temperatures, provided it is assumed streamer coronal temperatures first increase with altitude and then slowly decrease after reaching a maximum beyond $\approx 1.25\ R_\odot$. This behaviour is to be expected if the streamer plasma is approximately in thermal equilibrium and the scale-height temperature does not differ significantly from the electron temperature. The Gibson et al. (1999b) scale-height temperatures, for instance, peak at $\approx 1.3 - 1.4\ R_\odot$ and, at 1.6 $R_\odot$, are in the range $1.3 - 1.55 \times 10^6$ K, in good agreement with the present results.

Figure 4.6 gives (top panel) the "log R v. log T" curves (where R is the Raymond's ratio, see Equation (3.37)) for the March mid-latitude streamer, from Fe X, Fe XIII and Fe XV lines, at 1.58 $R_\odot$ (spectra taken at 1.6 $R_\odot$ contain too few iron ions to be used for this estimate). The temperature, given by the average value at the intersection of these curves, is found to be $1.4 \pm 0.2 \times 10^6$ K. The equatorial spectra did not contain enough iron lines for this technique to be applied. These temperature values for the March mid-latitude streamer agree fairly well with those derived from line ratios, the former being $\leq 10\%$ higher. However, in the May spectra, high temperature ions such as Fe XVIII (974.858 Å line), appear to coexist with the cooler ions (Fe X), indicating a multi-thermal plasma. This is confirmed by the bottom panel of Figure 4.6, where the log R v. log T curves for different ions intersect over a wide range of temperature.

It shall be noted that lines from Fe XII have not been used in Figure 4.6, because they seem to be inconsistent with all other Fe lines. This is also evident from the DEM analysis (this is discussed further, see Section 4.5.3).

The DEM analysis (see below) gives temperatures in agreement with those found by the other two methods. For the March streamers, the data points on the DEM plots (Figure 4.9) are localized in a narrow range of temperatures between $\log T = 6.05$ and $\log T = 6.20$, with no lines originating at higher or lower temperatures. This indicates a nearly isothermal streamer plasma at a temperature between 1.2 and 1.6×10^6 K, while in the May streamer, the data points spread over a wider range of temperatures ($6 < \log T < 6.7$) and any assumption of an isothermal streamer is clearly not justified. This agrees very

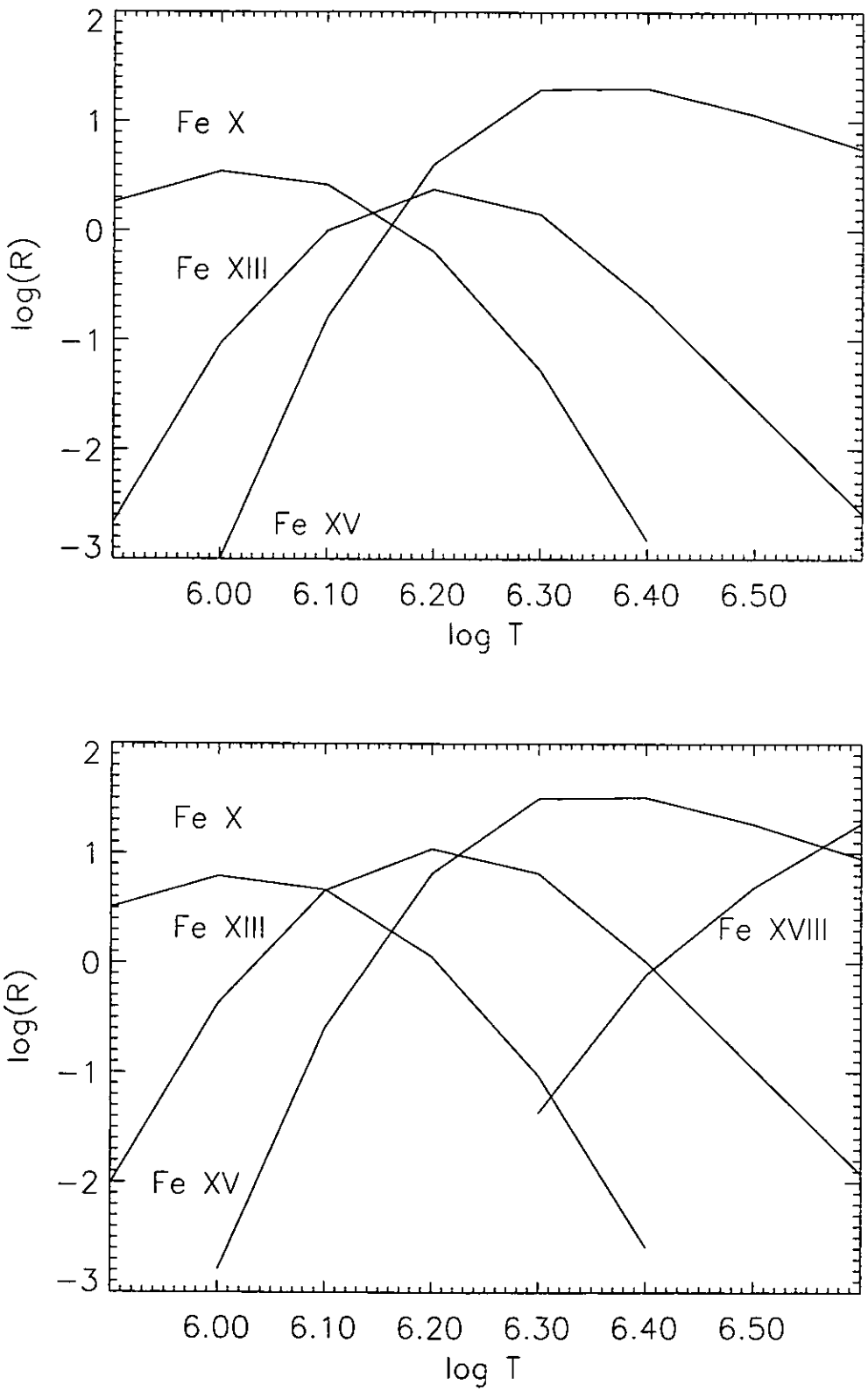

Figure 4.6: "log R v. log T^m (see 3.37) for the March mid-latitude data at 1.58 $R_\odot$ (top panel) and May mid-latitude data at 1.6 $R_\odot$ (bottom panel). Note: R is Raymond's ratio of theoretical to observed relative ion emission.

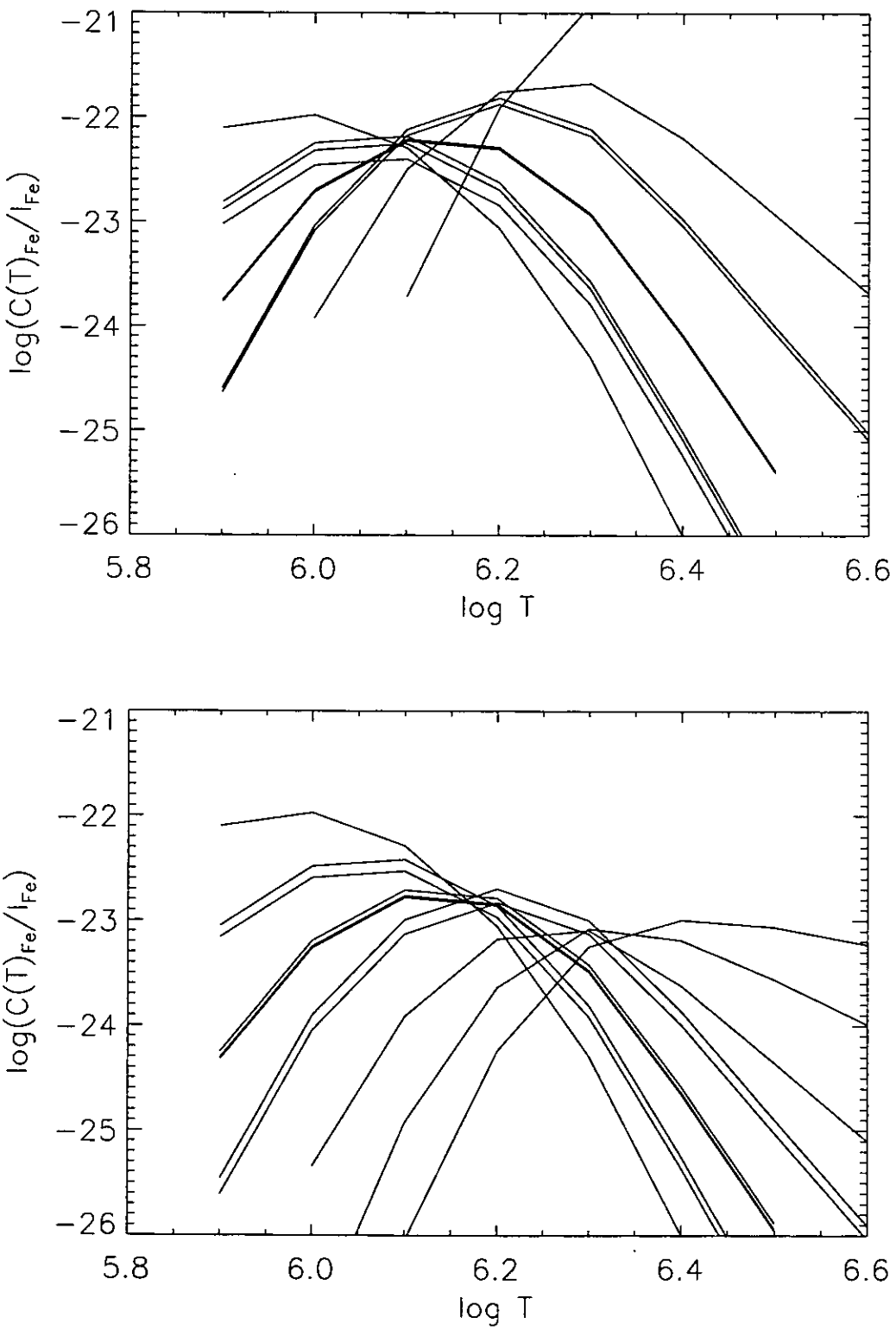

Figure 4.7: log $(C(T)_{Fe}/I_{Fe})$ v. log T for the March equatorial (top panel) and mid-latitude data (bottom panel) at 1.1 $R_{\odot}$.

well with the results obtained from the "log R v. log T" curves described above. Figure 4.7 gives the $\log(C(T)_{Fe}/I_{Fe})$ v. log T curves for the March CDS data. The observed lines of the iron ions are taken from Table 4.2. For the midlatitude streamer data (bottom panel) the intersection points of the different curves lie in the temperature interval $6.15 < \log T < 6.35$, which corresponds to the region of maximum emission derived from the DEM analysis (see Figure 4.10 below). The same is true for the equatorial streamer data (top panel), where temperatures given by the iron lines are limited to $6.1 < \log T < 6.2$. This is a clear indication of cooler and somewhat more isothermal plasma than that shown in the midlatitude streamer.

4.5.2 Densities

Profiles of density v. heliocentric distance have been derived from the March CDS data, using the same spectra averaged over concentric slices obtained from the raster (see Section 4.5.1). Densities derived from both Si IX and Si X line ratios are plotted v. solar distance for the equatorial and mid-latitude streamer data in Figure 4.8. Densities from the two ratios are in good agreement: in both streamers the density decreases with distance, but at any distance it is higher for the mid-latitude structure. In the latter, a signature of the loop present in the CDS field of view appears at about 1.09 $R_\odot$, with the density remaining almost constant over a distance of about 30arcsec. The fall in density then resumes.

In the same Figure, densities derived from the March UVCS data using Equation (3.38) have been plotted. The complete sets of densities derived from UVCS data are summarized in Table 4.6. UVCS results give higher densities at mid-latitude than at the

Table 4.6: Densities and temperatures derived from UVCS data for streamers. The temperatures are in 10^6 K units and densities in 10^6 cm^{-3}

Region	$I_{1032,rad}/I_{1032,col}$	T	N_e
Equator Mar 1.58 $R_\odot$	1.33	1.24 ± 0.01	4.9 ± 1.0
Equator Mar 1.6 $R_\odot$	1.81	1.23 ± 0.01	3.3 ± 0.7
Midlat Mar 1.58 $R_\odot$	0.69	1.28 ± 0.02	9.4 ± 1.9
Midlat Mar 1.6 $R_\odot$	0.80	1.28 ± 0.02	7.5 ± 1.5
Midlat May 1.6 $R_\odot$	1.00	1.26 ± 0.01	6.1 ± 1.1

equator: this is consistent with the CDS results. A linear least squares fit to the log–log variation of density with distance (using CDS Si IX and UVCS data), give indices for the

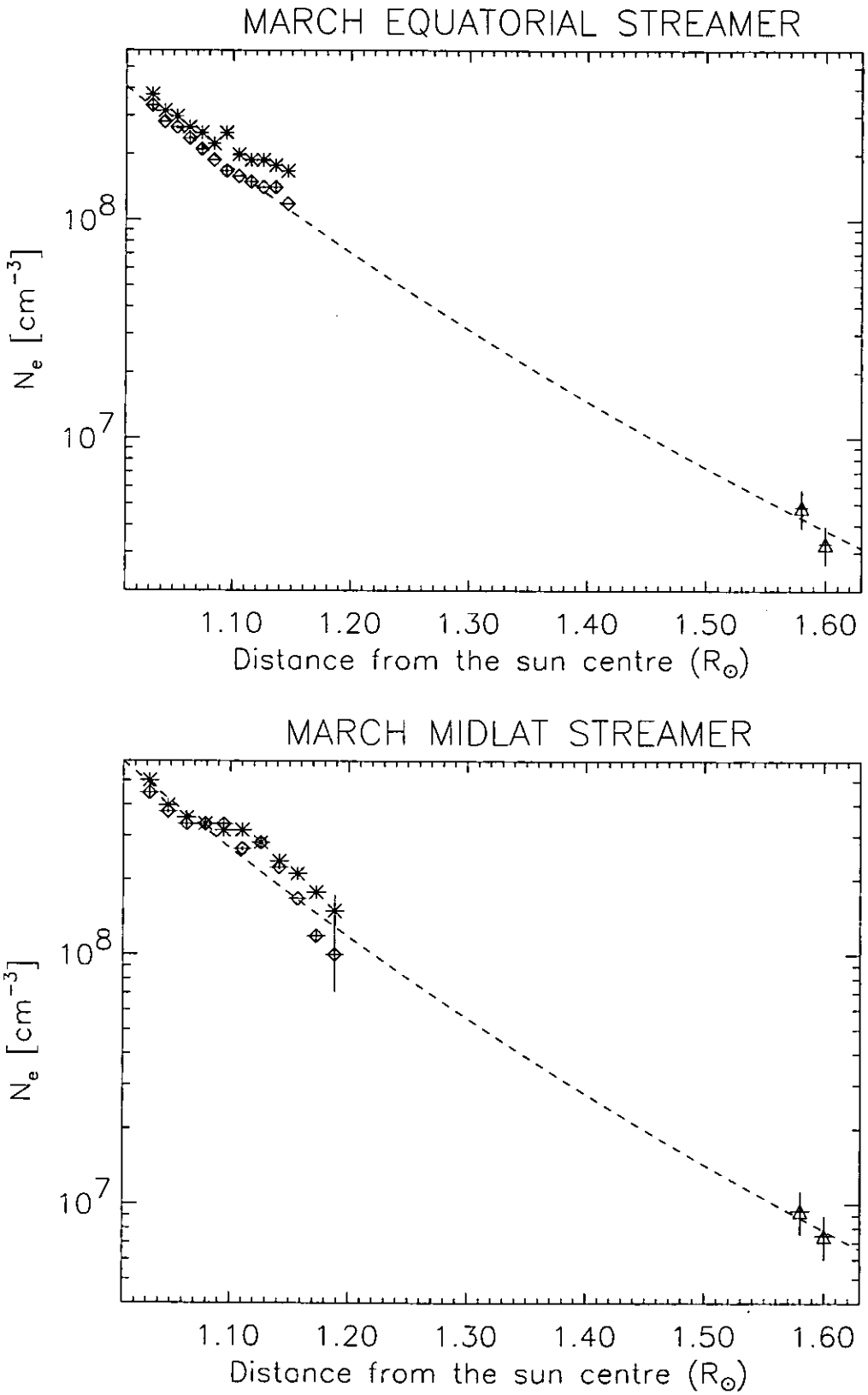

Figure 4.8: Density *v.* distance from the Sun centre for the two streamers. The diamonds represent the density from CDS Si IX 349.9/341.9, the asterisks from CDS Si X 356/347 and the triangles from UVCS. The dashed lines represent the least-square fits (see text), to the density from CDS Si IX and UVCS (O VI resonance doublet) data. Top panel: March equatorial data; Bottom: March midlatitude data.

power law variation of -10.1 for the equatorial data and -9.42 for the mid-latitude data. These fits have been superimposed on the plots in Figure 4.8, allowing for the now linear distance scale. If the initial density from this ion, and the temperatures (e.g. Fe XIII/X) from CDS are taken, and hydrostatic equilibrium is assumed, values of density of 6.7 $\times 10^7$ and 1.6 $\times 10^6$ cm^{-3} are predicted at 1.6 $R_\odot$ for, respectively, the equatorial streamers and mid-latitude. These values are close to the UVCS results, and this shows that the decreasing density with heliocentric distance over the CDS and UVCS altitude range can be reproduced by assuming hydrostatic equilibrium (as also found by e.g. Gibson et al. (1999b), and also see discussion in Section 4.6).

4.5.3 Element Abundances

Iron abundances were derived from the average value of the offset from 0 of log R at the intersection of the log R v. log T curves of Figure 4.6 (see Equation (3.37)). This technique gives the offset as a function of the ratio of the abundance of Fe to that of H. The abundance determined by this method is therefore an *absolute* value. The Fe abundance was found to be slightly less than photospheric in the March mid-latitude streamer, but it was 50% lower than the photospheric abundance in the May streamer (see Table 4.8).

Values of the oxygen abundance for the March and May streamers are presented in Table 4.7. They are calculated from the average of the "collisional" and "radiative" estimates obtained from Equation (3.39) and Equation (3.40). As Raymond et al. (1997) found, abundances from the collisional component appear to be systematically lower than abundances from the radiative component. They suggested that this was either because of a physical difference in the abundances of higher density regions (heavily weighted by the collisional contribution, which depends on the square of the density), or because of a small error in the separation of the collisional and radiative components of the Lyβ line. Notice also that abundances derived from Equation (3.38) strongly depend on the values assumed for the Lyβ and O VI (1032) disc intensities. Noci and Maccari (private communication), for instance, derive a different value (about 30% higher) for the ratio of the radiative components of the H Lyα and Lyβ lines than Raymond et al. (1997) found, mostly because of a different choice for the values of disc intensities. In the absence of simultaneous disc measurements in our coronal data, the Raymond at al. values have been adopted, but it may well be that the discrepancy in the calculations of abundances from radiative and collisional components has to be ascribed to an inaccurate knowledge of disc intensities at the time of the present streamer data. Based on this considerations, a 30% arror is then assumed for the O abundance values derived with this method.

Table 4.7: Absolute O abundance for the UVCS data, on log scale where [H]=12.00. The values presented here in column 4 are the average of those obtained separately from the radiative (column 3) and collisional (column 2) components of O VI (1032) and Lyβ lines. Note that the photospheric abundance of O is 8.93.

Region	O/H (Col)	O/H (Rad)	O/H (Aver.)
Equator Mar 1.58 $R_\odot$	8.15	8.42	8.29
Equator Mar 1.6 $R_\odot$	7.91	8.36	8.14
Midlat Mar 1.58 $R_\odot$	8.32	8.57	8.44
Midlat Mar 1.6 $R_\odot$	8.24	8.52	8.38
Midlat May 1.6 $R_\odot$	8.12	8.74	8.43

The results clearly show a depletion of oxygen compared with its photospheric value of 8.93 (Feldman, 1992) both at the equator and mid-latitudes. This will be discussed further in Section 4.6. So far, absolute abundance for Fe and O have been determined at approximately 1.6 $R_\odot$, from the UVCS data. In order to obtain the abundances of other elements, the DEM method described in Section 3.1 was used. This yields *relative* abundances. Here it was applied to both UVCS and CDS data.

In Figure 4.9, plots of log DEM v. log T are presented for the UVCS data. The observed data points are superimposed, plotted with the values

$$\frac{I_{\rm obs}}{I_{\rm th}}\, DEM(T_{\rm eff}) \tag{4.1}$$

at the effective temperature of the line ($T_{\rm eff}$). The effective temperature is defined as:

$$T_{\rm eff} = \frac{\int T\, C(T)_{\rm N_e}\, DEM(T)\, {\rm d}T}{\int C(T)_{\rm N_e}\, DEM(T)\, {\rm d}T} \tag{4.2}$$

where C(T), as said previously, is the contribution function for that line. This is a temperature average with respect to the DEM distribution and the contribution function.

To derive these curves, the observed collisional components of hydrogen Lyα, Lyβ and O VI intensities have been used, together with the other line intensities. The Fe absolute abundance was already derived from "log R v. log T" plots (Section 4.5.1) for the March mid-latitude and May data. Using this value for the iron abundance in the DEM analysis resulted in good agreement with the H data points, confirming the validity of the "log R v. log T" method for the iron absolute abundance determination. Therefore iron, together

with hydrogen, has been used as the reference element in the DEM analysis, for the rest of the elements. This provided more constraints on the DEM evaluation.

In the case of the March equatorial streamer, the "log R v. log T" method could not be applied. As already mentioned, iron was still used as the reference element together with hydrogen in the DEM analysis, but the photospheric abundance had to be assumed. However, comparing the iron and hydrogen points on the DEM plot, it seems that this assumption was a good approximation (see Figure 4.9). Similarly, the iron lines at 1.6 $R_\odot$ in the mid-latitude March data were not strong enough to determine the absolute abundances from the "log R v. log T" plots. For this reason the DEMs at 1.6 $R_\odot$ have been calculated assuming the iron abundance to be that derived for 1.58 $R_\odot$.

It should also be noted that in the following analysis the Fe XII line has not been used to constrain the fit because, compared to the other iron lines in the spectra, it appeared to be inconsistent. While for all the other iron ions, the ratio between the theoretical intensity and the observed intensity remains less than 2, for Fe XII it can reach 3.6 (for one of the equatorial regions). This problem is well known, and it can be partly attributed to uncertainty and failing in the atomic physics (Landi & Landini, 1998). Another possibility is an uncertainty in the sensitivities of the detector here, because of considerable 'burn-in' at the location of this line.

The derived abundances, in the usual logarithmic form, are listed in Table 4.8, while Table 4.9 shows the ratios of the derived abundances to photospheric values. To give an estimate of the errors in the abundance evaluation, a calculation of the largest change in abundances which is still compatible with the observed line intensities, (assumed to be subject to a 20% error, including atomic physics and observational error) is performed. This results in a logarithmic error for the abundance of the order of $\pm$ 0.05.

In concluding this description of UVCS results, it can be pointed out that the DEM analysis, as an independent method from that given in Equations (3.39) and (3.40), confirms the oxygen depletion, with respect to its photospheric abundance, also found from the collisional and radiative oxygen components (see Table 4.7). Next we move to the analysis of the streamer abundances from CDS data: this will indicate if there is a variation in abundance with altitude. However, to facilitate this comparison, Table 4.10 gives *relative* abundances, still derived from the DEM technique, but assuming Fe to have its photospheric abundance. This is because since no hydrogen line is present in CDS spectra, only *relative* abundances can be derived. The Table lists only values for the mid-latitude streamers as the equatorial streamer abundance relative to photospheric iron is already listed in Table 4.8. Differences in the values given in Table 4.10 may be considered an

indication of the uncertainties arising from errors in the determination of the absolute abundance of the iron.

Table 4.8: Absolute abundances obtained from UVCS data, in log scale where [H]=12.00. The Fe abundance not labelled with the asterisk was derived from Equation (3.37). The values labeled with the asterisk indicate the assumed photospheric value. The other element abundances were found relative to Fe, from DEM analysis.

Region	O	Mg	Al	Si	S	Ar	Ca	Fe
Photosphere	8.93	7.58	6.47	7.55	7.21	6.65	6.36	7.51
Equator Mar 1.58 $R_\odot$	8.15	-	-	7.25	-	6.30	-	7.51*
Equator Mar 1.6 $R_\odot$	8.00	7.10	6.00	7.25	-	6.30	-	7.51*
Midlat Mar 1.58 $R_\odot$	8.30	-	-	7.20	-	6.60	-	7.34
Midlat Mar 1.6 $R_\odot$	8.20	7.00	5.90	7.20	-	6.50	-	7.34
Midlat May 1.6 $R_\odot$	8.40	7.20	6.25	7.30	7.21	6.58	6.36	7.20

Table 4.9: $A_X(obs)\ /A_X(phot)$ derived from the UVCS data. The asterisk refers to assumed fotospheric aundance.

Region	O	Mg	Al	Si	Ar	Fe
Equator Mar 1.58 $R_\odot$	0.17	-	-	0.50	0.45	1.00*
Equator Mar 1.6 $R_\odot$	0.12	0.33	0.34	0.50	0.71	1.00*
Midlat Mar 1.58 $R_\odot$	0.23	-	-	0.45	0.89	0.68
Midlat Mar 1.6 $R_\odot$	0.17	0.26	0.27	0.45	0.71	0.68
Midlat May 1.6 $R_\odot$	0.29	0.42	0.60	0.56	0.85	0.48

As previously mentioned, CDS spectra include lines from ions which form over a wide range of temperatures. Iron, in particular, is present in a large number of ions, and this motivates the choice of iron as a reference element for the DEM technique. However, most of the lines in both the equatorial and the mid-latitude spectra, originate from high temperature ions: no Fe lines for $\log T \leq 5.95$ appear in the CDS data. The "coolest" lines are emitted by O III, O IV, O V, Ne VI and, at times, Ne VII ions (temperature of formation, $\log T$= 5, 5.2, 5.22, 5.61, 5.71, respectively). With no overlap with the elements that have high temperature lines, the DEM curves are not well constrained at

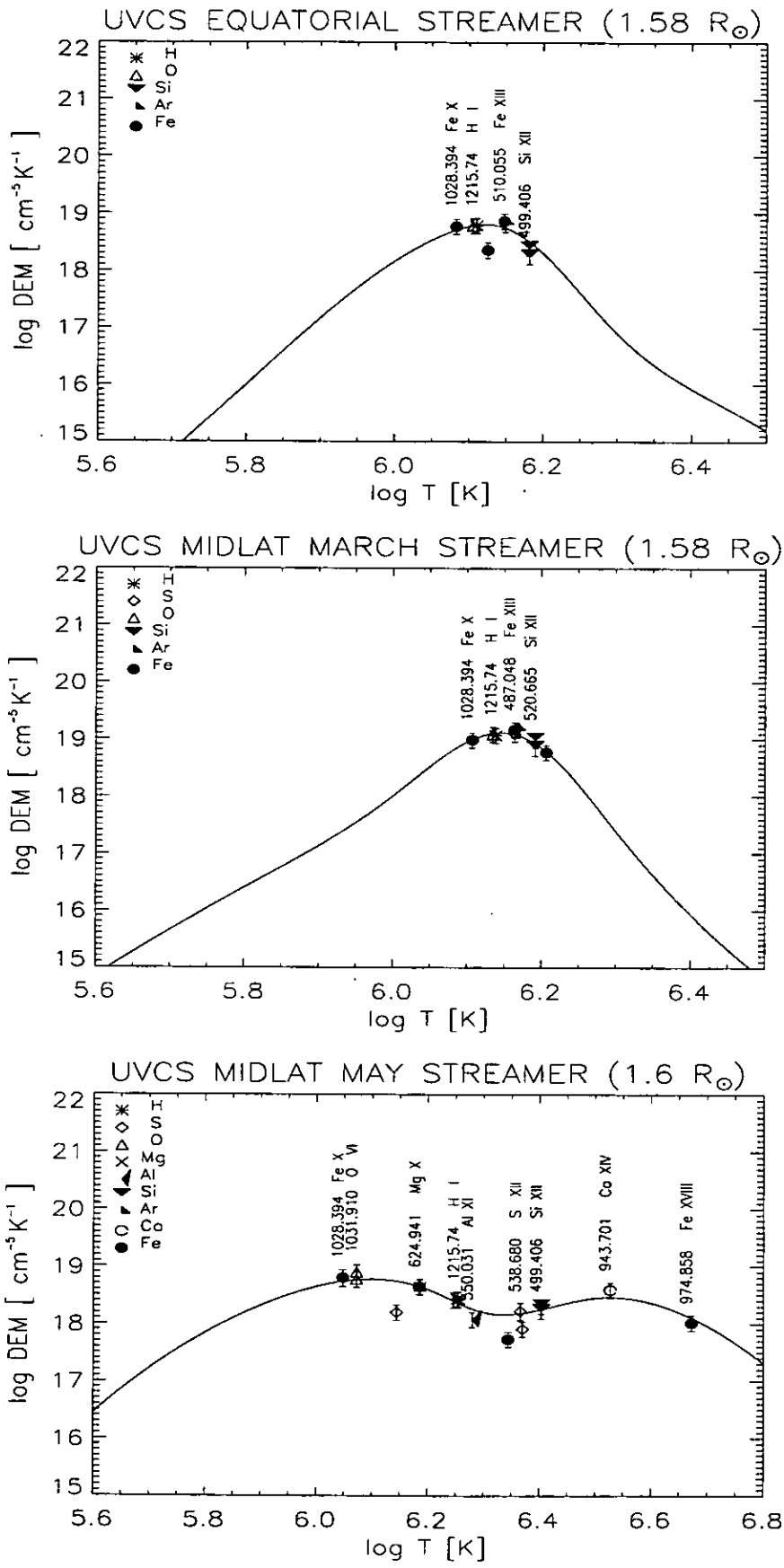

Figure 4.9: log DEM v. log T for UVCS data. Top panel: equatorial streamer; middle panel: mid-latitude streamer for March data; bottom panel: mid-latitude streamer for May data. The DEMs are relative to hydrogen, which abundances are taken from Table 4.8.

Table 4.10: Element abundances from UVCS data, obtained relative to the Fe photospheric abundance (indicated by a stars) on log scale where [H]=12.00. This analysis is provided for comparison with the CDS results given in Table 4.11

Region	O	Mg	Al	Si	Ar	Ca	Fe
Midlat Mar 1.58 $R_\odot$	8.40	-	-	7.30	6.65	-	7.51*
Midlat Mar 1.6 $R_\odot$	8.30	7.10	6.00	7.20	6.50	-	7.51*

low temperatures. For this reason, O and Ne abundances have not been directly obtained. However, attempting to overcome this problem, photospheric abundances for oxygen and neon can be assumed (8.93 and 8.11, respectively) and if we rely on UVCS streamer results, the oxygen abundance should be either lower than or equal to the photospheric one. Moreover, coronal abundances found in the literature (e.g. Meyer, 1985b) are lower than photospheric abundances, both for O (8.39) and Ne (7.54). With this assumption, *lower limits* to the log DEM v. log T curve at low temperatures are found. If the abundance is given, in the theoretical line calculation only the DEM is unknown. This is then found by minimizing the discrepancy between the theoretical intensity value and the observed intensity. In this case, the minimum value for the DEM at the temperature of the data point is derived via the relation between element abundance and DEM (see Equation (3.31)), with the assumption of photospheric abundances.

Figure 4.10 (top and bottom panels) shows the log DEM v. log T curves for, respectively, the equatorial and the mid-latitude streamers CDS data. The results from this analysis are listed in Appendix A.3. As discussed above, *relative* abundances have been estimated, with Fe as a reference element. Abundances for both streamers are given in Table 4.11 and, apart from Mg and perhaps S, do not significantly differ from photospheric abundances (shown in Table 4.8). Scarcely any FIP effect is seen in these CDS data, with respect to photospheric element abundances. Sulphur is the only case where a depletion with respect to the photospheric value is found. This element has a FIP of 10.36 eV, thus its behavior is not clearly recognizable as belonging either to high or low FIP elements. Raymond et al. (1998) found it to behave like a high FIP element, while Feldman et al. described its behaviour as an intermediate case.

A comparison of UVCS abundances with CDS abundances relative to Fe shows a decrease with height for all but one elements (Ca is the exception, but this line appears only in one UVCS spectrum) in the altitude interval between the regions observed by the

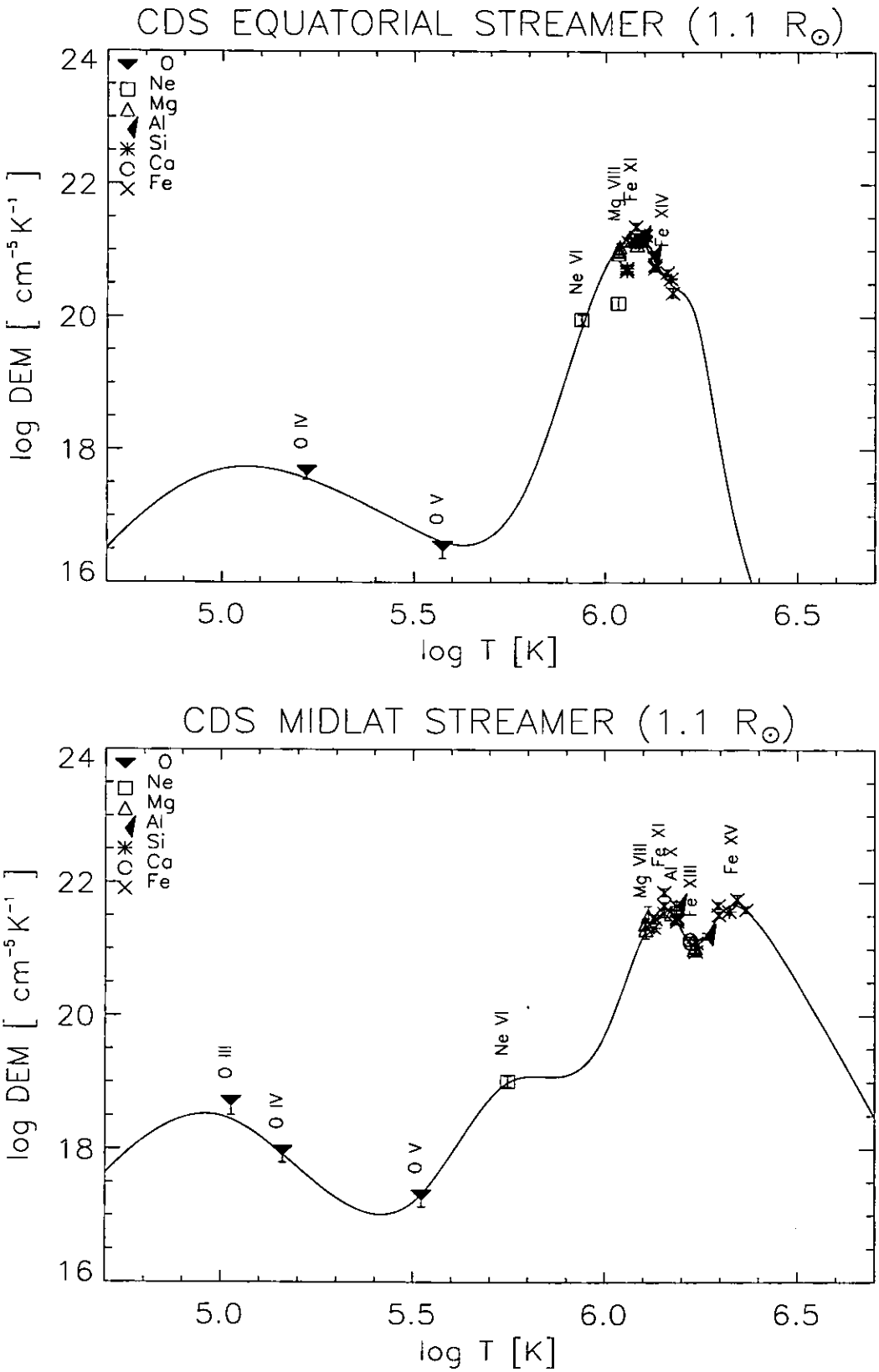

Figure 4.10: log *DEM* v. log *T* for March 1998 CDS data. Top panel: equatorial streamer; bottom panel: mid-latitude streamer. The DEMs are relative to photospheric iron; O and Ne abundances are assumed photospheric (see text).

two instruments.

Table 4.11: Element abundances obtained from the CDS data, on log scale where [H]=12.00, relative to the abundance of Fe which is assumed photospheric (asterisk).

Region	O	Ne	Mg	Al	Si	S	Ca	Fe
Equator Mar	8.93	8.11	7.4	6.47	7.55	-	6.3	7.51*
Midlat Mar	8.93	8.11	7.5	6.47	7.5	7.1	6.36	7.51*

4.6 General Discussion and Conclusions

4.6.1 Electron Temperatures

Using coordinated CDS and UVCS observations, profiles of electron temperatures v. solar distance have been derived for an equatorial and a mid-latitude streamer, over the range from 1.02 $R_\odot$ to 1.19 $R_\odot$ from CDS data and at $1.58 - 1.6$ $R_\odot$ from UVCS data.

CDS results show an electron temperature increasing with distance, up to the highest altitude reached by the data. This behaviour is consistent with results found for streamers' temperatures, during the Whole Sun Month campaign, by Gibson et al. (1999b), from radial power law fits to densities, and for equatorial regions, during the same campaign, by Fludra et al. (1999a), from the line ratio technique. These authors used ratios of lines from different elements, hence introducing possible uncertainties related to uncertainties in element abundances. Here this problem was avoided by using ratios of lines from different ionization stages of Fe. The Gibson et al. temperatures are obviously not electron temperatures, although apparently streamer conditions are such that electron scale-height and proton temperatures (Raymond et al., 1998) are about equal.

UVCS temperatures prove to be consistent with previous determinations (log T= 6.13-6.2) at approximately the same altitude (Raymond et al., 1997, 1998). When UVCS electron temperature results are considered in conjunction with simultaneous values obtained from CDS data, an extention of our knowledge of the electron temperature v. height profile is obtained, including the fact that the electron temperature reaches a peak at altitudes somewhere between 1.19 and 1.6 $R_\odot$.

Differences between electron temperatures in the three streamers analysed here are minor, with the mid-latitude streamers showing higher values, particularly at the lower coronal levels. These results together with the presence of the loop-system at the base

of the March mid-latitude streamer, indicate the presence of an "active" streamer for the mid-latitude case, and a "quiet" streamer for the equatorial case. Hence, streamer temperatures can range between 1.1 and 1.5×10^6 K, in the altitude range here analysed. These temperatures are somewhat higher than coronal hole temperatures (see, e.g. Fludra et al. (1999a); David et al. (1998)) and point to different mechanisms of heating deposition.

The temperature profiles of Figure 4.5 may be used to place constraints on the *ad hoc* heating functions often used when modelling different coronal structures (see, e.g. Wang et al. (1998); Suess et al. (1999)). A high priority for future observations will be to fill the gap between 1.2 and 1.6 $R_\odot$and locate where the electron temperature reaches a maximum, thus providing further constraints on the heating mechanism at different altitude.

At distances of the order of 1.5 - 1.6 $R_\odot$ streamers are usually said to be isothermal (see e.g. Raymond et al. (1997); Feldman et al. (1998)). It is interesting to note that both the convergence of the profiles from different ratios in Figure 4.5 (upper) and the DEM curves from CDS spectra show the plasma to be isothermal also at lower altitudes. The second peak in the March mid-latitude data is likely to be due to the hot loop system present in the CDS field of view. Although our March structures are more or less consistent with this claim, the May streamer shows evidence for a multi-temperature plasma, both from the DEM analysis and from the Fe log R v. log T curves. More extensive observations are needed in order to try to understand whether this is connected with relative instabilities in structures, or whether it is linked to a special time in the streamer's life. On the other hand, the presence of lines from low temperature plasma may possibly be due to cooler foreground or background material – Note in this connection that the corresponding EIT images show the streamer to be close to a coronal hole structure – which, however, could not affect the high temperature section of the DEM curve.

4.6.2 Electron Densities

Streamers' densities have been investigated for some time, because they can be derived from polarized brightness (pB) measurements. However, pB values usually only refer to levels $\geq$ 1.1 solar radii. The line ratio technique used have provide values at lower heliocentric distances.

Doschek et al. (1997) derived off-limb densities for coronal hole and quiet Sun, using Si VIII and S X line ratios for distances very close to the solar limb. Their results in the quiet region gave densities of 6-7 $\times10^7$ cm^{-3} for a distance of 1.15 $R_\odot$, somewhat lower than the present results. In a later study, Doschek et al. (1998a) used a Si VIII line ratio to derive a density profile with height, for an equatorial streamer. This profile shows a

trend similar to the one presented in this chapter, but again with lower values overall.

Figure 4.11 shows some recent determinations of streamer densities, along with the results presented here. The streamer densities from Gibson et al. (1999b) refer to a streamer observed only a few months after our observations were made. Gibson et al. in Figure 4.11 shows how the pB derived densities are consistent with the densities derived from line ratios at low altitude, yielding a less steep profile of N_e v. solar distance than would be extrapolated from white light measurements only. Our results from both streamers confirm this trend.

Density measurements from UVCS data by Strachan et al. (2000) and Ciaravella et al. (1999) are also shown in the Figure, together with another CDS study (Fludra et al., 1999a). It should be noted that the streamers reported in this thesis do not show evidence of the weak O VI emission core sometimes appearing in UVCS streamers. Hence the present densities have been compared with values given specifically for the streamers' "legs" by previous authors. Densities derived from UVCS measurements may vary from

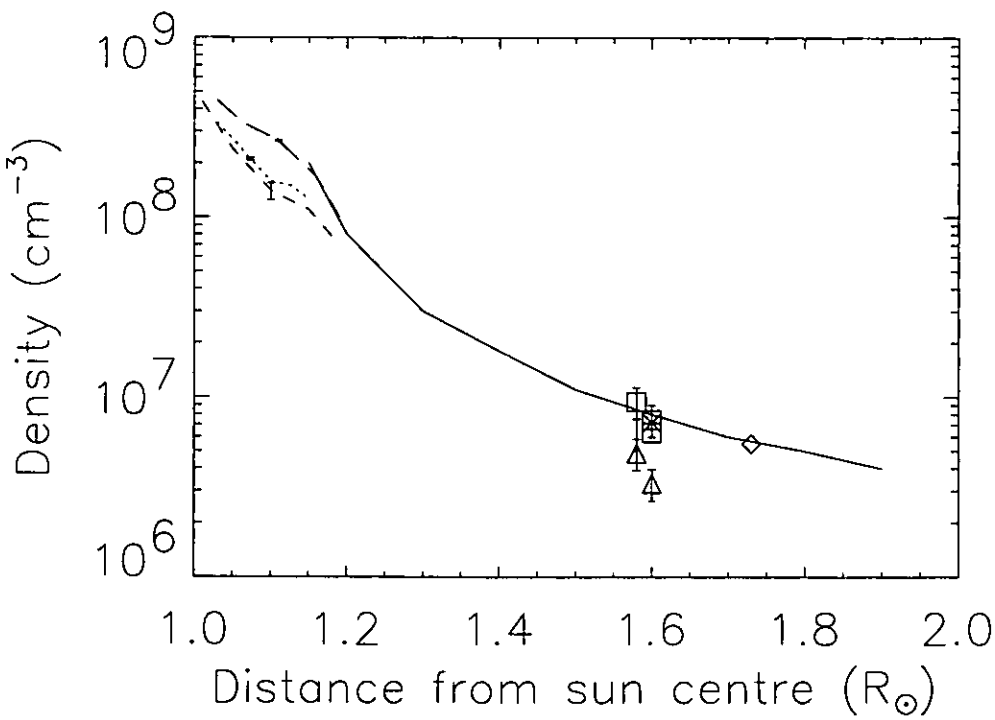

Figure 4.11: Streamer density v. solar distance for the present work compared to previous studies. Squares are mid-latitude streamer (UVCS), and triangles are equatorial streamer (UVCS); the long-dashed and dotted curves are from CDS Si IX ratios from, respectively, the mid-latitude and the equatorial streamers. Solid line is density from Gibson et al. (1999b); dashed line is from Fludra et al. (1999a); diamond from Strachan et al. (2000); asterisk from Ciaravella et al. (1999).

streamer to streamer not only because of real density differences but also because of lack of simultaneous measurements of disc intensities. These latter are needed for a correct usage of the relationship (see Section 4.5.2, Equation (3.38)) from which densities have been derived. The influence of this factor is difficult to quantify since the size of any variation in the O VI 1032 disc intensities cannot be easily predicted.

The March and May mid-latitude streamers appear to have higher densities than the equatorial March streamer. Although in the low corona the March mid-latitude structure may be affected by the presence of the hot loop at low altitude, the UVCS determination yields a higher density as well and thus supports the CDS results. Future observations will need to investigate whether this is an occasional episode or whether mid-latitude or active streamers do have higher densities than quiet structures.

4.6.3 Element Abundances

In this work, the absolute oxygen abundance in streamers at $1.58-1.6\ R_\odot$ has been derived by using two different methods: both agree in revealing an oxygen depletion, with respect to the O photospheric abundance (log A_O= 8.93), which can be as much as $\approx 80\%$ in an equatorial streamer (see Table 4.8). Even though it was not possible to identify the core and the legs of the streamer as in Raymond et al. (1997, 1998), the present results agree with the oxygen abundances found by these authors at 1.5 $R_\odot$ and 1.75 $R_\odot$. There are a few estimates of the oxygen streamer abundance in the literature: in the Raymond et al. work, the oxygen abundance was found to vary in the streamer core from 7.5 to 7.8 and in the streamer's legs – or, when core/legs cannot be identified, in the overall structure from 8.3 to 8.66, while in Ciaravella et al. (1999) a value of ≈ 8.8 is given for the O streamer abundance, and a value of only 8.1 in a related transient event. These values point to a large variation in O abundance, both within streamers and in different structures.

At lower altitudes, the oxygen abundance is hardly known and it is unfortunate that no value can be derived from our CDS data. From SUMER observations, Feldman et al. (1998) found (at heights $\leq 1.03\ R_\odot$) an oxygen abundance of 8.8 in equatorial regions. It is not possible to tell from this single measurement, whether the O abundance decreases with altitude, or whether the Feldman measurement refers to a particular streamer not showing oxygen depletion.

In the solar wind, there are a few abundance determinations for oxygen. Wimmer Schweingruber (1994) gives 8.72 for the slow wind and 8.8 for high speed wind: hence any depletion of oxygen in the solar wind is too marginal to be convincing. On the other hand, recent work by Aellig et al. (1999) finds an Fe/O ratio which changes as a function of the

solar wind speed. Their flux- weighted average for the Fe/O ratio is 0.11 ± 0.03 and this is consistent with the average Fe/O ratio of 0.13 derived here from UVCS abundances. In deriving this value, an average of the oxygen values from Table 4.7 was used. A slightly higher value is obtained if values from Table 4.8 are used, but it should be remembered that in this case only the collisional component of the oxygen lines was used. These values are also consistent with the in-ecliptic solar wind value given by Ipavich et al. (1992): it might be interesting to check on Fe/O variation along/across streamers, in order to get more insight into the slow wind origin.

For the other elements, at $1.58 - 1.6\ R_{\odot}$ all abundances show a depletion, with respect to their photospheric values, in agreement with the Raymond et al. (1997) results. Although spectra at different altitudes are slightly different, not always allowing multiple determinations of the abundance of the same element, the results I got are fairly consistent with each other.

The scarcity of high FIP elements in the present UVCS and CDS spectra prevents any detailed analysis of the FIP effect (e.g. Young & Mason (1997); Doschek et al. (1998b); Laming et al. (1999)) either at low heliocentric distances or near 1.6 $R_{\odot}$. However, streamers are known to behave anomalously, as far as the FIP effect is concerned: Schmelz (1999) pointed out that contrasting results have been obtained by Feldman et al. (1998) and Raymond et al. (1997).

Present UVCS results support Raymond's findings that low FIP elements are depleted, with respect to their photospheric abundances, but puzzling results were obtained for the (only) two high FIP elements in the present spectra. Raymond et al. (1997) find high FIP element depletion to be about a factor 2 larger, e.g. for O, Ar, S, than for low FIP elements, such as Si, Fe, Al. In the present analysis, oxygen is found to be more depleted than low FIP elements, but Ar is consistently found to be less depleted than low FIP elements. It is difficult to explain this behaviour, but it is not unusual to find some inconsistency in the "behaviour" of high FIP elements. For instance, in the 1997 Aug 21 streamer analysed by Raymond et al. (1998), an O enhancement of about a factor 2, with respect to coronal abundances, corresponds to a S depletion of about a factor 3.5 (still with respect to coronal abundances). The dependence of the FIP effect on the streamer type (whether it is a stable, quiescent structure, or an active phenomenon, to which fresh photospheric material can occasionally contribute), and possibly also on the streamer lifetime, are still poorly known issues, which deserve further study.

Chapter 5

Off-limb Observation of a Macrospicule

This chapter is dedicated to the description of the analysis of data obtained by a sequence of SOHO/CDS rasters taken off-limb in the south coronal hole on 6 March 1998. Three successive observations were made with the Normal Incidence Spectrometer (NIS), the first of which showed a jet-like feature visible in the chromospheric and low transition region lines. The morphological characteristics and the short duration of this feature suggested it was a macrospicule, such as previously seen in EUV images. The two remaining observations showed a quiet coronal hole. Their spectra were averaged and the results were studied for any indication of plumes. This averaged data was then used as "background" for the macrospicule plasma. The subtracted spectra showed clearer details of the feature. In particular, a cloud of plasma was detected at about 30,000 km from the limb. Density (N_e) and temperature (T_e) diagnostic studies were carried out on these data, revealing departures in N_e and T_e here, compared with the background values. A velocity study did not yield the results seen in previous work, with no evidence of rotational flows in the data studied here.

5.1 Introduction

In this work a feature visible above the limb in the south coronal hole which has the morphology of a macrospicule is investigated. The data available gave us the unique opportunity to obtain a *background* to be subtracted from the image containing the macrospicule. In this way, the characteristics of this feature could be studied and then compared with those of the surrounding coronal plasma.

5.2 The Observations

The data consisted of three successive off-limb observations of the same region in the south coronal hole made on 6 March 1998. The full spectra (from 308 to 381 Å and from 513 to 633 Å) of a 120″×120″ area were obtained by the Normal Incidence Spectrometer of CDS (Harrison et al., 1995). The raster was built up by scanning the slit from west to east over 30 steps, each of them with an exposure time of 160 s. The rasters were centred at a distance of 1.08 $R_\odot$ (1050″) from the Sun centre at longitude -89.9° (Figure 5.1) in the SE quadrant. The spatial resolution was about 4″ in both dimensions.

The standard CDS software was used for initial processing of the data (de-biasing, the flat-field and cosmic ray removal). The spectra were then fitted using multiple Gaussian line-fitting (Haugan, 1997), and the intensity calibration from Del Zanna (1999) was applied (see Chapter 2).

The first raster was obtained between 10:41 and the 12:57 UT. Monochromatic images of the observed region at this time are given in Figure 5.2. In this observation a spike-like feature appears at the top left corner of the raster, in images from chromospheric and low transition region lines, while it is scarcely visible in images from coronal lines (the Mg X shown in the Figure has a contribution from an O IV line; see discussion in Section 5.7). The solar limb is towards the top, just out of the field of view, at solar Y=974″, i.e. about 19″ from the top of the image.

It is useful to note that each raster contains both spatial and temporal information. As already stated, each raster is made up of a sequence of 30 exposures, obtained by moving the slit from west to east. Each exposure lasts 160 s and an interval of about 270 s passes between two successive slit positions. The solar rotation can be neglected, so two successive positions of the slit give the plasma intensity observed in different locations (4″ apart westward) with a time delay of about 270 s.

Referring to the raster images, each column represents the image of the slit obtained during one exposure. Numbering the columns from left to right, starting from 0, the feature is seen to be bright over several pixels along the Y-direction in the columns 4, 5 and 6 (corresponding to solar X $\sim$ -40″). The O V image shows the feature extending about 70″ from the limb with a width of $\approx$ 12″. This morphology and temperature of emission are characteristic of a macrospicule.

The other two successive observations of the same area at 12:57 - 15:13 UT and 15:13 - 17:29 UT, do not show any indication of the feature. Considering that the time between two successive rasters is about two hours, the feature appears to be short-lived, also

a characteristic of macrospicules. Moreover, the evolution of the feature in successive columns indicates a time scale of the order of 10 minutes (see below).

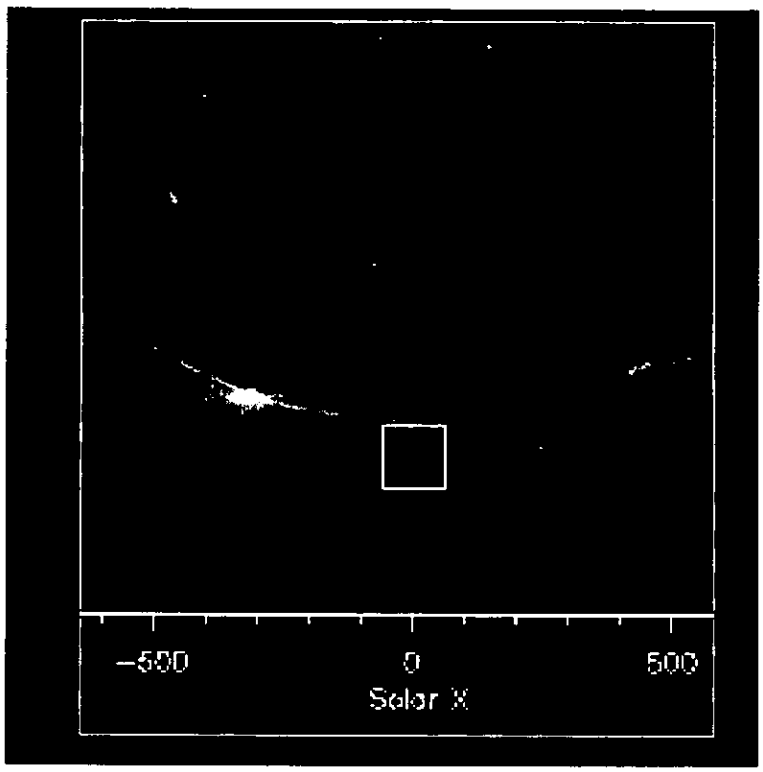

Figure 5.1: Detail of 195 Å SOHO/EIT image of the solar corona taken 6 March 1998. The CDS raster is superimposed as a white rectangle to show its field of view. The image shows a well defined coronal hole occupying the south pole.

5.3 The Background

The last two rasters show the coronal hole with no visible feature apparent in the location of the macrospicule. These two sets of observations were averaged to provide a *background* to be subtracted from the first raster. Figure 5.3 shows images of the averaged background data, in the same lines as shown in Figure 5.2. The two Figures show that the only apparent difference is the absence/presence of the feature. In order to ensure that these data taken as background were properly used without contaminating the macrospicule analysis, they were studied for evidence of plume plasma in the region occupied by the structure. A plume might be in the line of sight to the macrospicule. If one was present it might vary during the observations, this would affect the analysis of the macrospicule plasma after the background subtraction. A plume emits mainly at upper transition region temperatures, similar to the temperatures at which the macrospicule is seen here, and could therefore

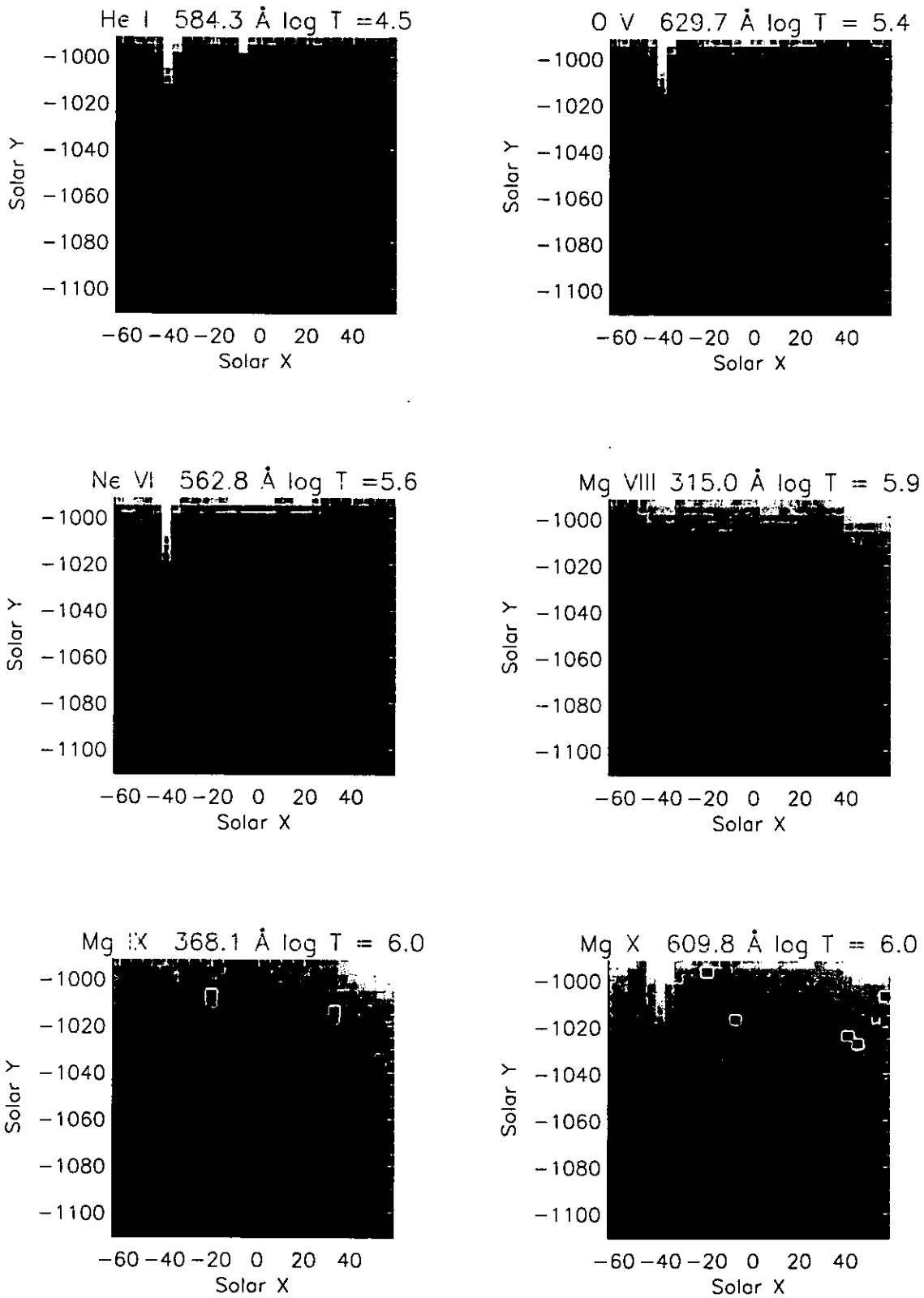

Figure 5.2: Monochromatic images of the first raster. The south solar limb is above the top margin of the image by about 20″. The feature is brightest at columns 4,5,6, counted from 0 at eastern edge of the image. It is clearly visible in the chromospheric and transition region lines and faintly visible in the low coronal emission.

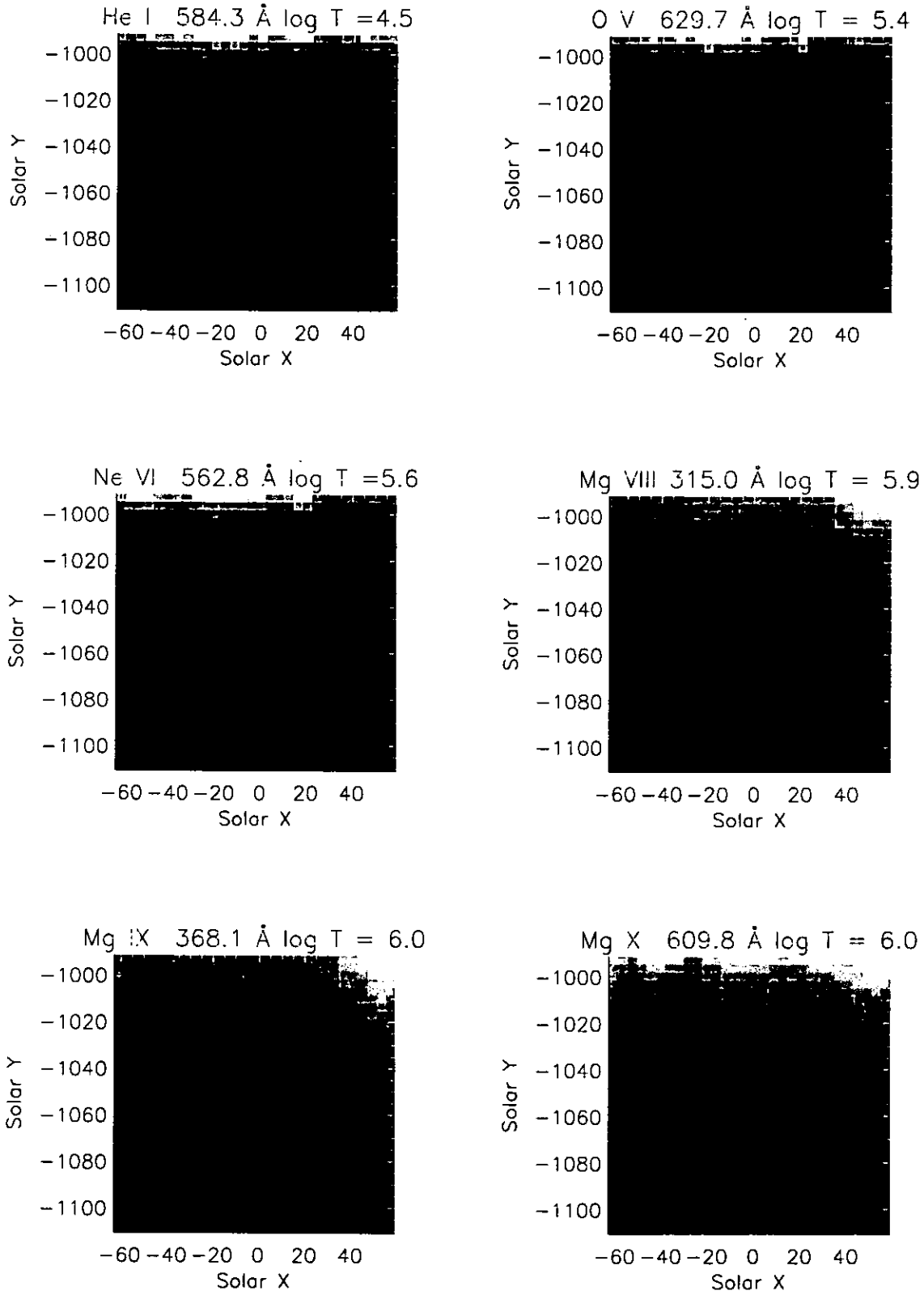

Figure 5.3: Monochromatic images of the raster obtained averaging the second and third rasters. The spectral lines are the same as Figure 5.2.

possibly cause confusion.

In averaging over the two observations there is no lack of information about the presence of plume plasma. The life-time for a plume is of the order of days (Deforest et al., 1997), while in our case, only information on a time scale of hours could be lost by averaging.

Once the average was formed, the first two rows of pixels closest to the limb (from -60″ up to 25″ along the east-west direction) were selected, and the average of the spectra over the two rows was obtained. A multi-Gaussian fit was performed, along the X-direction. The fitting procedure, as already pointed out, is time-consuming. For this reason the analysis was limited to the area of interest, and the data most distant from the the macrospicule were excluded from this analysis. Profiles of intensity over the X-direction were thus obtained by applying the fitting routine (Figure 5.4).

An intensity profile across plume and interplume regions generally shows an enhancement in the plume location, visible in the chromospheric and transition region lines (Young et al., 1999; Del Zanna, 1999). Figure 5.4 shows an example of the intensity profile obtained for the present data, covering the emission of plasma at different temperatures.

The only lines that show a trend in intensity along the X-direction are the Mg VIII and Mg IX lines. They increase towards the west. Looking at the full raster monochromatic images of Figure 5.2, in fact, in the top right corner a bright feature is visible at those wavelengths. The temperature of this emission indicates a plume. Of course, further analysis of the data is required to establish the nature of the feature, but at a first glance it appears to be a plume. In any case, the profile in intensity, is lower at the position (-40″) of the macrospicule. This means that even if this is plume material, the macrospicule appears to be outside this region. The line ratio technique (Mason et al., 1997) has been applied to obtain electron density and temperature using the CHIANTI database (Landi et al., 1999) and the Mazzotta et al. (1998) ionization equilibrium (see Chapter 3). The profile of density along the solar Y direction shown in Figure 5.5 has been obtained from the Si IX 349.87/345.13 Å ratio. Using the same line ratio Young et al. (1999) found a variation greater than a factor of two between the density in the plume and the interplume region at the plume base. Del Zanna & Bromage (1999c) analysing a plume at the coronal hole limb found very little variation in density between the plume and interplume regions at this temperature. Wilhelm et al. (1998b) using the Si VIII 1440/1445 Å found a variation of about two in density between the centre of the plume and the interplume region, over approximately the same solar distance as the data used in this thesis. The profile plotted in Figure 5.5 shows a fluctuation in density, along the X-direction, at maximum of a factor

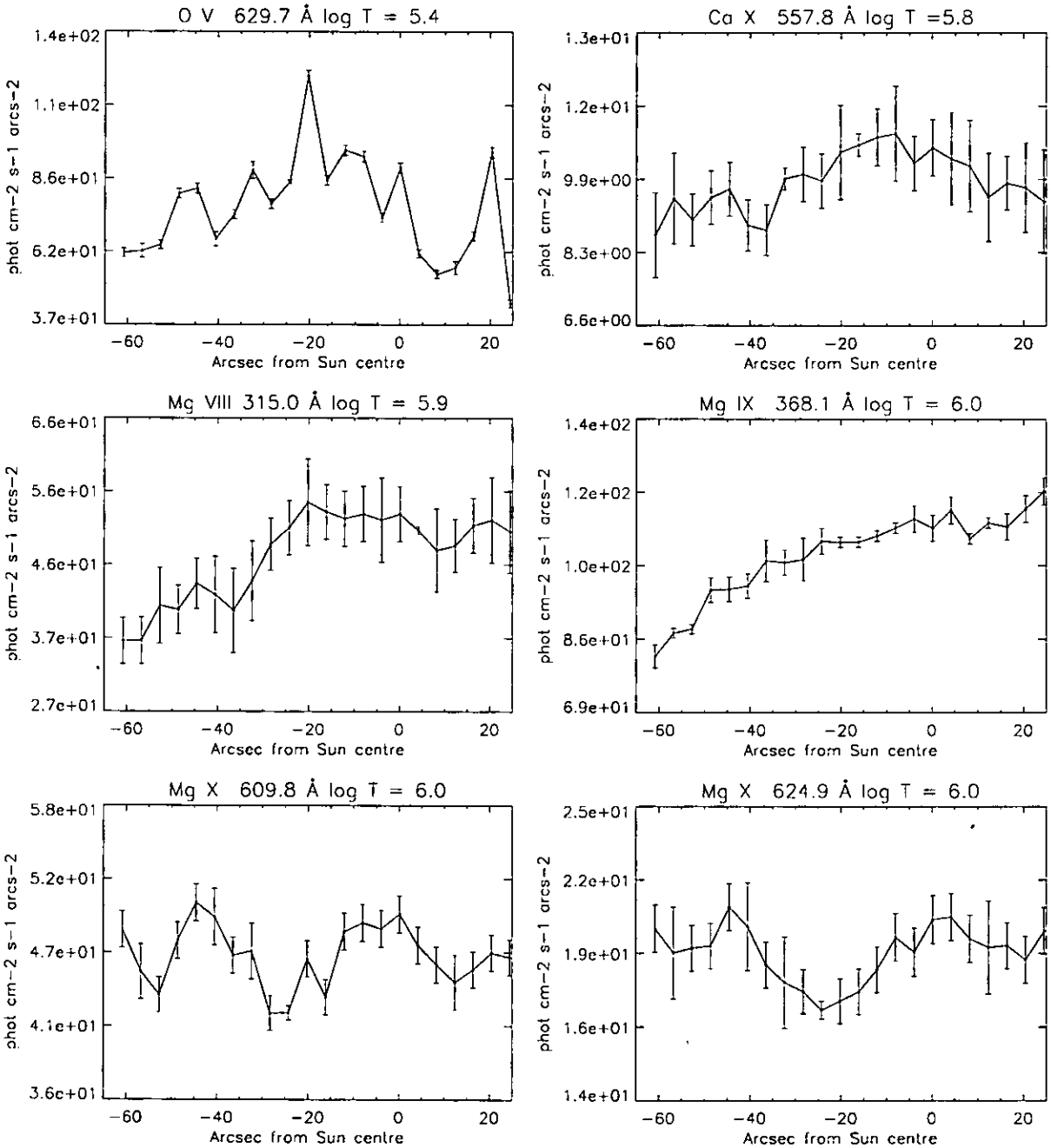

Figure 5.4: Profiles of integrated intensities along the X direction, at a solar distance of about -1000″ from the sun centre, for ions emitting at different temperature. The data relate to the observations taken as background.

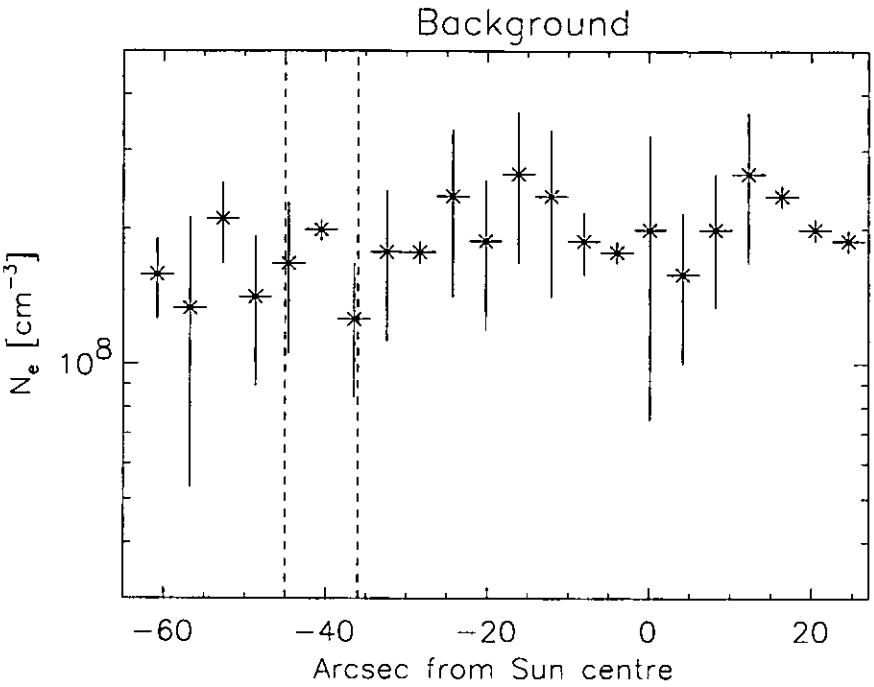

Figure 5.5: Electron density along the solar Y direction for the background coronal hole, derived from the ratio Si IX 349.9/345.1. The vertical dashed lines indicate the region occupied by the macrospicule.

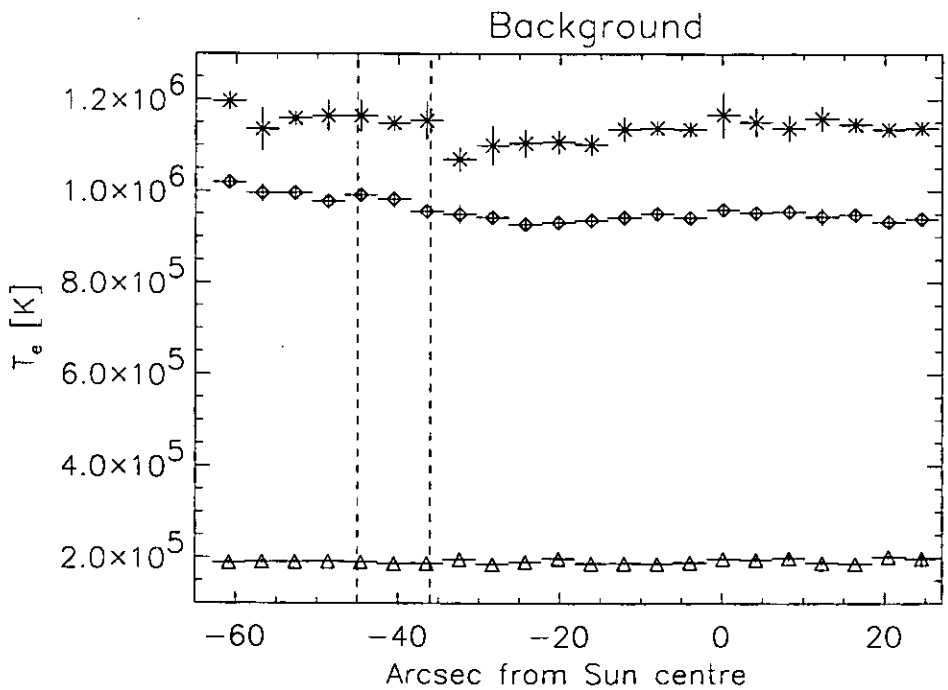

Figure 5.6: Electron temperature along the solar Y direction for the background coronal hole. Asterisks represent the temperature from the Fe XII 364.467 / Fe X 345.723; diamonds from Mg X 624.9 / Mg IX 368; triangles from O V 629.730 / O IV 554.513. The vertical dashed lines indicate the region occupied by the macrospicule.

two, but a clear shape of a profile across plume and interplume regions is not present.

Figure 5.6 shows the profile of temperature derived from the Fe XII 364.467 / Fe X 345.723, Mg X 624.9 / Mg IX 368 and O V 629.730 / O IV 554.513. Due to the vicinity of the solar limb, where the solar activity is more evident, the different ratios become more sensitive to the underlying multi-thermal plasma of the solar disc. However, while the temperature from the oxygen ratio remains almost constant, the temperatures from iron and magnesium ratios show a small increase from the west side of the raster (positive distances from the Sun centre) to the east (negative distances from the Sun centre). Wilhelm et al. (1998b) found a variation of about 20% in temperature between the plume and interplume regions, with the plume slightly cooler. Del Zanna & Bromage (1999c) also found plumes to be cooler than the surrounding coronal hole was.

What then appears from the present results is the possibility of plume material that fills the west side of the raster. However, the area occupied by the macrospicule (the region limited by the dashed line in the figure) is located away from that area. It needs to be pointed out, however, that the lines chosen here for density and temperature determination in plumes are not completely appropriate. Del Zanna & Bromage (1999c) found that the maximum emission of plume material is at about 8 $\times 10^5$ K, so that high transition regions lines are more suitable, but those lines are scarcely visible in the present data. This issue will be discussed later in the Section 5.7.

In conclusion, it can be said that the spectra obtained by averaging the two data sets show signatures of plume material but not in the area occupied by the macrospicule, so it can be used as a reasonable background for the macrospicule. It should be remembered that plumes emit mainly in transition region lines, which correspond also to part of the temperature range of emission of macrospicules. The plume material, if present in the data, would have contaminated the macrospicule emission, and hence the results of a diagnostic study.

5.4 Macrospicule Evolution

As mentioned, the feature that appears in these data occupies only about three pixels in the X-direction. This implies that the data do not have a sufficiently high spatial resolution to resolve the feature's morphology along that direction. What is more likely is that the data show, in the variation from one column to the next, *temporal* evolution of the macrospicule.

Figure 5.7 shows the intensity variation of O V 629.7 Å, along the Y-direction and

along the X-direction, for the exposures of the raster where the feature is visible. An example of the fitted spectrum is given in Appendix A.4 taken from the first pixel from the top of column 4. Both the macrospicule and its background spectra are plotted.

In Figure 5.7, both the original data (left column) and the data with the subtracted background (right column) are shown. Note that the time increases from top to bottom. The left column shows how big is the difference in intensity among the different columns. Column 5 is the most intense, while column 4 shows a shoulder around -1010″. This behaviour of the intensity is much more evident after subtracting the background (right column).

To estimate the off-limb extent of the feature it is necessary to estimate the size, in arcsec, of the solar radius at the time of the observation. This has been done by estimating first the location of the O V limb brightening, and then using the information that the O V peaks at 4″ above the photospheric limb (Mariska, 1992). To find the O V peak intensity, the CDS synoptic data of the day were used, and 3 columns at both the sides from the position X = 0 were selected from the raster. Then the O V signal was averaged over the X direction for each Y position. In this way a smoothed profile along the Y direction was obtained. Averaging over 6 pixels in the X direction removes small scale fluctuation of the signal. The profile for the O V obtained here peaked at -977.8″, so that 973.8″ is the limb radius derived. Moreover, this gives the relation 1″=714.7 km on the Sun.

Another effect to be considered in the present calculation, is that the X coordinate of the feature is at -40″ away from X = 0. This means that its distance from the Sun centre is bigger than that calculated at the position X=0. At this position, the Y coordinate of the closest row of pixels to the limb in the raster is -993″. A quick estimate gives that at the position X=- 40″ the distance from the Sun is 993.8″, a difference that is much smaller than the spatial resolution of the data (4″). Therefore this effect can be neglected.

For the results obtained here, the maximum of O V intensity plotted along column 4 corresponds to a height of 25,872 km (36.2″) from the limb. Interpreting the sequence of plots as a temporal evolution of the same feature (neglecting the variation with the width), columns 6 and 5 give the phase of expansion of the feature into the corona. In column 4 the intensity is already reducing and, looking at the right-hand figure, an isolated cloud remains with its peak of intensity at -1010″. In column 3 the intensity near the top is even lower than in column 6: just a faint brightness remains in the location of the cloud. A possible interpretation of the intensity shown in column 4 is in the signature of expelled cool material from the macrospicule. Unfortunately, the lack of data closer to the limb limit the information available here about how much this cloud extends and how the

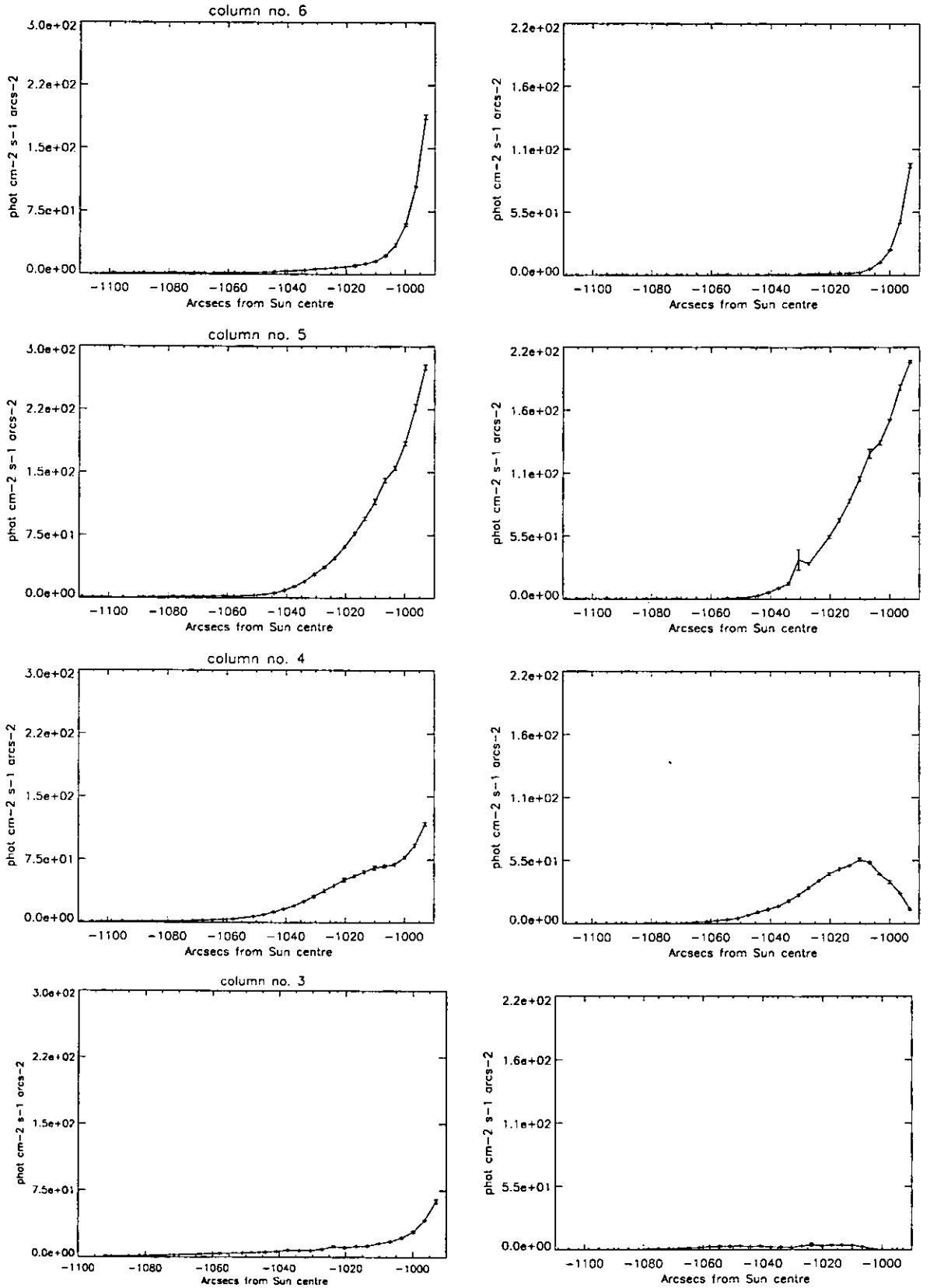

Figure 5.7: Profiles of the O V 629.7 Å intensity with the solar distance, along the columns, from top to bottom, 6,5,4 and 3. The left column shows the intensities from the unsubtracted observation. The right column shows the intensities after having subtracted the background. The time between exposures is 272 s while the exposure time is 160 s.

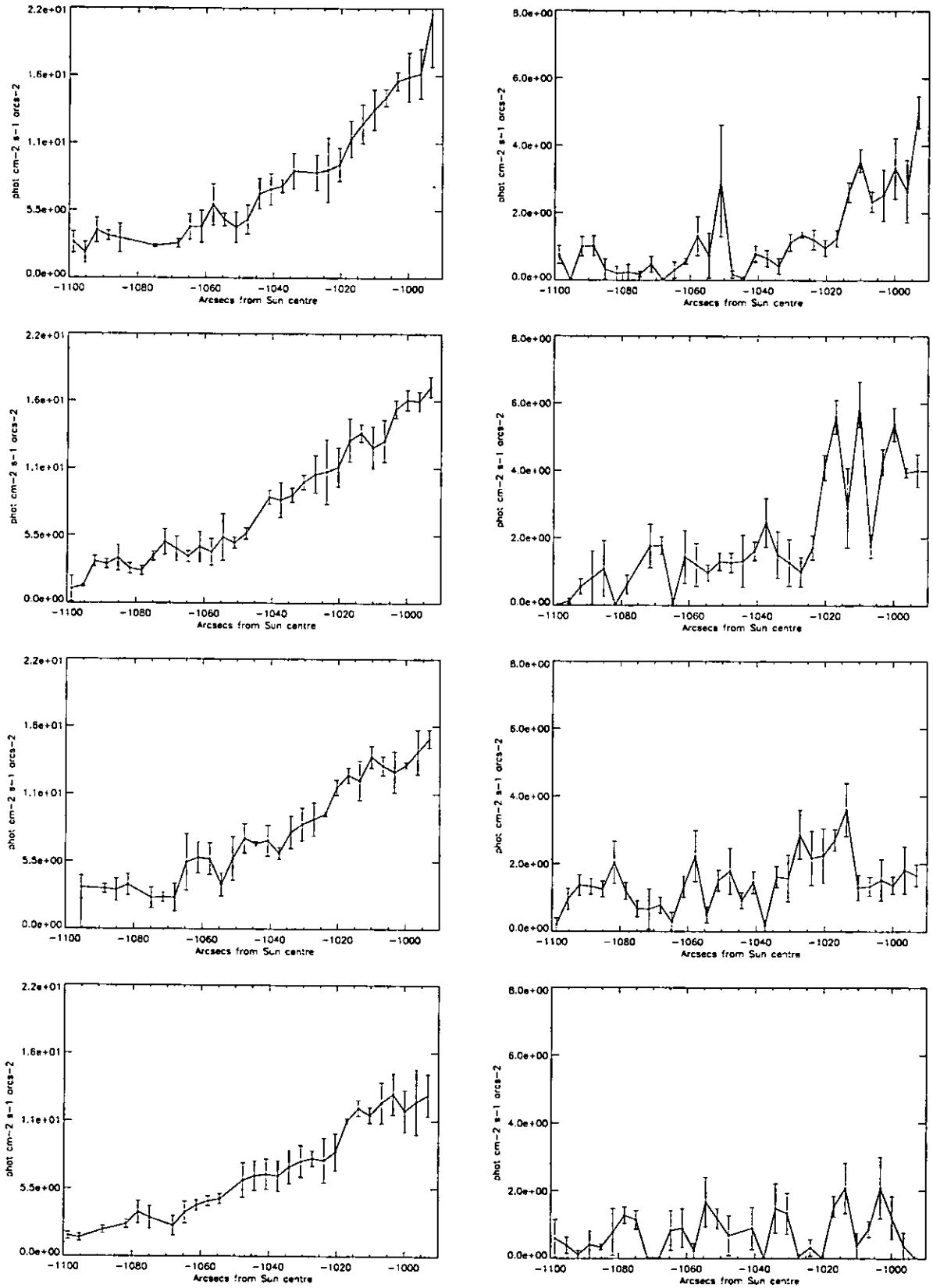

Figure 5.8: Profiles of Si IX line at 345.1 Å intensity with the solar distance, along the columns, from top to bottom, 6,5,4 and 3. The left column shows the intensities from the unsubtracted observation. The right column shows the intensities after having subtracted the background. The time between exposures is 272 s while the exposure time is 160 s.

macrospicule evolves nearer the Sun.

Figure 5.8 shows the same sequence for the coronal line Si IX 345.1 Å. As expected, the emission from hot plasma is less pronounced than from chromospheric temperature. After the subtraction of the background a very weak signal remains.

What emerged from the profiles shown in Figure 5.7, was the necessity to make an analysis of the plasma intensity pixel by pixel, instead of averaging over several of them to improve the signal/noise ratio. Column 4 appeared to be the most interesting and, considering that the signal there was good, it was decided to use that data to proceed in the study of the feature. The study then continues with the search for further indications that could eventually confirm the first interpretation of the data illustrated here. In the next sections the density, temperature and dynamics will be investigated.

5.5 Velocity

The O V line proved to be a good diagnostic line because it is bright enough to extend the study to several columns of data. The same four columns whose O V intensity profiles are plotted in Figure 5.7 were used to investigate the plasma dynamics.

The absence in the profiles shown in Figure 5.7 of the peak intensity positions in the exposures 5 and 6 (maybe situated out the field of view), led the author to estimate the radial velocity of the plasma by identifying the position of the expansion front of the macrospicule in each column. The first row of Table 5.1 gives the Y-distances from the sun centre where the O V intensity drops to zero. These values are derived from the right-hand column in Figure 5.7, representing the macrospicule data from which the background was subtracted. The threshold of the drop in intensity was chosen as a fixed value to be applied in all columns. The second row reports the distances in km from the limb. The averaged values between two successive position are also reported. The third row of the Table reports the time delay between the exposures. The fourth row gives the derived velocities assuming steady motion. These values were calculated by using the interval of distance between two successive exposures where the drop occurred, with the assumption that their time delay was 271.6 s, and that 1″ on the Sun corresponded to 714.7 km. The error on the velocity was estimated using the standard error propagation method, assuming 1 pixel error (4″) on the estimate of the interval of distance covered by the plasma between two successive columns on Table 5.1. The results clearly show a decrease in velocity with the distance from the Sun. It is important to remember that what is seen in each column is integrated over the 160 s exposure time. If the maximum

velocity of 80.5 km s^{-1} is considered, then during the exposure time the plasma would have travelled about 12880 km (18″). This indicates that during the integration time some information about the macrospicule evolution is lost. Moreover in this analysis the assumption of uniform velocity across the macrospicule is made. Figure 5.9 (left) shows

Table 5.1: Dynamic of the macrospicule plasma deduced by the extent of the O V emission.

Column	6		5		4		3
Position ± 4 (″)	-1027		-1058		-1068		-1078
(km from the limb)	38,880	49,458	60,035	63,680	67,325	70,899	74,472
Time (s)			271.6		543.2		814.8
Avg. Velocity ±10.5 (km s^{-1})		80.5		28.9		26.3	
Avg. Acceleration (km s^{-2})			-0.20		-0.01		

a plot of the velocity v. height reported in table 5.1. The graph on the right of the same Figure, shows the derived heights of the cloud of plasma in the four successive exposures. The time on the X axis starts (Time=0) with the first exposure. The overplotted curve is a second order polynomial fit to the points.

The result of the fit gives an initial velocity of 81 km s^{-1} and a (constant) deceleration of -0.095 km s^{-2}. The deceleration here estimated is much less than the gravitational deceleration of -0.274 km s^{-2}. However, this last value is for the Sun's surface, and it should be remembered that the location considered here is the corona, where a lower gravity is expected. An estimate of the gravity at this distance was made by using the expression $g(r) = (M_{\odot}\ G)/r^2$. Assuming a distance from the limb of 40,000 km, the deceleration due to gravity worked out to be -0.244 km s^{-2}. This connection is not enough to explain the present results. One reason for this difference could be an inclination of the trajectory with respect to the radial direction. If this was the case, then an angle of inclination of about 70° is derived. On the other hand, if this was the case, evidence of line-of-sight velocity should be seen in the data. From the parameters derived from the fit on the trajectory, a velocity of about 220 km s^{-2} would, in fact, the expected along the line of sight. This investigation is the next step in the present analysis.

Another interpretation of the dynamics can be made by looking at the left-hand plot of Figure 5.9. It seems that the deceleration is not constant as the plasmoid moves out from the limb. Hence, it could be that the approximation made in fitting the plasmoid

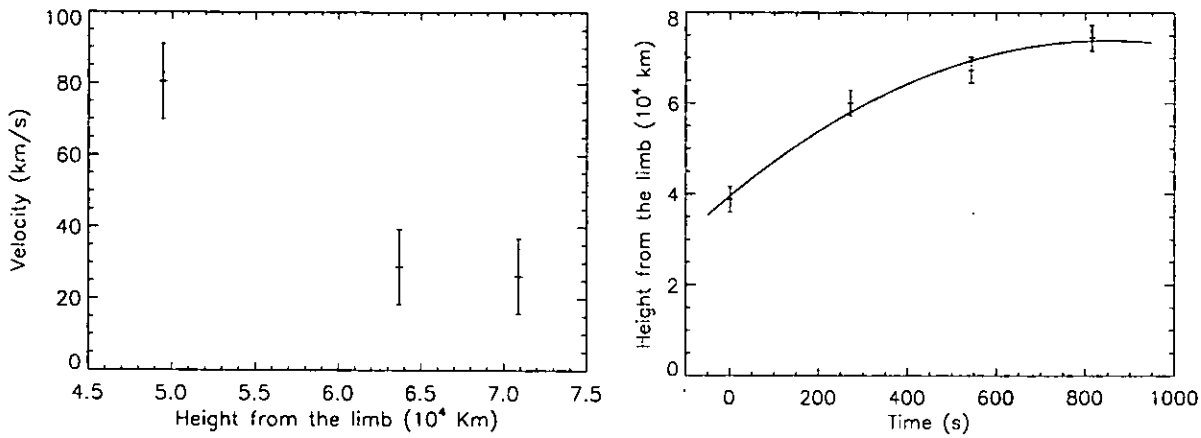

Figure 5.9: Left: velocity v. height from the limb of the plasmoid expelled by the macrospicule. The values are taken from Table 5.1. Right: Trajectory of the expelled plasmoid fitted over the estimated position. The data refers to column 4.

trajectory does not hold. The last row of Table 5.1 reports the average deceleration values derived from the velocity listed in the third row from the same Table. At the beginning of the plasmoid motion, the deceleration assumes a value close to the solar gravitation. Later, it is much lower, equal to the value found in the constant acceleration aproximation, and the velocity seems to tend towards a constant value close to 20 km s^{-1}.

Looking for a signature of transverse velocity, using Doppler shift analysis, was not an easy task. The first thing to be noted is that the spatial resolution of these observations is not ideal for this kind of study. In fact, the feature occupies about three spatial pixels along the X direction. If rotational velocity were present in these data, it would be quite difficult to see at this spatial resolution. Moreover, CDS was not designed for velocity studies and instrumental effects on line broadening and wavelength shifts have been found recently Haugan (1999). Using synoptic images, Haugan found that whenever a steep gradient of intensity exists along the slit, positioned along the N-S direction, a systematic red-shift is observed in the south hemisphere and a blue-shift is observed in the north hemisphere. These shifts correspond to about 5 km s^{-1}.

A tentative line-shift analysis was carried out on the O V line, and the results are shown in Figure 5.10. The figure shows the position of the peak of the fitted line along the slit, for the columns 3, 4, 5 and 6. The wavelength for the rest position is marked by the horizontal dashed line. The data were used without subtracting the background, in order to keep the signal/noise high. The Figure shows that in columns 3 and 6 the line position remains almost constant within the limit of the error. While the data in column

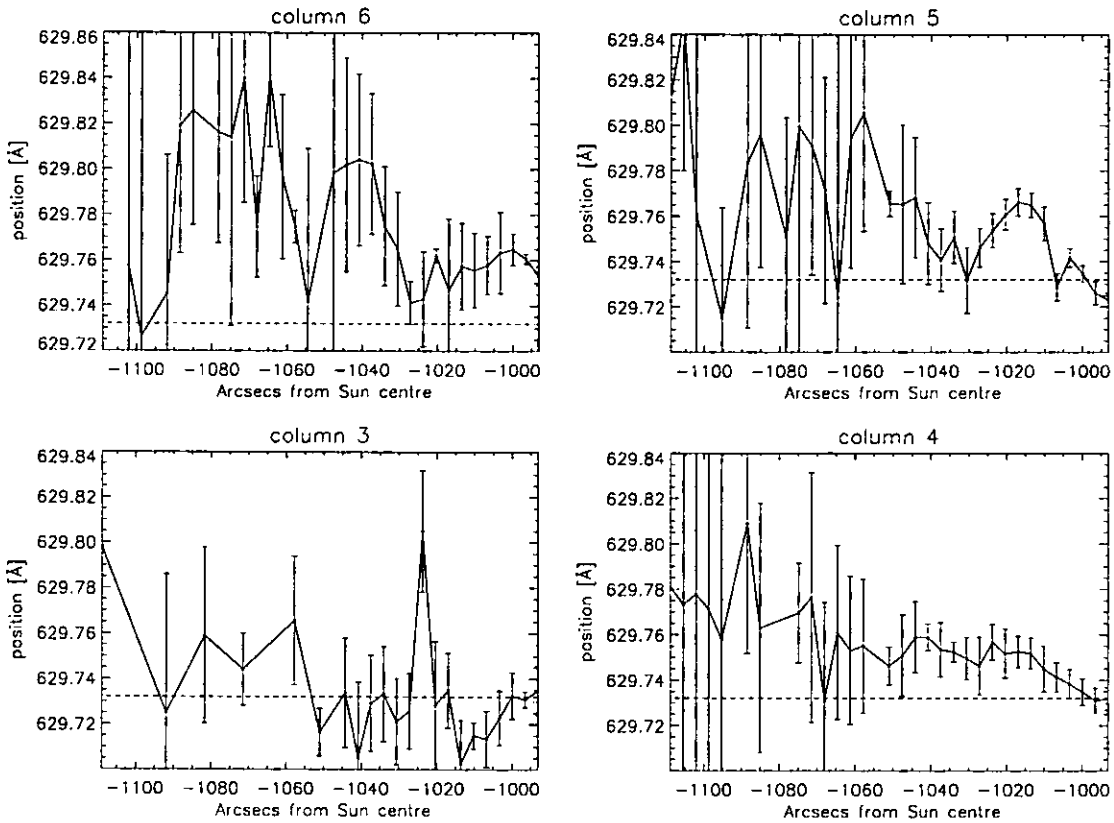

Figure 5.10: Positions of the centre of the peak line for the O V along the slit along each columns. From top left clockwise: column 6, 5, 4, 3. The rest position of the line is marked by the dashed horizontal line.

3 appear largely unshifted, there seems to be a red shift in the column 6 data of about 0.03 Å ($\sim$ 16 km s^{-1}). The isolated point at 629.8 Å in column 3 has been checked and found to be a spurious result due to the weak signal of the line. The other two columns (4 and 5) instead, show a different behaviour. Column 4 has a red-shift increasing up to -1025″ (629.757 Å), and then stabilized. The rest position of the line is 629.732 Å, so the corresponding velocity for that shift is about 12 km s^{-1}. Column 5 shows increasing red-shift up to about -1020″, with a peak velocity of about 17 km s^{-1}, followed by a return toward the starting wavelength value at -1030″. The point -1007″ showing low red-shift is the result of a bad of fit: part of the line is missing, probably caused by the incidence of a cosmic ray. After -1030″ the red-shift starts again, but the decreasing signal leads to high uncertainty. Comparing the line positions with the intensity profiles, it can be noticed that in column 4 there is a change in the intensity gradient at about -1010″. This is associated with a change in the gradient of the line shift.

The variation of the position of the line in column 5 seems not to have a corresponding counterpart in the change of the intensity gradient. So, it seem difficult to establish how

much the effects seen on the line position plot are due to the instrumental effect or to a physical process.

The effect described here has been checked for other lines on the same detector, such as Mg X (609.793 Å), O III (599.597 Å), Ne VI (562.8 Å), to look for evidence of the effect seen in the O V. Whenever there is a steep intensity gradient, like found for the O III, the red-shift is slightly visible, while for a line like Mg X, where this gradient is not seen, a constant position is found.

However, the velocities found are greater than 5 km s^{-1}, so even allowing for this, trasverse flows of about 17 km s^{-1} are found in columns 4-6. On the other hand, this flow does not reach the 200 km s^{-1} expected for the case of constant acceleration of the plasma and an inclination of the feature of about 70° to the radial direction mentioned above.

Evidence for O V line broadening have also been checked for in the single pixel data, without obtaining positive results.

5.6 Density and Temperature

In light of the discussion of Section 5.4, in which the ejection of a cloud of cool material from the chromosphere was proposed, to explain the observations its density and temperature characteristics needs to be considered. In the previous section it was shown that there was little evidence of bulk motion perpendicular to the radial direction. However, flows out from the limb in the radial direction were found. The speed appeared to decrease with time and tend towards about 20 km s^{-1}.

The data in column 4 clearly show the effect of the structure in the intensity, so these data were selected for further analysis, applying spectroscopic diagnostics to obtain temperature and density information. Implicit in the analysis was the assumption that by this time the flow was sufficiently reduced to allow ionization equilibrium. The unsubtracted data were used because of the low signal in column 4 after the subtraction of the background.

5.6.1 Density

Densities have been plotted in Figure 5.11 as a function of distance, measured in arcsec along the slit direction. Results are shown for ions with peak emission at temperatures ranging from chromospheric to low corona: O IV (T=2×10^5 K), Mg VII (T=6.3×10^5 K), Mg VIII (T=7.9×10^5 K) and Si IX (T=1.3×10^6 K).

In the Figure, the temperature of the emitting plasma increases from the top to the

bottom. Beside the quite large uncertainty, the density from O IV (logT=5.3) increases with the distance up to -1020″ by more than one order of magnitude, and then starts decreasing.

The Mg VII ratio shows instead a different behaviour: first the density decreases, then increases up to about -1030″ and then decreases again. Also in this case the density changes by more than one order of magnitude.

The profiles derived from Mg VIII lines and Si IX involve a minor variation of the density with the distance, but still enough to show a slight decrease between -1005″ and -1020″ where it raises towards higher values. Note that the raise visible in these last two profiles, is located two pixels ahead of the point where the density derived from O IV peaks, that is at -1020″.

If we rely on the trends shown in figure, a possible qualitative interpretation can be drawn. It was mentioned that the increase of O V intensity shown in Figure 5.7 column 4, has been interpreted as the signature of an expelled cloud. If this is the case, the hot coronal material previously occupying the cloud volume will be replaced by cooler macrospicule plasma and, eventually, will be pushed forward. This picture could justify the increase of density seen from the oxygen ratio and the decrease of densities from the other ratios, between -1005″ and -1020″-1030″. The constant densities from the coronal lines, obtained beneath -1005″, together with the decrease of density from Mg VII and increase from O IV at the same distances, may be the indication that at these distances the space is filling back with hot coronal plasma. Moreover, the step in density at 1030″ seen in the hottest lines, may be interpreted as the hot material pushed ahead of the cool cloud.

It is worth remembering that the density derived here is an average over the whole line of sight. This is the reason why major fluctuations in density are seen using ratios of cooler lines. The observed O intensities are emitted predominantly by the feature: it is not expected to see O IV and O V in the off-limb hot corona. The observed Mg VIII and Si IX are instead emitted in that region, and a very small contribution will then arrive from the volume occupied by the macrospicule. An attempt to compare the density obtained here for the macrospicule, and that from the background was made. The column 4 in the data used as background was selected and a check over the spectra revealed that the only ratios usable for density diagnostics were the Mg VII and Si IX. The O IV turned out to be too faint to be reliable.

The densities so derived in the background are shown in Figure 5.12 by the asterisks. The densities from the macrospicule derived using the same line ratios are overplotted in

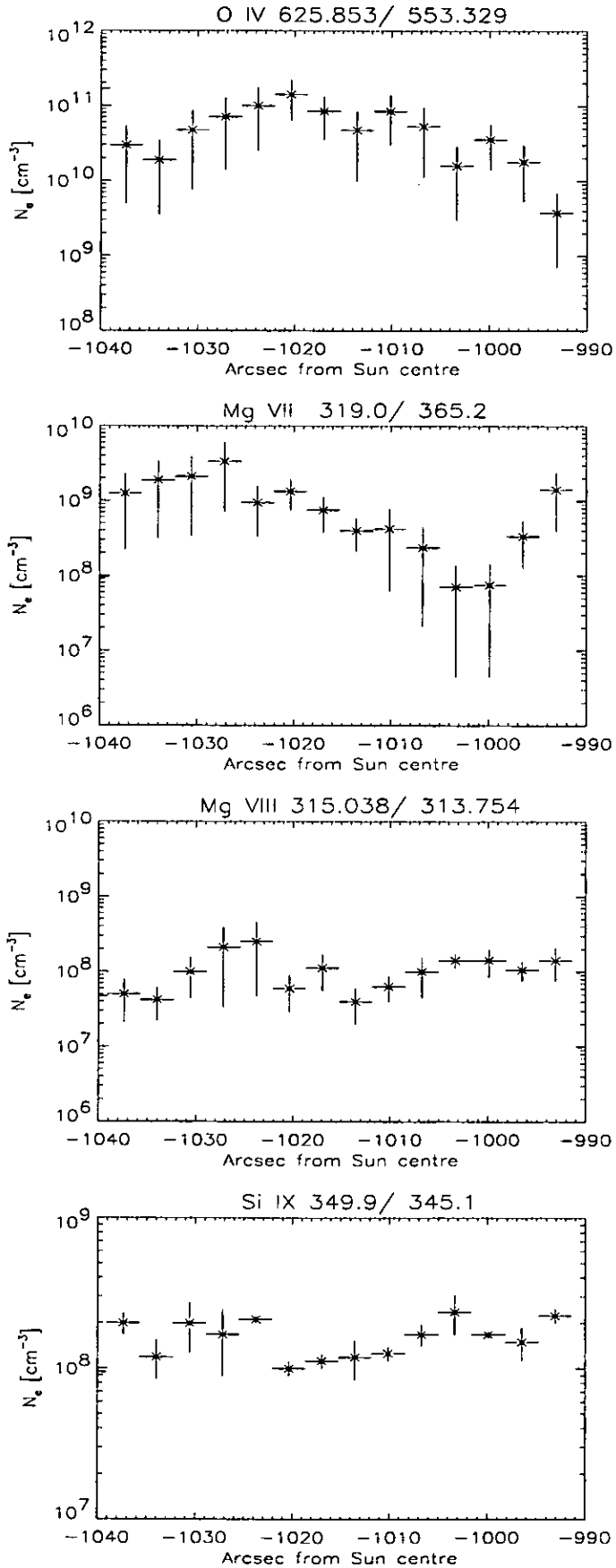

Figure 5.11: Density along the solar distance in the column 4 for the macrospicule data. The error bars represent the probable error.

the same figure using the diamond symbol. Looking at the magnesium ratio, for distances less than -1010″ the background density is higher than that in the macrospicule. Above that, the macrospicule material seems to become more dense. What the silicon ratio shows, instead, is that the densities are similar in the macrospicule and background. This again may be further evidence of the interpretation given above.

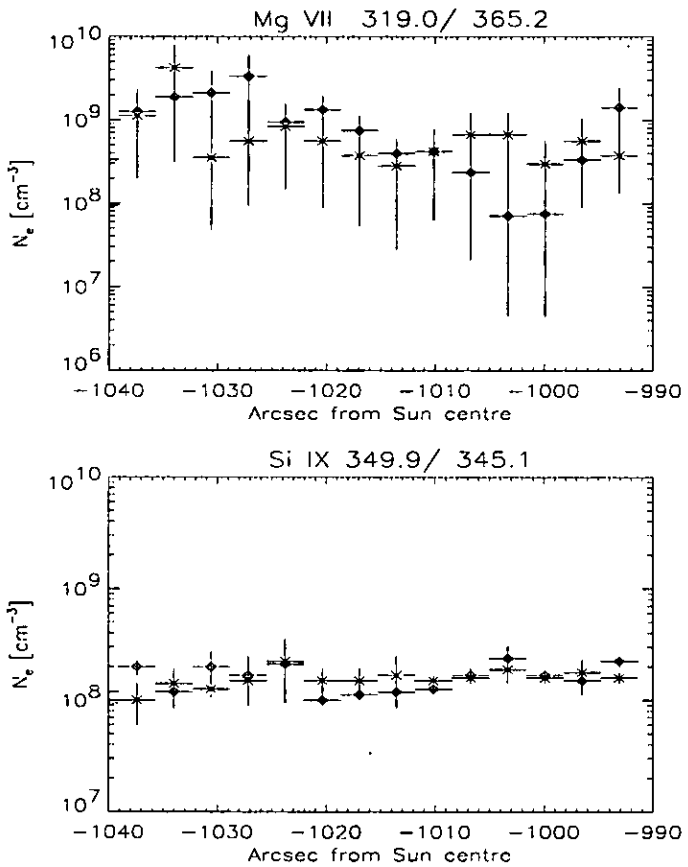

Figure 5.12: Density from Mg VII 319.0/365.2 (top) Si IX (bottom): asterisk represent the observed background; diamond is from the macrospicule.

5.6.2 Temperature

A comparison between the temperature behaviour of cool and hot plasma can be seen in Figure 5.13. Here the temperature profile derived from O V 629.7/ O IV 554.5 Å, Ne VI 562.803 / Ne V 572.33 Å and Mg X 624.9 / Mg IX 368 Å ratios are shown. Each plot shows the values derived from the observation of the background (asterisk) and the macrospicule (diamond). In coronal holes, lines like oxygen and neon become faint not far from the limb, so that here the temperatures have been derived only for distances up to -1040″. The results show a small change with the distance for both the macrospicule

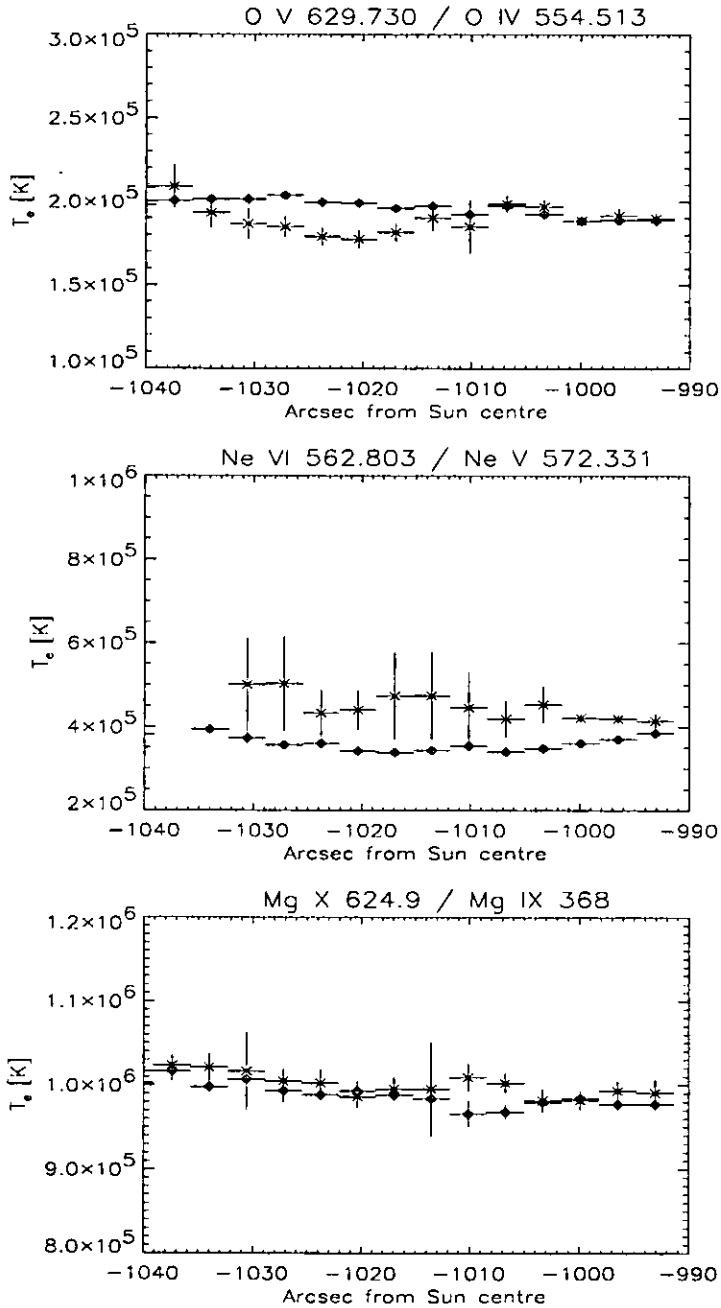

Figure 5.13: Temperature derived from: the O V/ IV (554.5); Ne VI 562.803 / Ne V 572.331; Mg X 624.9 / Mg IX 368; for the background (asterisk) and the exposure with the macrospicule (diamond).

and the background. Clearly the plasma is not isothermal, because different ratios gives different temperatures. Moreover, the Mg ratio indicates that there is no change in the temperature between the background and the macrospicule. On the other hand, visible fluctuations are visible in the background temperature from the O and Ne ratios, while the macrospicule seems to assume more stable values. In particular, the macrospicule oxygen temperature is higher than that of the background above -1010″. The temperature from the Ne shows, instead, to be always lower in the macrospicule than in the background.

This temperature behaviour is consistent with the presence of the cold cloud at about -1010″, as will be discussed in the next section.

5.7 Discussion

The observed feature discussed in this paper has been classified as a macrospicule. The cool line visible in our spectra, the He I (logT=4.5), showed it as a very bright feature, confirming that chromospheric material was ejected in the corona. The upper limit in temperature of the emitting macrospicule plasma was not easy to recognize. Clearly visible in transition region lines, the feature tended to disappear for temperatures above log T = 5.8. However, a faint signature of the feature was present in the Mg IX 368.070 Å (log T = 6, blended with a Mg VII log T = 5.8) and seemed to become brighter in the Mg X lines (log T = 6). The Mg X 624.941 Å line is blended with 0 IV 625.853, so it cannot be excluded that the visibility of the feature at this wavelength is due to the cool oxygen line. The O IV 608.397 Å is, instead, far enough from the Mg X 609.793 Å and can be deblended. On the other hand, the intensity profiles of the fitted Mg lines derived for column 4 do not show the same evolution as the O V, with a peak in intensity far away from the limb. It is therefore difficult to establish if there is any contribution from the macrospicule at coronal temperatures.

The intensity profile was also checked for other lines emitted over a logarithmic temperature interval of about 5.9-6.1 (Fe X 345.7 Å, Ca X 557.5 Å, Si VIII 319.5 Å, Fe XII 364.5 Å). No indication of the macrospicule was visible.

In the literature this issue is still open. Pike & Harrison (1997) and Banerjee et al. (2000), for example, claimed that their macrospicules were visible in the million degree temperature Mg IX line, while Wilhelm (2000) did not find any signature in the Mg X 624.41 Å. Withbroe et al. (1976) saw a depletion in the same Mg X line, attributing this effect to the absorption of Lyman continuum at that wavelength. They found that the maximum absorption was located 20″ from the limb. That corresponds approximatelly to

the starting point of the observations presented here. The absorption at the Mg X line could be the explanation for the non-visibility of the feature at that wavelength. Because the present data did not include points closer to the limb, it was not possible to check fully for this property, even if there is no signature of absorption in the available data.

In this work there are no significant indications in favour of hot material emitted by the macrospicule. The density and temperature results derived from different coronal line ratios in the macrospicule, showed that here there is no difference from the background values. The density values from the coronal Si IX line ratio are, moreover, in good agreement with the values derived by Fludra et al. (1999a) above the quiet coronal hole. Another factor that may explain the enhancement in the Mg X intensities is an enhancement in the element abundance (Section 3.11). If this were the case, all the visible Mg lines should show the same behaviour. However, this was shown not to be the case.

Density and temperature derived from ratios of lines emitted over transition region temperatures, instead, have fluctuations that resemble the presence of a feature already observed in the line intensities. Moreover, they are consistent with values derived from observations of macrospicules in radio wavelength (Habbal & Gonzalez, 1991), and in white light Hα (Loucif, 1994).

The data from column 4 led to the interpretation that a cloud of cooler and denser material was expelled in the macrospicule. Comparing the peak of intensity in the O V and the density derived from the same element, the maximum distance reached by the core of the cloud can be assumed to be 1020″ (46″ from the limb, or 33019 km). This is an encouraging result, considering that previous studies found expelled material reaching a maximum distance of 39,000 km (Karovska & Habbal, 1994) and 33,000 Withbroe et al. (1976). However, lower values for the maximum altitude reached by these plasmoids were also recorded in H_α and H-Lyman lines (Delannee et al., 1998; Georgakilas et al., 1999). The authors justify these as a probable consequence of the hydrogen ionization that occurs as soon the chromospheric material is ejected into the hotter corona.

The outflow velocity estimated here does not appear to be as large as found for other short time-scale events like jets and turbulent events (i.e. Brueckner & Bartoe (1983); Wilhelm et al. (1998a); Ryutova & Tarbell (2000)). The expansion velocities are comparable to the outflow velocity derived in the interplume regions (from O VI 1032/1037 ratio) of 67 km s^{-1} over the same distance by Patsourakos & Vial (2000), even thought Wilhelm et al. (1998b) found a slightly lower velocity of about 40 km s^{-1} at 1.1 $R_\odot$ from Si VIII line widths in the interplume region. Our results from the study of the background, confirms that the macrospicule is not located in a plume environment where, instead, no measurable

velocity was detected (Wilhelm et al., 1998b). If the macrospicule and surrounding plasma have comparable velocities, as the plasmoid moves in the corona, not much compression of the plasma would be expected on the expansion front (about -1030″ in our case), although some variation in density and temperature is reported here.

Transverse velocity components are not easily recognizable in these data. The maximum shift registered was about 17 km s^{-1} toward red, while no blue shift components were noted. The source of these small shifts was not easy recognizable and could have a possible instrumental contribution. Even if real, they tend to be a minor effect compared to previous studies. The maximum velocity previously deduced from doppler-shift EUV data, appeared to be located between 20″ and 30″ (Pike & Harrison, 1997) and 30″-43″ from the limb (Wilhelm, 2000) with values higher than 100 km s^{-1}. These distances fall at or outside the lower limit covered by our data (where 30″ above the limb is at about -1004″). On the other hand, Pike & Mason (1998) derived much lower values of a few tens of km s^{-1} at 40″-50″ from the limb. So this may mean that as the material reaches certain distances it merges with the rest of the coronal plasma and/or is ioised, also loosing velocity.

Studying the cloud trajectory, and applying a constant deceleration approximation, a value for the deceleration was found that is less than expected from the solar gravity. Previous studies attributed this to an inclination of the trajectory with respect to the line of sight (Karovska & Habbal, 1994; Suematsu et al., 1995). These studies refer to spicule and macrospicules, and the characteristic inclination found ranges from 61° to 74° with respect to the radial direction. The value found in the present study is included in that range. However, if this was the case, a line shift effect on the lines would be expected, because the lines shift when there are line-of-sight velocities. The line-shift study presented here, however, does not support this theory, because only velocities of the order of 17 km s^{-1} were found. Moreover, the data indicated that the deceleration was not constant. In particular, close to the limb it assumed a value close to the solar gravity, while at a larger distance it became almost zero. In conclusion, what seems more probable is that the feature was extending from the limb in an almost radial direction. Once the plasmoid was expelled, it changes its acceleration by merging with the surrounding ambient flow. However, note that here only an estimate of velocity and density are given. The method used to determine the cloud position in each exposure could have affected the results.

The important unresolved questions concern the mechanisms that generate these features and where they take place in chromosphere. Wilhelm (2000) discussed the origin of spicules and macrospicules and, as other authors, indicated explosive events or a sub-

class of them (Wang, 1998), due to reconnection in the chromospheric network boundary, as possible initial stage for these features. In support of this, (Karovska et al., 1994), using the image enhancement algorithm on Skylab images, resolved the fine structure at a macrospicule's base. They found a continuous interaction between these filamentary spicule-like substructure that evolved through reconnections. Unfortunately the present data lack any limb information and the macrospicula's base could not be studied.

In conclusion, the signature of chromospheric material expelled from a coronal hole was found in intensity, density and temperature from chromospheric lines. These properties lead to the classification of this event as a macrospicule. The data used here gave the unique opportunity to separate the emission of the feature from that of its background. This revealed the presence of a cool cloud released in the macrospicule, before its disappearance. The time evolution and outflow velocity of this cloud were studied, and the results showed that this short-lived feature expands into the corona with outflow velocity of the same order as that of the interplume regions.

The absence of the macrospicule base in the data limited the information that was possible to collect. Further work needs to be done to provide this information. Moreover, the understanding of the expulsion mechanism reported here and the frequency of its occurrence in the macrospicule events needs further investigation.

Chapter 6

CDS Observations of a Loop System and of a Coronal Hole Boundary Region

This chapter describes an analysis of CDS observations of two additional coronal structures: (*i*) a loop system and (*ii*) a coronal hole boundary region.

In the first section a detailed analysis is presented for a loop system which was observed off-limb with CDS/NIS on 8 March 1998 (previously described only briefly in Section 4.2.3 and Figure 4.1 bottom). The aim was to study the different parts of the structure in order to characterise their physical parameters (densities, temperatures and element abundances). The analysis mainly involves DEM evaluation.

The following section then describes the study of a coronal hole boundary region, observed off-limb on 7 March 1998. In these off-limb data, the NIS FOV clearly shows the boundary between the coronal hole and the streamer (Figure 6.10). A diagnostic study was again applied to the data, in order to characterise these boundary areas.

6.1 The Loop System

6.1.1 The Data

Referring to Figure 4.1 (bottom), the south-west part of the solar limb on 8 March 1998 is occupied by a loop system. This loop is clearly visible in many bright high-temperature coronal lines. The CDS data consisted of two successive observations of the same region taken with the UCLAN_N2 CDS study already described in Chapter 4. The data have then been processed following the standard procedures described in Section 2.3.1. Figure

6.1 shows the area covered by the first raster as it appears on monochromatic images in lines emitted by different stages of ionization of iron. The temperature of the maximum ionization fraction for each ion is indicated in the Figure, ordered from top to bottom. Clearly, the Figure shows the presence of plasma at different temperatures. Each image shows a different part of the loop, with the hottest region at the top of the loop.

Figure 6.2 shows the same area observed with the second raster. Some changes in the loop structure evidently occurred in the time between the various slit exposures. The purpose of this study was the analysis of the general characteristics of the loop and its surroundings. In fact, the spatial resolution of these data does not allow isolation of any fine structures of the loop system. Initially it was intended to average the two rasters in order to improve the S/N, but this plan was later abandoned. In fact, due to the changes in the loop configuration over time, such an average would have smoothed the spectra and it would have been more difficult to distinguish between the plasma loop and its surroundings. The first raster was chosen for the subsequent diagnostic analysis, because it appeared to have a more compact loop region towards the centre of the raster, clearly distinguishable from the surrounding material.

Two areas of the raster were selected (Figure 6.3): one at the *loop top*, where the loop is brighter in the highest-temperature lines; and one closer to the limb (hereafter named *loop base*) where the plasma appears to be cooler, as shown in Figure 6.1. The spectra have been spatially averaged over these two areas in turn, to obtain a higher signal/noise. The averaged spectra have then been analysed following the standard procedures described in Section 2.3.1. In particular, line positions and intensities were obtained for all the lines in the spectra, with multiple Gaussian fitting.

These spectra are unusual in that they were emitted by high temperature plasma, with negligible contribution from the cooler lines. Moreover, the scattered light background, which is usually present in NIS on-disc spectra, was almost absent. This has enabled the identification of lines that are not normally clearly visible. Many of these lines have been identified in CDS spectra for the first time here, as described in the next section.

6.1.2 Results

Line Identifications

Figures 6.4 and 6.5 show the parts of the NIS 1 and NIS 2 spatially-averaged spectra where the newly identified lines are. They have been indicated by an arrow. The spectra for the base of the loop system (bottom of both figures) show much higher intensities because that

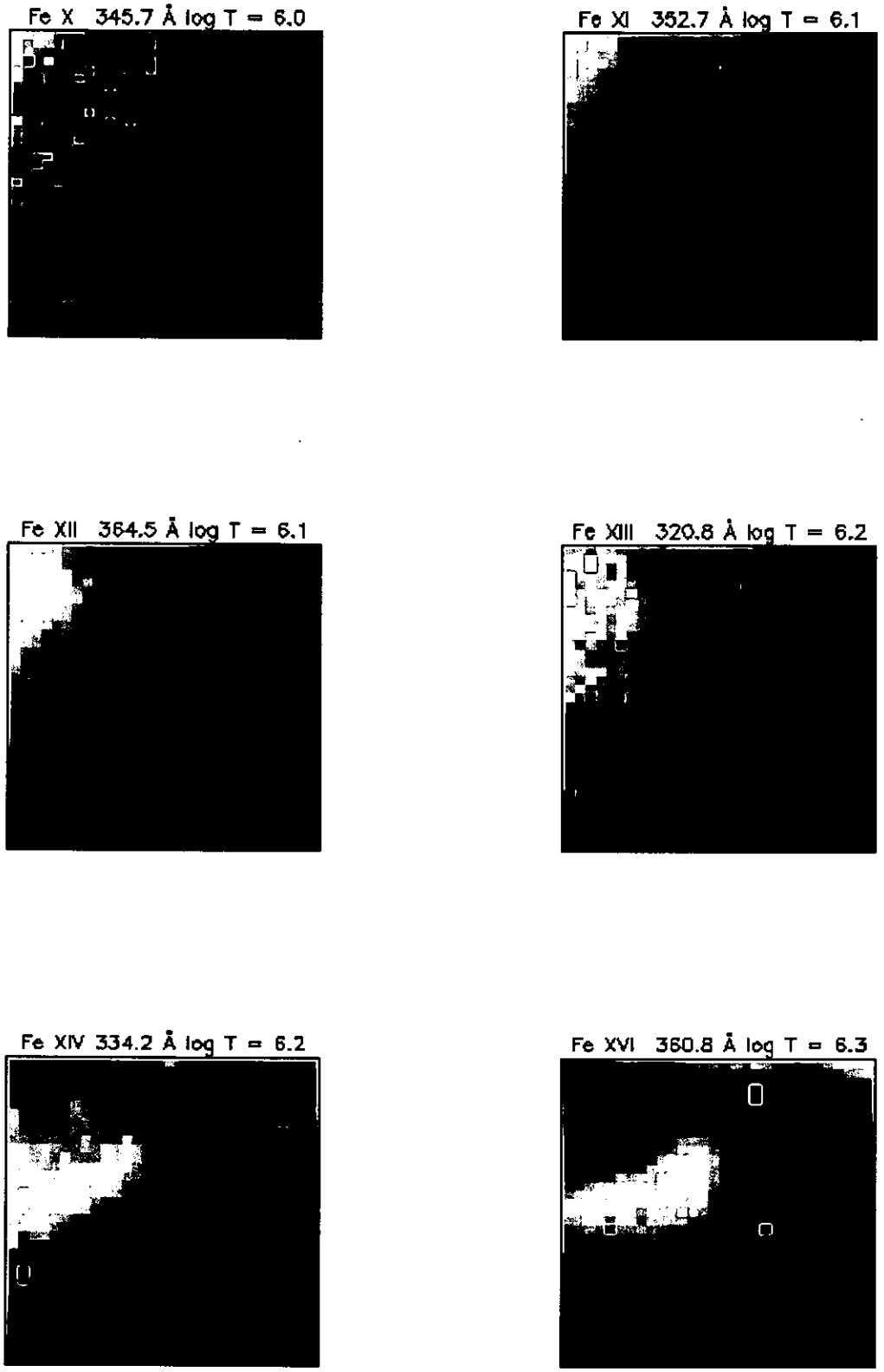

Figure 6.1: Monochromatic images of the first raster showing the loop system. The temperature of the emitting plasma increases with the stage of iron ionization.

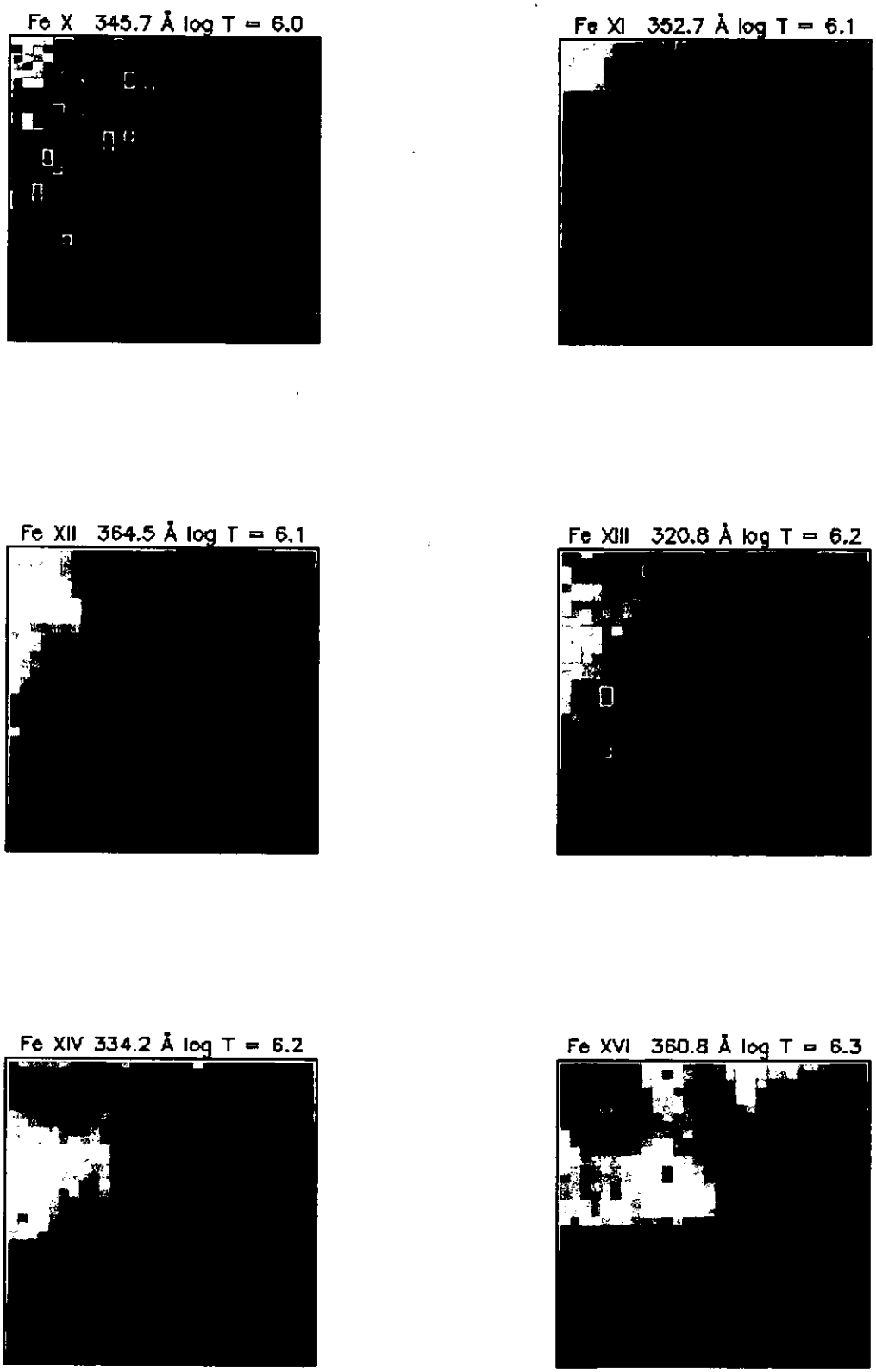

Figure 6.2: Monochromatic images of the second raster showing the loop system. The chosen lines are the same of the previous Figure.

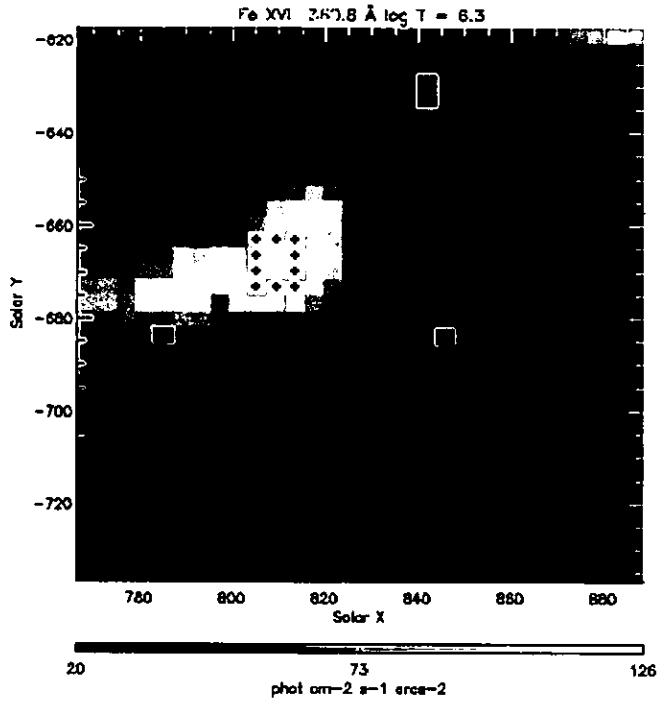

Figure 6.3: Areas of the raster selected for analysing the top and the base of the loop.

area was much closer to the limb. However, a few faint lines appear in the loop spectra that are not visible in the cooler spectra closer to the limb.

For line identifications in CDS/NIS spectra, the most complete references are Brooks et al. (1999) and Del Zanna (1999). The Brooks et al. (1999) atlas identifies most of the lines present in NIS spectra, but the cataloguing used quiet Sun data and so is not suitable for the present data. The more extensive compilations presented by Del Zanna (1999) included other line identifications, but no active region off-limb spectra were presented. Other useful references for line identifications in the NIS waveband are the papers based on the SERTS-89 active region observation. The SERTS spectra are particularly useful for line identification because of their higher spectral resolution. For example, Thomas & Neupert (1994) present a detailed line list that also includes high-temperature lines. Young et al. (1998) slightly revised the instrument calibration and some line identifications, and made detailed comparisons with the CHIANTI database.

However, further analysis was necessary here in order to identify those lines visible in the spectra of Figures 6.4 and 6.5, which were not previously catalogued. The CHIANTI database was used for this purpose. The first step involved looking for theoretical lines that the database predicts to be visible at the observed wavelengths. Given the CDS

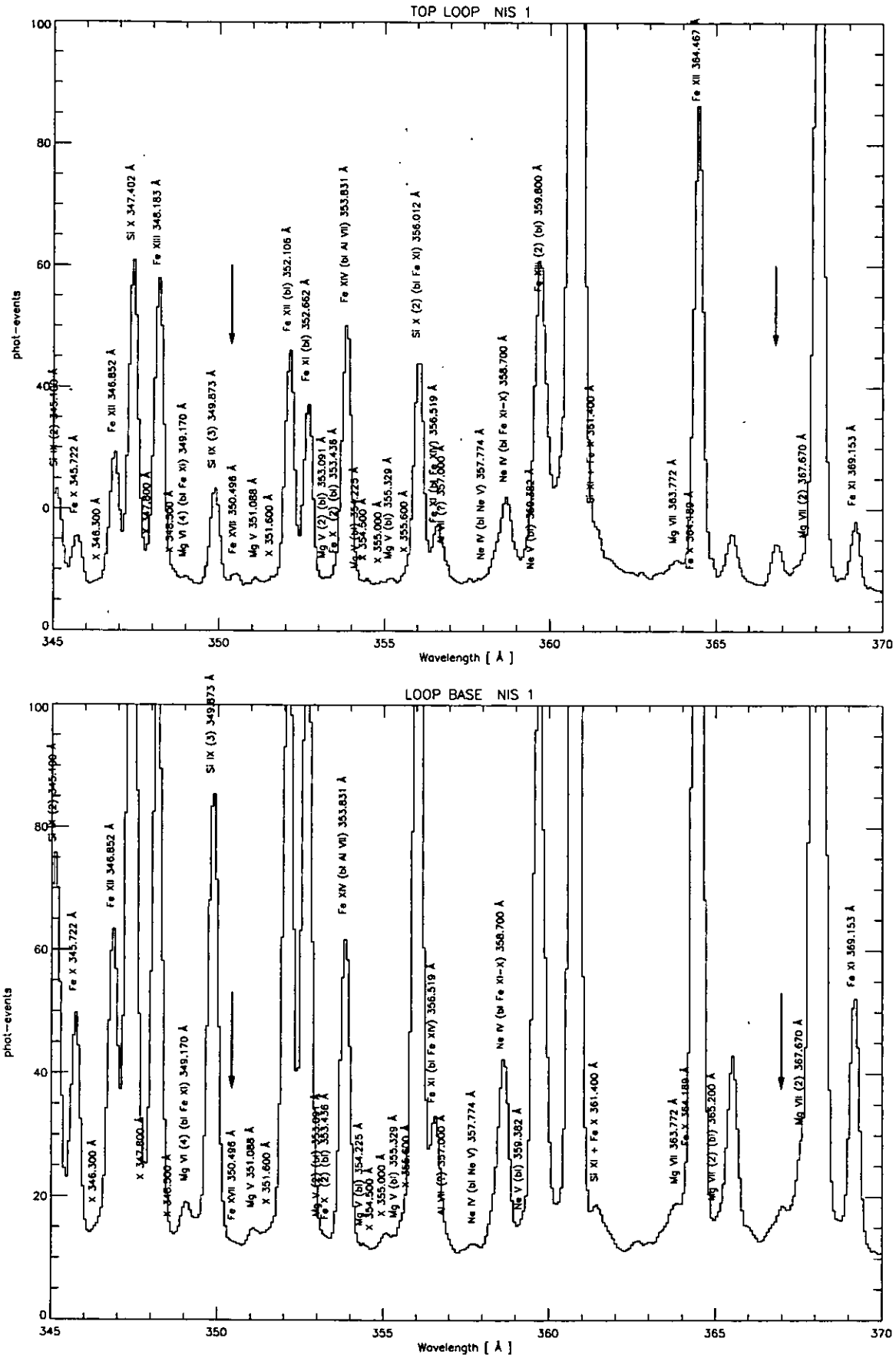

Figure 6.4: Average NIS 1 spectra for the loop top area (top) and the loop base (bottom). The new identified lines are indicated by an arrow.

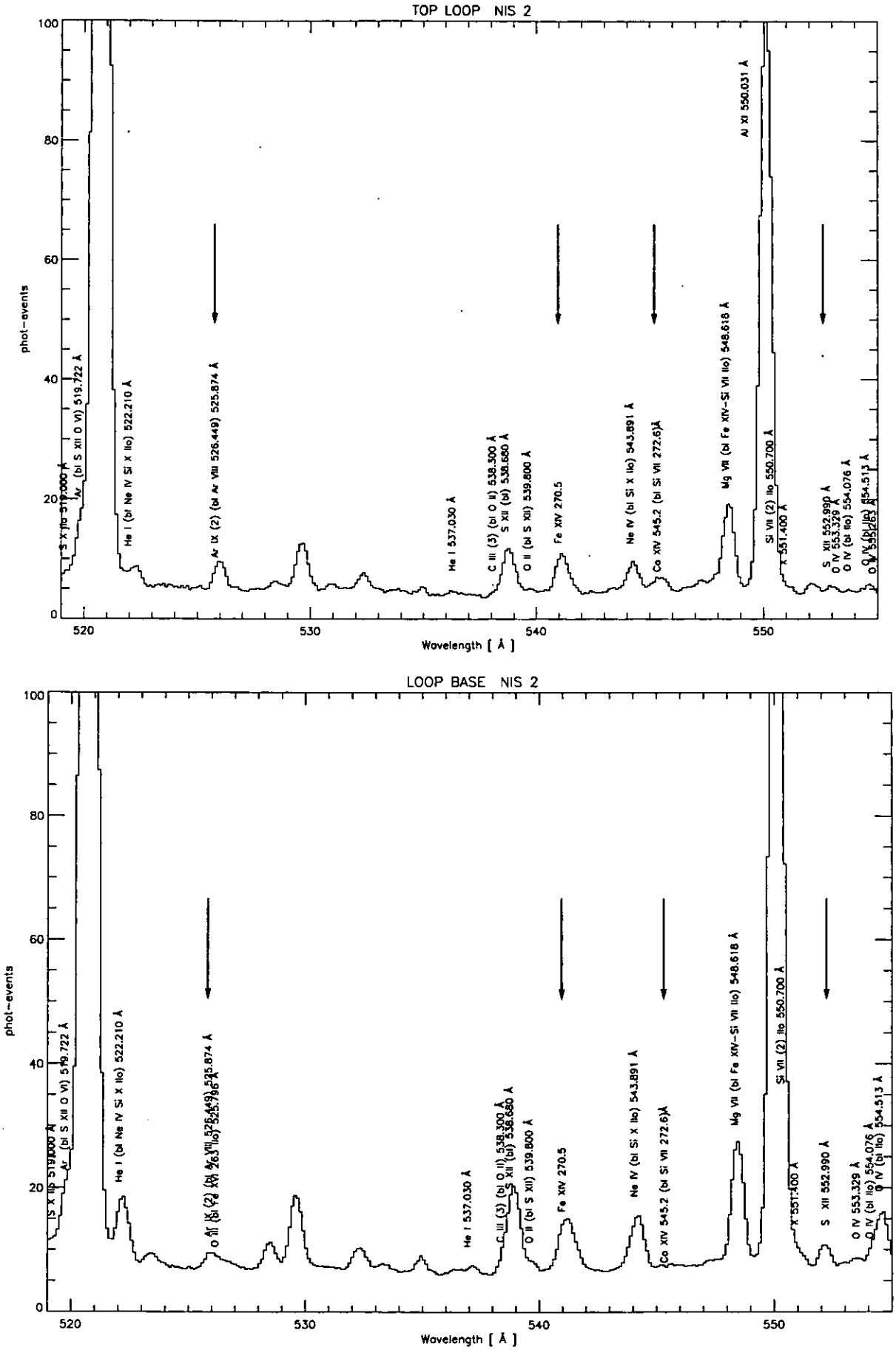

Figure 6.5: Average NIS 2 spectra for the loop top area (top) and the loop base (bottom). The new identified lines are indicated by an arrow.

spectral resolution, this implies the presence of more than one theoretical line for each observed line. The identification is made by selecting the lines with greater emission, given the physical conditions of the observed plasma (density and temperature). For example, Figure 6.6 shows the contribution functions (see Section 3.1.2) for the candidate lines to the observed line at 350.5 Å. From the figure, Na VII 350.645 Å and Fe XVII 350.496 Å appear to be two possible identifications. These two lines have peak emissivities at very different temperatures but of similar strength. A further selection can then be made by taking into account the plasma conditions: this observation was taken off-limb where any contribution from cool plasma is negligible, as verified by the spectra. Moreover, the presence of very bright high-temperature lines such as those emitted by Si XII and Fe XVI immediately suggests the presence of plasma at a temperature more than a million degrees. Therefore, Fe XVII seems to be the better candidate for the observed line. However, if we suppose that the plasma is isothermal at $\log T \approx 6.2$, then from the figure we could conclude that both lines equally contribute to the observed intensity. This example clearly shows that a definite line identification can only be obtained with a full DEM study. Moreover, possible second order lines in NIS 2 had to be considered.

Following the procedure used to identify the line 350.5 Å described above, the new lines listed in Table 6.1 have been identified.

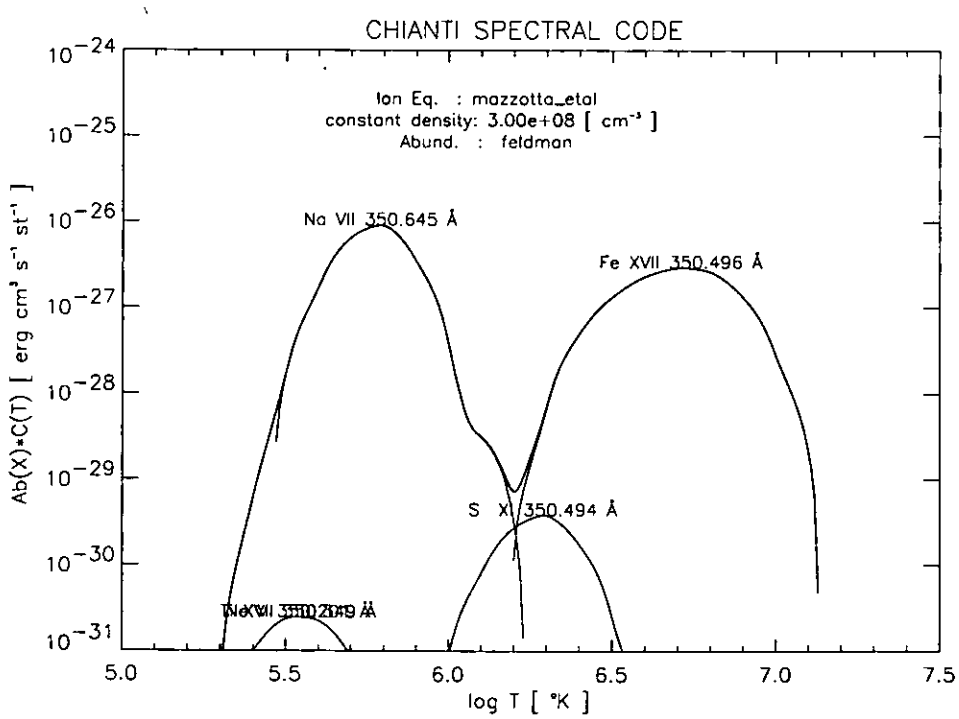

Figure 6.6: Contribution functions vs. temperature for the theoretical lines close to the line observed at 350.5 Å.

Table 6.1: List of newly identified lines (not previously identified in CDS spectra) visible in the data from the loop system . The first column gives the observed wavelength; the second column gives the identification; the third column gives the transition; the fourth column gives the logarithmic temperature for the emission peak.

Observed λ	Identification	Transition	log T
350.5	Fe XVII 350.496	$2p^5\ 3s\ ^3P_2$ - $2p^5 3p\ ^3D_3$	6.71
	Na VII 350.645	$2p\ ^2P_{1/2}$ - $2s\ 2p^2\ ^2P_{3/2}$	5.79
366.8	Fe X 366.589	$3s^2\ 3p^4(3P)\ 3d\ ^4F_{5/2}$ - $3s\ 3p^5(3P^*)\ 3d\ ^4F$	5.99
	Ni XVII 366.797	$3s^2\ ^1S_0$ - $3s\ 3p\ ^3P_1$	6.44
525.9	Ar IX (2 lines)	$2p^5\ 3p\ ^3D_3$ - $2p^5\ 3d\ ^3F_4$	6.07
	Ar VIII 526.449	$3p\ ^2P_{1/2}$ - $3d\ ^2D_{5/2}$	5.61
541.1	Fe XIV 270.507	$3s^2\ 3p\ ^2P_{3/2}$ - $3s\ 3p^2\ ^2P_{1/2}$	6.28
545.5	Ca XIV 545.213	$^4S_{3/2}$ - $^2P_{3/2}$	6.5
	Si VII 272.638	$2p^4\ ^3P_2$ - $2s\ 2p^5\ ^3P_1$	5.79
552.7	S XII 552.990	$2s^2\ 2p\ ^2P_{3/2}$ - $2s\ 2p^2\ ^4P_{1/2}$	6.32

Temperature and Density Diagnostics

Due to the hot environment of coronal loops, the electron density could be estimated by applying the line ratio technique not only to lines that are emitted at coronal temperatures (Si IX, Si X), but also to lines emitted by hotter plasma (Fe XIII and Fe XIV). The results are shown in Table 6.2.

The table shows that the densities derived from the ratios of cooler lines are lower than those derived from the high temperature ratios. Similar behaviour was found in a study of limb active regions by Mason et al. (1999).

Assuming that the emission of the hot lines, such as Fe XIV, comes almost completely from the loop, it appears that the loop is much denser than the ambient corona. However, the results from the iron line ratio for the loop base and for the top are not consistent. The Fe XIII ratios imply the loop top is denser than the base, while the opposite is obtained from Fe XIV lines.

Table 6.3 shows the electron temperatures derived using the line ratio technique. A range of lines that are emitted in the interval $5.98 < logT < 6.41$ has been chosen. The table shows that the plasma was not strictly isothermal, either at low or higher distances from the limb. In fact, different line ratios indicate different temperatures. In particular, line ratios derived using higher ionization stages indicate higher temperatures. This example clearly shows the importance of deriving a DEM distribution, since no single temperature can be defined in this case. Such a DEM analysis will be presented in the

Table 6.2: Electron densities derived from the line ratio technique. The columns indicate: (1) the ratio used; (2) the maximum temperature of emission; (3) the density values at the base of the loop area; (4) the density values at the top of the loop. The Mazzotta et al. (1998) ionization equilibrium balance was used.

Ratio	T_{max} (10^6 K)	N_e Loop Base (10^8 cm^{-3})	N_e Loop Top (10^8 cm^{-3})
Si IX 349.9/341.9	1.26	3.8 (-0.2; +0.2)	2.4 (-0.4; +0.3)
Si X 356./347.4	1.38	6.0 (-0.3; +0.3)	4.7 (-0.5; +0.3)
Fe XIII 320.809/348.183	1.58	9.6 (-0.2; +0.4)	13.0 (-0.6; +0.9)
Fe XIII 320.809/321.400	1.58	9.4 (-1.0; +0.6)	11.2 (-0.6; +1.4)
Fe XIV 353.831/334.172	1.81	20.0 (-0.5; +0.5)	16.0 (-1.1; +1.1)

next section.

The table also shows that the loop top has higher temperatures than the loop base. In particular, the difference in temperatures found at the loop base and at the loop top, derived from the lines at higher stage of ionization, is higher. This may be an indication that the line of sight of these latter lines is mainly limited to the loop.

The results from measurements of the background corona, over the hight considered here, generally give a temperature of about 1 MK. This is close to the values found from the Fe XI/Fe X ratio. This means that the contributions to these observed lines arise also from the foreground/background plasma in front or behind the loop system. The Mg ratio shows about the same variation, from the loop top to the loop base,as Fe XVI/XIV ($\approx$ 11%) and this may be due to using the Mg X line. This is a Li-like line and its contribution function is very extended at higher temperatures. In a plasma which is not strictly isothermal such as the one observed here, such a line has significant contributions from a wide range of temperatures, so that it is more sensitive when the temperature changes.

The temperatures derived from the highest stages of ionization of iron (Fe XVI/ Fe XIV and Fe XIV/ Fe XIII), are in agreement, and give a maximum temperature at the loop top of 2.33 10^6 K. It is interesting to compare these results with the temperature profile already shown in Chapter 4 (see Figure 4.5 bottom). In the latter case the profile was obtained by averaging the spectra from areas obtained by radial slices covering all the raster (for further details in 4.5.1). Even so, that profile shows clearly that the environment is not isothermal, from its base to the upper height covered by the observations.

Table 6.3: Electron temperature derived applying the line ratio technique for different ratios. The Mazzotta et al. (1998) ionization equilibrium was used.

Ratio	Loop Base T_e (10^6 K)	Top Loop T_e (10^6 K)
Mg X 609.793 / Mg IX 368	1.24 (-0.01; +0.01)	1.38 (-0.01; +0.01)
Fe XI 352.662 /Fe X 345.723	1.25 (-0.01; +0.01)	1.30 (-0.03; +0.03)
Fe XII 364.467/Fe XI 352	1.29 (-0.01; +0.01)	1.40 (-0.02; +0.02)
Fe XIII 348.183/ Fe XII 364.467	1.25 (-0.01; +0.01)	2.33 (-0.03; +0.03)
Fe XIV 334.172/ Fe XIII 348.183	1.94 (-0.01; +0.01)	2.33 (-0.03; +0.03)
Fe XVI 360.761/Fe XIV 334.172	2.00 (-0.01; +0.01)	2.29 (-0.01; +0.01)

The Differential Emission Measure and Element Abundances

The DEM technique (Section 3.2) was applied to these data in order to derive the relative element abundances and the temperature distribution. The analysis was done for two cases: (1) using the Arnaud & Raymond (1992) ionization equilibrium balances and the Feldman et al. (1992) coronal element abundances; (2) using the Mazzotta et al. (1998) ionization equilibrium and the photospheric abundances of Feldman (1992). The two results will be compared.

Figure 6.7 shows the DEMs of the loop top for the two cases (case 1:top; case 2:bottom). The relative element abundances were derived with respect to iron, following the technique described in Section 3.2. The abundance results for case 2 are shown in Table 6.4.

Referring to Figure 6.7, the two cases show very similar DEM distributions, with significant emission measure in of the off-limb plasma above a million degrees. Some of the differences are attributable to the use of different abundances. In particular, the DEM values are shifted because of the use of different absolute abundances, and because most of the lines are from low-FIP elements. This clearly shows the importance of knowing the absolute element abundances. In both cases the DEM shows a double peak with the two cases showing peaks at the same temperatures. The first peak is centred around log T=6.1, and corresponds to the standard temperature of the coronal background emission; the second peak is around log T=6.4, and is due to the emission of the loop system. The high emission measure of the second peak is expected, given the presence of hot lines like Fe XVII, which are usually not visible in off-limb spectra such as the equatorial streamer ones described in Chapter 4. Moreover, it is interesting to note that the amplitude of the second peak is higher than the first. The DEM of the second case (bottom figure) can be

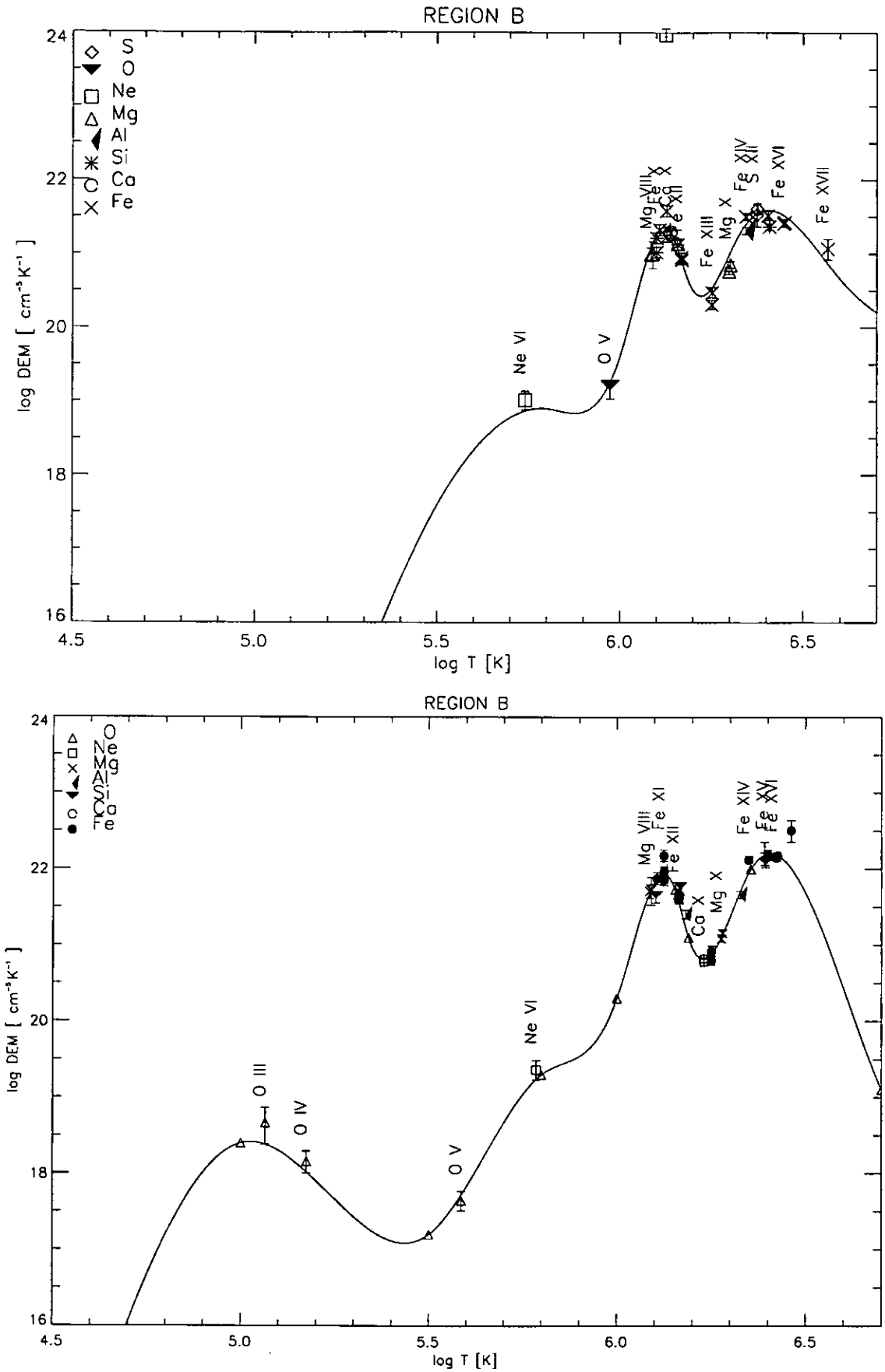

Figure 6.7: Differential Emission Measure vs. temperature for the top of the loop system. The ionization equilibrium used is top: Arnaud & Raymond (1992); bottom:Mazzotta et al. (1998). The temperature (T) are *effective* temperature (Section 4.5.3 and Equation 4.2).

compared with the one derived from the same raster but from a different area external to the loop system (see Section 4.2.2 and Figure 4.10 bottom), since they were both derived with the same ionization equilibrium and element abundances. The area external to the loop system chosen as representative of the quiet streamer (Chapter 4) was located at larger distances from the limb, compared with the loop top analysed here. Regarding the second peak, it can seen that the emission measures for the data in Chapter 4 are lower, to confirm that the higher temperature plasma is mainly confined in the loop. Moreover, the loop top shows higher temperatures than the "quiet streamer", as would be expected.

Regarding the first peak, centred at 1.26 10^6 K (Log T=6.1), we can see that in the "quiet streamer" case (Figure 4.10 bottom) the peak is shifted toward higher temperatures. This is as expected, since the emission measures of the first peak are associated with the diffuse background coronal emission, which increases in temperature with height. As already mentioned (Section 4.6), in the "quiet streamer" case even if the data refer to an area external to the loop system, the presence of hot plasma is still significant.

Table 6.5 lists the results from the DEM analysis of the loop top area, using the Mazzotta et al. (1998) ionization equilibrium. The ten columns, list, from left to right: the ion (or ions if a blend is present) used to calculate the DEM; the theoretical wavelengths of the ion, for all the lines that may contribute to the observed line; the observed wavelength of the line; the transition from which the line forms; the observed intensity in $erg\ cm^{-2}\ s^{-1}\ sr^{-1}$; the ratio of the theoretical flux to observed flux; the error estimated, given by a combination of the observed error and a assumed 10% error on the calculated values; the effective temperature, defined in Section 4.2; the temperature of the maximum of the contribution function; and finally, for a blended line, the percentage contributions to the total observed flux. Only the most significant blends are listed.

The newly identified lines are listed in Table 6.1. The S XII line is well reproduced by its theoretical line intensity, but this is not true for the Fe XVII line. The other lines (except Fe XIV which is a second order line) were first included in the DEM calculation, but were subsequently discarded, because their theoretical values included non-negligible contributions from blends and, as has been noticed before (Section 3.2) this may affect the DEM determination. For the Fe XVII line, the DEM derived here seemed to imply that contributions to the observed line from other lines such as Na VII 350.645 Å were unimportant. One possible explanation for the disagreement between its theoretical and observed value could then be an erroneous observed intensity determination. The observed line is very weak (see Figure 6.4) and an erroneous estimate of the background level may have affected the total intensity value. Another explanation could lie in an incorrect

ionization equilibrium using Mazzotta et al. (1998), rather then the Arnaud & Raymond (1992) calculations. In fact, these two cases are quite different, and the Fe XVII line is in good agreement with the other Fe lines if Arnaud & Raymond (1992) equilibrium is used.

Figure 6.8 shows the DEMs for the region at the base of the loop system. In both graphs, the curve follows a path similar to that shown in the previous figure. Being closer to the limb, the diffuse coronal emission (first peak) peaks at temperature lower than in the previous Figure (were the data referred to the top of the loop, placed further out from the limb). Moreover, the relative DEM is about three times higher the value for the loop top. The contribution to the emission measure of high temperature plasma from the loop is still present at the base of the loop, and with the same magnitude, but with its peak at a lower temperature (log$T$=6.3). Results from the DEM analysis using Mazzotta et al. (1998) are shown in Table 6.6. No specific studies of this kind have previously reported for off-limb loops. Sterling et al. (1999) analysed the temperature structure of an active region seen at limb, but did not present a DEM analysis. Most of the other detailed studies found in the literature referred to on-disc active region observations. Brosius et al. (1996) analysed EUV Rocket Telescope and Spectrograph (SERTS) data on active regions and quiet-sun data and gave results for DEM distributions. These authors found a single peak (logT=6.5) for one active region case, and a double peak (log T=6.2,6.7) for another case, together with evidence for multi-thermal plasma. The different behaviour of the two cases was explained by possibly different levels of activity in the two active regions analysed. Two peaks DEM was also found by Monsignori Fossi et al. (1994) in a active region study with SERTS.

Schmelz et al. (1999) also derived the DEM distribution for an active region combining SERTS and YOHKOH observations. The authors found a DEM with a wide peak of emission between log$T$=6 and log$T$=6.5. Their curve also included contributions from low transition region lines, which are absent in the off-limb case presented here.

Mason et al. (1999) derived DEMs of off-limb active regions, but they were very close to the limb. Similarly to Schmelz et al., the DEMs derived show the presence of significant amounts of plasma at $6.1 < logT < 6.7$. Another example of DEM distribution with temperature is found in an active-region CDS study by White et al. (2000). These authors found a double peaked DEM with the higher temperature peak at log T=6.4. The above sets of examples from the literature, taken together, imply that each active region is characterized by its own individual temperature distribution, and this would be also the case for the loops that emerge from it.

It should be remembered that a slight difference in DEM values can arise from the

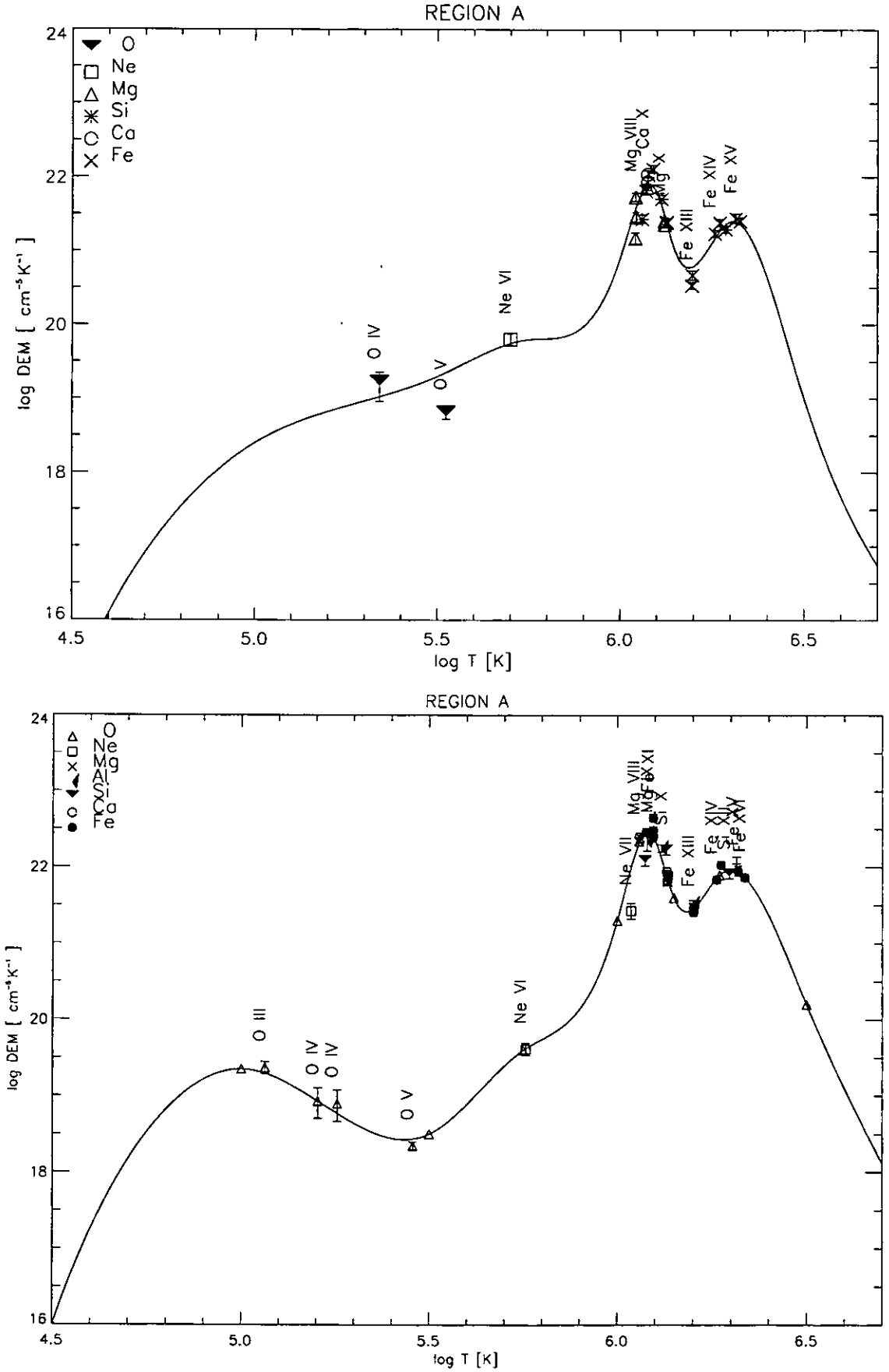

Figure 6.8: Differential Emission Measure vs. temperature for the base of the loop system. Top: the ionization equilibrium used is the Arnaud & Raymond (1992); bottom: the Mazzotta et al. (1998)

use of different abundances, as already shown. The element abundance results from the present study are shown in Table 6.4. The error on the listed values was estimated to be ± 0.03 in logarithmic scale. The Table also lists the abundances derived for the area external to the loop system (already listed in Table 4.11 (there referred as "Midlat Mar").

It can seen from Table 6.4 that differences in elements composition at the three locations are quite small. The O and Ne abundances were not varied from the photospheric values because there were no iron lines to constrain them. This argument has already been discussed in Section 4.5.3. As in that case, oxygen and neon lines have only been used here to constrain the DEM curve at low temperatures. The abundances of the other elements (relative to Fe) were found to be depleted for the loop top. Meyer (1996) pointed out

Table 6.4: The element abundances (values in usual 'dex' notation) found for the base and the top of the loop, and for the area external to the loop system. The abundances of O, Ne and Fe were fixed to the photospheric values of Feldman (1992). The Mazzotta et al. (1998) ionization equilibrium was used.

Region	O	Ne	Mg	Al	Si	S	Ca	Fe
Photosphere	8.93	8.11	7.58	6.46	7.55	7.21	6.36	7.51
Base	8.93	8.11	7.40	6.50	7.50	-	6.40	7.51
Top loop	8.93	8.11	7.35	6.47	7.42	6.9	6.30	7.51
External	8.93	8.11	7.50	6.47	7.50	7.10	6.36	7.51

that different active regions show different FIP biases, by up to a factor of 4. As already mentioned, it was not possible to measure the FIP bias in the present analysis. However, it can be noticed that the Mg/Fe ratio found here for the loop top (0.69) agrees (within the errors) with the value of 0.80 ± 19 found by McKenzie & Feldman (1992) from an active region observation. These values are quite different from the Mg/Fe photospheric value of 1.17.

Despite the small variation in abundances, it can also be noted that the Ca/Mg and Si/Mg values agree with the same ratio found by Widing & Feldman (1993) in Skylab data in diffuse active region plasma. The authors give Si/Mg = 1.06 ± 0.20 and Ca/Mg = 0.068 (Ca VIII) and 0.18 (Ca IX). The present data give the values of 1.26, 1.17, 1 of the Si/Mg for respectively, loop base, top loop and loop external. The same ratio gives 0.93 for photospheric values. The Ca/Mg found for these data are: 0.1, 0.09, 0.07 for the same three regions. The photospheric value for the ratio from the same elements is 0.06.

Table 6.5: Results from the DEM analysis on the top of the loop system. The theoretical lines are calculated using the Mazzotta et al. (1998) ionization equilibrium. For details on what each column lists, see text above.

Ion	λ_t (Å)	λ_o (Å)	Transition	I_o	I_t/I_o	+/-	T_{eff}	T_{max}	%
O III	599.597	599.5	$2s^2\ 2p^2\ ^1D_2$ - $2s2p^3\ ^1D_2$	0.3	0.52	0.23	5.06	5.03	
O IV	554.513	554.6	$2s^2\ 2p\ ^2P_{3/2}$ - $2s\ 2p^2\ ^2P_{3/2}$	0.7	0.73	0.18	5.17	5.23	
O V	629.730	629.9	$2s^2\ ^1S_0$ - $2s\ 2p\ ^1P_1$	0.8	1.20	0.25	5.59	5.38	
Ne VI	562.803	562.8	$2s^2\ 2p\ ^2P_{3/2}$ - $2s\ 2p^2\ ^2D_{5/2}$	0.8	0.75	0.16	5.79	5.62	
Mg VIII	315.039	315.0	$2p\ ^2P_{3/2}$ - $2s\ 2p^2\ ^2P_{3/2}$	19.6	0.95	0.14	6.09	5.91	
Mg VIII	339.006	339.0	$2p\ ^2P_{3/2}$ - $2s\ 2p^2\ ^2S_{1/2}$	4.4	1.01	0.33	6.09	5.91	
Si VIII	316.205	316.2	$2s^22p^3\ ^4S_{3/2}$ - $2s2p^{44}P_{3/2}$	36.6	1.69	0.20	6.10	5.93	
Fe X	345.723	345.7	$3s^23p^5\ ^2P_{3/2}$ - $3s\ 3p^6\ ^2S_{1/2}$	29.9	0.99	0.13	6.11	5.98	
Fe XI	341.113	341.1	$3s^2\ 3p^4\ ^3P_2$ - $3s\ 3p^5\ ^3P_1$	35.5	0.57	0.07	6.12	6.06	
Fe XI	369.153	369.2	$3s^2\ 3p^4\ ^3P_1$ - $3s\ 3p^5\ ^3P_2$	20.7	1.20	0.14	6.13	6.06	
Fe XI	352.662	352.7	$3s^2\ 3p^4\ ^3P_2$ - $3s\ 3p^5\ ^3P_2$	89.3	0.93	0.10	6.13	6.06	
Fe XII	352.106	352.1	$3s^2\ 3p^3\ ^4S_{3/2}$ - $3s\ 3p^4\ ^4P_{3/2}$	116.7	0.97	0.10	6.16	6.14	
Fe XII	346.852	346.8	$3s^23p^3\ ^4S_{3/2}$ - $3s\ 3p^{44}P_{1/2}$	72.1	0.81	0.09	6.16	6.14	
Fe XII	364.467	364.5	$3s^2\ 3p^3\ ^4S_{3/2}$ - $3s\ 3p^4\ ^4P_{5/2}$	199.0	0.84	0.09	6.17	6.14	
Mg IX	368.070	368.1	$2s^2\ ^1S_0$ - $2s\ 2p\ ^1P_1$	294.7	0.89	0.09	6.17	5.98	0.85
Fe XIII	368.2		$3s^2\ 3p^2\ ^3P_2$ - $3s\ 3p^3\ ^3D_3$					6.20	0.13
Si X	621.079	621.0	$2p\ ^2P_{1/2}$ - $2s\ 2p^2\ ^4P_{1/2}$	2.4	0.58	0.07	6.17	6.13	
Al X	332.789	332.8	$2s^2\ ^1S_0$ - $2s\ 2p\ ^1P_1$	110.4	0.68	0.07	6.18	6.10	
Ca X	574.010	574.0	$3s\ ^2S_{1/2}$ - $3p\ ^2P_{1/2}$	8.1	1.08	0.11	6.23	5.86	
Ca X	557.765	557.8	$3s\ ^2S_{1/2}$ - $3p\ ^2P_{3/2}$	18.0	0.98	0.10	6.23	5.86	
Fe XIII	348.183	348.2	$3s^2\ 3p2\ ^3P_0$ - $3s\ 3p^3\ ^3D_1$	146.1	1.20	0.13	6.25	6.20	
Fe XIII	321.400	321.5	$3s^2\ 3p^2\ ^3P_2$ - $3s\ 3p^3\ ^3P_1$	43.9	0.91	0.11	6.25	6.20	
Mg X	624.941	624.9	$2s\ ^2S_{1/2}$ - $2p\ ^2P_{1/2}$	146.8	1.05	0.10	6.28	6.05	
Mg X	609.793	609.8	$2s\ ^2S_{1/2}$ - $2p\ ^2P_{3/2}$	313.9	0.96	0.10	6.28	6.05	
Al XI	550.031	550.1	$2s\ ^2S_{1/2}$ - $2p\ ^2P_{3/2}$	50.3	1.14	0.11	6.33	6.16	
Fe XIV	334.172	334.2	$3s^2\ 3p\ ^2P_{1/2}$ - $3s\ 3p^2\ ^2D_{3/2}$	657.7	0.68	0.07	6.35	6.26	
S XII	552.990	552.7	$2s^22p\ ^2P_{3/2}$ - $2s\ 2p^2\ ^4P_{1/2}$	0.6	0.94	0.25	6.39	6.34	
Si XII	520.665	520.7	$2s\ ^2S_{1/2}$ - $2p\ ^2P_{1/2}$	226.2	1.34	0.13	6.39	6.28	
Fe XV	327.011	327.0	$3s3p\ ^3P_2$ - $3p^2\ ^1D_2$	59.4	1.05	0.11	6.40	6.33	
Fe XVI	360.761	360.8	$3s\ ^2S_{1/2}$ - $3p\ ^2P_{1/2}$	1733.0	1.09	0.11	6.42	6.41	
Fe XVI	335.410	335.4	$3s\ ^2S_{1/2}$ - $3p\ ^2P_{3/2}$	3755.5	1.01	0.10	6.43	6.41	
Fe XVII	350.496	350.5	$3s\ ^3P_2$ - $3p\ ^3D_3$	8.2	0.32	0.08	6.46	6.72	

Table 6.6: Results from DEM analysis for the base of the loop system. The ionization equilibrium used is Mazzotta et al. (1998). See text above for details on the columns.

Ion	λ_t (Å)	λ_o (Å)	Transition	I_o	I_t/I_o	+/-	T_{eff}	T_{max}	%
O III	599.597	599.6	$2s^2\ 2p^2\ ^1D_2$ - $2s2p^3\ ^1D_2$	2.0	0.84	0.11	5.06	5.03	
O IV	554.513	554.6	$2s^2\ 2p\ ^2P_{3/2}$ - $2s\ 2p^2\ ^2P_{3/2}$	5.1	1.00	0.36	5.20	5.23	
O IV	553.329	553.6	$2s^2\ 2p\ ^2P_{1/2}$ - $2s\ 2p^{22}P_{3/2}$	1.4	0.74	0.28	5.26	5.23	
O V	629.730	629.9	$2s^2\ ^1S_0$ - $2s\ 2p\ ^1P_1$	10.0	1.23	0.13	5.46	5.38	
Ne VI	562.803	562.9	$2s^2\ 2p\ ^2P_{3/2}$ - $2s\ 2p^2\ ^2D_{5/2}$	2.7	1.03	0.13	5.76	5.62	
Ne VII	561.728	561.6	$2s2p\ ^3P_2$ - $2p^2\ ^3P_2$	1.5	3.69	0.63	6.04	5.71	0.83
Ne VII	561.4		$2s2p\ ^3P_1$ - $2p^2\ ^3P_1$					5.71	0.17
Mg VIII	313.754	313.7	$2s^22p\ ^2P_{1/2}$ -$2s2p^{22}P_{1/2}$	49.3	0.91	0.11	6.06	5.91	
Mg VIII	315.039	315.0	$2p\ ^2P_{3/2}$ - $2s.2p^2\ ^2P_{3/2}$	125.7	0.95	0.10	6.06	5.91	
Mg VIII	339.006	339.0	$2p\ ^2P_{3/2}$ - $2s\ 2p^2\ ^2S_{1/2}$	31.8	0.90	0.10	6.06	5.91	
Si VIII	316.205	316.2	$2s^22p^3\ ^4S_{3/2}$ - $2s2p^{44}P_{3/2}$	138.2	2.37	0.25	6.07	5.93	
Fe X	345.723	345.7	$3s^2\ 3p^5\ ^2P_{3/2}$ - $3s\ 3p^6\ ^2S_{1/2}$	128.4	1.00	0.10	6.08	5.98	
Al VIII	325.276	325.4	$2p^2\ ^3P_1$ - $2s\ 2p^{33}P_0$	9.1	1.33	0.28	6.08	5.96	0.35
Al VIII	325.3		$2p^2\ ^3P_1$ - $2s\ 2p^3\ ^3P_2$					5.96	0.33
Al VIII	325.3		$2p^2\ ^3P_1$ - $2s\ 2p^3\ ^3P_1$					5.96	0.27
Mg IX	368.070	368.1	$2s^2\ ^1S_0$ - $2s\ 2p\ ^1P_1$	968.4	1.14	0.11	6.09	5.98	
Fe XI	341.113	341.1	$3s^2\ 3p^4\ ^3P_2$ - $3s\ 3p^5\ ^3P_1$	119.7	0.58	0.06	6.10	6.06	
Fe XI	369.153	369.2	$3s^2\ 3p^4\ ^3P_1$ - $3s\ 3p^5\ ^3P_2$	83.5	1.01	0.10	6.10	6.06	
Fe XI	352.662	352.7	$3s^2\ 3p^4\ ^3P_2$ - $3s\ 3p^5\ ^3P_2$	330.6	0.85	0.08	6.10	6.06	
Al X	332.789	332.8	$2s^2\ ^1S_0$ - $2s\ 2p\ ^1P_1$	290.0	0.74	0.07	6.12	6.10	
Si X	621.079	621.0	$2p\ ^2P_{1/2}$ - $2s.2p^2\ ^4P_{1/2}$	8.7	0.49	0.05	6.13	6.13	
Ca X	574.010	574.0	$3s\ ^2S_{1/2}$ - $3p\ ^2P_{1/2}$	32.9	0.87	0.09	6.13	5.86	
Ca X	557.765	557.8	$3s\ ^2S_{1/2}$ - $3p\ ^2P_{3/2}$	52.8	1.09	0.11	6.13	5.86	
Fe XII	352.106	352.1	$3s^2\ 3p^3\ ^4S_{3/2}$ - $3s\ 3p^4\ ^4P_{3/2}$	340.1	0.88	0.09	6.13	6.14	
Mg X	609.793	609.8	$2s\ ^2S_{1/2}$ - $2p\ ^2P_{3/2}$	718.4	0.99	0.10	6.13	6.05	
Mg X	624.941	624.9	$2s\ ^2S_{1/2}$ - $2p\ ^2P_{1/2}$	332.0	1.10	0.11	6.13	6.05	
Fe XII	346.852	346.9	$3s^23p^3\ ^4S_{3/2}$ - $3s\ 3p^4\ ^4P_{1/2}$	177.6	0.86	0.09	6.13	6.14	
Fe XII	364.467	364.5	$3s^23p^3\ ^4S_{3/2}$ - $3s\ 3p^4\ ^4P_{5/2}$	525.6	0.83	0.08	6.13	6.14	
Al XI	568.120	568.2	$2s\ ^2S_{1/2}$ - $2p\ ^2P_{1/2}$	44.1	0.87	0.09	6.20	6.16	
Al XI	550.031	550.1	$2s\ ^2S_{1/2}$ - $2p\ ^2P_{3/2}$	78.5	1.00	0.11	6.20	6.16	
Fe XIII	348.183	348.2	$3s^2\ 3p2\ ^3P_0$ - $3s\ 3p^3\ ^3D_1$	301.0	1.13	0.11	6.20	6.20	
Fe XIII	321.400	321.5	$3s^23p^2\ ^3P_2$ - $3s\ 3p^3\ ^3P_1$	79.4	0.99	0.11	6.20	6.20	
Fe XIV	353.831	353.8	$3s^2\ 3p\ ^2P_{3/2}$ - $3s\ 3p^2\ ^2D_{5/2}$	161.7	1.05	0.11	6.26	6.26	
Fe XIV	334.172	334.2	$3s^2\ 3p\ ^2P_{1/2}$ - $3s\ 3p^2\ ^2D_{3/2}$	706.2	0.77	0.08	6.27	6.26	
Si XII	520.665	520.7	$1s^22s\ ^2S_{1/2}$ - $1s^22p\ ^2P_{1/2}$	220.9	1.16	0.12	6.30	6.28	
S XII	538.680	538.8	$2s^2\ 2p\ ^2P_{3/2}$ - $2s\ 2p^2\ ^4P_{3/2}$	5.0	0.78	0.11	6.31	6.34	
Fe XV	327.011	327.0	$3s3p\ ^3P_2$ - $3p^2\ ^1D_2$	37.3	0.96	0.11	6.32	6.33	
Fe XVI	360.761	360.8	$3s\ ^2S_{1/2}$ - $3p\ ^2P_{1/2}$	631.8	0.99	0.10	6.34	6.41	0.87
Fe XIV	360.8		$3s\ 3p^2\ ^2D_{3/2}$ - $3p^3\ ^2D_{3/2}$					6.25	0.13

Monsignori Fossi et al. (1994) studing active region composition with the DEM technique, derived abundances relative to Fe, and found departure from photospheric composition that are similar to those derived here.

From these results, it appears that: (1) the abundance distribution deviates from photospheric values; (2) Even if this loop system does not have a bright active region at its base, its abundances are similar to those of active regions.

6.2 The Coronal Hole Boundary

On March 7th 1998, further CDS observations were made at the off-limb mid-latitude position, in order to observe a polar coronal hole boundary region.. As described in Chapter 1, in many cases, at the boundary of polar coronal holes the quiet Sun consists of an arcade system. The study of such region forms an important aspect in the understanding of coronal hole structures and, how they interact with, and evolve with respect to, the surrounding environment.

6.2.1 The Data

Figure 6.9 shows how the solar corona appeared with the SOHO/EIT 171 Å filter on the 7th of March 1998. The dark polar holes are visible at both the poles, together with the bright arcade system that surrounded them (more clearly visible at the north pole). The CDS observations that were made on that day were full NIS spectra with the $120'' \times 120''$ raster (white square on the figure). The figure shows that the area observed included the boundary between the coronal hole and a large streamer. Four successive CDS rasters of the same area were carried out. These observations were analysed with the standard procedures. An IDL routine was then written to average the four observations before further data processing. This was done to increase the signal-to-noise and to remove the cosmic rays at the same time. Before the average was performed, each raster was processed for debias correction. The average was performed using the routine AVG_WO_CR of the CDS software package. This procedure averages all the data for each co-spatial pixel, but discards those which are more than 3 sigma above the rest of the pixels making up that average. In this way, the cosmic rays are automatically discarded. The next step of the analysis was the application of the calibration, and then line intensities were calculated in the usual way. An example of images formed from the resulting spectra is shown in Figure 6.10.

Figure 6.10 shows monochromatic images in a few iron lines, formed at increasingly

higher temperatures, from 1×10^6 K to 2.57×10^6 K (from top left to bottom right). The top left corner of the raster is very close to the limb and, in fact, it appears very bright at lower temperatures. The boundary between the coronal hole and the streamer becomes more evident when observed in lines that are formed at higher temperatures (particularly Fe XVI).

Figure 6.11 shows examples of images made from line ratios sensitive to variations in density (top) and temperature (bottom), at coronal temperatures. It is evident from the figure that the coronal hole differs from the streamer both in terms of densities and temperatures.

In order to study in more detail the general plasma characteristics of the coronal hole and streamer regions, two areas were selected for further analysis. They consist of two

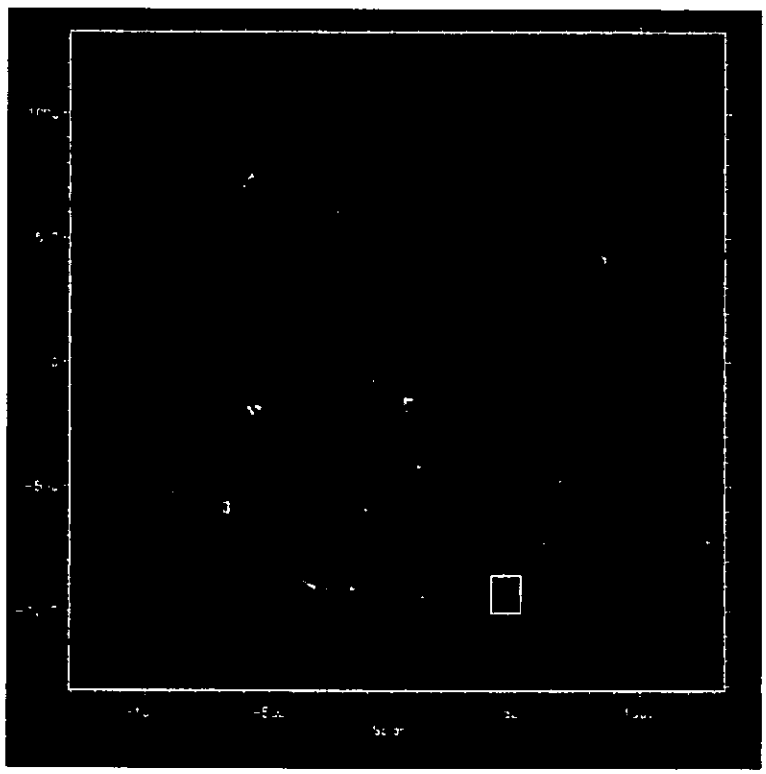

Figure 6.9: EIT 171 Å (Fe IX/X) image of the solar corona for 7 March 1998. The south and north polar regions are clearly occupied by dark coronal holes. The bright arcade system is visible at the edges of them. The white rectangle in the south-west quadrant indicates the position of the CDS/NIS raster.

equal square areas whose centre is placed at $1063.1''$ from Sun centre ($\approx 1.1 R_\odot$), in both coronal hole and the streamer. The selected areas are labelled in Figure 6.12, and are named "A" for the coronal hole, and "B" for the streamer. The two areas were chosen to be at the same radial distance from Sun centre, in order to remove any dependence of the various parameters on the radial distance. The two spatially averaged spectra are shown

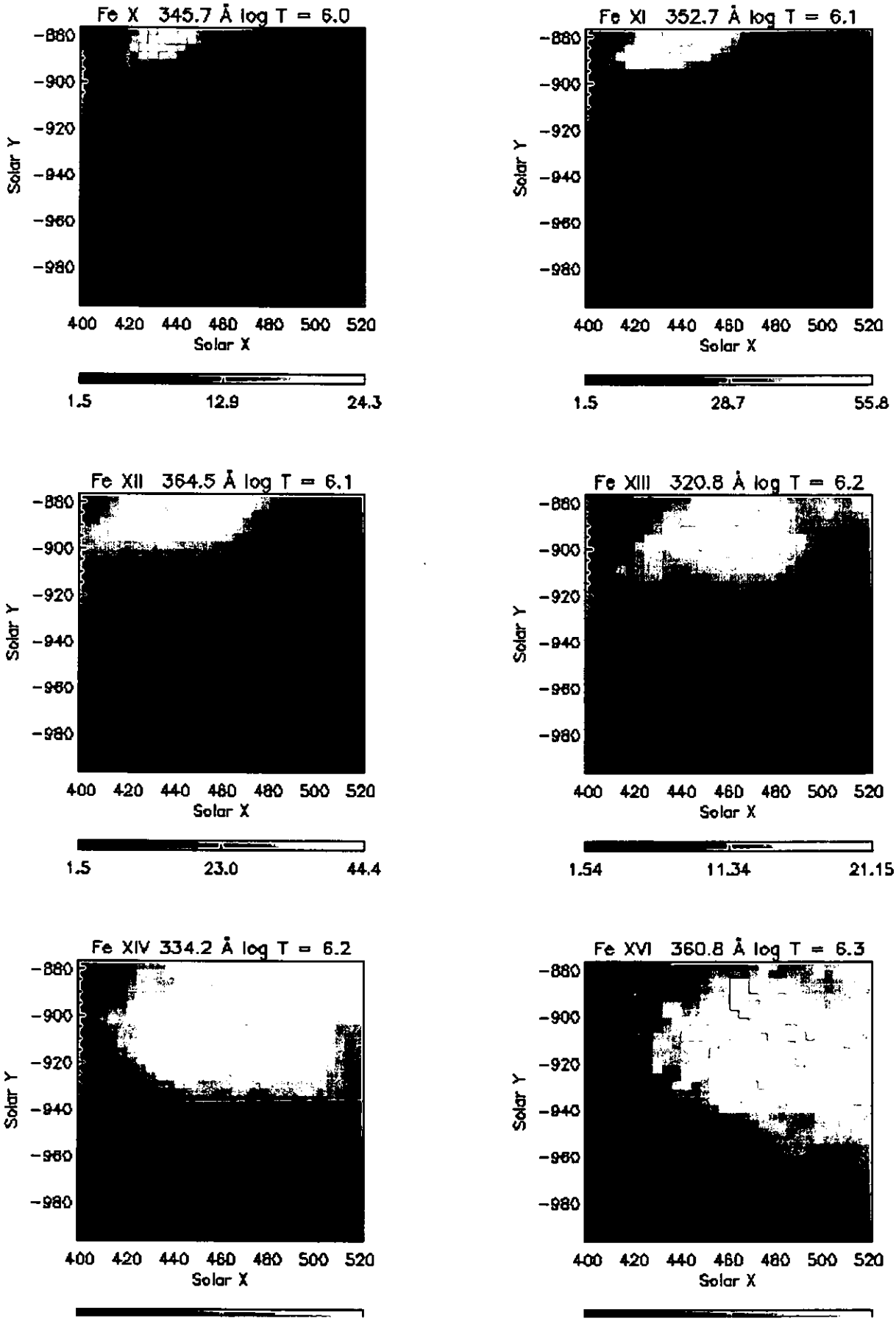

Figure 6.10: Monochromatic images of the s10562 raster. The temperature of the emitting plasma increases with the stage of iron ionization. The edge of the streamer is visible at high temperatures.

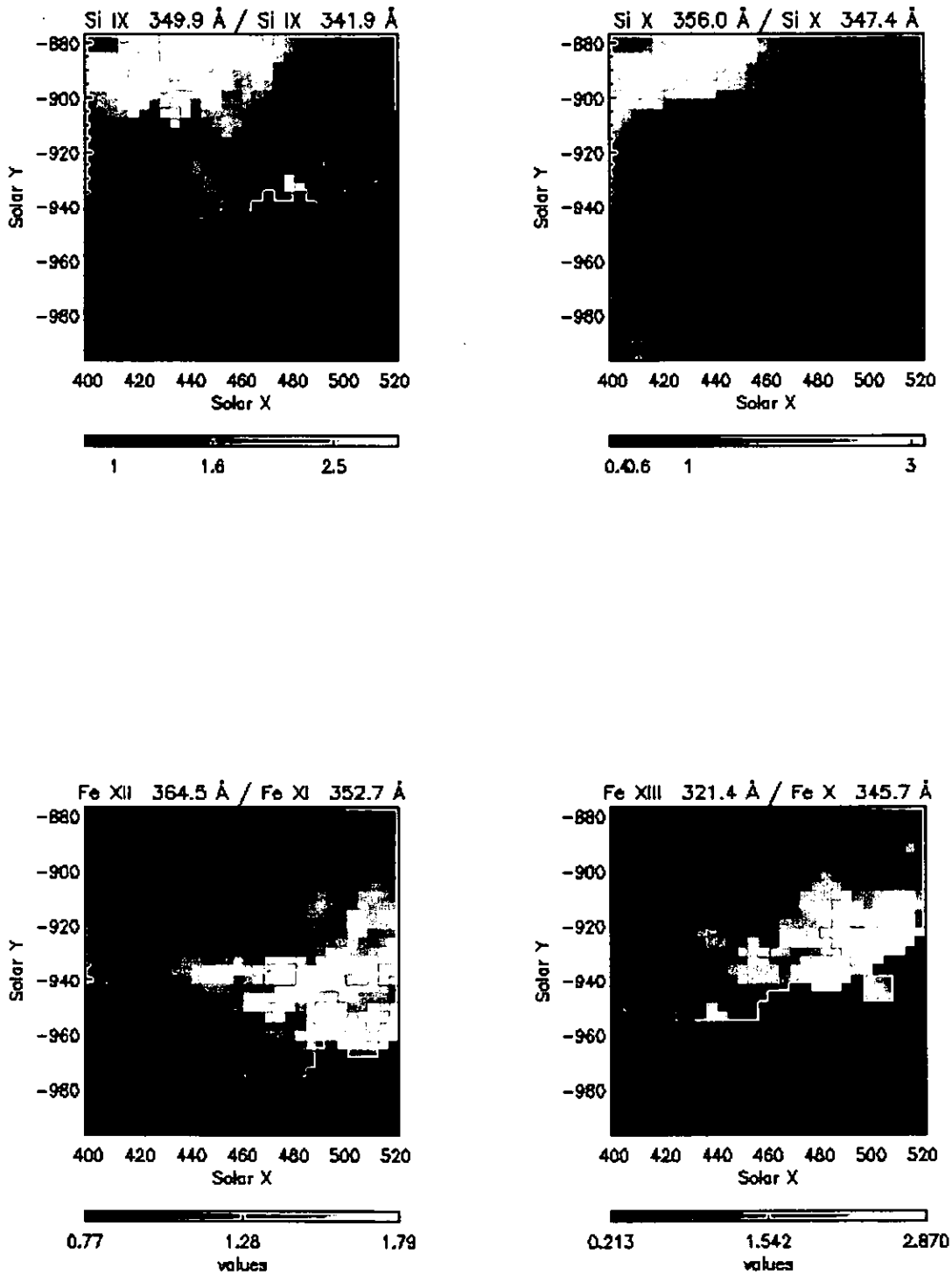

Figure 6.11: Results from line ratios sensitive to density (Top) and temperature (Bottom) applied to all the raster. The coronal hole boundary is visible as density and temperature structure

in Figures 6.13-6.16, together with the line fits.

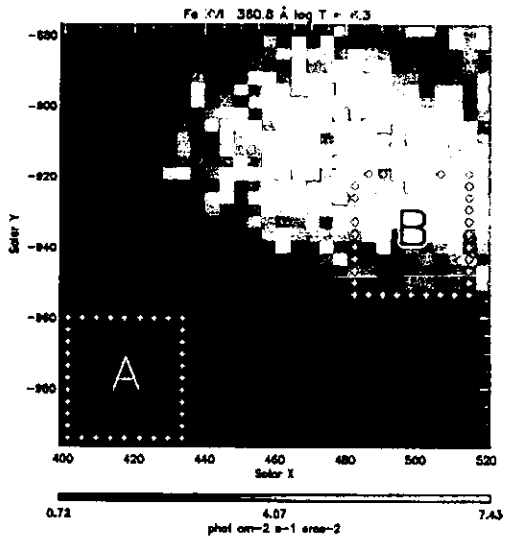

Figure 6.12: The white squares represent the two areas selected for the analysis of the ambient coronal hole ('A') and streamer ('B').

6.2.2 Results

For EUV coronal hole studies, density-sensitive lines that emit at lower temperatures than 1 $\times 10^6$ K (transition region lines) would be useful, because this area is generally cooler than the quiet Sun. However, the data presented here refer to off limb observations where the temperature is expected to be higher than on the disk. The emission from transition region lines drops drastically there because the density drops quickly with height, and at the same time the temperature increases. Only density-sensitive coronal lines can therefore be used to infer the density profile in the coronal holes as already discussed in Chapter 5.

For this study, as before the Si IX 349.9/341.9 Å, Si X 356./347.4 Å, Fe XIII 320.809/ 348.183 Å and Fe XIII 320.809/ 321.400 Å ratios have been used for electron density determination. In addition, the Mg VIII 315.038/313.754 Å ratio has been used (as in Section 5.6), as shown in Table 6.7. This ratio is only marginally density-sensitive in the range $6 < logN < 8$. However, in the present data these lines were sufficiently bright to obtain another measurement of the averaged densities of the lower temperature plasma, where Mg VIII is formed. As in the case of the density estimate, the choice of the lines to be used for the temperature determination was guided by the expectation that the plasma

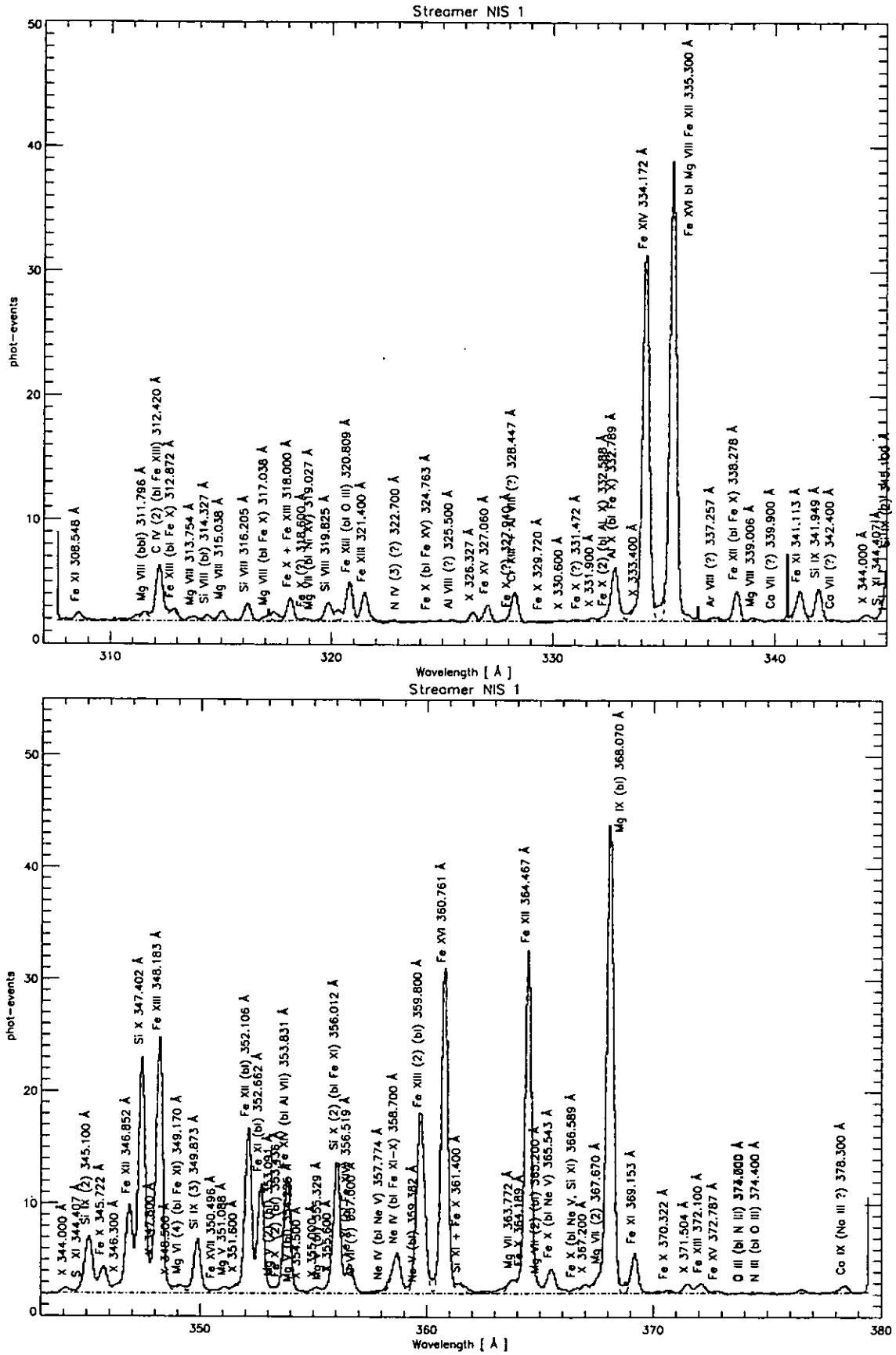

Figure 6.13: NIS 1 spectra of the selected streamer area (area 'B'). The fitted Gaussian and background are over-plotted.

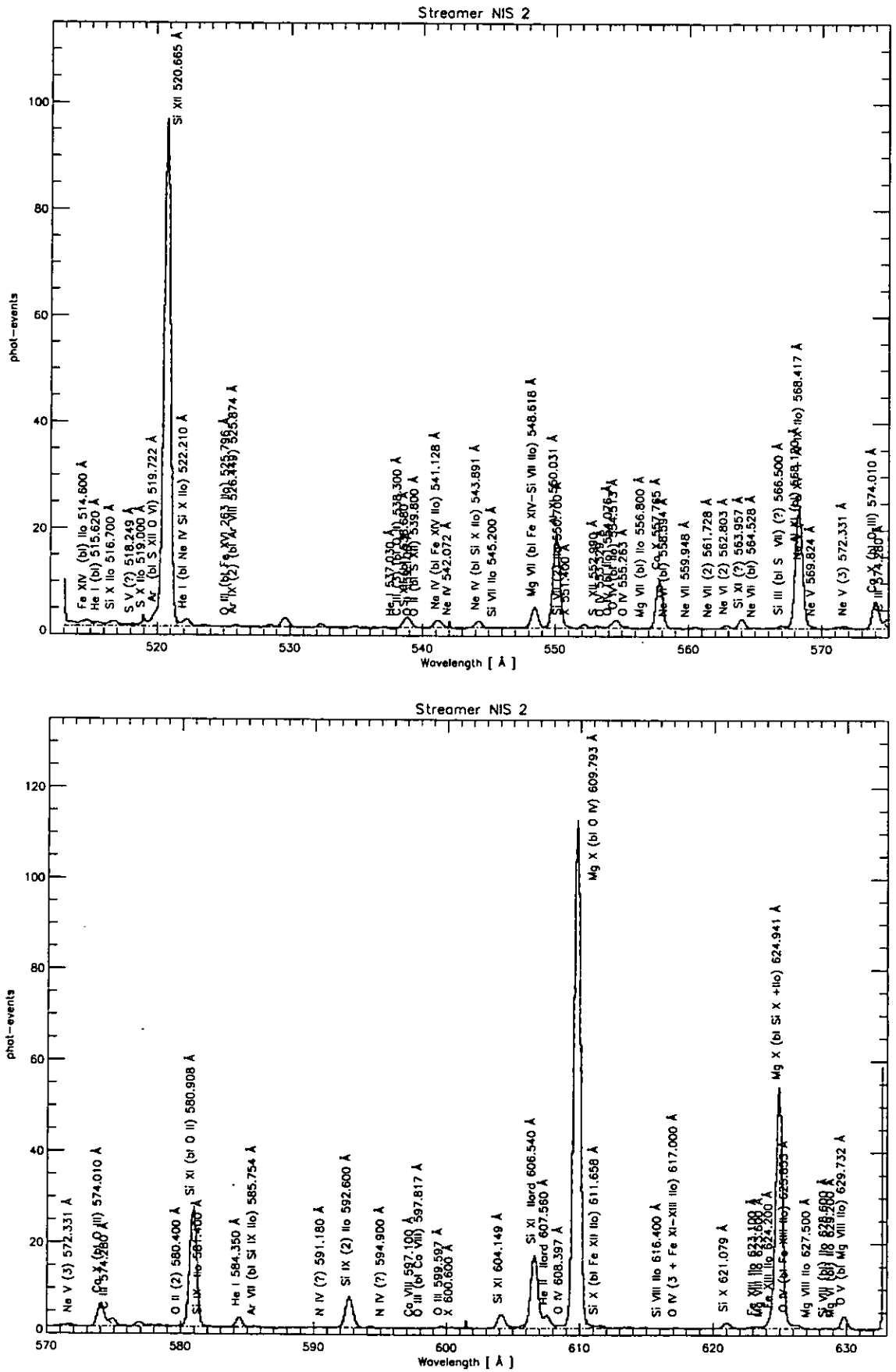

Figure 6.14: NIS 2 spectra of the selected streamer area (area 'B'). The fitted Gaussian and background are over-plotted.

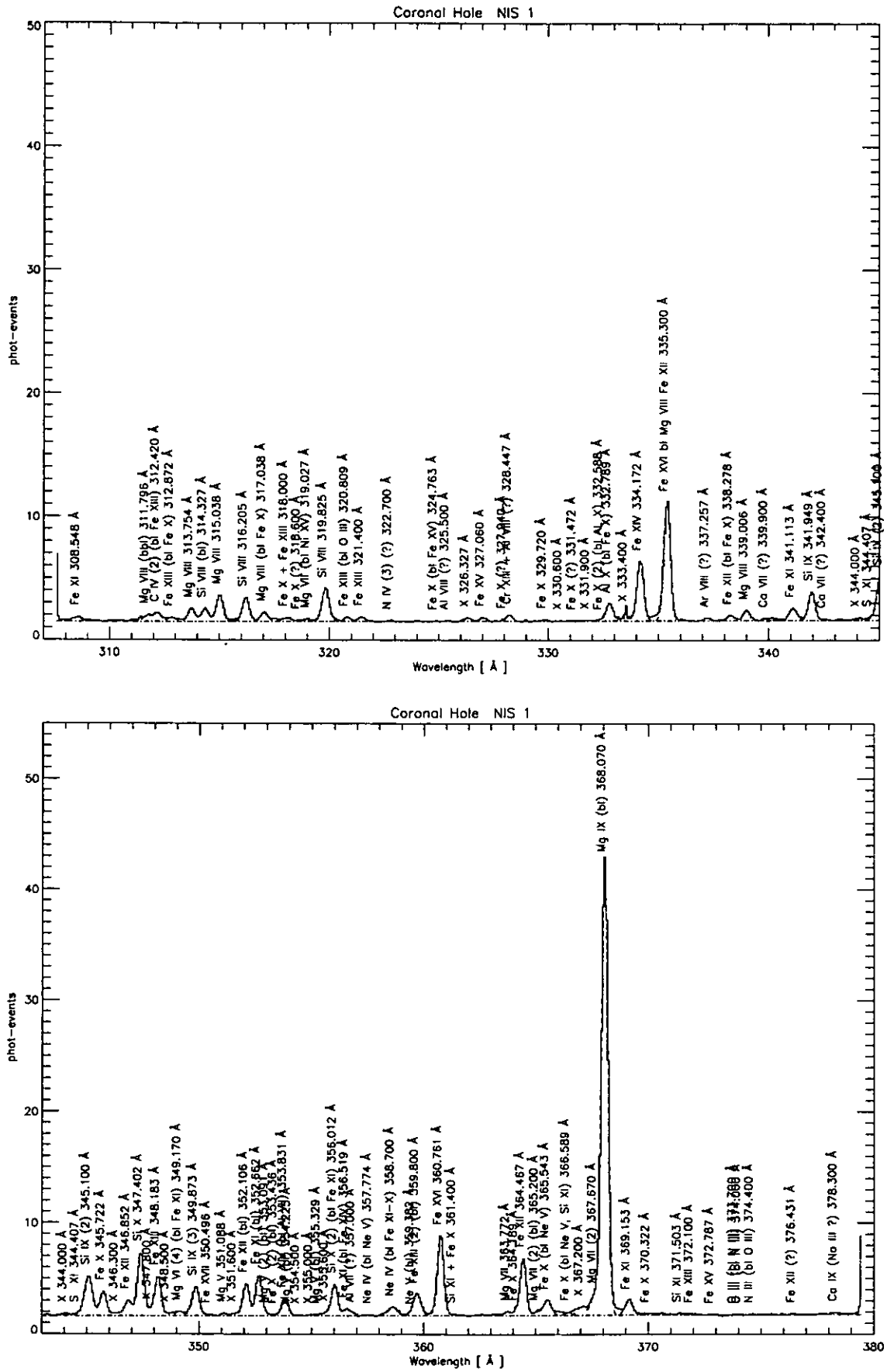

Figure 6.15: NIS 1 spectra of the selected coronal hole area (area 'A'). The fitted Gaussian and background are over-plotted.

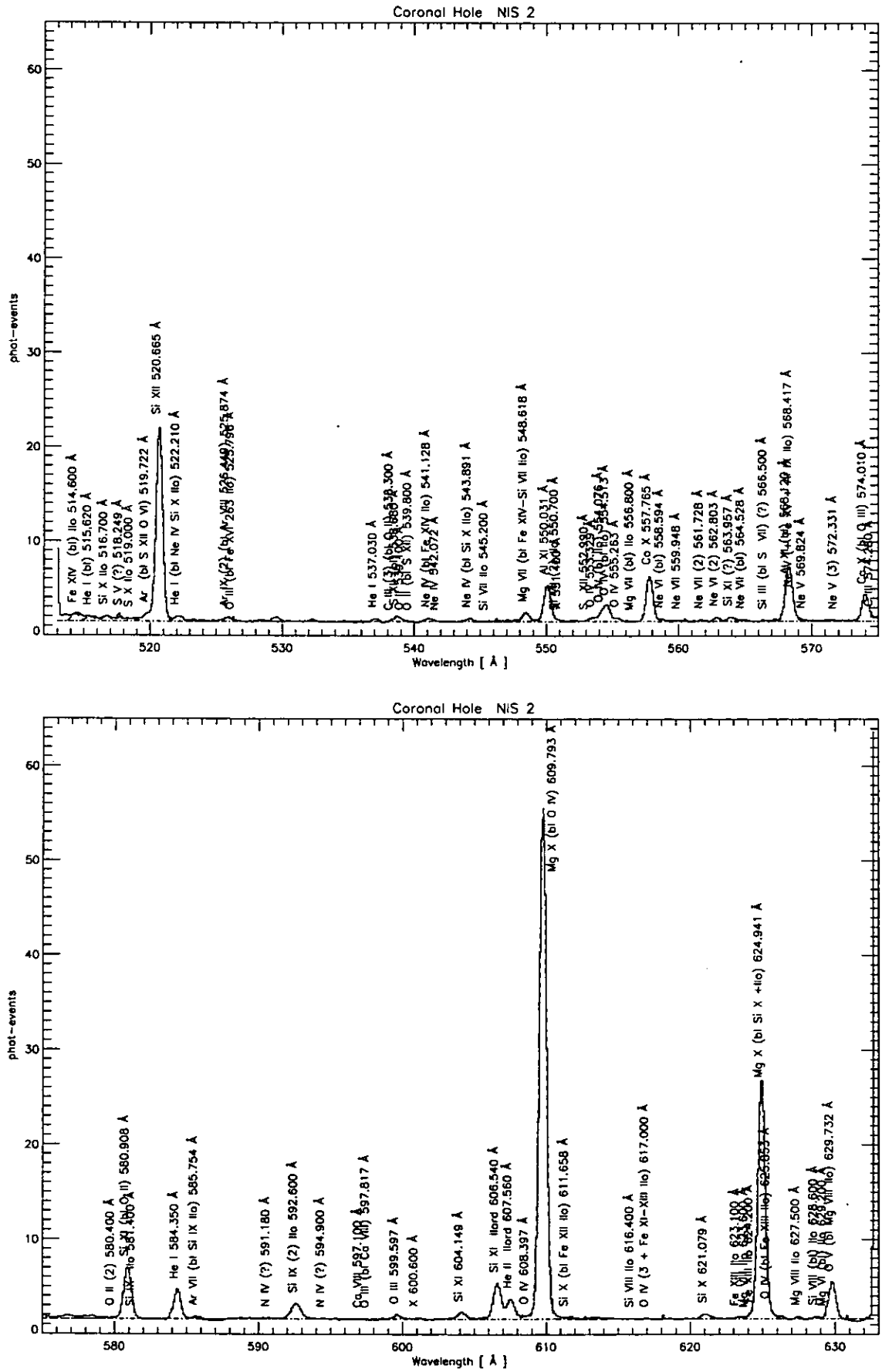

Figure 6.16: NIS 2 spectra of the selected coronal hole area (area 'A'). The fitted Gaussian and background are over-plotted.

Table 6.7: Electron densities derived from the line ratio technique for the coronal hole and its boundary. The first column gives the ratio used, the second gives the temperature at which the emissivities were calculated (equal to the temperature of maximum ionization fraction derived from Mazzotta et al. (1998)), the third shows results for the arcade system (region 'B') the last column shows the results for coronal hole (region 'A'). The values for the density are given in cm^{-3} and the errors associated are listed in brackets.

Ratio	T_{max} 10^6 (K)	N_e Streamer (10^8 cm^{-3})	N_e Coronal Hole (10^8 cm^{-3})
Mg VIII 315.038/313.754	0.79	0.9 (-0.7; +0.7)	0.7 (-0.2; +0.2)
Si IX 349.9/341.9	1.26	2.1 (-0.1; +0.1)	1.1 (-0.1; +0.1)
Si X 356./347.4	1.38	2.8 (-0.2; +0.2)	2.0 (-0.1; +0.1)
Fe XIII 320.809/348.183	1.58	5.4 (-0.2; +0.2)	3.7 (-0.6; +0.7)
Fe XIII 320.809/321.400	1.58	6.0 (-0.6; +0.4)	3.8 (-0.9; +1.0)

Table 6.8: Electron temperature derived applying the line pairs technique for different ratios. The Mazzotta et al. (1998) ionization equilibrium was used.

Ratio	Streamer T_e (10^6 K)	Coronal Hole T_e (10^6 K)
Mg X 609.793 / Mg IX 368	1.29 (-0.01; +0.01)	1.09 (-0.01; +0.01)
Fe XI 352.662 /Fe X 345.723	1.22 (-0.02; +0.02)	1.07 (-0.01; +0.01)
Fe XII 364.467/Fe XI 352	1.45 (-0.01; +0.01)	1.20 (-0.01; +0.01)
Fe XIII 348.183/Fe XII 364.467	1.40 (-0.01; +0.01)	1.38 (-0.01 ; +0.01)
Fe XIV 334.172 / Fe XIII 348.183	1.92 (-0.01; +0.01)	1.94 (-0.02; +0.02)
Fe XVI 360.761/Fe XIV 334.172	1.90 (-0.01; + 0.01)	1.99 (-0.01; +0.01)

would have a temperature of about a million degrees. Moreover, lines had to be chosen that were suitable for the diagnostics of both selected regions. The line ratios chosen are listed in Table 6.8. The temperature of maximum emission of the lines falls in the range $9.54 \times 10^5 < T < 2.57 \times 10^6$ K.

6.2.3 Discussion

The densities derived from all the ratios consistently show that the coronal hole is more rarefied than the streamer. This is an expected result, but a few comments need to be added. Densities from the two Fe XIII ratios agree in their values and show higher densities than those derived from Si and Mg ratios. The density from Si IX indicates that the streamer has twice the density of the coronal hole. This difference is less in the values

found from the other ratios, but is still significant. Moreover, in each region, the density increases with increasing the temperature of emission of the ion, as an indication of the presence of multi-temperature plasma.

Similar results were found by other authors, when examining off-limb CDS observations of both coronal holes and streamers (Del Zanna, 1999; Fludra et al., 1999a). Slightly higher densities derived from the same Si ratios but referring to on-disc coronal hole observations, were previously obtained by Del Zanna & Bromage (1999b). Moreover, these authors found a similar discrepancy between the Si X and Si IX ratios. On the other hand, other studies (Wilhelm et al., 1998b; Doyle et al., 1999), based on different ratios (mainly Si VIII), found slightly lower densities at the same radial distances. The density derived here from the upper transition region lines of Mg VIII (which form at the same temperatures as Si VIII, log T=5.9), also show lower densities. However, note that the values derived from Mg VIII have large uncertainties, mainly due to the lower sensitivity of the ratio, which means that the observed plasma has almost reached the high-temperature limit for the emission of Mg VIII.

It is interesting to note that the densities found here for the arcade structure are close to those found for the loop top observed on the 8th of March (see Table 6.2). In fact, the two observations were taken at similar radial distances, the loop top being only about $20''$ closer to the limb. Note from Table 6.2 that density derived from the Si IX ratio are consistent within the errors, but results from Si X show the loop system has higher density. This discrepancy between results from different line ratios may be attributed to the emission from a multi-thermal plasma, which is very likely in the presence of solar activity.

The non uniformity of plasma temperatures derived from these data is clearly shown in Table 6.8. The temperatures derived from different line ratios generally give different values, with the coronal hole being cooler than the streamer. However, while in the coronal hole the measured temperature increases as the stage of ionization of the ion used increases, this is not completely true for the streamer. It appears that using ratios of successively higher stages of ionization, the derived temperatures first increase and then tend to level at about 1.44 10^6 K (log T=6.2).

Further information on the temperature of the plasma is also given by the DEM (Figure 6.17, Tables 6.10 and 6.11). The DEM derived for the coronal hole (top figure) has a double peak at about 1 $\times 10^6$ K and 2.24 $\times$ 10^6 K (log T=6.35). The streamer instead shows a DEM with a single peak at 1.58 $\times$ 10^6 K (log T=6.2), but broader than the one shown for the coronal hole. It is clear from these results that the hotter emission from the

coronal hole comes from the foreground off-limb corona. The second (cooler) peak in the coronal hole DEM curve is typical of disc coronal hole observations. The streamer emits mainly at log T=6.2 but, as previously noted, has contributions from a broad range of temperatures. Even though this peak is positioned at lower temperature than the second peak of the coronal hole, the DEM values are higher in the streamer at both temperatures. This confirms the results for temperature and density discussed above.

At the beginning of this discussion section it was pointed out that the coronal hole/ streamer boundary is characterised by emission from hot plasma in the streamer. It is important then to compare these results with those from the analysis of the loop system of the previous section. The top of the loop DEM (Figure 6.7) peaks at much higher temperatures. This is probably a signature of the different origin of the two structures, one well inside the base of a streamer and the other just on the border.

The abundances derived with the DEM method are listed in Table 6.9. These have been derived using the Mazzotta et al. (1998) ionization equilibrium balance and by fixing the Fe abundance to the Feldman (1992) photospheric value. Effectively, the element abundances were derived relative to Fe. The error for the given values was estimated to be ± 0.03. As discussed in the previous case, these off-limb observations do not allow the determination of oxygen and neon abundances and therefore cannot provide an estimate of the FIP effect. The Ne and O abundances were kept fixed at their photospheric values, which are shown in the Table for completeness. The table shows an increase of almost all the abundances in the coronal hole with respect to their photospheric values. In the coronal belt instead there is a general decrease from the photospheric values. Most previous abundance studies have used the oxygen as reference element, so a direct comparison with the results obtained here is not possible. Note, that the analysis made on disc data generally use the oxygen as reference element because its lines are quite bright and so well defined. On off-limb data, instead, this is not the case. For this reason in the present analysis the Fe was chosen as the reference element.

A comparison with the abundances found in the loop system of March 1998 (Table 6.4) shows that they are different from those of the coronal hole, especially considering the loop top. In particular Al, Si and S appear to be more abundant in the coronal hole. In the literature there have been reports of the very low FIP elements showing an extra step in the FIP pattern (see Chapter 1). In the present case only Al belongs to that category and the data indeed indicate an increase of the Al/Fe ratio. The Si is found to have photospheric abundance, while the S is found to be enhanced considerably with respect to its photospheric value. As discussed in Section 4.6, S is an intermediate FIP element and

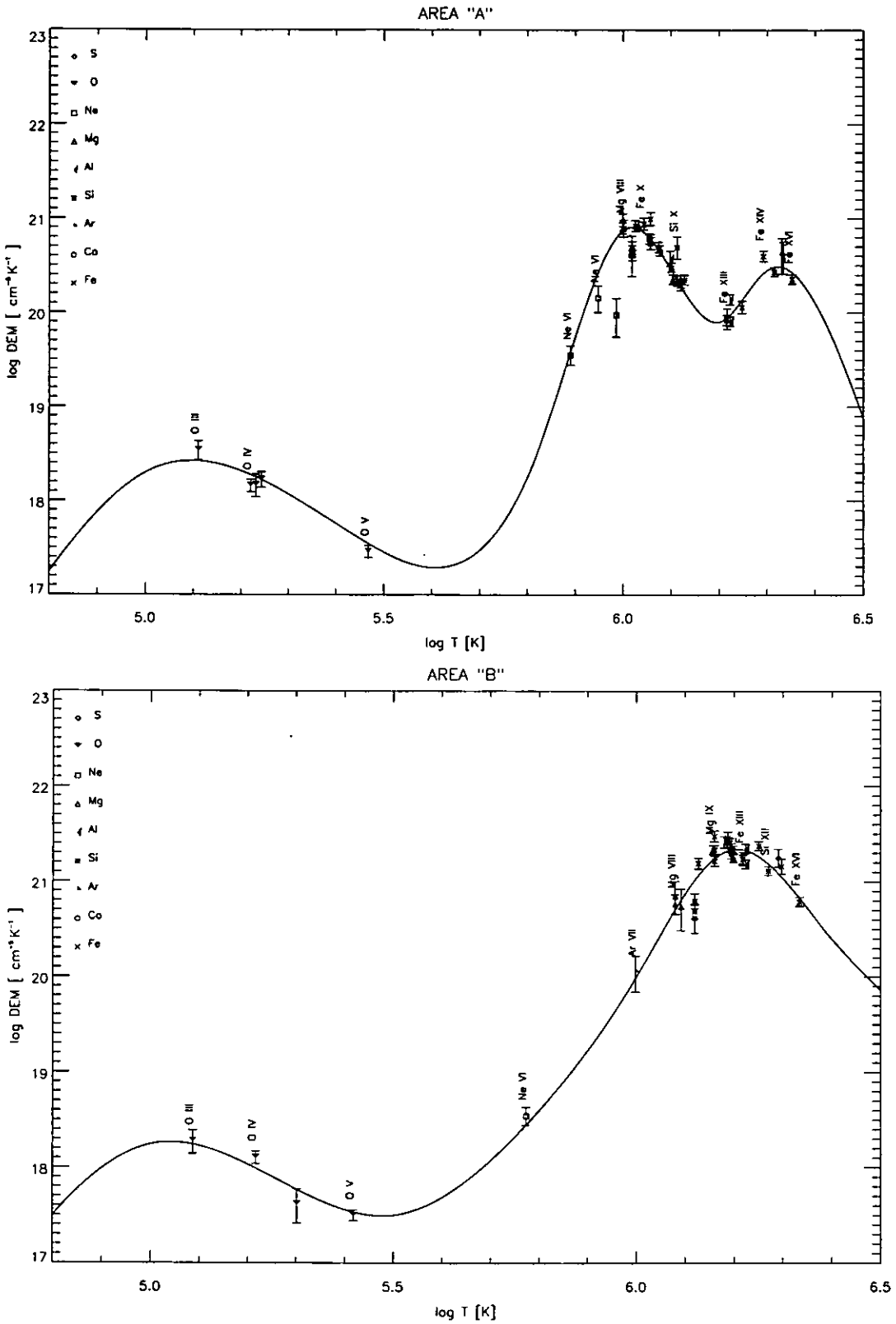

Figure 6.17: Differential Emission Measure vs. Temperature for the coronal hole (Top) and the streamer (bottom). The ionization equilibrium used is Mazzotta et al. (1998). The temperature (T) are *effective* temperature (Section 4.5.3 and Equation 4.2).

large variations in its abundance have been reported, with values similar to both those of the low and high FIP elements. The data analysed in this thesis also lead to a similar conclusion: the S found at the top of the loop is more depleted than its photospheric value, while in the coronal hole data the opposite is found.

A comparison between the streamer abundances and those from the same loop system just mentioned, shows that even if the single element abundances are different for the two structures, the general behaviour is similar. The decrease of abundances in the arcade system streamer can be associated with those in the loop top abundances, which have the lowest values of the three regions.

Table 6.9: Relative element abundances, specified in "dex", relative to the abundance of Fe, assumed photospheric from Feldman (1992).

Region	O	Ne	Mg	Al	Si	S	Ca	Fe
Photosphere	8.93	8.11	7.58	6.46	7.55	7.21	6.36	7.51
Coronal Hole	8.93	8.11	7.48	6.57	7.55	7.50	6.36	7.51
Streamer	8.93	8.11	7.40	7.47	7.45	7.36	6.25	7.51

Table 6.10: Results from the DEM analysis of the streamer. The theoretical lines are calculated using the Mazzotta et al. (1998) ionization equilibrium.

Ion	λ_t (Å)	λ_o (Å)	Transition	I_o	I_t/I_o	+/-	T_{eff}	T_{max}	%
O III	599.597	599.6	$2s^2\ 2p^2\ ^1D_2$ - $2s2p^3\ ^1D_2$	0.2	0.93	0.20	5.09	5.03	
O IV	554.513	554.6	$2s^2\ 2p\ ^2P_{3/2}$ - $2s\ 2p^2\ ^2P_{3/2}$	0.8	0.78	0.09	5.22	5.23	
O IV	555.263	555.3	$2s^2\ 2p\ ^2P_{3/2}$ - $2s\ 2p^2\ ^2P_{1/2}$	0.1	1.43	0.46	5.30	5.23	
O V	629.730	629.8	$2s^2\ ^1S_0$ - $2s\ 2p\ ^1P_1$	1.3	1.09	0.11	5.42	5.38	
Mg V	355.329	355.3	$2p^4\ ^3P_1$ - $2s\ 2p^5\ ^3P_2$	0.6	0.01	0.00	5.73	5.47	
Ne VI	562.803	562.9	$2s^2\ 2p\ ^2P_{3/2}$ - $2s\ 2p^2\ ^2D_{5/2}$	0.2	0.81	0.12	5.77	5.62	
Ar VII	585.754	585.6	$3s^2\ ^1S_0$ - $3s.(2s).3p\ ^1P_1$	0.1	0.85	0.29	6.00	5.54	
Mg VIII	315.039	315.0	$2p\ ^2P_{3/2}$ - $2s.2p^2\ ^2P_{3/2}$	5.4	0.88	0.15	6.08	5.91	
Mg VIII	313.754	313.7	$2s^22p\ ^2P_{1/2}$ -$2s2p^{22}P_{1/2}$	2.6	0.72	0.22	6.08	5.91	
Mg VIII	339.006	339.0	$2p\ ^2P_{3/2}$ - $2s\ 2p^2\ ^2S_{1/2}$	1.1	1.17	0.46	6.09	5.91	
Si VIII	314.327	314.4	$2s^22p^{34}S_{3/2}$ - $2s2p^4\ ^4P_{1/2}$	3.2	2.49	0.64	6.12	5.93	
Si VIII	319.826	319.9	$2s^22p^3\ ^4S_{3/2}$ - $2s^2p^4\ ^4P_{5/2}$	10.8	2.14	0.27	6.12	5.93	
Si VIII	316.205	316.2	$2s^22p^3\ ^4S_{3/2}$ - $2s2p^4\ ^4P_{3/2}$	9.1	1.66	0.21	6.12	5.93	
Fe X	345.723	345.7	$3s^2\ 3p^5\ ^2P_{3/2}$ - $3s\ 3p^6\ ^2S_{1/2}$	8.9	0.75	0.08	6.13	5.98	
Mg IX	368.070	368.1	$2s^2\ ^1S_0$ - $2s\ 2p\ ^1P_1$	86.9	0.79	0.08	6.16	5.98	0.84
Fe XIII		368.2	$3s^2\ 3p^2\ ^3P_2$ - $3s\ 3p^3\ ^3D_3$					6.20	0.14
Fe XI	341.113	341.1	$3s^2\ 3p^4\ ^3P_2$ - $3s\ 3p^5\ ^3P_1$	9.5	0.59	0.06	6.16	6.06	
Fe XI	369.153	369.2	$3s^2\ 3p^4\ ^3P_1$ - $3s\ 3p^5\ ^3P_2$	6.5	1.07	0.11	6.16	6.06	
Fe XI	352.662	352.7	$3s^2\ 3p^4\ ^3P_2$ - $3s\ 3p^5\ ^3P_2$	28.6	0.82	0.08	6.16	6.06	
Al X	332.789	332.8	$2s^2\ ^1S_0$ - $2s\ 2p\ ^1P_1$	25.9	0.79	0.08	6.18	6.10	
Si X	621.079	621.0	$2p\ ^2P_{1/2}$ - $2s.2p^2\ ^4P_{1/2}$	0.7	0.74	0.08	6.19	6.13	
Fe XII	346.852	346.9	$3s^23p^3\ ^4S_{3/2}$ - $3s\ 3p^4\ ^4P_{1/2}$	26.4	0.83	0.08	6.19	6.14	
Fe XII	364.467	364.5	$3s^23p^3\ ^4S_{3/2}$ - $3s\ 3p^4\ ^4P_{5/2}$	73.6	0.85	0.09	6.19	6.14	
Ca X	574.010	574.0	$3s\ ^2S_{1/2}$ - $3p\ ^2P_{1/2}$	1.9	1.10	0.11	6.19	5.86	
Ca X	557.765	557.8	$3s\ ^2S_{1/2}$ - $3p\ ^2P_{3/2}$	4.4	0.96	0.10	6.19	5.86	
Mg X	609.793	609.8	$2s\ ^2S_{1/2}$ - $2p\ ^2P_{3/2}$	67.8	1.02	0.10	6.20	6.05	
Mg X	624.941	624.9	$2s\ ^2S_{1/2}$ - $2p\ ^2P_{1/2}$	29.1	1.23	0.12	6.20	6.05	
Fe XIII	348.183	348.2	$3s^2\ 3p2\ ^3P_0$ - $3s\ 3p^3\ ^3D_1$	65.4	1.27	0.13	6.22	6.20	
Fe XIII	321.400	321.5	$3s^23p^2\ ^3P_2$ - $3s\ 3p^3\ ^3P_1$	14.3	1.25	0.14	6.22	6.20	
Al XI	568.120	568.2	$2s\ ^2S_{1/2}$ - $2p\ ^2P_{1/2}$	6.3	0.97	0.10	6.22	6.16	
Al XI	550.031	550.1	$2s\ ^2S_{1/2}$ - $2p\ ^2P_{3/2}$	8.9	1.40	0.14	6.22	6.16	
Fe XIV	334.172	334.2	$3s^2\ 3p\ ^2P_{1/2}$ - $3s\ 3p^2\ ^2D_{3/2}$	148.2	0.78	0.08	6.25	6.26	
Si XII	520.665	520.7	$1s^22s\ ^2S_{1/2}$ - $1s^22p\ ^2P_{1/2}$	37.2	1.19	0.12	6.27	6.28	
S XII	538.680	538.8	$2s^2\ 2p\ ^2P_{3/2}$ - $2s\ 2p^2\ ^4P_{3/2}$	0.9	0.69	0.11	6.29	6.34	
Fe XV	327.011	327.0	$3s3p\ ^3P_2$ - $3p^2\ ^1D_2$	7.2	0.78	0.10	6.30	6.33	
Fe XVI	360.761	360.8	$3s\ ^2S_{1/2}$ - $3p\ ^2P_{1/2}$	84.0	1.10	0.11	6.33	6.41	0.81
Fe XIV	360.8		$3s\ 3p^2\ ^2D_{3/2}$ - $3p^3\ ^2D_{3/2}$					6.25	0.19

Table 6.11: Results from the DEM analysis of the coronal hole. The theoretical lines are calculated using the Mazzotta et al. (1998) ionization equilibrium.

Ion	λ_t (Å)	λ_o (Å)	Transition	I_o	I_t/I_o	+/-	T_{eff}	T_{max}	%
O III	599.597	599.7	$2s^2\ 2p^2\ ^1D_2$ - $2s2p^3\ ^1D_2$	0.3	0.78	0.13	5.11	5.03	
O IV	554.513	554.6	$2s^2\ 2p\ ^2P_{3/2}$ - $2s\ 2p^2\ ^2P_{3/2}$	0.8	1.31	0.15	5.22	5.23	
O IV	555.263	555.4	$2s^2\ 2p\ ^2P_{3/2}$ - $2s\ 2p^2\ ^2P_{1/2}$	0.2	1.22	0.25	5.23	5.23	
O IV	554.076	554.2	$2s^2\ 2p\ ^2P_{1/2}$ - $2s\ 2p^2\ ^2P_{1/2}$	0.4	1.00	0.13	5.24	5.23	
O V	629.730	629.8	$2s^2\ ^1S_0$ - $2s\ 2p\ ^1P_1$	2.0	1.23	0.14	5.47	5.38	
Ne VI	562.803	562.9	$2s^2\ 2p\ ^2P_{3/2}$ - $2s\ 2p^2\ ^2D_{5/2}$	0.2	1.08	0.18	5.89	5.62	
Ne VII	558.609	558.8	$2s2p\ ^3P_1$ - $2p^2\ ^3P_2$	0.1	1.87	0.46	5.95	5.71	0.60
Ne VI	558.6		$2s^2\ 2p\ ^2P_{1/2}$ - $2s\ 2p^2\ ^2D_{3/2}$					5.62	0.40
Ne VII	561.728	561.8	$2s2p\ ^3P_2$ - $2p^2\ ^3P_2$	0.1	6.56	2.42	5.99	5.71	
Mg VII	319.027	319.0	$2s^22p^2\ ^1D_2$ - $2s^2p^3\ ^1D_2$	1.4	0.20	0.06	5.99	5.81	
Mg VIII	315.039	315.0	$2p\ ^2P_{3/2}$ - $2s.2p^2\ ^2P_{3/2}$	14.9	0.94	0.10	6.00	5.91	
Mg VIII	313.754	313.7	$2s^22p\ ^2P_{1/2}$ -$2s2p^{22}P_{1/2}$	7.8	0.76	0.09	6.00	5.91	
Mg VIII	339.006	339.0	$2p\ ^2P_{3/2}$ - $2s\ 2p^2\ ^2S_{1/2}$	3.7	0.96	0.14	6.00	5.91	
Ne VII	559.948	560.0	$2s2p\ ^3P_0$ - $2p^2\ ^3P_1$	0.1	1.89	0.74	6.02	5.71	0.87
Cr XIII	560.1		$3s\ 3p\ ^1P_1$ - $3p^2\ ^1D_2$					6.17	0.13
Si VIII	314.327	314.4	$2s^22p^3\ ^4S_{3/2}$ - $2s2p^4\ ^4P_{1/2}$	7.6	1.67	0.19	6.02	5.93	
Si VIII	319.826	319.8	$2s^22p^3\ ^4S_{3/2}$ - $2s2p^4\ ^4P_{5/2}$	18.4	2.01	0.21	6.02	5.93	
Si VIII	316.205	316.2	$2s^22p^3\ ^4S_{3/2}$ - $2s2p^{44}P_{3/2}$	13.5	1.80	0.19	6.02	5.93	
Fe X	345.723	345.7	$3s^2\ 3p^5\ ^2P_{3/2}$ - $3s\ 3p^6\ ^2S_{1/2}$	7.4	0.97	0.10	6.03	5.98	
Ar VIII	337.257	337.2	$3d\ ^2D_{5/2}$ - $4p\ ^2P_{3/2}$	1.0	0.00	0.00	6.03	5.64	
Mg IX	368.070	368.1	$2s^2\ ^1S_0$ - $2s\ 2p\ ^1P_1$	81.5	0.94	0.09	6.03	5.98	
Fe X	365.543	365.5	$3s^2\ 3p^5\ ^2P_{1/2}$ - $3s\ 3p^6\ ^2S_{1/2}$	3.9	0.82	0.09	6.04	5.98	
Si IX	345.124	345.1	$2s^22p^2\ ^3P_1$ - $2s2p^3\ ^3D_2$	14.0	1.04	0.11	6.05	6.06	0.74
Si IX	345.0		$2s^22p^2\ ^3P_1$ - $2s2p^3\ ^3D_1$					6.06	0.26
Fe XI	341.113	341.1	$3s^2\ 3p^4\ ^3P_2$ - $3s\ 3p^5\ ^3P_1$	4.2	0.62	0.07	6.06	6.06	
Fe XI	352.662	352.7	$3s^2\ 3p^4\ ^3P_2$ - $3s\ 3p^5\ ^3P_2$	10.7	1.02	0.10	6.06	6.06	
Fe XI	369.153	369.1	$3s^2\ 3p^4\ ^3P_1$ - $3s\ 3p^5\ ^3P_2$	2.9	1.12	0.12	6.06	6.06	
Ca X	574.010	574.0	$3s\ ^2S_{1/2}$ - $3p\ ^2P_{1/2}$	1.3	0.95	0.10	6.07	5.86	
Ca X	557.765	557.8	$3s\ ^2S_{1/2}$ - $3p\ ^2P_{3/2}$	2.5	0.99	0.10	6.08	5.86	
Al X	332.789	332.8	$2s^2\ ^1S_0$ - $2s\ 2p\ ^1P_1$	9.4	0.80	0.10	6.10	6.10	
Mg X	609.793	609.8	$2s\ ^2S_{1/2}$ - $2p\ ^2P_{3/2}$	33.6	0.94	0.09	6.10	6.05	
Mg X	624.941	624.9	$2s\ ^2S_{1/2}$ - $2p\ ^2P_{1/2}$	13.6	1.18	0.12	6.10	6.05	
Si X	621.079	621.1	$2p\ ^2P_{1/2}$ - $2s\ 2p^2\ ^4P_{1/2}$	0.3	0.45	0.09	6.11	6.13	
Fe XII	352.106	352.1	$3s^2\ 3p^3\ ^4S_{3/2}$ - $3s\ 3p^4\ ^4P_{3/2}$	9.0	1.01	0.10	6.11	6.14	
Fe XII	346.852	346.8	$3s^2\ 3p^3\ ^4S_{3/2}$ - $3s\ 3p^4\ ^4P_{1/2}$	4.9	0.90	0.10	6.12	6.14	
Fe XII	364.467	364.5	$3s^2\ 3p^3\ ^4S_{3/2}$ - $3s\ 3p^4\ ^4P_{5/2}$	12.8	0.98	0.10	6.12	6.14	
Si X	347.403	347.4	$2p\ ^2P_{1/2}$ - $2s\ 2p^2\ ^2D_{3/2}$	18.0	0.74	0.08	6.13	6.14	
Fe XIII	348.183	348.2	$3s^2\ 3p^2\ ^3P_0$ - $3s\ 3p^3\ ^3D_1$	11.0	1.06	0.11	6.22	6.20	

Fe XIII	321.400	321.5	$3s^2\ 3p^2\ {}^3P_2$ - $3s\ 3p^3\ {}^3P_1$	2.4	1.02	0.19	6.22	6.20	
Al XI	568.120	568.2	$2s\ {}^2S_{1/2}$ - $2p\ {}^2P_{1/2}$	1.8	0.68	0.07	6.22	6.16	
Al XI	550.031	550.1	$2s\ {}^2S_{1/2}$ - $2p\ {}^2P_{3/2}$	2.1	1.17	0.12	6.22	6.16	
Fe XIV	353.831	353.8	$3s^2\ 3p\ {}^2P_{3/2}$ - $3s\ 3p^2\ {}^2D_{5/2}$	4.7	1.19	0.13	6.25	6.26	0.78
Al VII	353.8		$2s^22p^3\ {}^4S_{3/2}$ - $2s2p^4\ {}^4P_{3/2}$					5.82	0.19
Fe XIV	334.172	334.2	$3s^2\ 3p\ {}^2P_{1/2}$ - $3s\ 3p^2\ {}^2D_{3/2}$	25.9	0.66	0.07	6.29	6.26	
Si XII	520.665	520.7	$1s^22s\ {}^2S_{1/2}$ - $1s^22p\ {}^2P_{1/2}$	8.5	1.13	0.11	6.32	6.28	
S XII	538.680	538.7	$2s^2\ 2p\ {}^2P_{3/2}$ - $2s\ 2p^{24}P_{3/2}$	0.3	0.73	0.24	6.33	6.34	
Fe XV	327.011	327.0	$3s3p\ {}^3P_2$ - $3p^2\ {}^1D_2$	1.7	0.76	0.23	6.33	6.33	
Fe XVI	360.761	360.8	$3s\ {}^2S_{1/2}$ - $3p\ {}^2P_{1/2}$	20.9	1.18	0.12	6.35	6.41	0.90
Fe XIV	360.8		$3s\ 3p^2\ {}^2D_{3/2}$ - $3p^3\ {}^2D_{3/2}$					6.25	0.10

Chapter 7

The SOHO-Sun-Ulysses quadrature observations

7.1 Introduction

Section 2.5 describes the quadrature configuration that is periodically reached by the SOHO and Ulysses satellites while moving around their orbits. In the last part of this research programme, the author was involved in an international collaboration aimed at studying the coronal and solar wind compositions. The Joint Observing Program, JOP 112, is aimed mainly at deriving the profile of element abundances as a function of solar distance. It involves several instruments on SOHO (CDS, UVCS, SUMER, LASCO) and Ulysses (SWOOPS, SWICS) which carried out measurements during the Winter 1999 and Summer 2000 quadratures.

The author was involved in planning the CDS observations and in the analysis of both CDS and UVCS data. Details are given in the following sections. The UVCS data were made available by the Osservatorio Astrofisico di Arcetri (IT).

Further ultraviolet measurements were made by the spectrometer SUMER. The data were provided by Max-Planck-Institut für Aeronomie (Germany).

The LASCO coronagraphs provide measurement of the K corona from 2 to 32 $R_{\odot}$. The data used in this JOP were provided by Naval Research Laboratory (US).

The SWOOPS instrument on Ulysses is composed of two electrostatic analizers for electrons and positive ions measurements. It provides 3-d velocity of protons, electrons and double ionized He in the solar wind. The data for the JOP were provided by Los Alamos National Laboratory (US).

The SWICS is a mass spectrometer able to measure element and ionic-charge com-

position of all major solar wind ions. Moreover, it provides their temperature and mean speed. The data for the JOP 112 were provided by the University of Maryland (US).

7.2 The Winter 1999 Quadrature

The JOP 112 was first made ready for the 8 December 1999 quadrature. Coordinated observations among several SOHO instruments were planned between the 4th and 12th December. The quadrature was expected to occur when Ulysses was at a distance of about 2.2 AU at a latitude of -80° in the south-west quadrant.

The planning for CDS occurred at the Multi-Experiment Data Operation Centre for SOHO (MEDOC) in France. This centre has the same facilities as the EOF at Goddard Space Flight Center (US) (Section 4.2). Near real-time SOHO images arrive at MEDOC, so that it is possible to properly point the instruments during the scheduling of observations.

Unfortunately, when everything was ready for the observations, SOHO had problems and the coordinated observations could not take place. On 1999 November 28 one of the computers on board SOHO reset for an unknown reason. This automatically switched the satellite into Emergency Sun Reacquisition (ESR) mode. During ESR, the spacecraft broadcasts low-rate engineering data only without any science. During the following days a standard manoeuvre to recover the satellite was performed, but a series of problems were encountered and the satellite was only back to Normal Mode two weeks later. CDS was only able to run on the 11th and 17th of December. UVCS data were obtained for the 11 and 12 December.

During this time, the author learned to use the program MK_PLAN to plan CDS observations. This included learning: how to choose the study that was most suitable for the scientific targets; to program a new study; to plan the time of exposures, pointing the observations and fitting them in with the rest of the daily CDS observing plan.

Once the JOP was definitely cancelled, it was decided to use the observations of the few available days to test the exposure times of the observations for the conditions that were expected in case the JOP could be rescheduled for the next quadrature.

It was then planned to carry out the UCLAN_N2/v36 NIS study, which consists of a $120'' \times 150''$ raster of full spectra (see Figure 7.1). The first raster, which is closer to the limb, was repeated three times, while the second was run five times. Each observation lasted 1^h20^m. Multiple observations of the same target were made to improve the signal/noise ratio. On the 17th some GIS observations were taken using the 8^m20^s GIS2SIN/v2 study, that consists of a $4'' \times 4''$pixel.

Not much work has been done on these data. As mentioned, the data were just used to

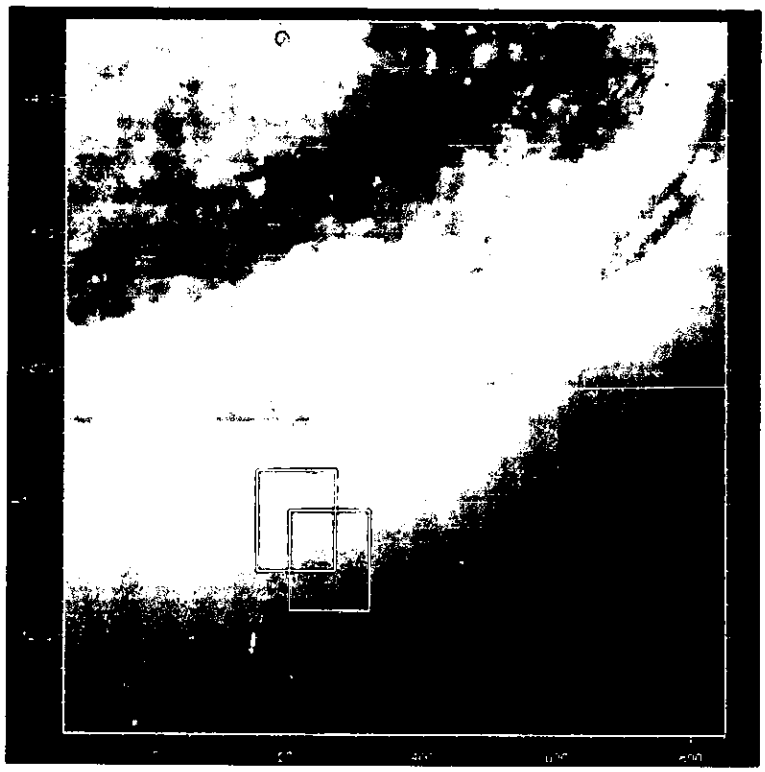

Figure 7.1: NIS rasters for the pointing of the 11 December 1999. The spectrometer field of view is marked by the white squares over imposed to an EIT 171 Å image of the corona for that day.

test the exposure time. The NIS data that relate to the same area covered were averaged. The resulted spectra appear to be sufficiently intense to be used for the scientific purpose.

7.3 The Summer 2000 Quadrature

7.3.1 The Data

The next quadrature occurred on the 13th June 2000. By that time Ulysses was at a heliocentric latitude of 58.2° in the south-east quadrant at a distance of about 3.3 AU. Due to the uncertainty in mapping the Ulysses observations back to the Sun (Section 2.5), the coordinated observations were made over a period of approximately two weeks (5th-18th June for SOHO and 20th June - 7th July for Ulysses). The delay in the Ulysses observations in comparison to those of SOHO, takes into account the 2-3 weeks that the plasma takes to reach Ulysses once it has left the Sun. During the SOHO observations, due mainly to the motion of this satellite around the Sun, the SOHO-Sun-Ulysses angle changed from 82.5° to 94.5°.

In the following sections the coordinated observations taken with CDS and UVCS are

explained. Figure 7.2 illustrates the field of view of the instruments during the observations. The UVCS slit at 1.6 $R_\odot$ is marked by a dark thick line, the CDS raster by small white squares.

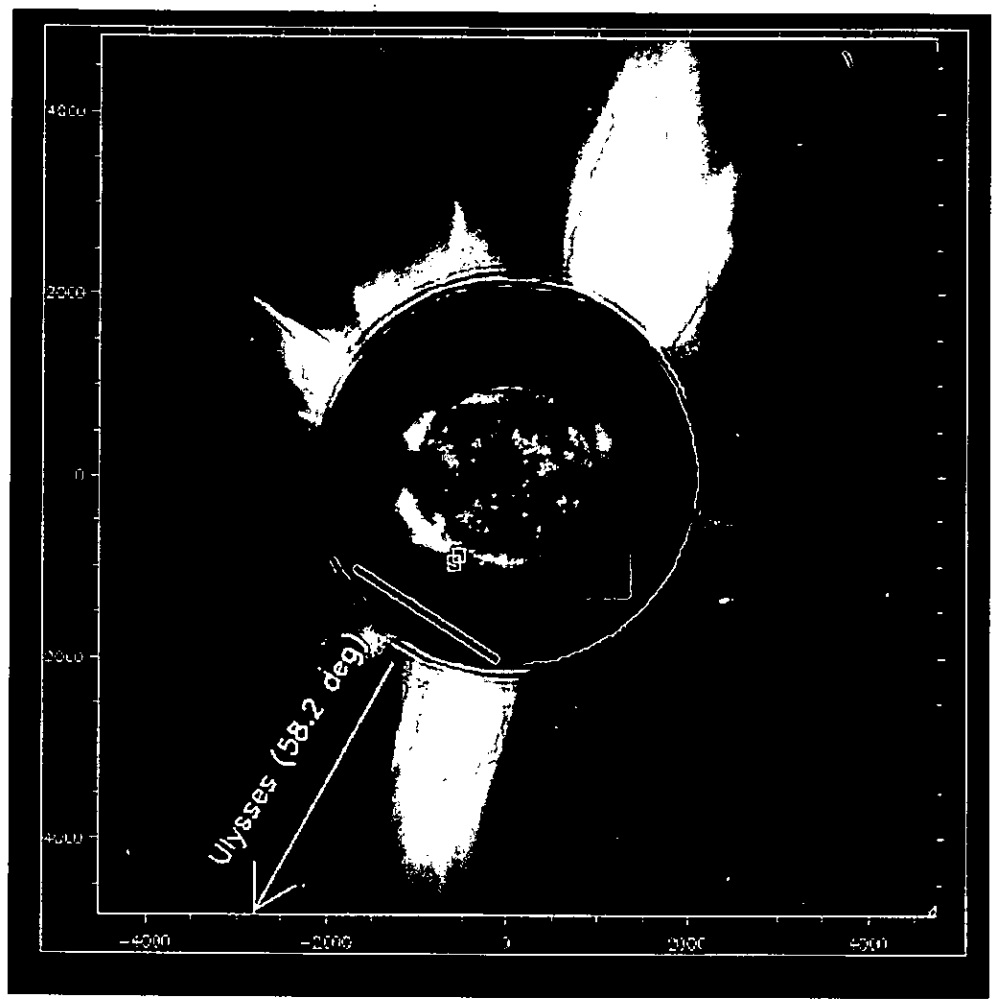

Figure 7.2: Lasco C2 and EIT composite image of the solar corona on the 13th of June 2000. The direction of Ulysses in indicated by the white arrow; the UVCS slit at 1.6 $R_\odot$ is marked by the dark thick line; the CDS field of view is indicated by the white rectangles (NIS rasters) and dots (GIS pixels) within the rectangle.

The CDS Observations

The CDS observations were taken on the 12,13,16 and 17 June 2000. Both the NIS and GIS spectrometers were used. The NIS data are composed of 120″× 150″ rasters of full spectra. The GIS data are composed of a 4″×4″ pixel positioned at different points within the NIS field of view. The NIS study was UCLAN_N2/v36, the same used for the streamer study (see Chapter 4), for the GIS observations the study GIS2SIN/v2 was used. For details on the instruments see Chapter 2.

On the 12th June the centres of the rasters were at a latitude of about -66°. The NIS observations of the raster closest to the Sun was repeated three times while the raster further out was observed five times. Each of them lasted about 1^h20^m. Each of the GIS observations, of duration of about 8^m20^s, was repeated more than once depending on their distance from the limb. The spectra from the repeated observations of the same place will be averaged in order to increase the signal/noise ratio. The configurations used here for the observations, in fact, reach distances of more than 1.2 $R_\odot$. At this distance the signal is very low and multiple observations are required.

On the 13th June the NIS rasters were centred at the Ulysses latitude (58.2°). Similarly to the previous day, multiple observations with NIS and GIS were made, covering different distances and latitudes, in order to be able to derive variations in the physical parameters with latitude and with distance from the Sun. On the 16th the configuration used on the 12th was repeated, while on the 17th the Ulysses direction was again targeted. On this last day we tried to reach much greater distances from the limb, centring the more distant rasters at 1.27 $R_\odot$. This observation required six exposures.

The UVCS Observations

The UVCS observations were carried out from the 6th to the 19th of June. The instrument configuration had the slit perpendicular to the radial direction from the Sun, with the centre at -58.2° in the south-east direction. The heights of the observations above the limb were: 1.6, 1.9 and 2.2 $R_\odot$. The observations were taken with the OVI channel, using the grating positions: 45000, 56000, 83000, 98000, 192000, 168208, 226000. In this way the wavelengths covered spanned about 951 Å to 1117 Å for the primary channel, and about 1180 Å to 1260 Å for the redundant channel. The Lyα channel was not used, and the H-Lyα line together with other important lines visible there, were observed on the redundant channel. A more extensive waveband available here allows the observation of more lines than previously observed in the streamer study of Chapter 4. This includes lines such as O V (629.73 Å II order), Ca X (557.74 Å II order), Mg X (609.76 Å II order) and Mg X (624.95 Å).

The observations consist of sequences of 200 sec exposures, that will be combined to obtain a total exposure time of about 2^h for each grating positions where there is no H-Lyα 1215 Å, and 1^h10^m if the H-Lyα is observed. A 100μm slit was used, which gives $70''$ of spatial resolution and a spectral resolution of 0.1986 Å for the primary channel and 0.0182 Å for the redundant.

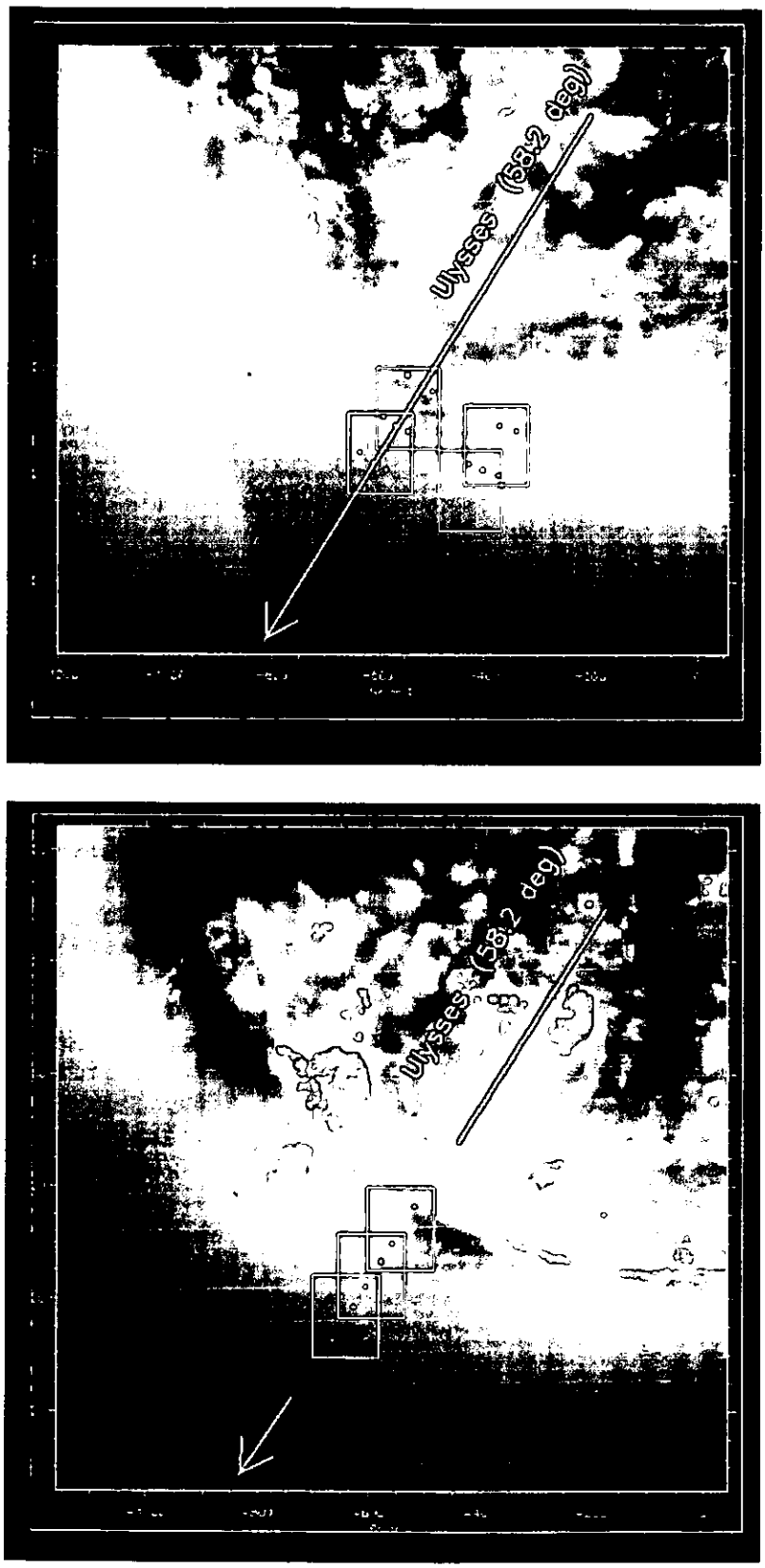

Figure 7.3: NIS rasters (white squares) and GIS pixels (dots) indicating the fields of view of CDS observations superimposed on an EIT image of the solar corona. The Ulysses direction is labelled by the white arrow. Top: on the 12th June the raster centres were at about -66°; and 58.2° on the 13th June. On the 16th June the same configuration as on the 12th was repeated. Bottom: CDS field of view on the 17th June.

7.4 Solar Conditions During the Observations

Figure 7.4 shows a sequence of EIT 171 Å images of the solar corona during the period of the quadrature, apart from the first one (top left) that refers to a week before the start of it. The images refer to the days, from top left cklockwise, 1, 6, 11 and 15 June. The image of the Sun on 1 June (top left image) shows, close to the west limb, a small coronal hole at the equatorial region. On 5 June it has already reached the west limb. As it will be shown below (Figure 7.5) this coronal hole may be responsible for the dark region seen by LASCO at the equator, in the extended coronal images at the beginning of the quadrature. During the whole period of the quadrature the Sun appears active at all the latitudes, and other small coronal holes are seen at various latitudes.

Figure 7.5 shows a sequence of LASCO C2 images of the solar corona over a period of time that covers the quadrature (Suess, 2001). Superimposed as black lines on each image are the equator and the direction of Ulysses (-58.2°). From these images it is clear that the corona was evolving quite rapidly as the days passed. The corona has the characteristic appearence of high activity, typical of this period, approaching the maximum of the solar cycle: bright streamers extend over most latitudes and appear and disappear over a few days. From these images it seems that at the beginning of the quadrature the direction to Ulysses passed through a dark area, possibly a small coronal hole, while later on it intercepted the bright streamers. Dark regions near the equator suggest the presence of low-latitude coronal holes. *In situ* observations during the quadrature were taken by SWICS and SWOOP instruments on Ulysses. The footpoints on the Sun of the plasma sampled by Ulysses have been derived with the "constant velocity approximation" (see above). Figure 7.6 shows the Ulysses footpoint (red thick line) between the 5th and 18th June 200 overplotted on a Wilcox Solar Observatory source surface (2.5 $R_{\odot}$) model magnetic field for the Carrington rotations 1963-1964 (JOP 112 WWW page). The Figure shows the Ulysses footpoint passing through a unipolar region (a coronal hole) at the beginning of the quadrature, and then from the 15th remaining in the streamer belt. It is likely that the source of this unipolar magnetic field is one of the low-latitude coronal holes, seen in LASCO images, expanding towards the polar regions with increasing distance from the Sun.

7.5 Preliminary UVCS Results

A preliminary analysis of the UVCS data has been carried out. The purpose was to extract information about density and temperature along the Ulysses direction. The diagnostic

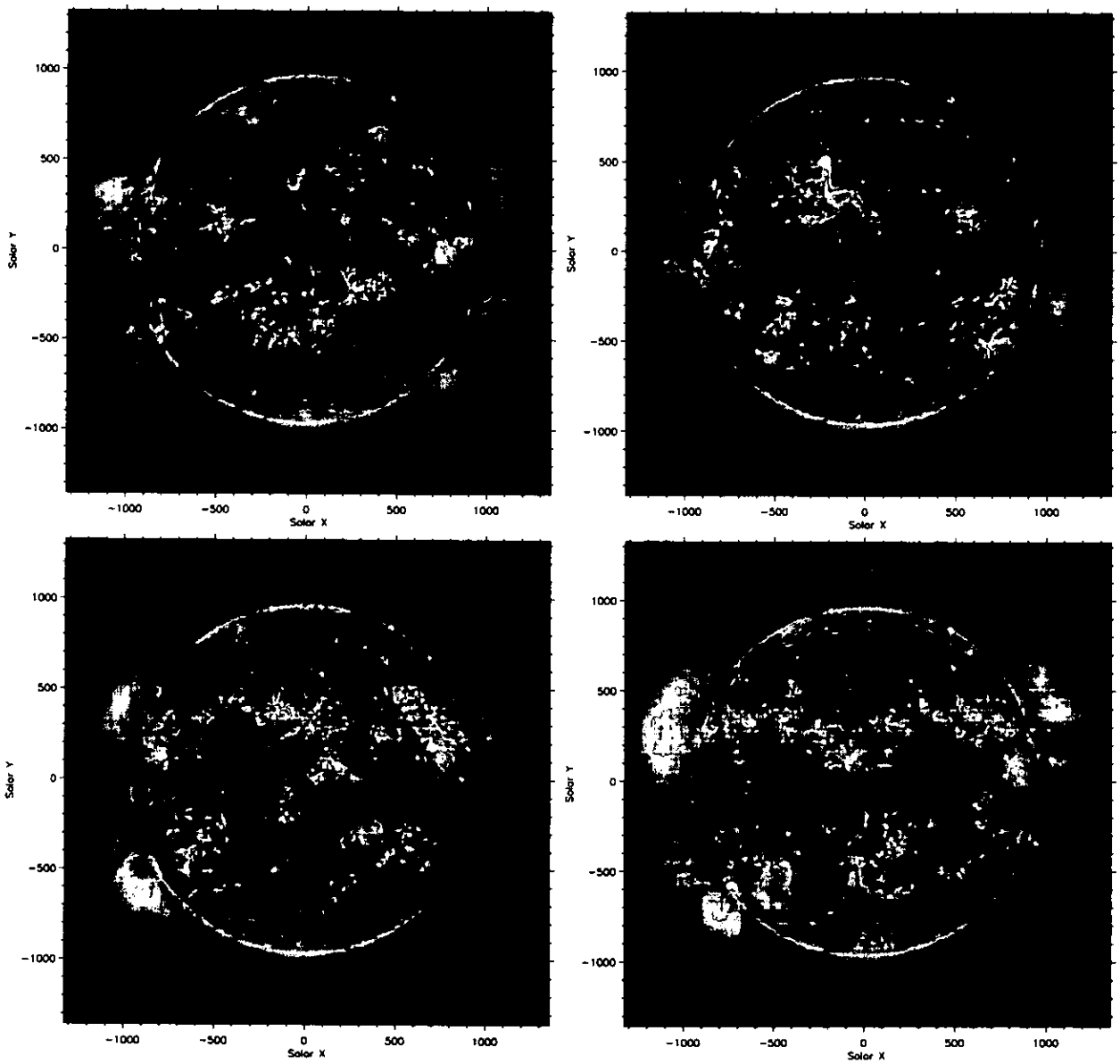

Figure 7.4: SOHO/EIT 171 Å images of the solar corona during the quadrature. From top left clockwise direction, the imeges refer to the 1, 5, 11 and 15 June.

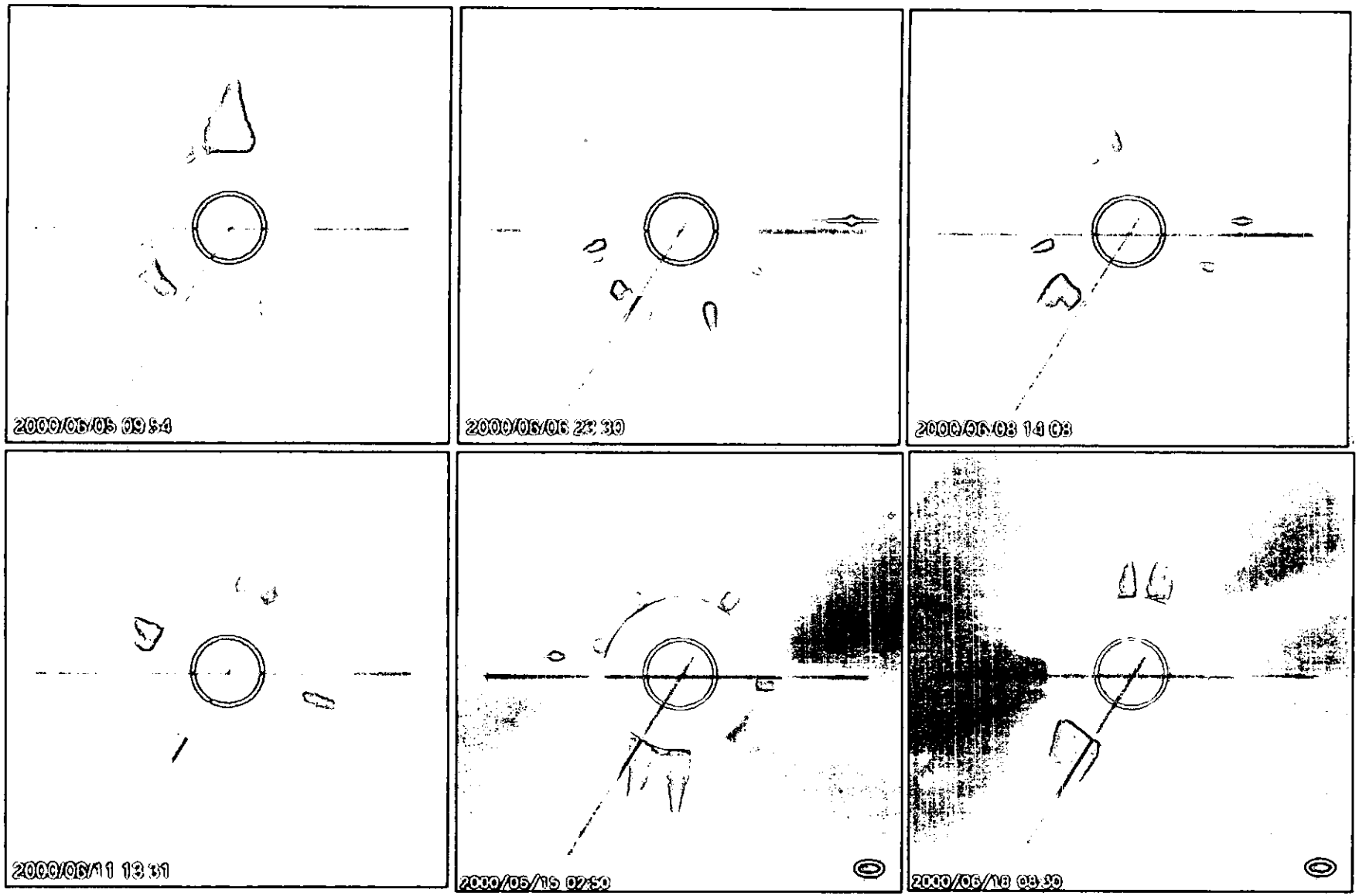

Figure 7.5: LASCO C2 images of the solar corona, from 2 to 6 $R_{\odot}$, during the quadrature. The black lines indicate the solar equator and the direction to Ulysses in the south-east quadrant. (Figure taken from the JOP 112 WWW page.

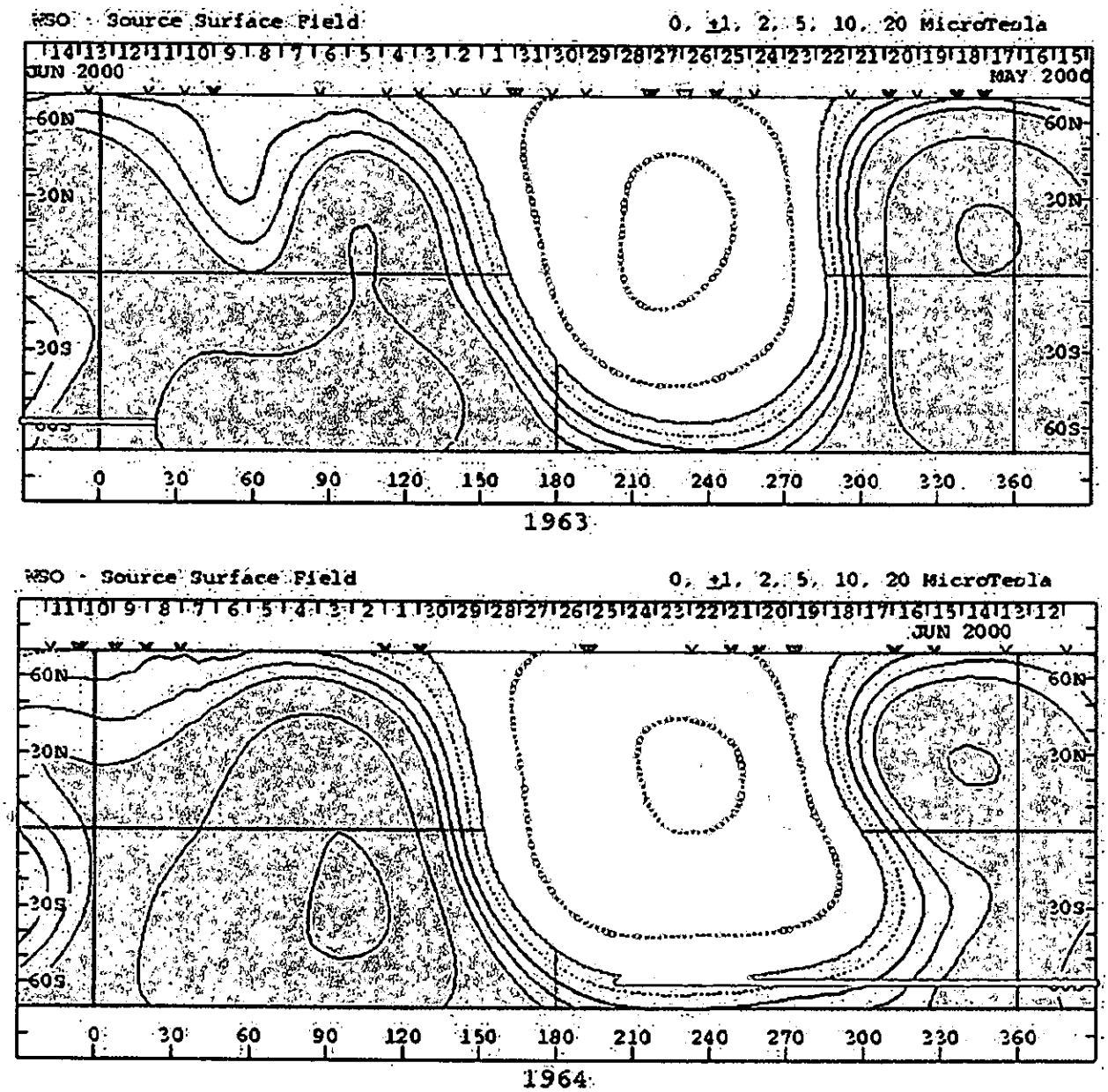

Figure 7.6: Source surface magnetic field at 2.5 $R_\odot$ with the Ulysses foot point during the quadrature superimposed (red thick line). The date is shown on the upper axis. Before the 15th June Ulysses was passing through a unipolar region, and then it entered the streamer belt for the rest of the time covered by the quadrature observations. It was close to the boundary of an open field region (with opposite polarity to the first) after the 20th June. These data correspond to Ulysses *in situ* observations obtained from 20 June to 7 July. (Figure provided from the JOP 112 WWW page).

techniques applied in the streamer study of Chapter 4 have also been applied here. In the future a more extensive study of the data will be performed.

The data were received in FITS format already calibrated. The repeat exposures of the same observation were added together as explained in Section 2.2.3.

At this stage, only the data from the part of the slit intersecting the Ulysses direction were selected and analysed. These data are from the single spatial pixel located at the centre of the slit.

The following step consisted of identifying the lines. So far this is not complete, because the spectra contain several unidentified lines. For the purpose of this preliminary study only the brighter and well-known lines were used. Figures A.17 and A.16 reported in the Appendix A.5 show examples of the UVCS spectra at 1.6 and 1.9 $R_{\odot}$. An example of the redundant spectrum is also included. Part of the line intensities were provided (G. Poletto private communication), other were calculated by the author using the method described in Section 2.2.3. Figures 7.7 and 7.8 (provided by G. Poletto) show the O VI 1032 Å integrated intensities as a function of the slit position, at 1.6 and 1.9 $R_{\odot}$. These positions are indicated in arcsec from the slit centre (0 position). The arrows indicate the Ulysses direction. These profiles underline the streamer morphology, which is characterised by a bright O VI "core" that weakens toward its "edges". As anticipated by the LASCO images (Figure 7.5), the Ulysses direction crosses the streamer in different parts as the day of observation changes. Moreover, a change in the streamer's morphology is also seen going from 1.6 $R_{\odot}$ to 1.9 $R_{\odot}$. These Figures show that on the 11th and 13th June the Ulysses direction was crossing through the streamer "edge" (or "leg"), which can be recognised as a steep intensity gradient. On the 16th June the Ulysses direction is clearly crossing the streamer "core". The situation on the 12th June is less clear, because of the change in morphology of the streamer between 1.6 and 1.9 $R_{\odot}$. The fact that the Ulysses direction crosses different parts of the streamer in different days, gives the possibility of studying the physical parameters across the streamer. Table 7.1 lists the integrated intensities of the UVCS lines used for this preliminary study. The estimated error is 20% of the calculated intensity.

7.5.1 Electron Density and Temperature

This preliminary analysis is based on the assumption that the observed plasma is at rest. This assumption generally holds in streamers up to 2 $R_{\odot}$. A way to check this is by the ratio of O VI 1032/1037 lines. As described in Section 3.1.2 in the presence of high flow velocity this ratio changes. The check was made all along the slit, with a negative result

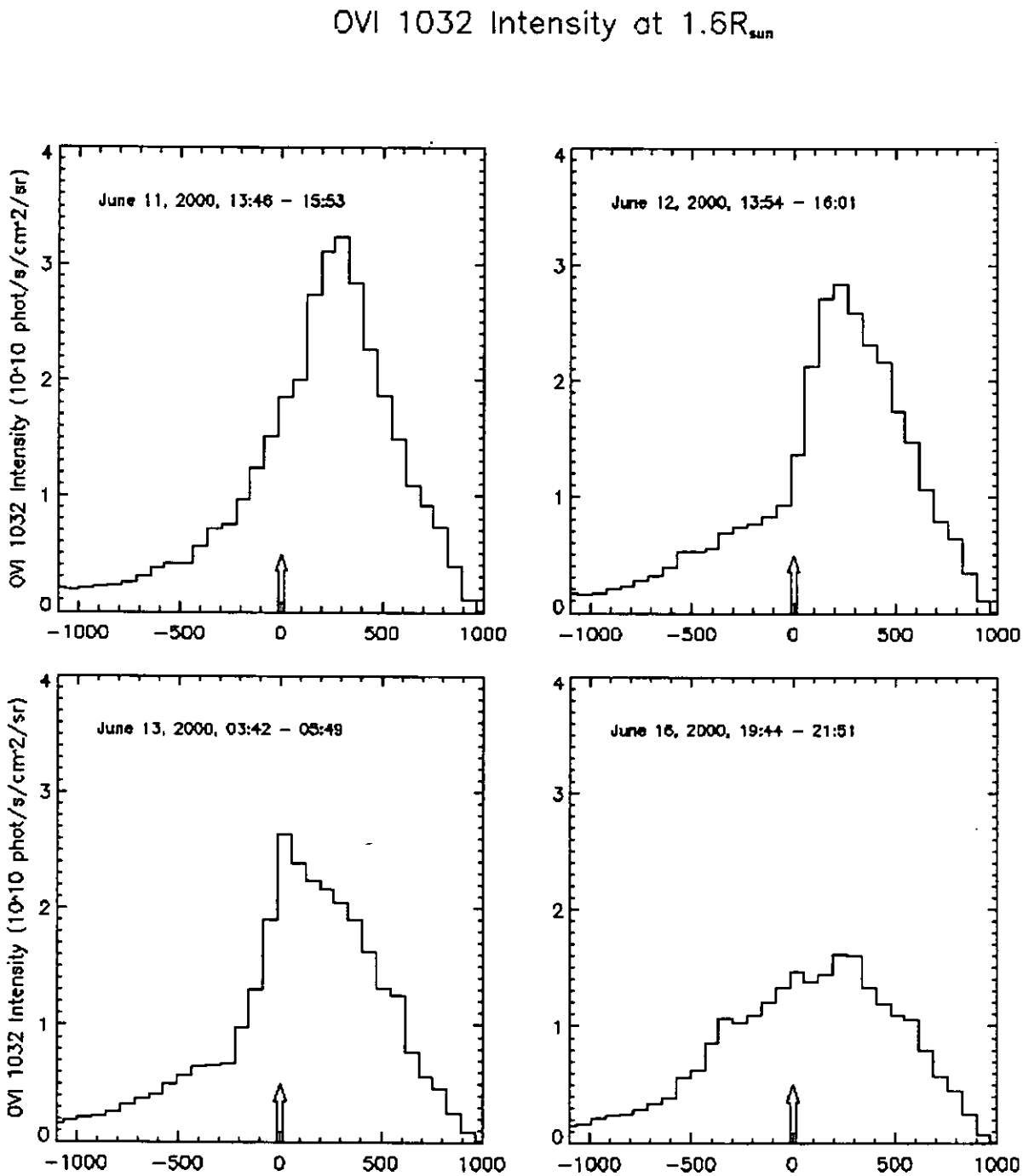

Figure 7.7: O VI 1032 Å integrated intensities at 1.6 $R_{\odot}$ as a function of the slit position on the 11th, 12th, 13th and 16th June 2000. The distance from the slit centre is given in arcsec. The arrows indicate the Ulysses direction. (Figure provided byG. Poletto)

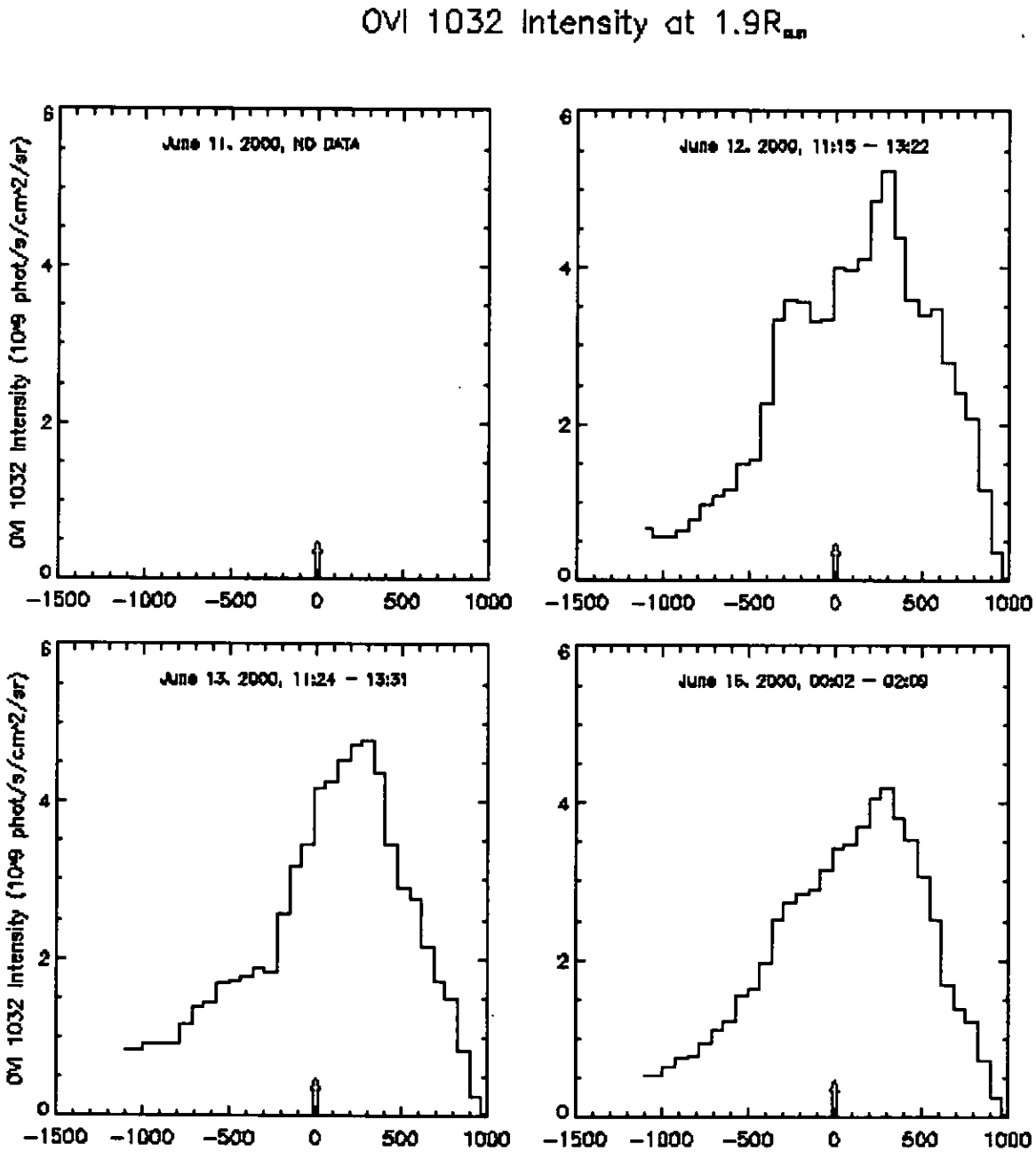

Figure 7.8: Same as previous Figure (7.7) but obtained for data taken at 1.9 $R_{\odot}$. No data are available for the 11th June. (Figure provided by G. Poletto).

Table 7.1: Line intensities from UVCS observations, at the slit centre, in 10^7 phot cm^{-2} s^{-1} sr^{-1}. λ_{ID} indicates the theoretical wavelength (in Å) taken from the CHIANTI database. The error on the intensity was estimated to be ±20%.

Spectrum and	Transition	11 June	12 June		13 June		16 June	
λ_{ID} (Å)		1.6 $R_\odot$	1.6 $R_\odot$	1.9 $R_\odot$	1.6$R_\odot$	1.9$R_\odot$	1.6 $R_\odot$	1.9$R_\odot$
Fe XIII] 510.055	$3s^2\ 3p^2\ ^3P_2$ - $3s3p^3\ ^5S_2$	6.48	-	-	11.3	2.79	8.84	1.17
H I 1025.720	Lyβ	31.3	605	14.6	69.4	13.3	74.4	16.5
[Fe X] 1028.394	$3d\ ^4D_{7/2}$ - $3d\ ^4F_{7/2}$	21.9	7.9	1.94	23.5	2.03	7.33	1.84
O VI 1031.912	$2s\ ^2S_{1/2}$ - $2p\ ^2P_{3/2}$	1588	100	350	2182	334	1360	361
O VI 1037.614	$2s\ ^2S_{1/2}$ - $2p\ ^2P_{1/2}$	579	365	112	807.8	107	508	124
H I 1215.740	Lα	26400	17464	10000	27300	10000	22500	8500
[Fe XII] 1242.005	$3p^3\ ^4S_{3/2}$ - $3p^3\ ^2P_{3/2}$	172	115	16.0	192	10	124	24.8

(G. Poletto, private commumication).

As described in Section 3.3, H-Lyman and O VI lines on UVCS are affected by the double contributions of radiative and collisional excitations. Following the methods described in Section 3.3, these components were separated. Unlike the case of the streamer study described in Chapter 4, this time more up-to-date disc intensities were available (G.Poletto private communication), covering the period of the present observations. This enabled a more reliable separation of the radiative and collisional components of the H-Lyman lines.

The lines listed above have been used to estimate electron density and temperature. Electron temperature was derived by applying the diagnostic technique indicated in this thesis as "log R v. log T" (Section 3.4 for the theory and Section 4.5.1 for previous applications). The collisional component of the Lyβ together with the three iron lines listed in Table 7.1 were used for this purpose. It should be remembered that this technique allowes the determination of the absolute element abundance (of the iron for the present case) of the observed plasma, from the assumed abundance used in deriving the theoretical intensities of the lines used. As with the streamer study of Chapter 4, the Feldman (1992) photospheric abundance for iron was taken as the reference element. The theoretical intensities were derived using the Mazzotta et al. (1998) ionization equilibrium in the CHIANTI database. For the days where the Fe XIII line was not visible, the electron temperature was derived by applying the line ratio technique using Fe XII/Fe X (see Section 3.4). Table 7.2 lists the results.

The Table shows the temperature to be higher at 1.6 $R_\odot$ than at 1.9 $R_\odot$, apart from on the 12th June. However, on this day, the slit profiles reveal significantly different

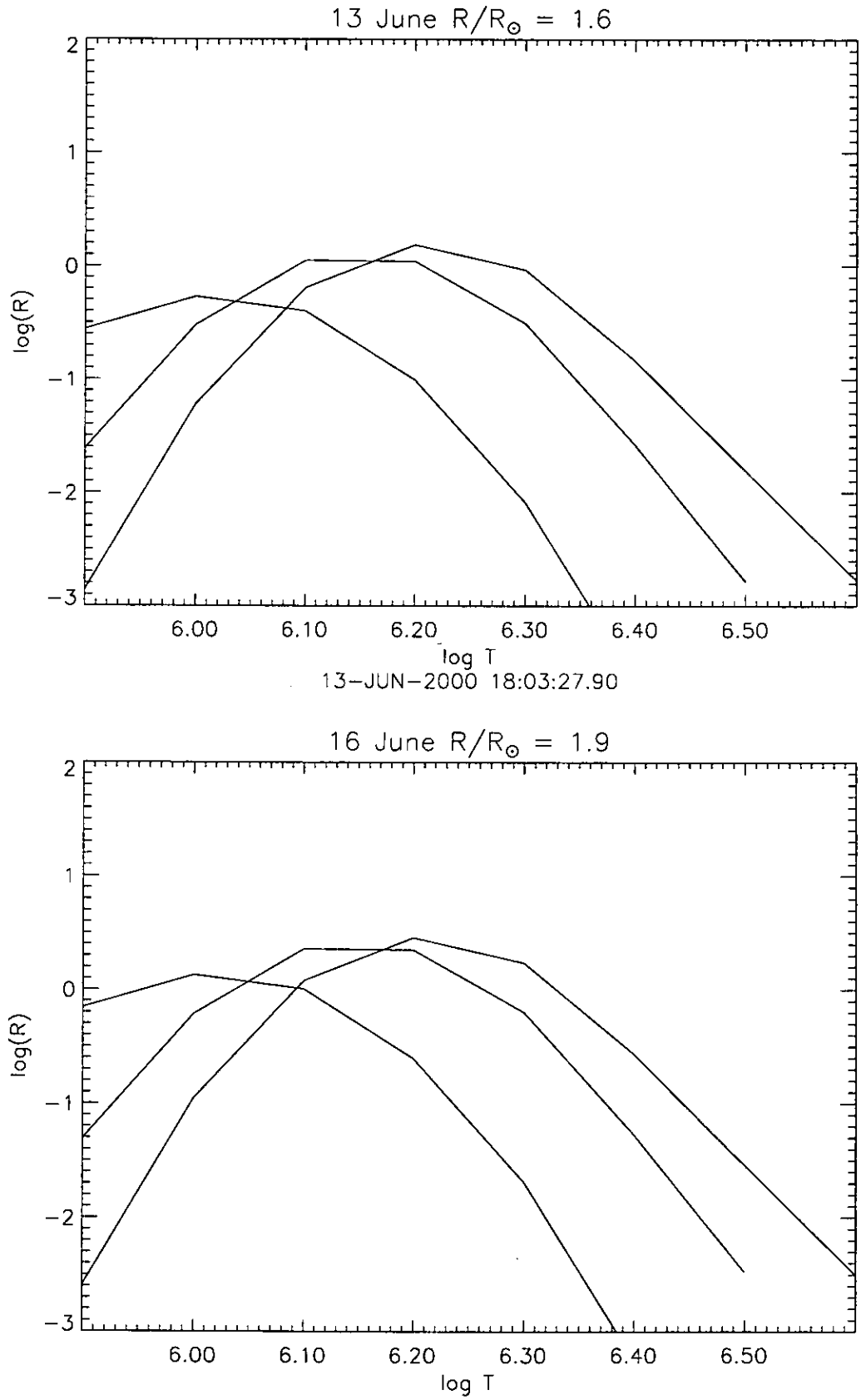

Figure 7.9: "log R v. log T" plots for the 13th June at 1.6 $R_\odot$, and 16 June at 1.9 $R_\odot$. Fe X, Fe XII, Fe XIII and Lyβcollisional intensities listed in Table 7.1 were used.

conditions at the two distances. At 1.9 $R_\odot$ (Figure 7.8) there appears to be a strong secondary component close to the slit centre. This does not appear at 1.6 $R_\odot$ (Figure 7.7), and so could indicate a brightening of this part of the streamer, or a nearer of a second streamer into the field of view when observing at 1.9 $R_\odot$.

Apart from the 12th June, the results in the Table indicate that at 1.9 $R_\odot$ the temperature has already passed the maximum value found in the coronal temperature profile. This is in agreement with the results found in the streamer study of Chapter 4 (Section 4.5.1). Moreover, comparing 13th and 16th June, it seems that the temperature decreases from the streamer core to the edge at both the solar distances. This last result appears as a "tendency" of the temperature to decrease toward the edge. However, for some of the values the errors are of the same order as the change so it is not a significant result. This aspect needs more investigation in the future.

Electron densities were derived using the O VI 1032 Å lines in the diagnostic technique described in Section 3.5 Equation 3.38. The parameters used in the Equation 3.38 are the same as those listed in Section 3.5. The electron temperatures used are those listed in Table 7.2 and the resulting densities are listed in the same Table. As expected, the

Table 7.2: Electron densities and temperatures derived from UVCS data for June data. The temperatures are in 10^6 K units and densities in 10^6 cm^{-3}

Date	T_e		N_e	
	1.6 $R_\odot$	1.9 $R_\odot$	1.6 $R_\odot$	1.9 $R_\odot$
11 June	1.17 ± 0.23	-	5.0 ± 1.0	-
12 June	1.20 ± 0.01	1.48 ± 0.01	4.6 ± 0.9	1.7 ± 0.3
13 June	1.23 ± 0.24	1.03 ± 0.01	5.6 ± 1.1	1.5 ±0.3
16 June	1.38 ± 0.28	1.26 ± 0.25	5.6±1.1	2.5 ±0.5

density decreases with the distance, but a distinct variation between the streamer core and its edge is not seen. However, it seems that the density gradient is higher in the leg than in the core.

The results presented here are preliminary and need further investigation before they can be confirmed.

7.6 The Future Work

The main purpose of JOP 112 was the study of element abundances in the upper corona and in the solar wind. However, in this preliminary study the attention has focused on the temperature and density variations of the plasma travelling in the direction of Ulysses. The aim was to establish which part of the streamer, if any, might correspond to the plasma sampled by Ulysses.

To confirm or not the results presented above, a more extended analysis needs to be done. The same study will be carried out throughout the streamer, determining temperature and electron density distributions along the streamer. It is important to note that this will be the first time that this kind of analysis has been done.

For the main purpose of the JOP, the data along the Ulysses direction will be analysed to extract information on element composition. The evolution in time of the observed streamer will allow, as in the temperature and density cases, the study of the variation in composition across the streamer. Previous results on this topic have already been discussed in Chapter 4. Here the attention will be given to the connection between the corona and the solar wind, to contribute to the knowledge of the origin of the slow wind. In a model recently developed (Ofman, 2000), the streamer legs have been referred as the source of the slow wind. The model is able to explain the enhancement of the O VI abundance in these regions with respect to the streamer core, as the results of the Coulomb friction between the O VI ions and outflow protons. The author showed that in a magnetic configuration like that of a streamer (closed field in the core and open field at the edges), together with an increase of proton flow velocity toward the streamer edge, the friction results in an increase of the minor ion (in the sense of less common) density and flow in the streamer legs. This friction is also expected to affect other minor ions.

The importance of the study of abundances in streamers as a way to trace the slow solar wind source low in the corona and into the extended corona is evident. For this purpose the CDS data collected during the JOP will be used to connect the results found with UVCS with the properties of the low corona. The large range of Fe ions available between NIS and GIS spectra will enable the derivation of temperature over a wider range of plasma temperature than previously(Chapter 4). Moreover, O VI is also visible in GIS spectra, so that it would be of interest to compare it with the O VI from UVCS.

Chapter 8

Conclusions and Suggestions for Further Work

In this chapter the main findings and results obtained during this research project will be summarized. Some of these have already been published (Parenti et al., 1999b,a, 2000a,b, 2001).

Data from CDS and UVCS instruments on SOHO have been used to carry out EUV and UV spectroscopic studies of several different coronal structures, including streamer, coronal holes, a hot-loop system and a macrospicule. Various spectroscopic diagnostic techniques were used to derive electron densities, electron temperatures, element abundances and, for the macrospicule, outflow velocity of the structure.

The CDS data covered areas from 1.02 $R_\odot$ to 1.2 $R_\odot$ in the lower corona. Long-lived and short-lived off-limb structures were studied with the CDS/NIS, including streamer bases, a loop system, macrospicule, coronal holes and coronal hole boundary region. The variety of these observations was made possible by the versatility of the CDS instrument which also includes a large wavelength range. However, off-limb observations produce spectra that are mainly dominated by high-temperature emission lines, and the lack of low temperature lines limited the results obtained from such analyses (see discussion in Section 5.6).

The UVCS data covered regions from about 1.6 $R_\odot$ to 1.9 $R_\odot$ in the upper corona. Observation of equatorial and high latitude streamers were coordinated with those of CDS. The aim was to study the variation with solar distance of the streamers' physical parameters. Moreover, for the first time the DEM technique was applied to off-limb data of the upper corona, for the study of temperature and absolute element abundances.

The diagnostic studies carried out in this thesis have been performed with the use of

the latest available version of the CHIANTI atomic database. This is one of the most up-to-date and complete databases for UV and EUV spectral lines. With the aid of this database, a few new lines, not previously observed in any CDS spectra, were identified.

8.1 Coronal Streamer Studies

In March and May 1998, CDS and UVCS coordinated observations were made with the aim of studying coronal streamers' parameters at the streamer "core", for various plasma conditions (Chapter 4). Studies of the "quiet" equatorial streamer and of the "active" mid-latitude streamers gave the following main results:

- **Electron temperature** profiles versus the solar distance were obtained using the line ratio technique, applied to iron lines for different stages of ionization (Section 4.5.1). This technique gives averaged temperatures along the line of sight. The distances covered are from 1.02 $R_\odot$ to 1.19 $R_\odot$ (CDS) and 1.58-1.6 $R_\odot$ (UVCS). The profiles obtained agreed with temperatures previously obtained for an equatorial streamer, using a power law fit to electron density, and with the assumption that hydrostatic equilibrium holds (*c.f.* Gibson et al., 1999b).

- The temperature profile derived from different line ratios for the "quiet" streamer showed that, as the solar distance increases to around 1.15 $R_\odot$, the plasma tends to become isothermal. On the other hand, different results were obtained for the "active" streamers. In one case the streamer appeared to be multithermal in the lower corona and then thermalise toward one temperature at 1.6 $R_\odot$ in the upper corona. In the other case, where only the upper coronal data were available, the streamer appeared to be non-isothermal.

- These temperature results were confirmed by the use of a different diagnostic technique: the DEM (Section 4.5.3). Previous studies of quiescent streamers in the lower corona (Feldman et al., 1998) and in the upper corona (Raymond et al., 1997), had suggested isothermal plasmas. Thus, it appears to be important to carry out further investigations in order to establish if isothermal plasma is a characteristic of quiescent streamers and multithermal plasma is a characteristic of active streamers.

- The importance of obtaining temperature profiles that cover an extended range of solar distances is a key factor for modelling the solar corona (e.g Wang et al., 1998; Cranmer et al., 1999; Suess et al., 1999). The profiles may constrain the heating

functions used in the models. For such purposes, coordinated observations with various instruments are absolutely necessary.

- **Electron density** profiles were obtained over the same solar distances as those covered for the temperatures (Section 4.5.2). In this case the results obtained are averaged values along the line of sight. Different diagnostic techniques were used for CDS and UVCS data, but the results were in good agreement. The active streamers appeared to have higher density. It was found that the pattern derived for the density profiles can be reproduced by assuming hydrostatic equilibrium. A similar result had already been obtained by Gibson et al. (1999b) for a quiescent streamer, by deriving the density from polarized brightness measurements.

- As in the case of electron temperature, these results need to be confirmed by extending the measurements to a greater solar distance, and filling the gap from 1.19 $R_\odot$ and 1.58 $R_\odot$ that was present in the March 1998 data.

- **Oxygen absolute abundances** were found from UVCS data in the upper corona using two independent methods (Tables 4.7 and 4.8). These agreed in showing a depletion compared to the photospheric abundance of O. The depletion was more marked in the equatorial streamer.

- The streamers studied here did not show the same morphology as that shown by the quiescent streamers studied in the past (which were characterised by a peak in Lyα intensity in the core coinciding with a depletion in O VI intensity). However, the present results for the oxygen abundance are in agreement with others found in the literature for the *active* streamer (Raymond et al., 1997; Marocchi et al., 2001). Further studies need to be made to establish whether or not the different morphology of the streamer observed using the O VI intensity may be to an abundance effect (see Section 4.5.3).

- **Iron absolute abundance** was determined from UVCS data in the upper corona (Table 4.8). In this case too, photospheric or less-than-photospheric values were found in these streamers. The averaged Fe/O ratio found here was consistent with the values found in the slow solar wind (Aellig et al., 1999; Ipavich et al., 1992), which is an indication of the streamers' contribution to the wind. Further studies addressing this topic need to be performed.

- **The absolute abundance of other elements** was found by applying the DEM technique to the UVCS data (Table 4.8 and Figure 4.9). For H reference lines, the

collisional components of the H-Lyα and Lyβ lines were used, adding them to the set of lines to be studied. This is the first time that absolute element abundances have been found using this technique. Previous studies from other authors, instead made use of the isothermal approximation in streamers, but with the present method it was shown that one of the observed streamers was not composed of isothermal plasma. The results obtained for the element compositions were consistent with a previous study (Raymond et al., 1997) in found a general depletion from photospheric values, even if differences were rescontred. However, further studies are needed on this topic. In the present case it was not possible to discriminate between the core and the leg of the streamer, and so it was impossible to establish whether the differences between abundances found here and those of previous studies were due to different types of streamer being observed.

- **Element abundances relative to Fe** were found from CDS data (Table 4.11 and Figure 4.10). Some differences were found relative to photospheric values. Abundances relative to Fe, from the lower (CDS) and upper corona (UVCS) (Table 4.10) showed a general depletion with solar distance. Further studies are needed on this topic, because the mechanisms that generate this depletion are still not completely identified. Gravitational settling appears to be one of those mechanisms (Feldman et al., 1998; Raymond et al., 1998), and this may explain the decrease in abundances with solar distance of elements heavier than H. Moreover, in a scenario where the solar wind flows from the streamer edges (Raymond et al., 1997), the streamer core is more affected by gravitational settling than the edges are, which could explain the greater depletions within this area.

- Further work could also include testing the theory of Ofman (2000) who developed a 3D model for the streamer belt in which Coulomb friction is one of the mechanisms responsible for enhancement of less common ions in streamer legs. The results of this model showed that in areas at streamer edges, where the magnetic field is open, there is an increase in both ion density and outflow velocity. It would be interesting to study the element abundances across the streamer to test this theory. Moreover, Wimmer Schweingruber (1994) found H/O = 1890 $\pm$ 600 for the slow-speed solar wind, and H/O=1590 $\pm$ 500 for high-speed solar wind. It would be interesting to compare these values with those for the streamer core and edge, as a possible signature of the origin of the slow wind.

In June 2000, CDS and UVCS coordinated observations were carried out as part of JOP 112, during the SOHO-Ulysses quadrature. The JOP aim was to study variations in composition, from the lower corona to the solar wind. The observations mainly involved streamers and streamer edges. With these new data, it will be possible to contribute to the unresolved problems mentioned above. The author was involved in planning the CDS observations and has carried out some preliminary analysis.

- CDS and UVCS coordinated observations (Chapter 7) were extended to a wider range of distances than in the March 1998 study (Chapter 4). In this way the gaps in temperature and density profiles with solar distance, were partially covered.

- Preliminary results indicate that the **edge of the streamer may have a lower electron temperature than the streamer core** (Table 7.2). If confirmed, this would be a completely new result.

- A more extended wavelength coverage in the UVCS data provides more lines for DEM studies. This will result in a more thorough diagnostic of element abundances. This in turn could establish whether differences in abundances found from various previous studies are due to differences between streamers or simply due to limitations of the DEM technique.

- The line of sight from Ulysses to the Sun crossed various parts of a streamer on different days. Since the main aim of the JOP was to study data along this direction, it should be possible to extract information on H/O values for different parts of the streamer. As explained above, this is an important diagnostic to test connections between the solar wind and various coronal structures. In particular, it could test the hypothesis that the slow wind originates from streamer edges.

- The new CDS data include GIS data. This extends the wavelength band and hence the number of lines available. As in the UVCS case, the DEM study will be improved considerably as a result. Moreover, a higher stage of ionization of O is observed in these GIS spectra. This will probably allow a determination of the oxygen abundance to be made from these CDS data, which was not possible for the March 1998 data.

8.2 Macrospicule Studies

An off-limb CDS study of a coronal hole was carried out using the March 1998 data. One of the three observations showed a spike-like feature, visible in low temperature emission lines,

which extended from the limb into the corona. This was identified as a "macrospicule". Due to the short-lived nature of the feature, two of the three successive observations made did not show it. This gave the unique possibility of using these two sets of data as "background", distinguishing the macrospicule plasma from it. No such analysis has been reported before in the literature to the author's knowledge. A diagnostic study on the ambient coronal hole that surrounded the feature and of the macrospicule itself was carried out indicating that the features was located in an interplume region. The main results were as follows.

- The **electron density** close to the solar limb (estimated by applying the line ratio technique to the Si IX lines) was calculated to be $\approx 2 \times 10^8$ cm^{-3}. Values for densities obtained at the base of the streamer studied in this thesis (Section 4.5.2), were at least double this value. Similar results were obtained by Gallagher et al. (1999).

- The **electron temperature** in the ambient coronal hole was obtained by the line ratio technique applied using ratios of several different ions. The results showed the presence of a multi-temperature plasma, possibly due to the vicinity of the limb. Similar results were obtained by Doschek et al. (2001) using SUMER spectra.

- Using successive exposures from the CDS raster that showed the macrospicule, and selecting the O V line, the time evolution of the macrospicule was studied. Subtracting the background radiation from these data, it has been shown that this feature reached a maximum in brightness, with the release of a plasmoid and rapidly disappeared. The maximum distance from the limb reached by this plasmoid was estimated to be $\approx$ 40,000 km.

- For the first time, density and temperature were estimated along a macrospicule. These values showed a signature of the plasmoid expelled. In particular, the feature appeared to reach temperatures of at least 5 $\times 10^5$ K, and possibly as much as 1 $\times 10^6$ K. (Some of the lines that emit at 1 $\times 10^6$ K show the feature whilst others do not).

- **The outflow velocity** of the ejected plasmoid was estimated, with an initial mean value of some 80 km s^{-1}. This is consistent with interplume outflow velocity (Patsourakos & Vial, 2000), further indicating that macrospicule sites may be interplume regions.

- These observations did not include data on the macrospicule's base. It is not easy to plan observations of such features, because of their short lifetime and rar-

ity of occurence, but future plans should attempt a more complete observation of macrospicules, including if possible their base.

8.3 Off-limb Loop System

The CDS observations on 6 March 1998, included an off-limb hot loop system, and Section 6.1 described a detailed study of different parts of this loop system.

- The loop system was composed of hot plasma. One of the main results of this study was the preliminary identification of lines (of highly ionised ions) not previously observed by CDS (Table 6.1). The highest temperature lines observed in these spectra were found to be Fe XVII, which emits at about 5.1 $\times 10^6$ K.

- A **temperature** study, using the line ratio technique and the DEM technique, revealed a multithermal structure. In addition, the top of the loop system showed higher temperatures than its base. The DEM study showed two main temperature components, one of which could be associated with the ambient corona (log T = 6.1), and the other with the loop (log T = 6.4).

- **Element abundances relative to photospheric Fe** were derived using the DEM technique. Little variation from photospheric values was detected, although a slighty depletion of all the values was indicated for the top of the loop. Comparison with previous studies revealed that these results are consistent with the composition of active regions.

8.4 Coronal Hole Boundary

CDS observations of a coronal hole boundary region were made in March 1998 (Section 6.2). This appeared as a bright streamer, visible in hot coronal lines, that bounds a dark area (the coronal hole). Two regions at 1.1 $R_\odot$, one in the coronal hole and the other in the streamer, were selected for a diagnostic study.

- **Electron density** was derived applying the line ratio technique with different ratios, ranging from upper transition region to coronal temperatures. Densities in the streamer, obtained from different ratios, are 1.3–2 times higher than that in the coronal hole.

- **Electron temperature** was derived from the line ratio technique and through the DEM technique. The streamer is hotter than the coronal hole by up to about 20 %.

- The DEM study revealed that in the sample taken here for the coronal hole data, the temperature has two main contributions: one at 1×10^6 K, typical of the ambient coronal hole, and the other at about 2.2×10^6 K. The result of the DEM analysis for the streamer shows a single peak at 1.6×10^6 K on a broad DEM curve, indicating a multi-temperature plasma.

- **Element abundances relative to Fe** were derived in both the coronal hole and the streamer. The general tendency of the streamer composition seems to follow the behaviour found for that of the mid-latitude loop system. However, few studies of polar boundary streamers are found in the literature, and further investigations need to be carried out on the study of abundances in these structures, to confirm the results obtained here.

In this thesis new insights into physical properties (electron density, temperature and element abundances) of several coronal structures have been presented. However, the solar corona is a very complex environment and a great deal move remains to be done. From what has been found in this work, it is clear that a more complete picture of the coronal environment can be made by taking advantage of coordinated observations using various instruments, to cover different wavebands and/or distances from the Sun centre.

Building on what has been learned from several successful solar missions, such as SOHO, Yohkoh, TRACE and Ulysses, some ambitions future missions are now planned. Solar-B (Davis, 2000; Solar-B WWW page, 2001), the launch of which is due to 2005, has the objective to investigate the solar variability, by the use of coordinated observations of the photosphere, transition region and corona. The satellite will carry a Solar Optical telescope (SOT), an X-ray telescope (XRT) and an EUV imaging telescope (EIS). All these instruments will be characterised by high spatial and spectral resolutions. Solar Orbiter (Marsch et al., 2000), a near-Sun (0.21 AU) and out-of ecliptic mission, will provide *in situ* measurements, high resolution imaging and spectroscopy of the solar corona, and is planned to be launched in 2009. The high quality data expected from these new missions will provide opportunities to test and improve the results presented in this thesis.

Appendix A

A.1 March and May 1998 UVCS Streamers Spectra

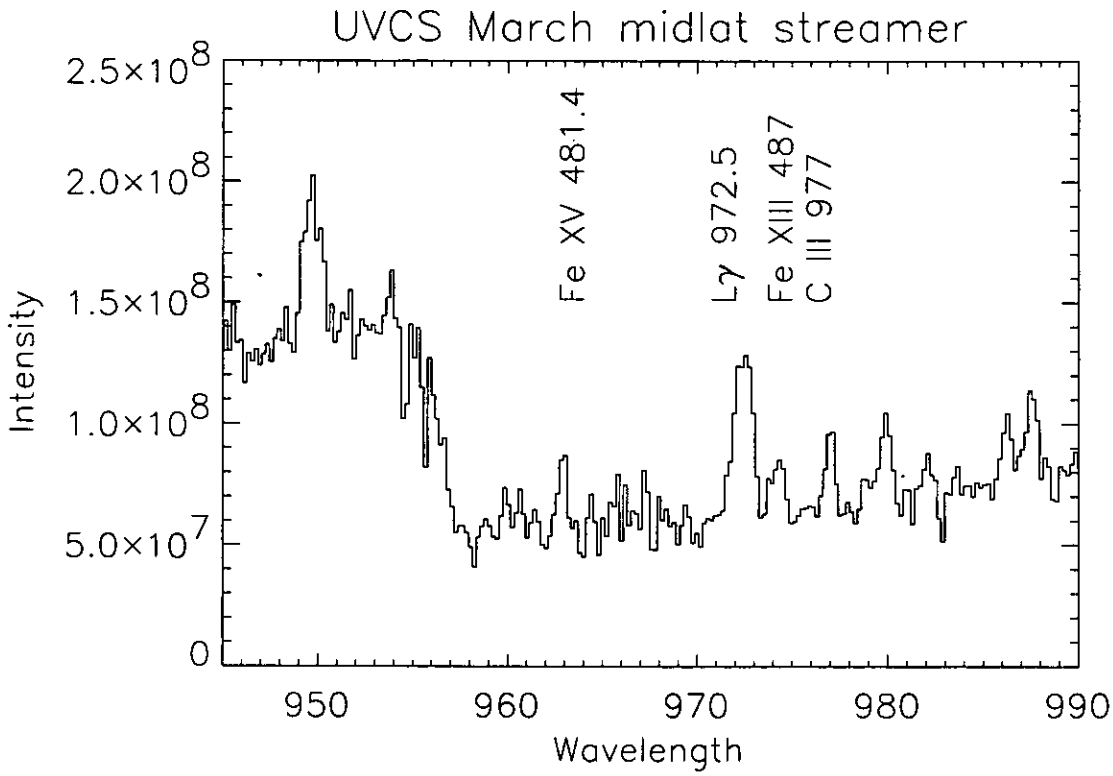

Figure A.1: Example of the O VI channel spectra from the UVCS March 1998 midlatitude streamer. The main lines are labeled. On the left of the figure it is visible the step in intensity due to the overposition of the reduntant spectra and the primary spectra. The intensity are given in phot/(cm^2 s str Å).

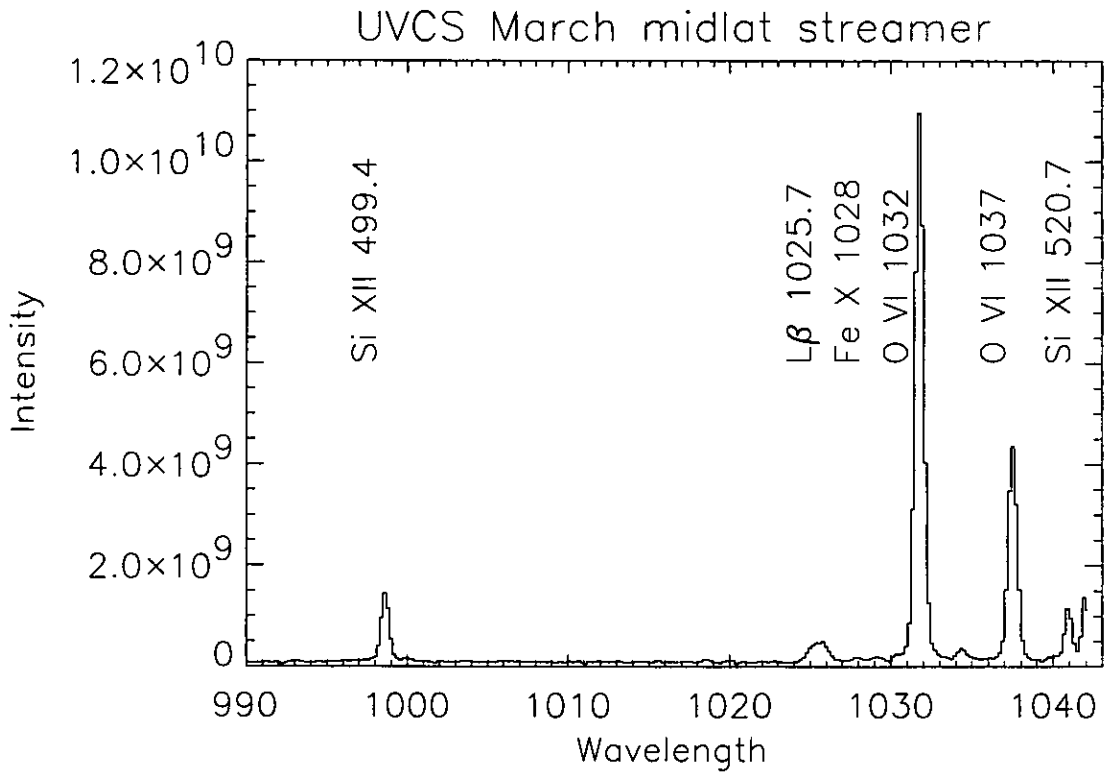

Figure A.2: Example of the O VI channel spectra from the UVCS March 1998 midlatitude streamer. The intensity are given in phot/(cm^2 s str Å).

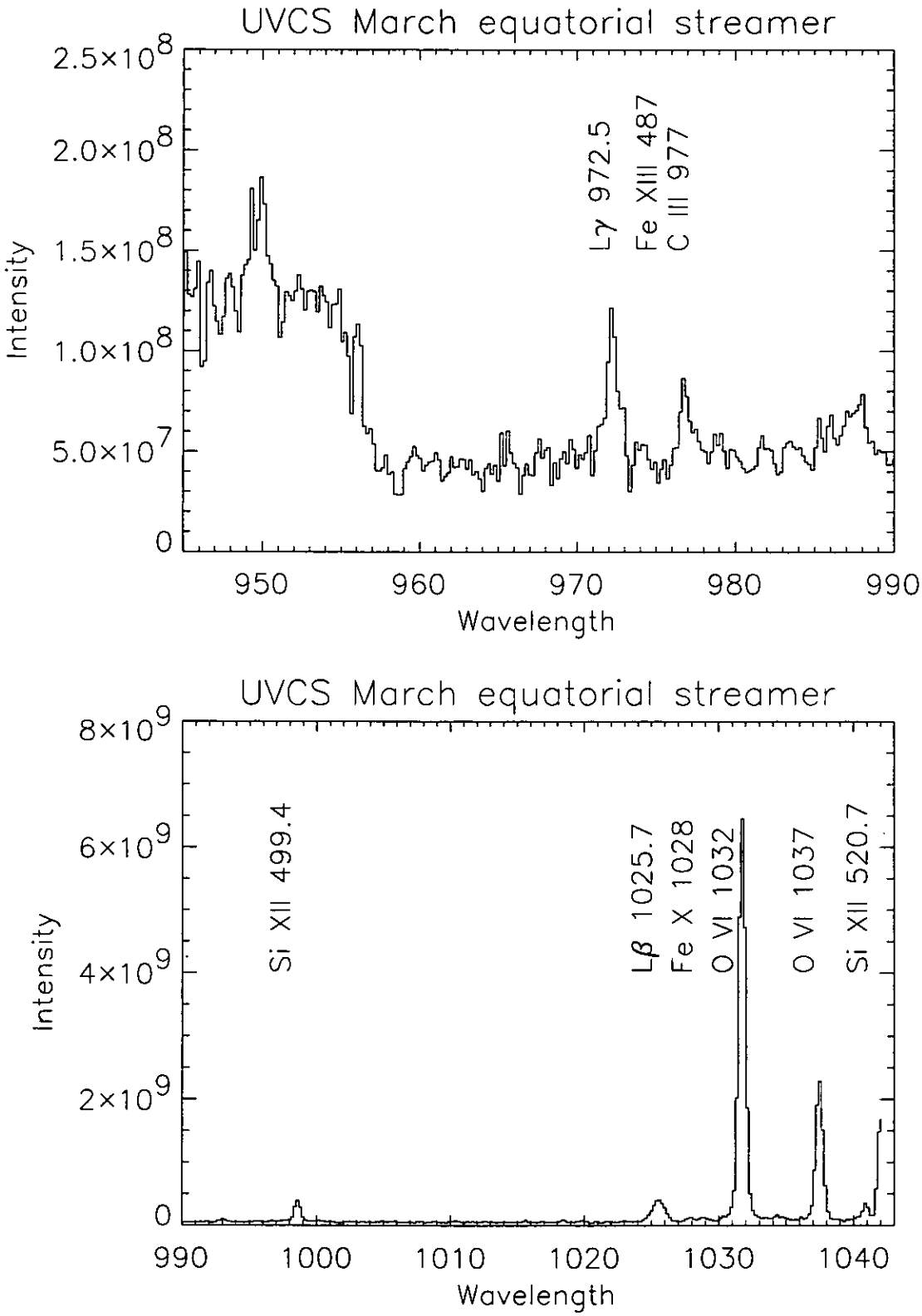

Figure A.3: Example of the O VI channel spectra from the UVCS March equatorial streamer. The intensity are given in phot/(cm^2 s str Å).

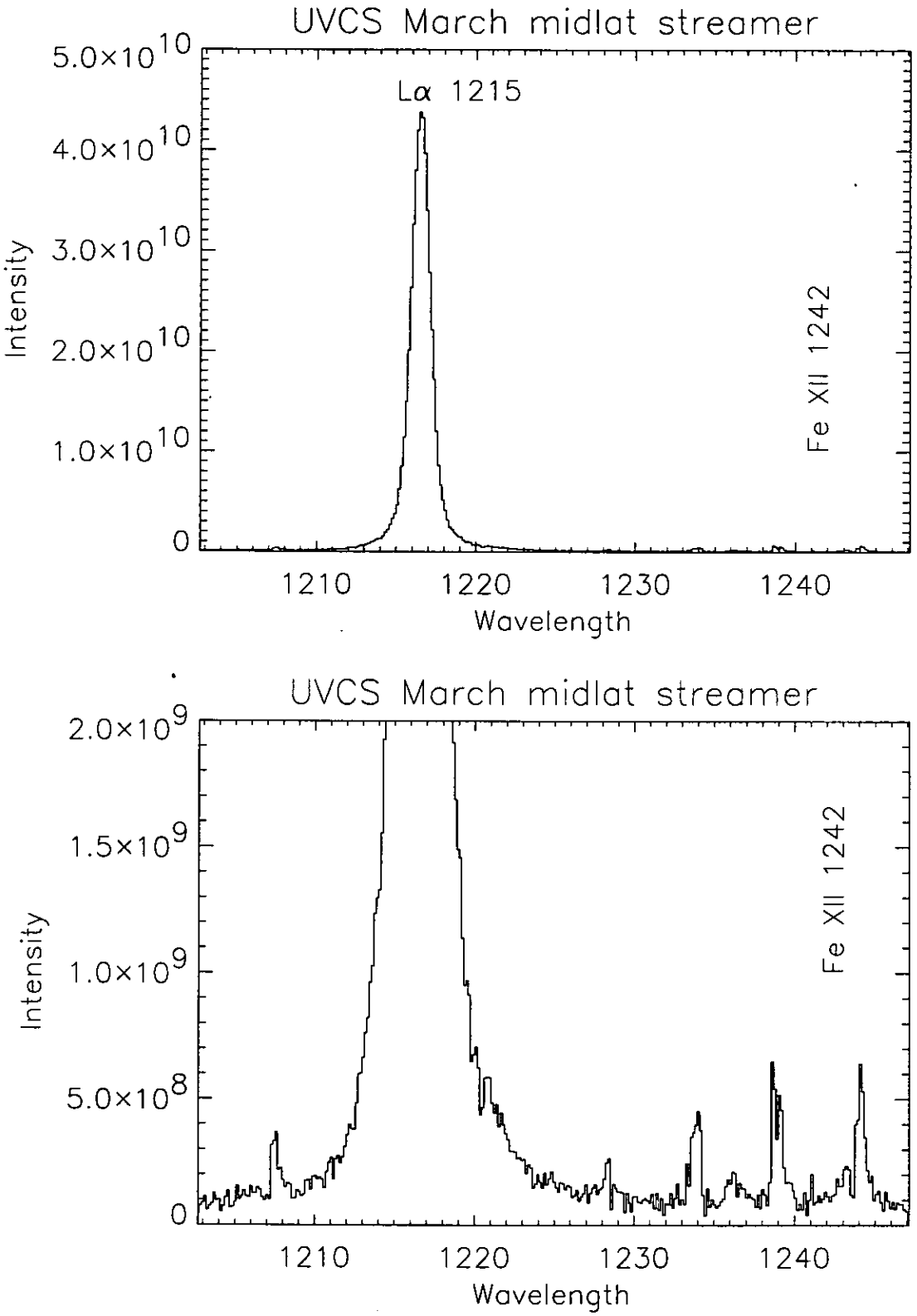

Figure A.4: Example of the spectra from Lyα channel for the midlatitude streamer. A closer view, shown in the figure at the bottom page, shows artificial spikes due to some problems in the flat field, that have not permitted the use of the Fe XII line.

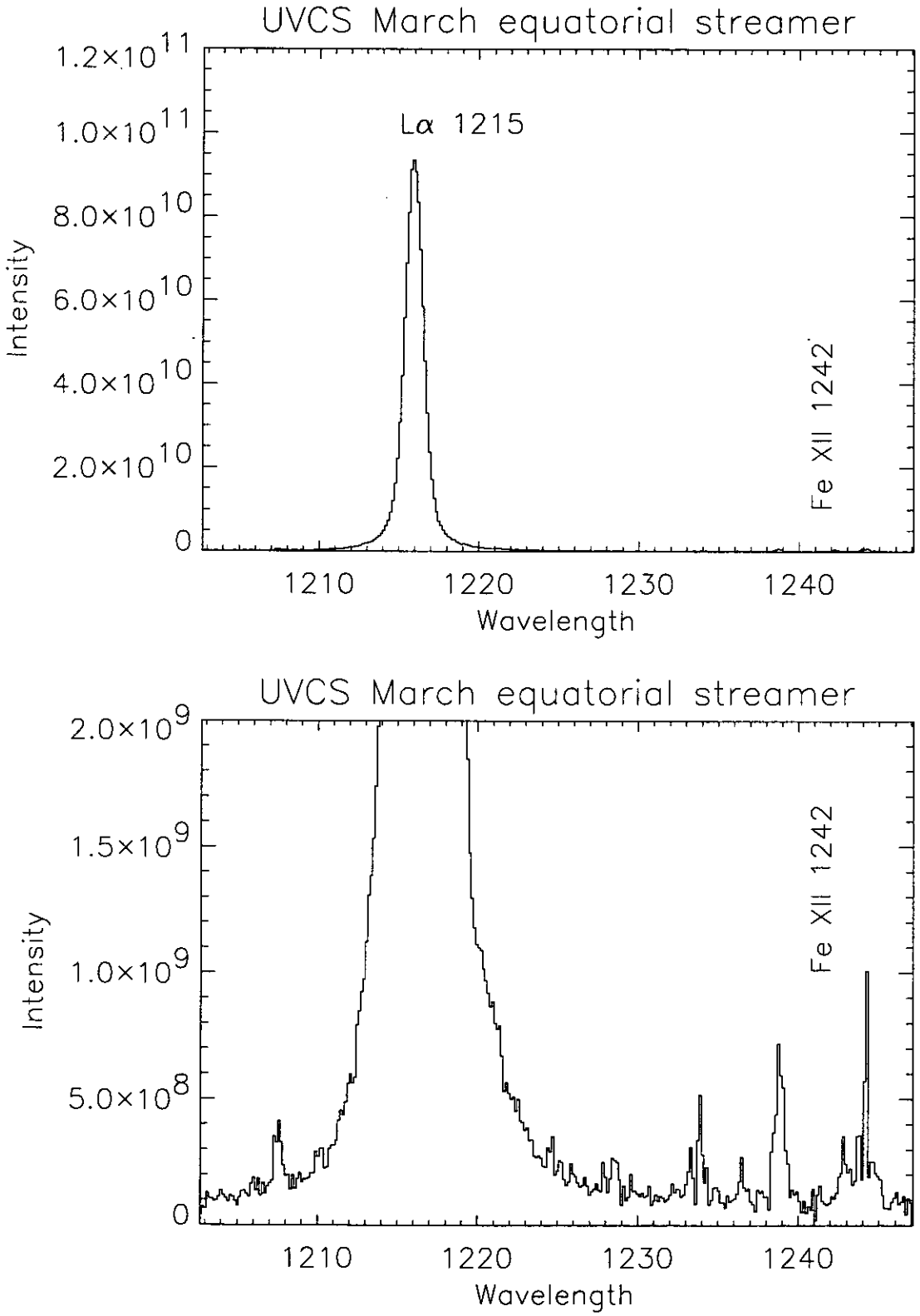

Figure A.5: Example of the spectra from Lyα channel for the equatorial streamer. A closer view, is shown in the figure at the bottom page.

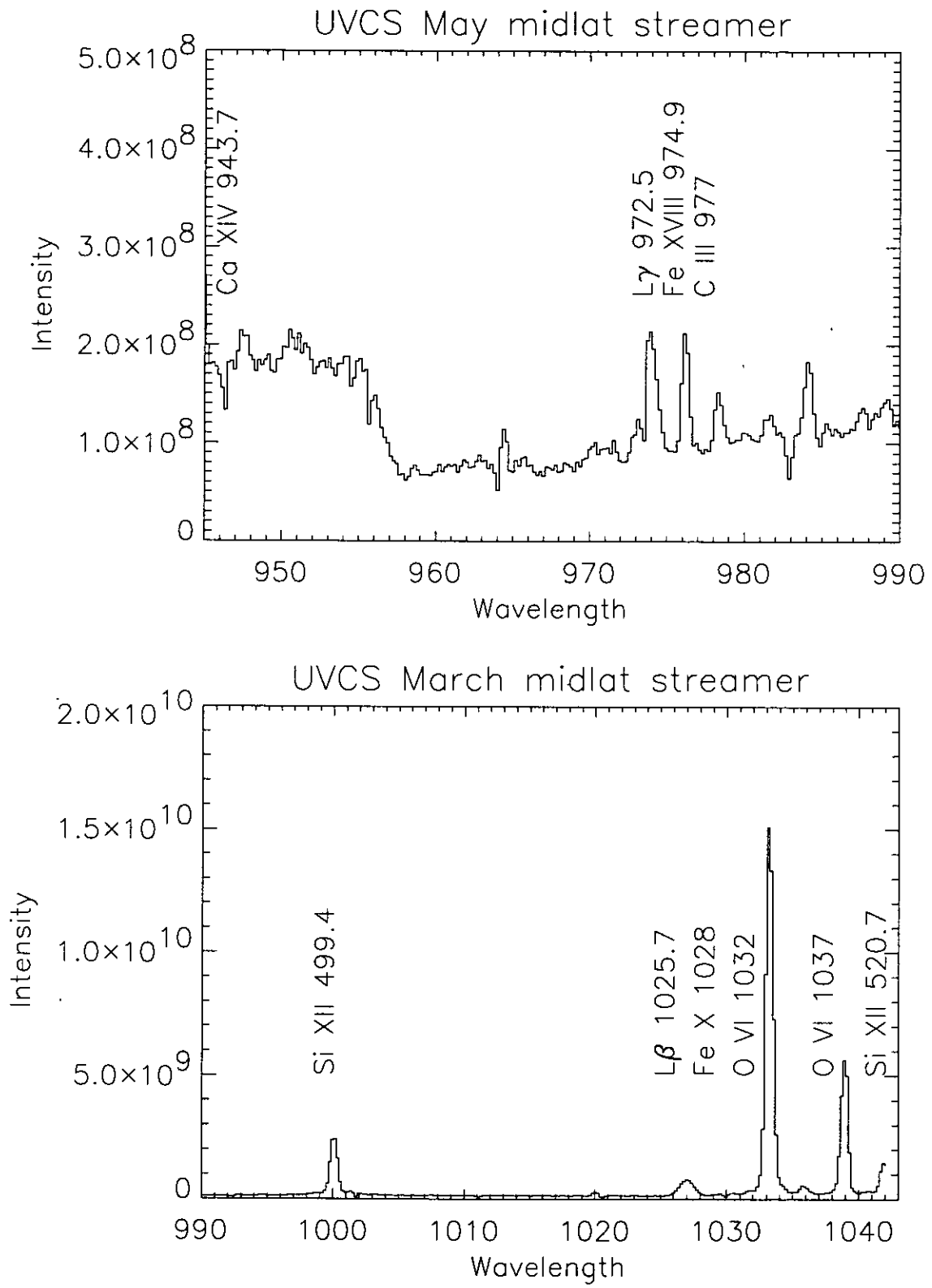

Figure A.6: Example of the O VI channel spectra from the UVCS May 1998 midlatitude streamer.

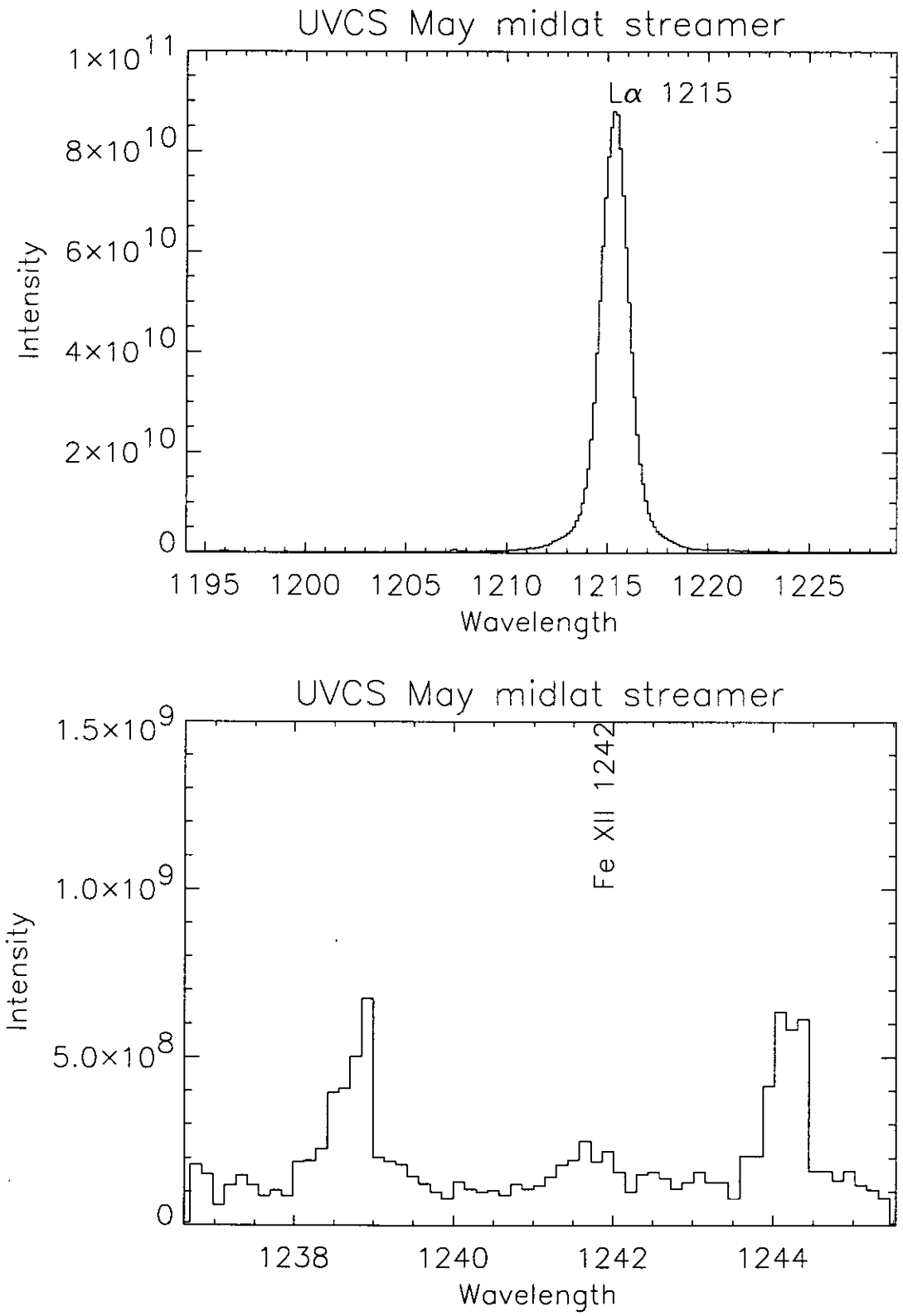

Figure A.7: Example of the spectra from Lyα channel for the midlatitude May streamer.

A.2 March 1998 streamers CDS spectra

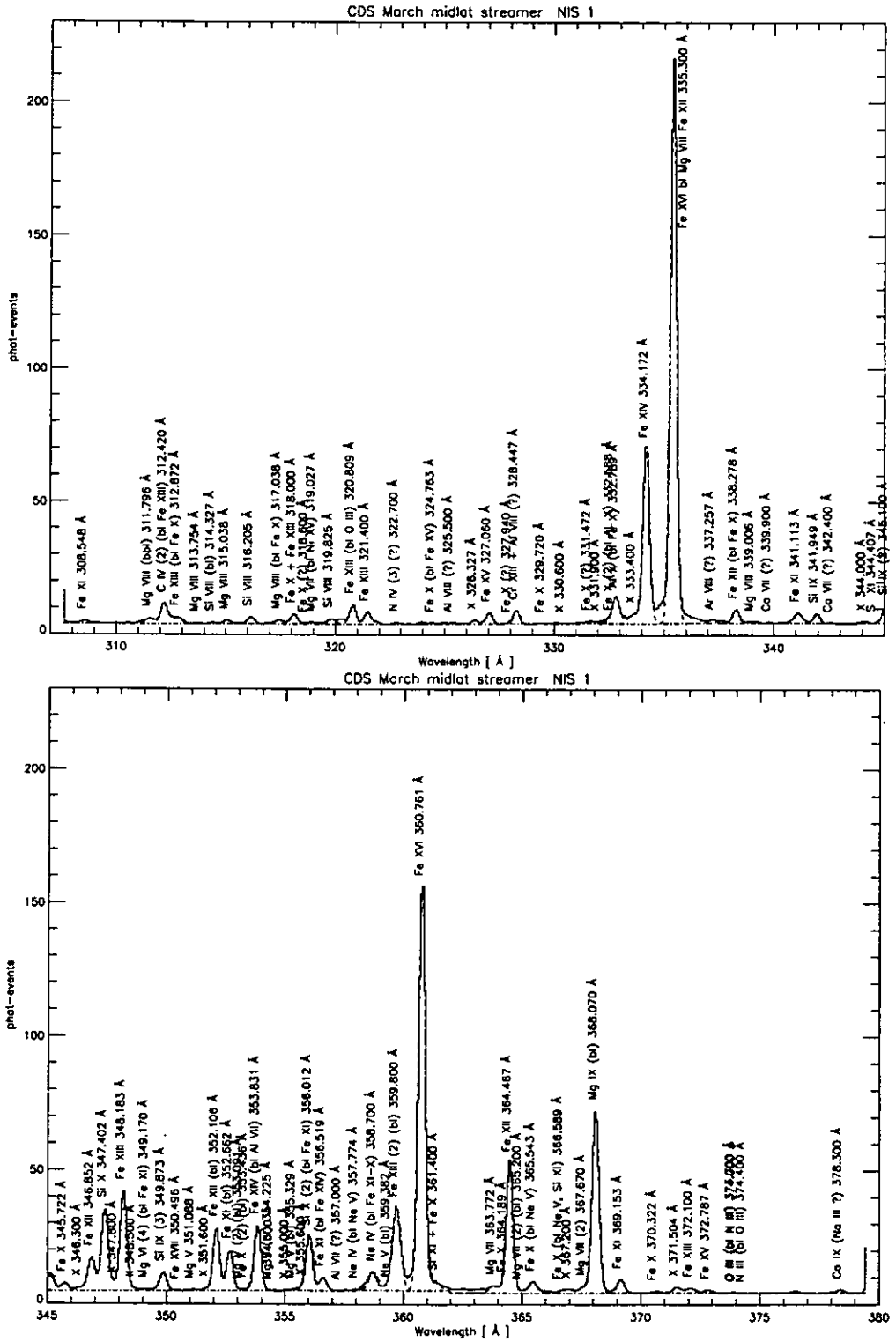

Figure A.8: CDS NIS 1 spectra for the March 1998 midlatitude streamer. The fitted background and Gaussian profiles for the lines are overplotted.

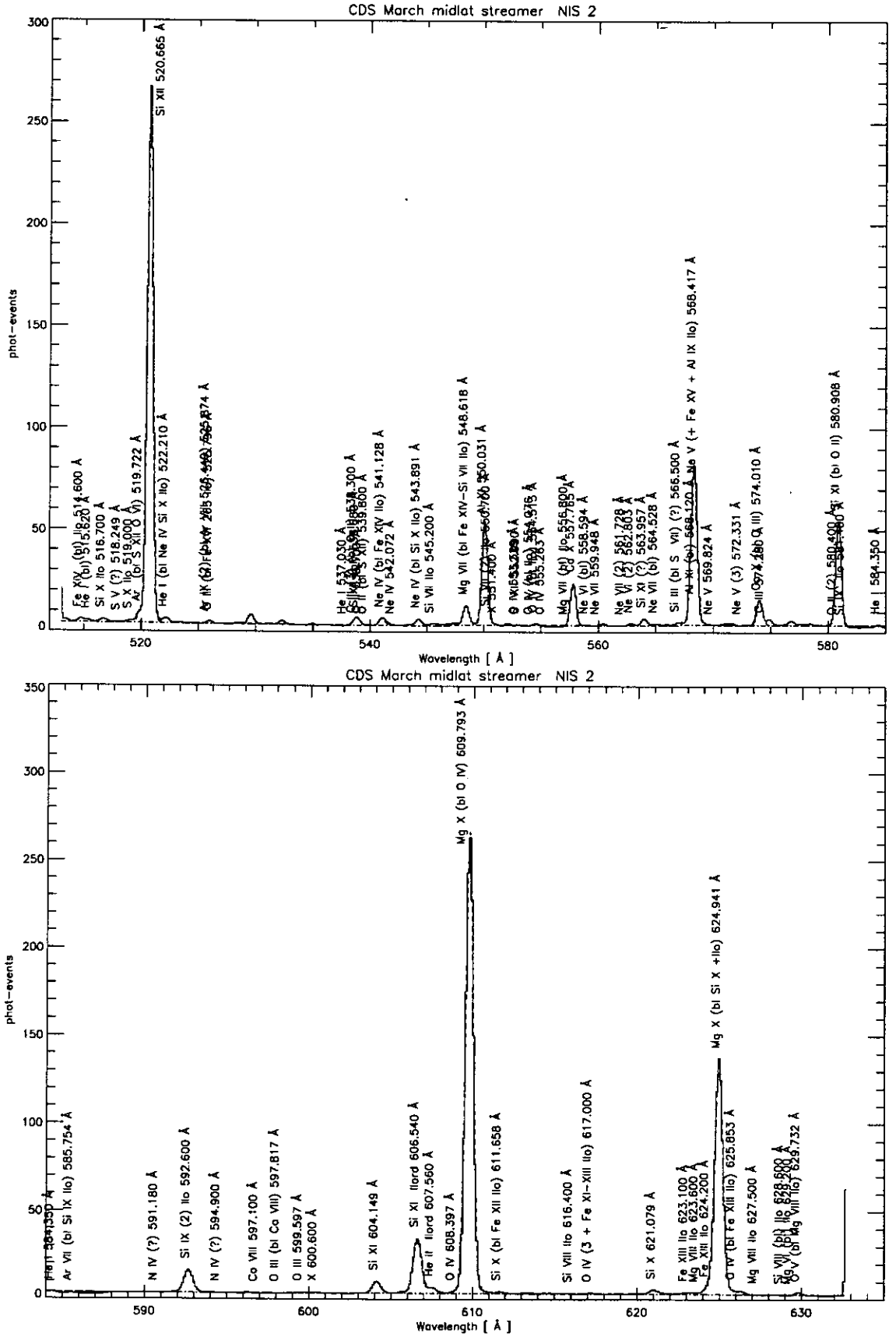

Figure A.9: CDS NIS 2 spectra for the March 1998 midlatitude streamer. The fitted background and Gaussian profiles for the lines are overplotted.

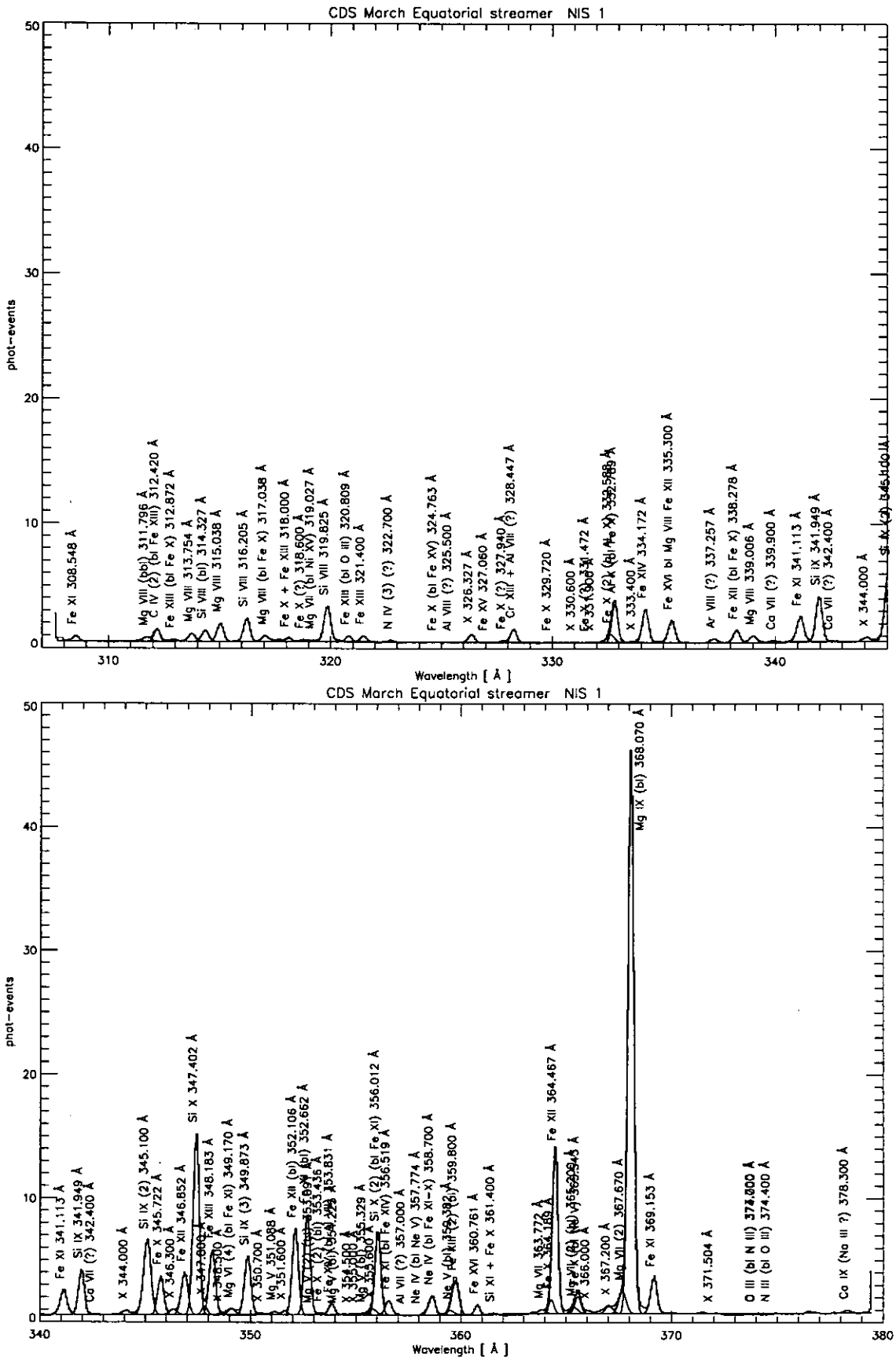

Figure A.10: CDS NIS 1 spectra for the March 1998 equatorial streamer. The fitted background and Gaussian profiles for the lines are overplotted.

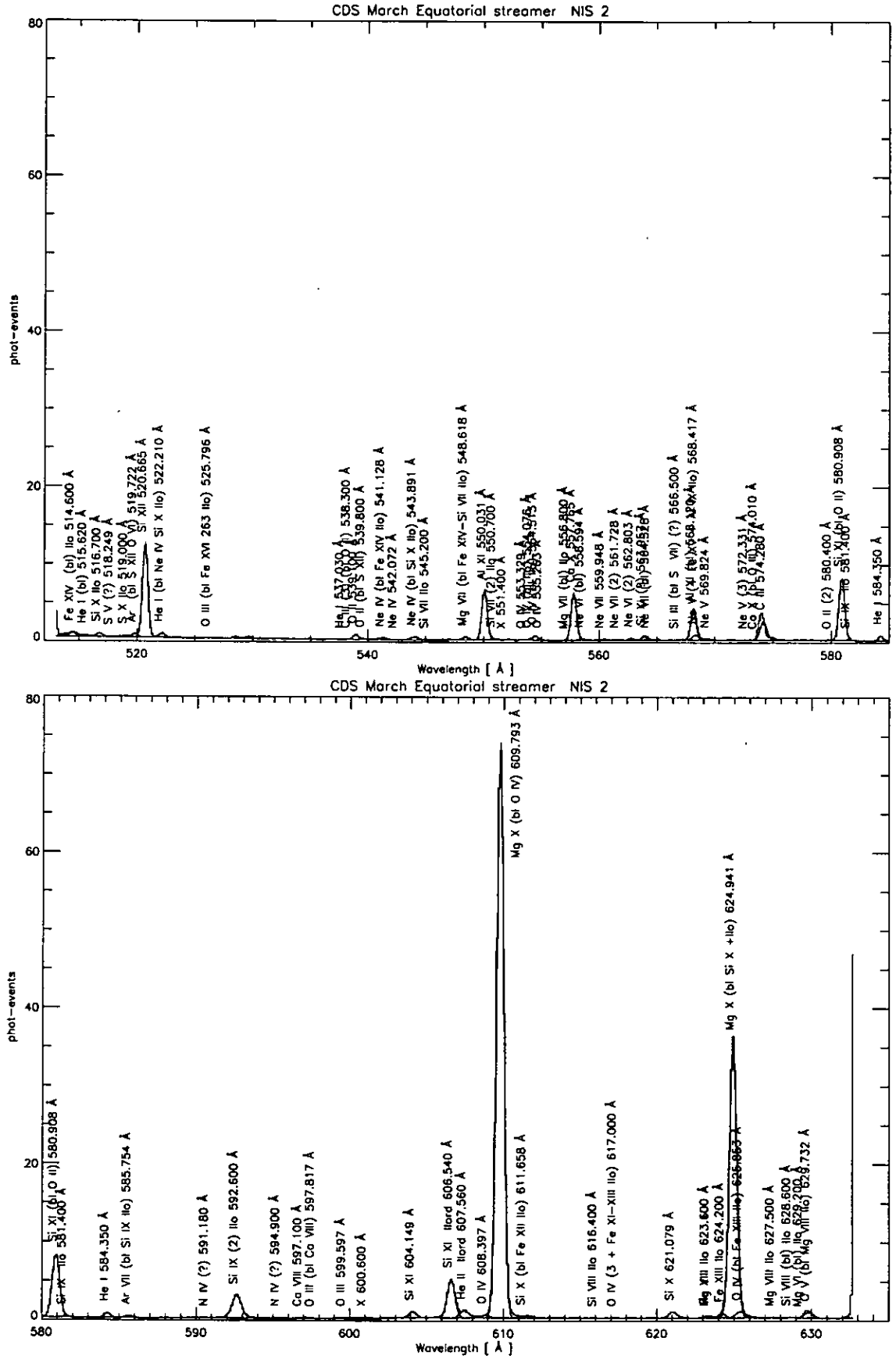

Figure A.11: CDS NIS 2 spectra for the March 1998 equatorial streamer. The fitted background and Gaussian profiles for the lines are overplotted.

A.3 Results from March 1998 streamers study with CDS

The Tables here listed report the results from the DEM analysis using the Mazzotta et al. (1998) ionization equilibrium. Each of the columns, starting from the first, reports: the ion (or ions if a blend is present) used to calculate the DEM; the theoretical values of the line wavelength of the ion; the observed wavelength of the line; the transition from which the line forms; the observed intensity in $ergcm^{-2}\ s^{-1}\ sr^{-1}$; The ratio of the theoretical flux to observed flux; the error estimated, given by a combination of the observed error and a assumed 10% error on the calculated values; the effective temperature, defined in 4.2; the temperature of the maximum of the contribution function; in case of a blended line, the percentage of contribution of each line to the total observed flux. Only the most significant blends are listed.

Table A.1: Results from 8 March 1998 midlatitude streamer study with the DEM.

Ion	λ_t (Å)	λ_o (Å)	Transition	I_o	I_t/I_o	+/-	T_{eff}	T_{max}	%
O III	599.597	599.5	2s22p2 $^1D_2$ - 2s2p3 $^1D_2$	0.3	0.63	0.14	5.03	5.03	
O IV	554.513	554.6	2s2 2p $^2P_{3/2}$ - 2s 2p2 $^2P_{3/2}$	0.4	1.05	0.17	5.16	5.23	
O V	629.730	629.8	2s2 $^1S_0$ - 2s.2p $^1P_1$	0.6	1.21	0.21	5.52	5.38	
Ne VI	562.803	562.9	2s2 2p $^2P_{3/2}$ - 2s 2p2 $^2D_{5/2}$	0.5	0.95	0.13	5.75	5.62	
Mg VIII	313.754	313.7	2p $^2P_{1/2}$ - 2s.2p2 $^2P_{1/2}$	3.5	0.96	0.21	6.11	5.91	
Mg VIII	315.039	315.1	2p $^2P_{3/2}$ - 2s.2p2 $^2P_{3/2}$	10.5	0.79	0.10	6.11	5.91	
Mg VIII	339.006	339.0	2p $^2P_{3/2}$ - 2s.2p2 $^2S_{1/2}$	2.9	0.72	0.20	6.11	5.91	
Si VIII	316.205	316.2	2s22p3 $^4S_{3/2}$ - 2s2p4 $^4P_{3/2}$	19.3	1.47	0.16	6.13	5.93	
Fe X	345.723	345.7	3s2.3p5 $^2P_{3/2}$ - 3s.3p6 $^2S_{1/2}$	9.7	1.16	0.13	6.13	5.98	
Fe XI	341.113	341.1	3s2.3p4 $^3P_2$ - 3s.3p5 $^3P_1$	16.9	0.56	0.06	6.15	6.06	
Fe XI	369.153	369.1	3s2.3p4 $^3P_1$ - 3s.3p5 $^3P_2$	10.4	1.15	0.13	6.16	6.06	
Fe XI	352.662	352.7	3s2.3p4 $^3P_2$ - 3s.3p5 $^3P_2$	44.5	0.89	0.09	6.16	6.06	
Mg IX	368.070	368.1	2s2 $^1S_0$ - 2s.2p $^1P_1$	137.1	1.04	0.10	6.17	5.98	0.87
Fe XIII	368.2		3s2 3p2 $^3P_2$ - 3s 3p3 $^3D_3$					6.20	0.11
Si X	621.079	621.0	2p $^2P_{1/2}$ - 2s.2p2 $^4P_{1/2}$	1.6	0.62	0.07	6.19	6.13	
Al X	332.789	332.8	2s2 $^1S_0$ - 2s.2p $^1P_1$	59.9	0.61	0.07	6.19	6.10	
Fe XII	352.106	352.1	3s2.3p3 $^4S_{3/2}$ - 3s.3p4 $^4P_{3/2}$	68.2	1.02	0.10	6.19	6.14	
Fe XII	346.852	346.9	3s2.3p3 $^4S_{3/2}$ - 3s.3p4 $^4P_{1/2}$	41.5	0.87	0.09	6.19	6.14	
Fe XII	364.467	364.5	3s2.3p3 $^4S_{3/2}$ - 3s.3p4 $^4P_{5/2}$	113.2	0.91	0.12	6.19	6.14	
Ca X	574.010	574.0	3s $^2S_{1/2}$ - 3p $^2P_{1/2}$	5.7	0.88	0.09	6.22	5.86	
Ca X	557.765	557.8	3s $^2S_{1/2}$ - 3p $^2P_{3/2}$	10.4	0.97	0.10	6.22	5.86	
Mg X	624.941	624.9	1s2.(1s).2s $^2S_{1/2}$ - 1s2.(1s).2p $^2P_{1/2}$	75.9	1.17	0.12	6.23	6.05	
Mg X	609.793	609.8	1s2.(1s).2s $^2S_{1/2}$ - 1s2.(1s).2p $^2P_{3/2}$	160.7	1.08	0.11	6.24	6.05	
Fe XIII	348.183	348.2	3s2 3p2 $^3P_0$ - 3s 3p3 $^3D_1$	110.8	1.26	0.13	6.24	6.20	
Fe XIII	321.400	321.5	3s2 3p2 $^3P_2$ - 3s 3p3 $^3P_1$	32.2	0.93	0.10	6.24	6.20	
Al XI	550.031	550.1	1s2.(1s).2s $^2S_{1/2}$ - 1s2.(1s).2p $^2P_{3/2}$	24.7	1.02	0.10	6.26	6.16	
Fe XIV	334.172	334.2	3s2 3p $^2P_{1/2}$ - 3s 3p2 $^2D_{3/2}$	358.7	0.69	0.07	6.30	6.26	
Fe XIV	353.831	353.8	3s2 3p $^2P_{3/2}$ - 3s 3p2 $^2D_{5/2}$	70.3	0.99	0.10	6.30	6.26	
Si XII	520.665	520.7	1s2.2s $^2S_{1/2}$ - 1s2.2p $^2P_{1/2}$	107.4	1.22	0.12	6.32	6.28	
Fe XV	327.011	327.0	3s3p $^3P_2$ - 3p2 $^1D_2$	24.3	0.81	0.09	6.34	6.33	
Fe XVI	360.761	360.8	3s $^2S_{1/2}$ - 3p $^2P_{1/2}$	434.3	0.95	0.10	6.37	6.41	

Table A.2: Results from the March 1998 8 equatorial streamer study with the DEM.

Ion	λ_t (Å)	λ_o (Å)	Transition	I_o	I_t/I_o	+/-	T_{eff}	T_{max}	%
O IV	554.513	554.5	2s2 2p $^2P_{3/2}$ - 2s 2p2 $^2P_{3/2}$	0.2	0.89	0.10	5.22	5.23	
O V	629.730	629.8	2s2 $^1S_0$ - 2s.2p $^1P_1$	0.4	1.37	0.26	5.57	5.38	
Ne VI	562.803	562.8	2s2 2p $^2P_{3/2}$ - 2s 2p2 $^2D_{5/2}$	0.1	0.73	0.09	5.94	5.62	0.80
Ne VII	563.0		2s2p $^3P_1$ - 2p2 $^3P_0$					5.72	0.11
Ne VII	561.728	561.6	2s2p $^3P_2$ - 2p2 $^3P_2$	0.1	7.12	1.06	6.03	5.71	0.83
Ne VII	561.4		2s2p $^3P_1$ - 2p2 $^3P_1$					5.71	0.17
Mg VIII	315.039	315.0	2p $^2P_{3/2}$ - 2s.2p2 $^2P_{3/2}$	9.4	1.30	0.13	6.03	5.91	
Mg VIII	313.754	313.7	2p $^2P_{1/2}$ - 2s.2p2 $^2P_{1/2}$	4.4	1.20	0.12	6.03	5.91	
Mg VIII	339.006	339.0	2p $^2P_{3/2}$ - 2s.2p2 $^2S_{1/2}$	2.6	1.19	0.13	6.04	5.91	
Mg VIII	317.039	317.1	2p $^2P_{3/2}$ - 2s.2p2 $^2P_{1/2}$	3.6	1.06	0.11	6.04	5.91	
Si VIII	319.826	319.8	2s22p3 $^4S_{3/2}$ - 2s2p4 $^4P_{5/2}$	19.5	2.72	0.27	6.06	5.93	
Si VIII	316.205	316.2	2s22p3 $^4S_{3/2}$ - 2s2p4 $^4P_{3/2}$	11.6	3.00	0.30	6.06	5.93	
Mg IX	368.070	368.1	2s2 $^1S_0$ - 2s.2p $^1P_1$	88.7	1.04	0.10	6.06	5.98	
Fe X	345.723	345.7	3s2.3p5 $^2P_{3/2}$ - 3s.3p6 $^2S_{1/2}$	9.8	1.13	0.12	6.06	5.98	
Ca X	557.765	557.8	3s $^2S_{1/2}$ - 3p $^2P_{3/2}$	2.9	1.07	0.11	6.07	5.86	
Fe XI	341.113	341.1	3s2.3p4 $^3P_2$ - 3s.3p5 $^3P_1$	7.9	0.66	0.07	6.08	6.06	
Fe XI	352.662	352.7	3s2.3p4 $^3P_2$ - 3s.3p5 $^3P_2$	23.5	0.94	0.10	6.08	6.06	
Fe XI	369.153	369.2	3s2.3p4 $^3P_1$ - 3s.3p5 $^3P_2$	6.0	1.11	0.11	6.08	6.06	
Mg X	609.793	609.8	1s2.(1s).2s $^2S_{1/2}$ - 1s2.(1s).2p $^2P_{3/2}$	43.9	1.05	0.11	6.08	6.05	
Mg X	624.941	624.9	1s2.(1s).2s $^2S_{1/2}$ - 1s2.(1s).2p $^2P_{1/2}$	19.5	1.22	0.12	6.08	6.05	
Al X	332.789	332.8	2s2 $^1S_0$ - 2s.2p $^1P_1$	15.6	0.86	0.09	6.09	6.10	
Si X	621.079	621.0	2p $^2P_{1/2}$ - 2s.2p2 $^4P_{1/2}$	0.5	0.70	0.08	6.10	6.13	
Fe XII	346.852	346.9	3s2.3p3 $^4S_{3/2}$ - 3s.3p4 $^4P_{1/2}$	11.6	0.88	0.09	6.10	6.14	
Fe XII	364.467	364.5	3s2.3p3 $^4S_{3/2}$ - 3s.3p4 $^4P_{5/2}$	31.5	0.91	0.09	6.10	6.14	
Si X	347.403	347.4	2p $^2P_{1/2}$ - 2s.2p2 $^2D_{3/2}$	44.6	0.68	0.07	6.10	6.14	
Al XI	568.120	568.2	1s2.(1s).2s $^2S_{1/2}$ - 1s2.(1s).2p $^2P_{1/2}$	1.5	1.04	0.13	6.12	6.16	
Al XI	550.031	550.1	1s2.(1s).2s $^2S_{1/2}$ - 1s2.(1s).2p $^2P_{3/2}$	3.1	1.02	0.10	6.12	6.16	
Fe XIII	348.183	348.2	3s2 3p2 $^3P_0$ - 3s 3p3 $^3D_1$	16.6	1.15	0.12	6.13	6.20	
Fe XIII	321.400	321.5	3s2 3p2 $^3P_2$ - 3s 3p3 $^3P_1$	3.1	1.26	0.13	6.13	6.20	
Fe XIV	334.172	334.2	3s2 3p $^2P_{1/2}$ - 3s 3p2 $^2D_{3/2}$	13.6	0.77	0.08	6.16	6.26	
Si XII	520.665	520.7	1s2.2s $^2S_{1/2}$ - 1s2.2p $^2P_{1/2}$	4.6	0.83	0.08	6.17	6.28	
Fe XIV	360.827	360.8	3s.3p^2 $^2D_{3/2}$ - 3p^3 $^2D_{3/2}$	2.0	1.28	0.15	6.17	6.25	0.70
Fe XVI	360.8		3s $^2S_{1/2}$ - 3p $^2P_{1/2}$					6.41	0.30

A.4 Ambient Coronal Hole and Macrospicule CDS Spectra

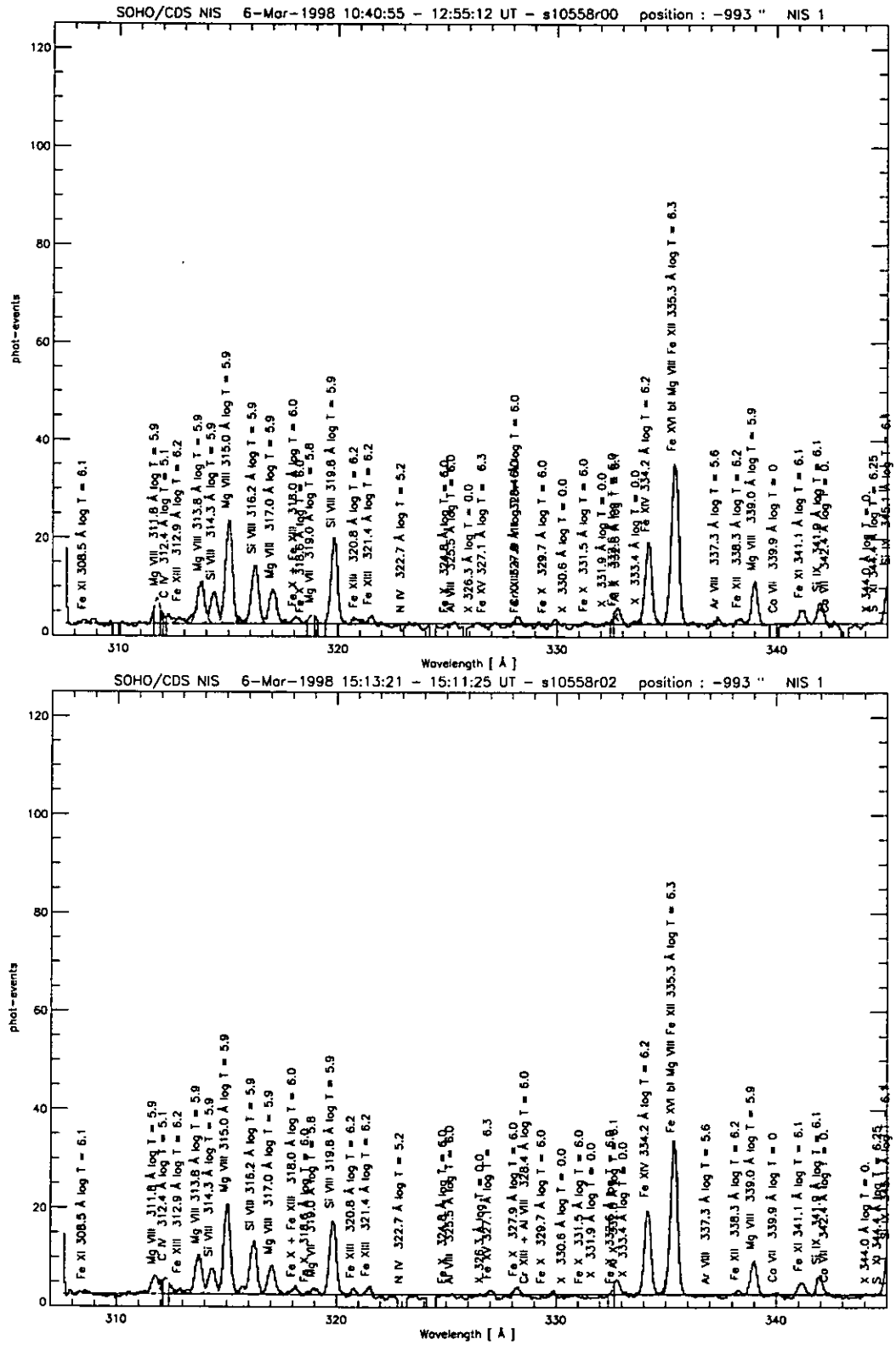

Figure A.12: First part of the CDS NIS 1 spectra of the macrospicule (top) and its background (bottom) (columns 4) in the spatial pixel closest to the limb. The fitted background and Gaussian profiles for the lines are overplotted.

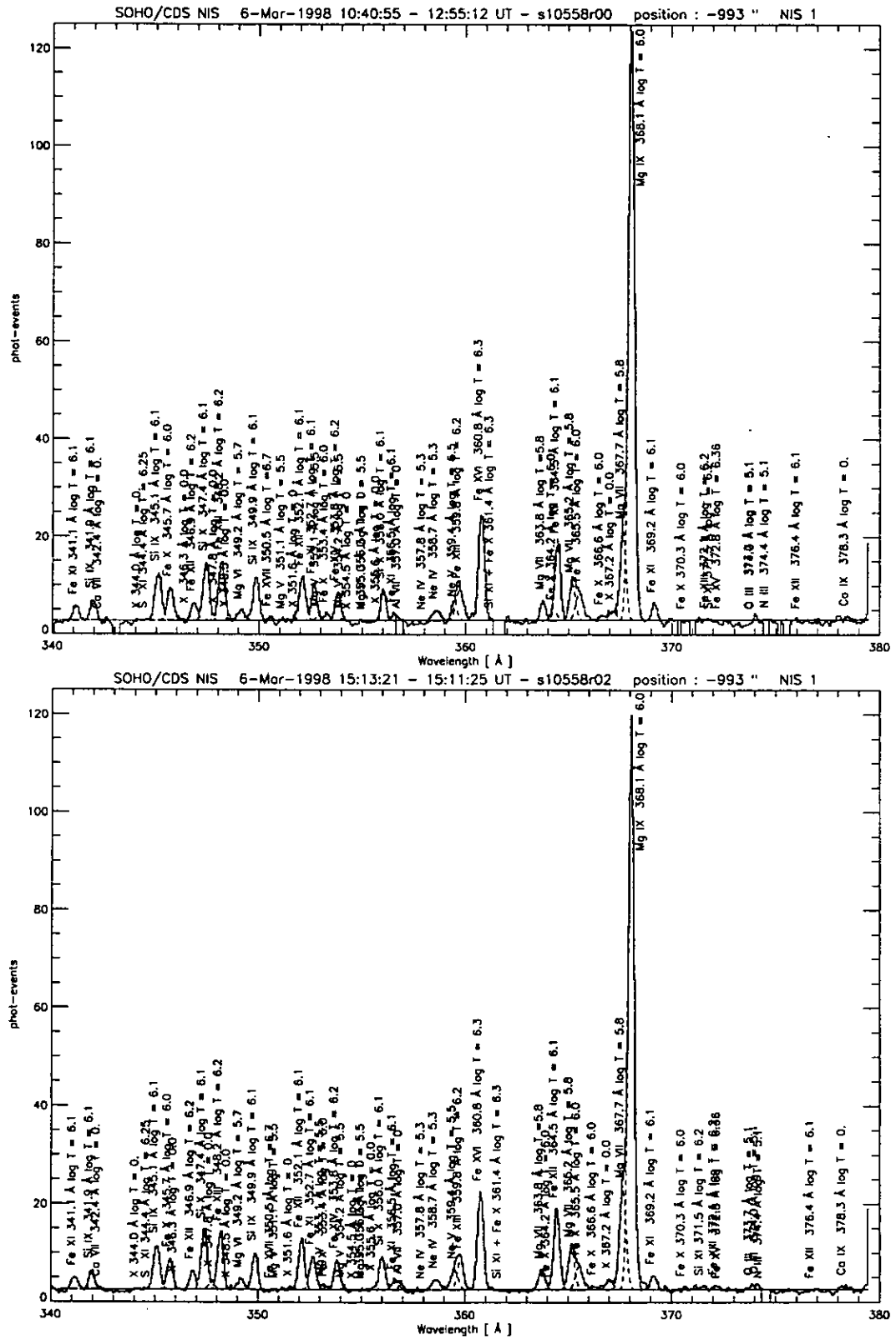

Figure A.13: Second part of the CDS NIS 1 spectra of the macrospicule (top) and its background (bottom) (columns 4) in the spatial pixel closest to the limb. The fitted background and Gaussian profiles for the lines are overplotted.

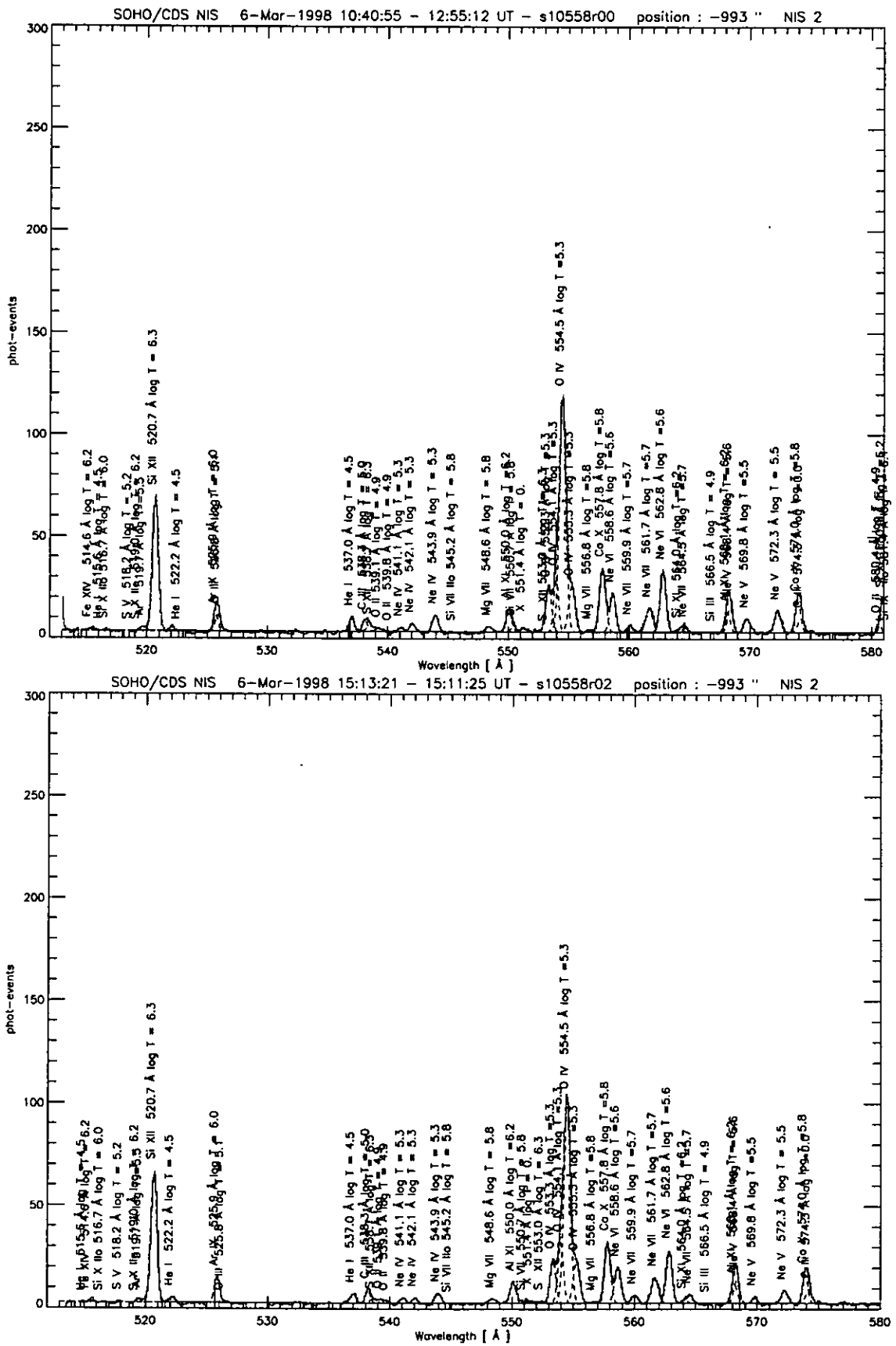

Figure A.14: First part of the CDS NIS 2 spectra of the macrospicule (top) and its background (bottom) (columns 4) in the spatial pixel closest to the limb. The fitted background and Gaussian profiles for the lines are overplotted.

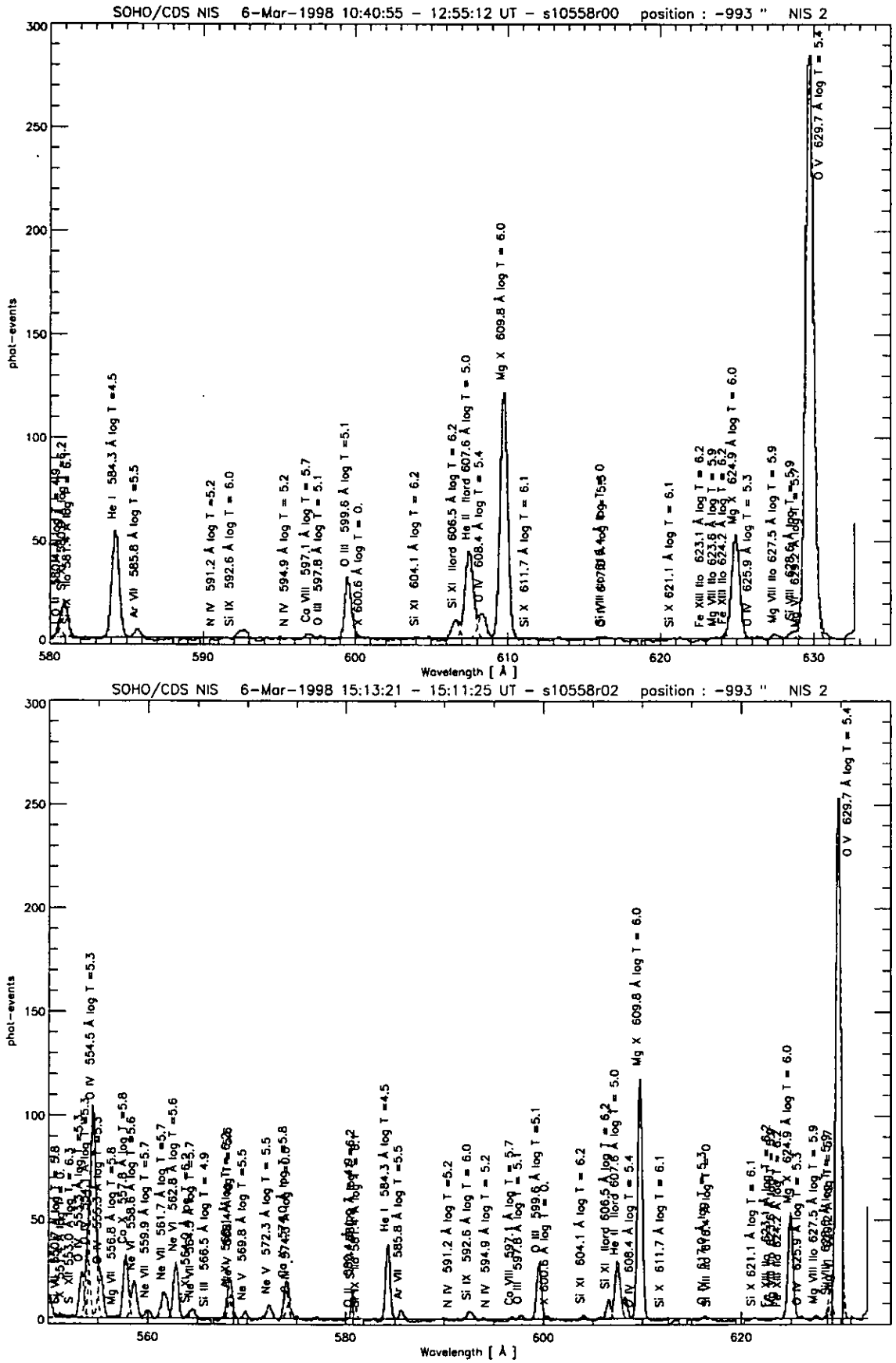

Figure A.15: Second part of the CDS NIS 2 spectra of the macrospicule(top) and its background (bottom)(columns 4) in the spatial pixel closest to the limb. The fitted background and Gaussian profiles for the lines are overplotted.

A.5 June 2000 UVCS spectra

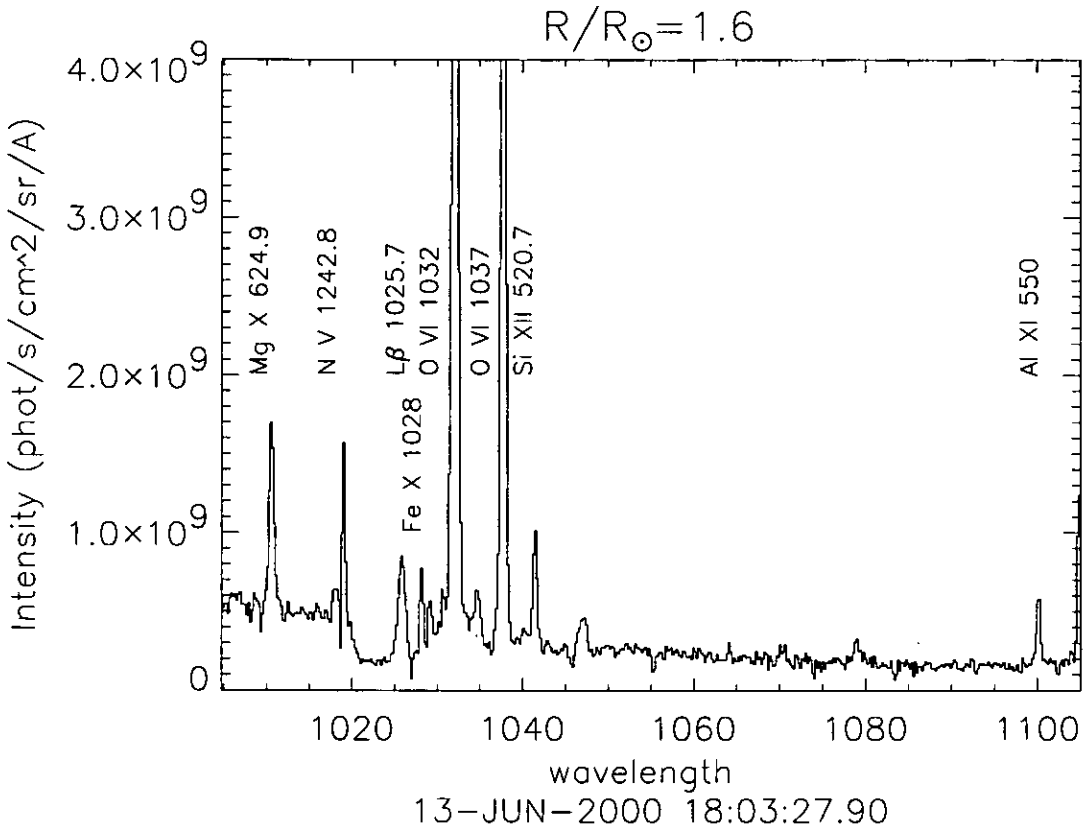

Figure A.16: Example of the O VI channel spectra from the UVCS June 2000 data at 1.6 $R_\odot$. The step in the background intensity at 1020 Å indicate the border with the redundant spectra, that cointains the Mg X and the N V lines. The main lines are labeled.

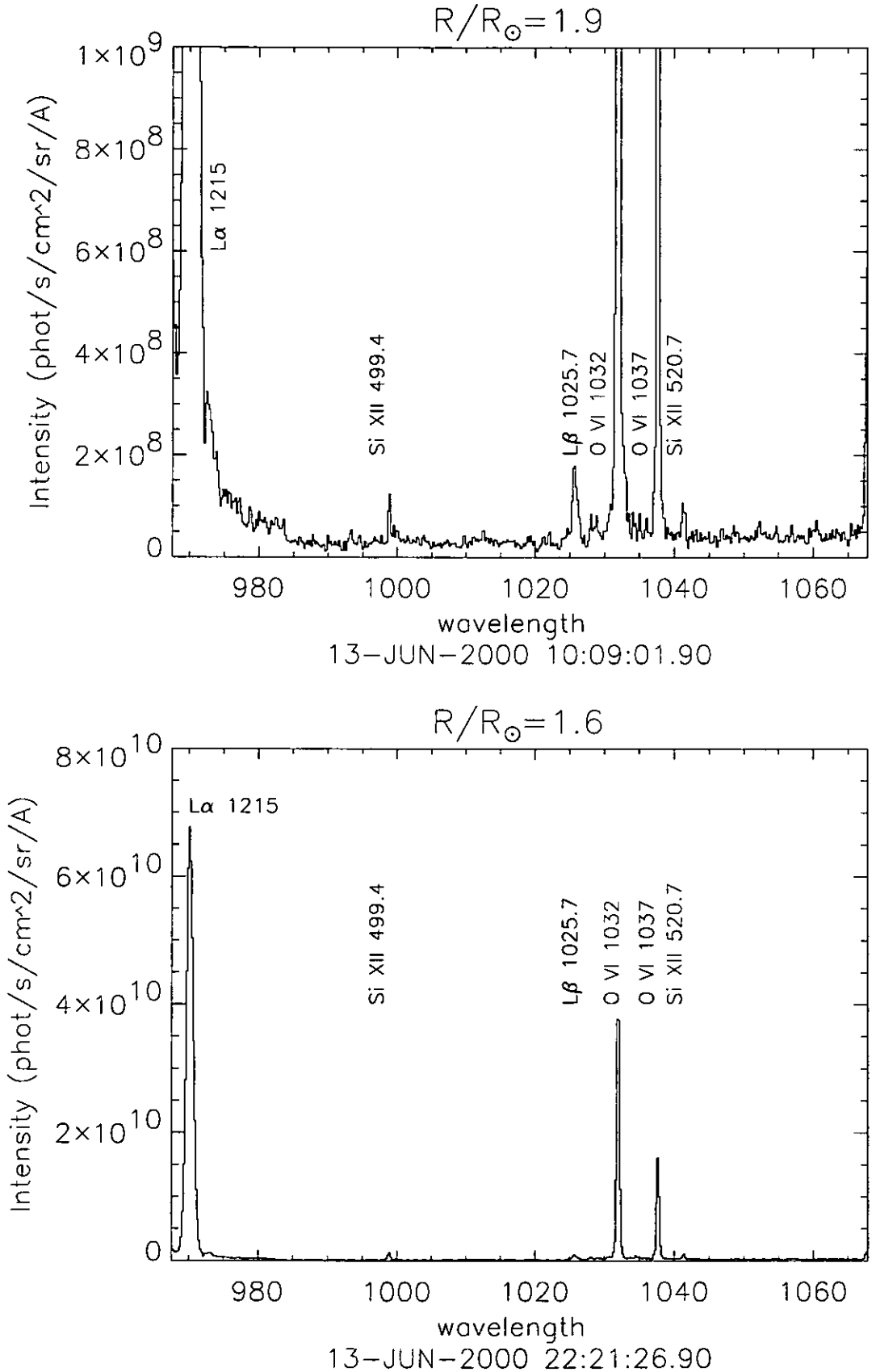

Figure A.17: Example of the O VI channel spectra from the UVCS June 2000 data. The main lines are labeled. Top: Spectra for 1.9 $R_\odot$. Bottop: Spectra for 1.6 $R_\odot$. The intensity are given in phot/(cm^2 s str Å).

References

Aellig, M. R., Hefti, S., Grünwaldt, H., Bochsler, P., Wurz, P., Ipavich, F. M., & Hovestadt, D. 1999, JGR, 104, 24769

Ahmad, I. A. & Withbroe, G. L. 1977, Sol. Phys., 53, 397

Allen, C. W. 1963, Astrophysical quantities (London: University of London, Athlone Press, 1963, 2nd ed.)

Allen, R., Landi, E., Landini, M., & Bromage, G. E. 2000, Astron. Astrophys., 358, 332

Arnaud, M. & Raymond, J. 1992, ApJ, 398, 394

Arnaud, M. & Rothenflug, R. 1985, Astron. Astrophys. Suppl. Ser., 60, 425

Athay, R. G. 1981, ApJ, 250, 709

Banerjee, D., O'Shea, E., & Doyle, J. G. 2000, Astron. Astrophys., 355, 1152

Beckers, J. M. & Chipman, E. 1974, Sol. Phys., 34, 151+

Bhattacharya, J. C. 1973, Bulletin of the Astronomical Society of India, 1, 25

Bohlin, J. D., Vogel, S. N., Purcell, J. D., Sheeley, N. R., Tousey, R., & Vanhoosier, M. E. 1975, Astrophys. J. Letters, 197, L133

Brekke, P., Thompson, W. T., Woods, T. N., & Eparvier, F. G. 2000, ApJ, 536, 959

Bromage, B. J. J., Alexander, D., Breen, A., Clegg, J. R., Del Zanna, G., DeForest, C., Dobrzycka, D., Gopalswamy, N., Thompson, B., & Browning, P. K. 2000, Sol. Phys., 193, 181

Bromage, B. J. J., Breeveld, A., Kent, B. J., Pike, C. D., & Harrison, R. A. 1996, University Of Central Lancashire Report CFA, 09

Brooks, D. H., Fischbacher, G. A., Fludra, A., Harrison, R. A., Innes, D. E., Landi, E., Landini, M., Lang, J., Lanzafame, A. C., Loch, S. D., McWhirter, R. W. P., Summers, H. P., & Thompson, W. T. 1999, Astron. Astrophys., 347, 277

Brosius, J. W., Davila, J. M., Thomas, R. J., & Monsignori-Fossi, B. C. 1996, Astrophys. J. Suppl. Ser., 106, 143+

Brueckner, G. E. & Bartoe, J. . F. 1983, ApJ, 272, 329

Callaway, J. 1994, Atomic Data and Nuclear Data Tables, 57, 9

Ciaravella, A., Raymond, J. C., Strachan, L., Thompson, B. J., Cyr, O. C. S., Gardner, L., Modigliani, A., Antonucci, E., Kohl, J., & Noci, G. 1999, ApJ, 510, 1053

Cook, J. W., Brueckner, G. E., Bartoe, J. . F., & Socker, D. G. 1984, Advances in Space Research, 4, 59

Cranmer, S. R., Kohl, J. L., Noci, G., Antonucci, E., Tondello, G., Huber, M. C. E., Strachan, L., Panasyuk, A. V., Gardner, L. D., Romoli, M., Fineschi, S., Dobrzycka, D., Raymond, J. C., Nicolosi, P., Siegmund, O. H. W., Spadaro, D., Benna, C., Ciaravella, A., Giordano, S., Habbal, S. R., Karovska, M., Li, X., Martin, R., Michels, J. G., Modigliani, A., Naletto, G., O'Neal, R. H., Pernechele, C., Poletto, G., Smith, P. L., & Suleiman, R. M. 1999, ApJ, 511, 481

David, C., Gabriel, A. H., Bely-Dubau, F., Fludra, A., Lemaire, P., & Wilhelm, K. 1998, Astron. Astrophys., 336, L90

Davis, J. M. 2000, in AAS/Solar Physics Division Meeting, Vol. 32, 1602

Deforest, C. E., Hoeksema, J. T., Gurman, J. B., Thompson, B. J., Plunkett, S. P., Howard, R., Harrison, R. C., & Hasslerz, D. M. 1997, Sol. Phys., 175, 393

Del Zanna, G. 1999, PhD thesis, , Univ. of Central Lancashire, (1999)

Del Zanna, G. & Bromage, B. J. I. 1999a, Space Science Reviews, 87, 169

—. 1999b, JGR, 104, 9753

Del Zanna, G. & Bromage, B. J. I. 1999c, in Ninth European Meeting on Solar Physics: Magnetic Fields and Solar Processes. Ninth Meeting of the Solar Physics Section of the Joint Astrophysics Division of the European Physical Society (EPS) and of the European Astronomical Society (EAS). Florence, Italy, 12-18 September, 1999. Proceedings published in ESA SP Series (SP-448), ed. A. Wilson., E245

Delannee, C., Koutchmy, S., Delaboudiniere, J. ., Hochedez, J. ., Vial, J. ., Dara, H., & Georgakilas, A. 1998, in ESA SP-421: Solar Jets and Coronal Plumes, 129+

Dere, K. P., Bartoe, J. . F., Brueckner, G. E., Cook, J. W., & Socker, D. G. 1989, Sol. Phys., 119, 55

Dobrzycka, D., Cranmer, S. R., Panasyuk, A. V., Strachan, L., & Kohl, J. L. 1999, JGR, 104, 9791

Domingo, V., Fleck, B., & Poland, A. I. 1995, Sol. Phys., 162, 1

Doschek, G. A., Feldman, U., Laming, J. M., Schühle, U., & Wilhelm, K. 2001, ApJ, 546, 559

Doschek, G. A., Feldman, U., Laming, J. M., Warren, H. P., Schüle, U., & Wilhelm, K. 1998a, ApJ, 507, 991

Doschek, G. A., Feldman, U., & Seely, J. F. 1985, Mon. Not. R. Astron. Soc., 217, 317

Doschek, G. A., Laming, J. M., Feldman, U., Wilhelm, K., Lemaire, P., Schuehle, U., & Hassler, D. M. 1998b, ApJ, 504, 573+

Doschek, G. A., Warren, H. P., Laming, J. M., Mariska, J. T., Wilhelm, K., Lemaire, P., Schuehle, U., & Moran, T. G. 1997, Astrophys. J. Letters, 482, L109

Doyle, J. G., Keenan, F. P., Ryans, R. S. I., Aggarwal, K. M., & Fludra, A. 1999, Sol. Phys., 188, 73

Falconer, D. A., Davila, J. M., & Thomas, R. J. 1997, ApJ, 482, 1050+

Feldman, U. 1992, Phys. Scripta, 46, 202

—. 1993, ApJ, 411, 896

Feldman, U., Mandelbaum, P., Seely, J. F., Doschek, G. A., & Gursky, H. 1992, Astrophys. J. Suppl. Ser., 81, 387

Feldman, U., Schühle, U., Widing, K. G., & Laming, J. M. 1998, ApJ, 505, 999

Feldman, U. & Widing, K. G. 1993, ApJ, 414, 381

Fineschi, S., Romoli, M., Gardner, L. D., Kohl, J. L., Noci, G., & Tondello, G. 1994, Proc.SPIE, 2283, 30

Fisher, R. & Guhathakurta, M. 1995, Astrophys. J. Letters, 447, L139

Fleck, B. 1997, Astrophysics and Space Science, 258, 57

Fludra, A., del Zanna, G., Alexander, D., & Bromage, B. J. I. 1999a, JGR, 104, 9709

Fludra, A., Saba, J. L. R., Henoux, J. ., Murphy, R. J., Reames, D. V., Lemen, J. R., Strong, K. T., Sylwester, J., & Widing, K. G. 1999b, in The many faces of the sun: a summary of the results from NASA's Solar Maximum Mission., 89+

Fludra, A. & Schmelz, J. T. 1995, ApJ, 447, 936+

—. 1999, Astron. Astrophys., 348, 286

Forsyth, R. J., Balogh, A., Horbury, T. S., Erdoes, G., Smith, E. J., & Burton, M. E. 1996, Astron. Astrophys., 316, 287

Foukal, P. 1990, Solar Astrophysics (John Wiley & Sons)

Gabriel, A. H. 1971, Sol. Phys., 21, 392+

Gallagher, P. T., Mathioudakis, M., Keenan, F. P., Phillips, K. J. H., & Tsinganos, K. 1999, Astrophys. J. Letters, 524, L133

Gardner, L. D., Kohl, J. L., Noci, G., Antonucci, E., Tondello, G., Huber, M. C. E., Ciaravella, A., Fineschi, S., Giordano, S., Moran, T., Naletto, G., Nicolosi, P., Romoli, M., Strachan, L., Benna, C., Pernechele, C., Raymond, J. C., Siegmund, O. H. W., Spadaro, D., & Smith, P. L. 1996, in American Astronomical Society Meeting, Vol. 188, 3705+

Geiss, J. 1998, Space Science Reviews, 85, 241

Geiss, J., Gloeckler, G., von Steiger, R., Balsiger, H., Fisk, L. A., Galvin, A. B., Ipavich, F. M., Livi, S., McKenzie, J. F., Ogilvie, K. W., & Wilken, B. 1995, Science, 268, 1033+

Georgakilas, A. A., Koutchmy, S., & Alissandrakis, C. E. 1999, Astron. Astrophys., 341, 610

Gibson, S. E., Biesecker, D., Guhathakurta, M., Hoeksema, J. T., Lazarus, A. J., Linker, J., Mikic, Z., Pisanko, Y., Riley, P., Steinberg, J., Strachan, L., Szabo, A., Thompson, B. J., & Zhao, X. P. 1999a, ApJ, 520, 871

Gibson, S. E., Fludra, A., Bagenal, F., Biesecker, D., del Zanna, G., & Bromage, B. 1999b, JGR, 104, 9691

Giordano, S. 1998, PhD thesis, , Univ. Torino, (1998)

Goldberg, L., Muller, E. A., & Aller, L. H. 1960, Astrophys. J. Suppl. Ser., 5, 1

Gosling, J. T., Asbridge, J. R., Bame, S. J., Feldman, W. C., Borrini, G., & Hansen, R. T. 1981, JGR, 86, 5438

Gosling, J. T., Bame, S. J., Feldman, W. C., McComas, D. J., Phillips, J. L., Goldstein, B., Neugebauer, M., Burkepile, J., Hundhausen, A. J., & Acton, L. 1995, Geophys. Res. Lett., 22, 3329

Guhathakurta, M., Sittler, E., Fisher, R., McComas, D., & Thompson, B. 1999, Geophys. Res. Lett., 26, 2901

Habbal, S. R. 1992, Annales Geophysicae, 10, 34

Habbal, S. R., Esser, R., & Arndt, M. B. 1993, ApJ, 413, 435

Habbal, S. R. & Gonzalez, R. D. 1991, Astrophys. J. Letters, 376, L25

Habbal, S. R. & Woo, R. 2001, Astrophys. J. Letters, 549, L253

Habbal, S. R., Woo, R., Fineschi, S., O'Neal, R., Kohl, J., Noci, G., & Korendyke, C. 1997, Astrophys. J. Letters, 489, L103

Haisch, B., Saba, J. L. R., & Meyer, J. 1996, in IAU Colloq. 152: Astrophysics in the Extreme Ultraviolet, 511+

Handy, B. N., Acton, L. W., Kankelborg, C. C., Wolfson, C. J., Akin, D. J., Bruner, M. E., Caravalho, R., Catura, R. C., Chevalier, R., Duncan, D. W., Edwards, C. G., Feinstein, C. N., Freeland, S. L., Friedlaender, F. M., Hoffmann, C. H., Hurlburt, N. E., Jurcevich, B. K., Katz, N. L., Kelly, G. A., Lemen, J. R., Levay, M., Lindgren, R. W., Mathur, D. P., Meyer, S. B., Morrison, S. J., Morrison, M. D., Nightingale, R. W., Pope, T. P., Rehse, R. A., Schrijver, C. J., Shine, R. A., Shing, L., Strong, K. T., Tarbell, T. D., Title, A. M., Torgerson, D. D., Golub, L., Bookbinder, J. A., Caldwell, D., Cheimets, P. N., Davis, W. N., Deluca, E. E., McMullen, R. A., Warren, H. P., Amato, D., Fisher, R., Maldonado, H., & Parkinson, C. 1999, Sol. Phys., 187, 229

Harrison, R. A., Sawyer, E. C., Carter, M. K., Cruise, A. M., Cutler, R. M., Fludra, A., Hayes, R. W., Kent, B. J., Lang, J., Parker, D. J., Payne, J., Pike, C. D., Peskett, S. C., Richards, A. G., Culhane, J. L., Norman, K., Breeveld, A. A., Breeveld, E. R., Janabi, K. F. A., McCalden, A. J., Parkinson, J. H., Self, D. G., Thomas, P. D., Poland, A. I., Thomas, R. J., Thompson, W. T., Kjeldseth-Moe, O., Brekke, P., Karud, J., Maltby, P.,

Aschenbach, B., Brauninger, H., Kuhne, M., Hollandt, J., Siegmund, O. H. W., Huber, M. C. E., Gabriel, A. H., Mason, H. E., & Bromage, B. J. I. 1995, Sol. Phys., 162, 233

Harrison, R. A. & Thompson, A. M. 1992, RAL, 91, 092

Hassler, D. M., Wilhelm, K., Lemaire, P., & Schuehle, U. 1997, Sol. Phys., 175, 375

Haugan, S. V. H. 1997, CDS software note, 47

—. 1999, Sol. Phys., 185, 275

Hubeny, I., Hummer, D. G., & Lanz, T. 1994, Astron. Astrophys., 282, 151

Hummer, D. G. & Storey, P. J. 1987, Mon. Not. R. Astron. Soc., 224, 801

Hundhausen, A. J. 1972, Coronal Expansion and Solar Wind (Springer-Verlag Berlin Heidelberg New York)

Ipavich, F. M., Galvin, A. B., Geiss, J., Ogilvie, K. W., & Gliem, F. 1992, in Solar Wind Seven Colloquium, 369–373

Jenkins, F. A. & White, H. E. 1957, Fundamentals of optics (New York: McGraw-Hill, 1957, 3rd ed.)

Joselyn, J., Munro, R. H., & Holzer, T. E. 1979, Sol. Phys., 64

Karovska, M., Blundell, S. F., & Habbal, S. R. 1994, ApJ, 428, 854

Karovska, M. & Habbal, S. R. 1994, Astrophys. J. Letters, 431, L59

Ko, Y., Fisk, L. A., Geiss, J., Gloeckler, G., & Guhathakurta, M. 1997, Sol. Phys., 171, 345

Kohl, J. L., Esser, R., Gardner, L. D., Habbal, S., Daigneau, P. S., Dennis, E. F., Nystrom, G. U., Panasyuk, A., Raymond, J. C., Smith, P. L., Strachan, L., van Ballegooijen, A. A., Noci, G., Fineschi, S., Romoli, M., Ciaravella, A., Modigliani, A., Huber, M. C. E., Antonucci, E., Benna, C., Giordano, S., Tondello, G., Nicolosi, P., Naletto, G., Pernechele, C., Spadaro, D., Poletto, G., Livi, S., von der Luhe, O., Geiss, J., Timothy, J. G., Gloeckler, G., Allegra, A., Basile, G., Brusa, R., Wood, B., Siegmund, O. H. W., Fowler, W., Fisher, R., & Jhabvala, M. 1995, Sol. Phys., 162, 313

Kohl, J. L. & Withbroe, G. L. 1982, ApJ, 256, 263

Koutchmy, S. 1977, Sol. Phys., 51, 399

Laming, J. M., Feldman, U., Drake, J. J., & Lemaire, P. 1999, ApJ, 518, 926

Landi, E. & Landini, M. 1998, Astron. Astrophys., 340, 265

Landi, E., Landini, M., Dere, K. P., Young, P. R., & Mason, H. E. 1999, Astron. Astrophys. Suppl. Ser., 135, 339

Landi, E., Landini, M., Pike, C. D., & Mason, H. E. 1997, Sol. Phys., 175, 553

Lang, J., Kent, B. . J., Breeveld, A. . A., Breeveld, E. . R., Bromage, B. . J. I., Hollandt, J., Payne, J., Pike, C. . D., & Thompsom, W. . T. 1999, Technical Report

Li, J. Z. & Hu, J. Y. 1998, Astron. Astrophys. Suppl. Ser., 132, 173

Loucif, M. L. 1994, Astron. Astrophys., 281, 95

Mariska, J. T. 1978, ApJ, 225, 252

—. 1992, The solar transition region (Cambridge Astrophysics Series, New York: Cambridge University Press, —c1992)

Marocchi, D., Antonucci, E., & Giordano, S. 2001, Annales Geophysicae, 19, 135

Marsch, E., Schwenn, R., Antonucci, E., Bochsler, P., Bougeret, J. ., Fleck, B., Harrison, R., Marsden, R., & Vial, J. . 2000, in IAU Symposium, Vol. 203, E177

Mason, H. E., Landi, E., Pike, C. D., & Young, P. R. 1999, Sol. Phys., 189, 129

Mason, H. E. & Monsignori Fossi, B. C. M. 1994, Astron. Astrophys. Rev., 6, 123

Mason, H. E., Young, P. R., Pike, C. D., Harrison, R. A., Fludra, A., Bromage, B. J. I., & del Zanna, G. 1997, Sol. Phys., 170, 143

Mazzotta, P., Mazzitelli, G., Colafrancesco, S., & Vittorio, N. 1998, Astron. Astrophys. Suppl. Ser., 133, 403

McComas, D. J., Bame, S. J., Barraclough, B. L., Feldman, W. C., Funsten, H. O., Gosling, J. T., Riley, P., Skoug, R., Balogh, A., Forsyth, R., Goldstein, B. E., & Neugebauer, M. 1998, Geophys. Res. Lett., 25, 1

McComas, D. J., Barraclough, B. L., Funsten, H. O., Gosling, J. T., Santiago-Muñoz, E., Skoug, R. M., Goldstein, B. E., Neugebauer, M., Riley, P., & Balogh, A. 2000, JGR, 105, 10419

McKenzie, D. L. & Feldman, U. 1992, ApJ, 389, 764

Meyer, J. . 1985a, Astrophys. J. Suppl. Ser., 57, 151

—. 1985b, Astrophys. J. Suppl. Ser., 57, 173

Meyer, J. 1991, Advances in Space Research, 11, 269

Meyer, J. P. 1996, in The sun and beyond /edited by J. Tran Thanh Van, L. M. Celnikier, Hua Chon Trung, S. Vauclair , Proceedings of the Second Recontres du Vietnam, October 22-28, 1995. Cedex, France : Editions Frontieres, c1996, p. 27., 27+

Monsignori Fossi, B. C., Landini, M., Thomas, R. J., & Neupert, W. M. 1994, Advances in Space Research, 14, 163

Moore, R. L., Tang, F., Bohlin, J. D., & Golub, L. 1977, ApJ, 218, 286

Munro, R. H. & Mariska, J. T. 1977, Bull. Am. Astron. Soc., 9, 370

Naletto, G. 1996

Noci, G. & al. 1997, in Fifth SOHO Workshop: The Corona and Solar Wind Near Minimum Activity, 75+

Noci, G., Kohl, J. L., & Withbroe, G. L. 1987, ApJ, 315, 706

Noci, G. & Maccari, L. 1999, Astron. Astrophys., 341, 275

Ofman, L. 2000, Geophys. Res. Lett., 27, 2885

Parenti, S., Bromage, B. J. I., Poletto, G., Noci, G., Raymond, J. C., & Bromage, G. E. 2000a, Astron. Astrophys., 363, 800

Parenti, S., Bromage, B. J. I., Poletto, G., Noci, G., Raymond, J. C., & Bromage, G. E. 2000b, in IAU Symposium, Vol. 203, E147

Parenti, S., del Zanna, G., & Bromage, B. J. I. 1999a, in Ninth European Meeting on Solar Physics: Magnetic Fields and Solar Processes. Ninth Meeting of the Solar Physics Section of the Joint Astrophysics Division of the European Physical Society (EPS) and of the European Astronomical Society (EAS). Florence, Italy, 12-18 September, 1999. Proceedings published in ESA SP Series (SP-448), ed. A. Wilson., E131

Parenti, S., Poletto, G., Bromage, B. J. I., Suess, S., Raymond, J. C., & Noci, G. 2001, in Joint SOHO-ACE workshop 2001, submitted

Parenti, S., Poletto, G., Raymond, J. C., & Bromage, B. J. I. 1999b, in 8th SOHO Workshop: Plasma Dynamics and Diagnostic in the Solar Transition Region and Corona, 531

Patsourakos, S. & Vial, J. . 2000, Astron. Astrophys., 359, L1

Pike, C. D. & Harrison, R. A. 1997, Sol. Phys., 175, 457

Pike, C. D. & Mason, H. E. 1998, Sol. Phys., 182, 333

Pneuman, G. W. & Kopp, R. A. 1971, Sol. Phys., 18, 258+

Pottasch, S. R. 1963, ApJ, 137, 945+

—. 1964, Space Sci. Rev., 3, 816

Priest, E. R. 1982, Solar magneto-hydrodynamics (Dordrecht, Holland ; Boston : D. Reidel Pub. Co. ; Hingham,)

Raymond, J. C. 1988, in Hot Thin Plasmas in Astrophysics, 3

Raymond, J. C., Kohl, J. L., Noci, G., Antonucci, E., Tondello, G., Huber, M. C. E., Gardner, L. D., Nicolosi, P., Fineschi, S., Romoli, M., Spadaro, D., Siegmund, O. H. W., Benna, C., Ciaravella, A., Cranmer, S., Giordano, S., Karovska, M., Martin, R., Michels, J., Modigliani, A., Naletto, G., Panasyuk, A., Pernechele, C., Poletto, G., Smith, P. L., Suleiman, R. M., & Strachan, L. 1997, Sol. Phys., 175, 645

Raymond, J. C., Suleiman, R., & Kohl, J. L. 1998, Space Science Reviews, 85, 283+

Romoli, M., Weiser, H., Gardner, L. D., & Kohl, J. L. 1993, Applied Optics, 32, 3559

Rosembauer, H. R. 1977, J. Geophys., 42, 561

Ryutova, M. P. & Tarbell, T. D. 2000, Astrophys. J. Letters, 541, L29

Saito, K. 1965, Publ. Astron. Soc. Japan, 17, 1

—. 1970, Ann. Tokyo Astron. Obs. Ser. 2, 12, 53

Schmelz, J. T. 1999, in 8th SOHO Workshop: Plasma Dynamics and Diagnostic in the Solar Transition Region and Corona, 585

Schmelz, J. T., Saba, J. L. R., Strong, K. T., Winter, H. D., & Brosius, J. W. 1999, ApJ, 523, 432

Scholz, T. T. & Walters, H. R. J. 1991, ApJ, 380, 302

Schwadron, N. A., Fisk, L. A., & Zurbuchen, T. H. 1999, ApJ, 521, 859

Siegmund, O. H., Stock, J. M., Marsh, D. R., Gummin, M. A., Raffanti, R., Hull, J., Gaines, G. A., Welsh, B. Y., Donakowski, B., Jelinsky, P. N., Sasseen, T., Tom, J. L., Higgins, B., Magoncelli, T., Hamilton, J. W., Battel, S. J., Poland, A. I., Jhabvala, M. D., Sizemore, K., & Shannon, J. 1994, Proc.SPIE, 2280, 89

Solar-B WWW page. 2001, http://www.mssl.ucl.ac.uk/Solar-B/index.html

Sterling, A. C., Pike, C. D., Mason, H. E., Watanabe, T., & Antiochos, S. K. 1999, ApJ, 524, 1096

Strachan, L., Panasyuk, A. V., Dobrzycka, D., Kohl, J., Noci, G., Gibson, S. E., & Biesecker, D. A. 2000, JGR, 105, 2345+

Suematsu, Y., Wang, H., & Zirin, H. 1995, ApJ, 450, 411

Suess, S. T. 2001, http://cfa-www.harvard.edu/ yko/JOP112/index.html

Suess, S. T., Poletto, G., Romoli, M., Neugebauer, M., Goldstein, B., & Simnett, G. 2000, JGR, 105, 25033

Suess, S. T., Wang, A. ., & Wu, S. T. 1996, JGR, 101, 19957

Suess, S. T., Wang, A. ., Wu, S. T., Poletto, G., & McComas, D. J. 1999, JGR, 104, 4697

Summers, H. P. 1979, AL

Thomas, R. J., Davila, J. M., Thompson, W. T., Kent, B. J., & Hollandt, J. 1999, in American Astronomical Society Meeting, Vol. 194, 1606+

Thomas, R. J. & Neupert, W. M. 1994, Astrophys. J. Suppl. Ser., 91, 461

Thompson, W. 1998, CDS Software Note, 49

Uchida, Y., McAllister, A., Strong, K. T., Ogawara, Y., Shimizu, T., Matsumoto, R., & Hudson, H. S. 1992, Publ. Astron. Soc. Japan, 44, L155

Vernazza, J. E. & Reeves, E. M. 1978, Astrophys. J. Suppl. Ser., 37, 485

von Steiger, R. 1998, in Solar Composition and Its Evolution – From Core to Corona, 407

von Steiger, R., Schwadrom, N. A., Fisk, L. . A., Geiss, J., Gloeckler, G., Hefti, S., Wilken, B., Wimmer-Schweingruber, R. . F., & H., Z. T. . 2000, JGR, 105, 27217

von Steiger, R., Schweingruber, R. F. W., Geiss, J., & Gloeckler, G. 1995, Advances in Space Research, 15, 3

Walker, A. B. C., Deforest, C. E., Hoover, R. B., & Barbee, T. W. 1993, Sol. Phys., 148, 239

Walker, A. B. C., Lindblom, J. F., Barbee, T. W., & Hoover, R. B. 1988, Science, 241, 1781

Wang, A. H., Wu, S. T., Suess, S. T., & Poletto, G. 1998, JGR, 103, 1913+

Wang, H. 1998, ApJ, 509, 461

Wenzel, K. P., Marsden, R. G., Page, D. E., & Smith, E. J. 1992, Astron. Astrophys. Suppl. Ser., 92, 207+

White, S. M., Thomas, R. J., Brosius, J. W., & Kundu, M. R. 2000, Astrophys. J. Letters, 534, L203

Widing, K. G. & Feldman, U. 1989, ApJ, 344, 1046

—. 1992a, ApJ, 392, 715

Widing, K. G. & Feldman, U. 1992b, in Solar Wind Seven Colloquium, 405–410

—. 1993, ApJ, 416, 392+

Wiese, W. L., Smith, M. W., & Glennon, B. M. 1966, Atomic transition probabilities. Vol.: Hydrogen through Neon. A critical data compilation (NSRDS-NBS 4, Washington, D.C.: US Department of Commerce, National Buereau of Standards, 1966)

Wilhelm, K. 2000, Astron. Astrophys., 360, 351

Wilhelm, K., Curdt, W., Marsch, E., Schuhle, U., Lemaire, P., Gabriel, A., Vial, J. ., Grewing, M., Huber, M. C. E., Jordan, S. D., Poland, A. I., Thomas, R. J., Kuhne, M., Timothy, J. G., Hassler, D. M., & Siegmund, O. H. W. 1995, Sol. Phys., 162, 189

Wilhelm, K., Innes, E. E., Curdt, W., Kliem, B., & Brekke, P. 1998a, in ESA SP-421: Solar Jets and Coronal Plumes, 103

Wilhelm, K., Marsch, E., Dwivedi, B. N., Hassler, D. M., Lemaire, P., Gabriel, A. H., & Huber, M. C. E. 1998b, ApJ, 500, 1023+

Wimmer Schweingruber, R. F. 1994, PhD thesis, , Univ. Bern, (1994)

Withbroe, G. L. 1978, ApJ, 225, 641

—. 1988, ApJ, 325, 442

Withbroe, G. L., Jaffe, D. T., Foukal, P. V., Huber, M. C. E., Noyes, R. W., Reeves, E. M., Schmahl, E. J., Timothy, J. G., & Vernazza, J. E. 1976, ApJ, 203, 528

Withbroe, G. L., Kohl, J. L., Weiser, H., & Munro, R. H. 1982, Space Science Reviews, 33, 17

Woo, R. & Habbal, S. R. 1997, Astrophys. J. Letters, 474, L139

Woo, R., Habbal, S. R., Howard, R. A., & Korendyke, C. M. 1999, ApJ, 513, 961

Young, P. R., Klimchuk, J. A., & Mason, H. E. 1999, Astron. Astrophys., 350, 286

Young, P. R., Landi, E., & Thomas, R. J. 1998, Astron. Astrophys., 329, 291

Young, P. R. & Mason, H. E. 1997, Sol. Phys., 175, 523